University of Naples Federico II

Department of Chemical, Materials and Production Engineering

Ph.D. thesis in
INDUSTRIAL PRODUCT AND PROCESS ENGINEERING
XXXV cycle

IMPACT OF MATERIAL ENGINEERING ON STABILITY OF LIPID-BASED NANOPARTICLES AND THEIR APPLICATION TO MICRORNAS

Scientific Committee:
Prof. Enza Torino (Supervisor)
Prof. Paolo Antonio Netti,
Prof. Giuliana Salvatore,
Prof. Laura Mezzanotte,
Prof. Patrick Tabeling

Candidate:
Felicia Roffo

Ph.D. program coordinator:
Prof. Andrea D'Anna

TABLE OF CONTENT

BACKGROUND, AIM OF THE WORK AND MAJOR FINDINGS

Nanomedicine is a flourishing field where the nanotechnology, pharmaceutical and biomedical science converge to develop of nanoformulations, defined by the Food and Drug Administration (FDA) as the product associated with nanoparticles ranging from 1-100 nm that show size-dependent properties[1-3]. The size reduction down to the nanoscale hugely benefits the loaded pharmaceutical active, regarding high bioavailability, enhanced delivery ability and improved pharmacokinetics[2, 4]. These objects are designed as real nanovehicles using different materials and characteristics that offer unique properties for cancer treatment due to the possibility of regulating the release kinetics of the active cargo in adjustable manner and exploiting the passive targeting through the EPR (Enhanced Permeability Retention) effect and active targeting by specific functionalization of the NPs[5-7]. Indeed, increasing of local dose in the disease site reduces systemic toxicity for cancer therapy and improves the sensitivity in the detection of cancer lesions with respect to healthy tissue for diagnosis[2, 8, 9].

Among different categories of NPs, polymeric NPs have demonstrated high structural integrity, controlled release behaviour and stability during storage [2]. Compared to polymeric material, the lipids, being basically analogues of biological membranes, made the liposomes as almost ideal drug delivery vehicles to overcome the limitation of polymer nanoparticles because of their superior biocompatibility[6, 10, 11].

Indeed, around 16 nanopharmaceuticals for cancer therapeutics are currently on the market and the majority of them are liposome-based formulations; notably, the lipid-based formulations have entered in the clinical use against coronavirus disease 2019 (COVID-19)[6, 12, 13].

Liposomes are composed of single or mixtures of lipids, that naturally self-assemble in bilayer aggregates when placed in polar environments due to their amphiphilic nature [14, 15]. Liposomes are nano-sized vesicles made up of one bilayer or multiple layers enclosing an aqueous core, and this dual nature allows the loading of hydrophobic compounds in the lipid layer while hydrophilic ones in the core[16]. The optimization of liposome-based formulation took more than two decades of fundamental research in the scientific community, from their first discovery of liposome by Alec Bangham[17, 18]. Only back in 1995, there was the first approval by the Food and drug administration of a nano-drug with Doxil, a liposome-based product containing Doxorubicin. Compared to free Doxorubicin, the liposome formulation modified the drug's pharmacokinetics, prolonging the circulation time and increasing the targeting ability and efficacy of the treatment. Moreover, they lessened the side effects of Doxorubicin, reducing chronic cardiomyopathy and congestive heart failure[1, 19]. Since then, a variety of cytotoxic agent-loaded liposomes have been approved for clinical uses or are under clinical trials, such as DaunoXome®, Marqibo®, Depocyt®, MM-398®, Onivyde™, Myocet®[16, 20]. Also noteworthy is the use of the lipid-

based NPs as vehicles to deliver the antigen mRNA in two authorized vaccines against COVID-19, mRNA-1273[21] and BNT162b[13, 22]. The lipid components confer to the carrier unique features for nano-pharmaceutical applications, spanning from high biocompatibility, low immunogenicity, prolonged blood circulation, improved fluidity and deformability[1, 6, 13].

These multifaceted and flexible properties have put lipid-based carriers at the forefront of nanomedicines for cancer treatment. However, low chemical and colloidal stability, high drug release, high instability in biological fluids and rapid degradation by the reticuloendothelial system have been conferred upon liposomes, consequently reducing their therapeutic efficacy[23, 24]. Up to now, the big challenges to face in order to improve the carriers' limited therapeutic are the stability issues, including physico-chemical and biological ones[25-27]. Indeed, liposomes are prone to fusion, aggregation and leakage of compounds loaded. Their nature makes them sensitive to damage due to lipids' oxidative degradation or hydrolysis. In this regard, in 2018, the FDA published a guideline addressed to industries that clarified the need for stress test studies on liposome formulations to assess their structural integrity in different microenvironmental conditions[28]. One critical parameter for the stability of lipid-based carriers is the temperature which forces their storage at 4°C due to their loss of integrity at room temperature. These degradation pathways not only limit the stability of liposomes in the shelf-life and storage but also have been shown to affect their performance in a biological context[29]. The transition temperature of lipids makes a considerable difference in liposome stability in media and affects the drug release profiles. Any variations of in vitro stability, such as alteration of drug release kinetics and colloidal stability, aggregation and fusion, have an impact on in vivo applications[29, 30].

Generally, the physicochemical properties of carriers, named synthetic identities, dictate their biological identities, a contextual property corresponding to ‘what is seen’ by the cell during nano-cellular process of recognition that, in turn, guides their interaction with tissue, organs, and cells. Consequently, any changes in shape, size and charge due to stability issues directly affect the nano-bio interactions of the carrier and their therapeutic outcomes [31, 32]. Indeed, upon intravenous administration, the framework of sequential biological barriers encountered by NPs hinders efficacious, site-specific delivery to tumours. Firstly, protein will absorb on NPs creating a protein corona that will begin the new interface for the NPs with cells/tissue, consequently dictating the NPs uptake, biodistribution and immune response[31, 33-35]. Moreover, the protein corona helped the macrophage uptake and systemic clearance by Mononuclear Phagocyte System (MPS)[36]. To reach the tumour site, NPs should exit the vasculature, avoiding the filtration by the kidney[31, 37] and the clearance by the reticuloendothelial system of liver and spleen[31, 37]. Once inside the target tissue, they have to travel in the stroma and avoid degradation or sequestration in the extracellular matrix (ECM) and off-target cells[38, 39]. Finally, inside the cells, they should escape the endosome and reach the target site, cytoplasm[31, 40].

In particular, once injected into the body, these lipid-based structures, according to their charge, interact with proteins and blood cells with a higher binding for positive liposomes than negative ones[25]. Possible effects of these interactions could be shrinkage of liposomes, lipid bilayer disruption, and protein-mediated aggregation[36]. Following the pioneering clinical results on Doxil and Genexol, PEGylation has been considered a possible solution to increase the liposomes half-live, but its employment is debated[36, 41, 42]. Emerging studies emphasize a shift in composition of the protein corona between Pegylated and no- Pegylated liposomes, reporting a higher affinity of the former to serum proteins[36, 43]. Moreover, the steric hindrance of PEG coatings has been known to alter the cellular uptake and intracellular fate of liposome, so losing the peculiar cellular affinity with the cells[16].

Despite the instability issues, the rigidity and fluidity of lipid-based carriers emerged as novel concepts to refine the nano-bio interactions. The ability to alter the liposome membrane rigidity has been proven to enhance the interactions with proteins, cells and tissue[44-47].

In this sense, reduced adsorption of serum proteins with liposomes was reported upon the incorporation of cholesterol in the liposomal formulation[25, 48, 49]. Indeed, the cholesterol, through hydrogen binding to fatty acids, alters the fluidity of the lipid bilayer, increasing its cohesiveness and mechanical strength, reducing lipid leakage and increasing liposome integrity[50-52].

This capability of modulating the liposome elasticity have been investigated to face the rate-limiting step in cancer treatment, the tumour penetration[53, 54]. Indeed, once reached the tumour periphery, the liposomes should penetrate into the core portion of tumour tissues overcoming the larger diffusion hindrance in the tumour matrix[16]. To face this challenge, the soft colloidal nature of liposomes, that allows to infiltrate in tumour by particle diffusion through the intercellular space and cellular uptake[55-57], has been modified with surface functionalization or improved with environmentally sensitive components[58, 59], reporting antitumoral results. However, recent studies showed an enhanced penetration in 3D tumour spheroids of liposomes, without any specific modifications, only modulating the rigidity of liposomes for cholesterol addition[44]. Wu et al.[44] reported that liposomes with moderate membrane rigidity, diffuse higher in fibrotic structure and penetrate deeply into spheroids. Differently, liposome with lower or higher rigidity might be trapped in the surface of the tumour spheroids. Furthermore, Takechi-Haraya et al.[45] reported a higher diffusion efficiency in the intercellular space of tumour spheroids liposomes with larger bending moduli (Kc) due to their ability of being less deformable to the shear force effects of collagen and hyaluronic acid in the extracellular matrix. Therefore, the ability of modulating the liposomes fluidity becomes a tool for achieving superiority therapeutic efficacy in tumours with dense stroma, representing an alternative to PEGylation and liposome functionalization.

At cellular level, Bompard et al.[47] reported that the liposome fluidity determines liposome–cell interaction specificity and subsequent their fusion with cellular membrane.

Liposomes offer high cellular affinity and can be internalized in multiple ways, including fusion, micropinocytosis, clathrin-mediated and caveolae-mediated endocytosis[13]. Furthermore, liposomes can mix, exchange and merge phospholipids with the cytoplasmic membrane, releasing their content intact within the cytoplasm of the cell[60, 61], overcoming the issue of endosomal and lysosomal degradation of cargo.

Recently, hybrid carriers that combine the lipid components with not-lipid materials have been proposed with to overcome the limitations mentioned above the liposomes while preserving their advantageous features, such as deformability, fluidity, endosomal escape and cytosolic penetration[24, 62]. Among several materials, natural and synthetic polymers offer several advantages due to their versatile loading capability, controllable release kinetics, enhanced biological stability, due to the electrochemical interaction of the individual lipid-polymer components, and tunable mechanical properties[11, 63, 64]. Their mechanical properties can be tuned by varying the extent of crosslinking of the polymer core or the amount of water between the lipid shell and polymer core[65]. This adjustable elasticity improves their nano-bio interactions at multiple levels, spanning blood circulation performances, macrophage sequestration, squeezing through pores[66, 67], tumour tissue penetration[68] and NP-cell interaction[69].

These sophisticated nanoparticles require high control of process conditions to obtain NPs with well-defined synthetic identities. Two main categories of approaches have been developed for the production of lipid-polymer NPs, the two-step method that consists of the complexation of pre-formed liposomes and polymer NPs, and one step method where the polymer nanoprecipitation is combined to the self-assembly of lipids[11]. The latter was explored through microfluidics in terms of two-stage devices, micromixers and multi-inlet vortex microreactors. The microfluidics ability to deal with fluids in the macroscale domain enables higher control of microreactor conditions and, consequently, of NPs formation[70, 71]. Several microfluidic strategies were exploited to produce lipid-polymer NPs. Hong et al. [72] combined the on-chip formation with off-chip UV-polymerization to form a hydrogel core within the liposomes, and in the same year Valencia et al.[73] placed a Tesla micromixer in series with a Hydrodynamic Flow Focusing (HFF) junction to increase the mixing among species. Kim et al. [74] proposed a 3D pattern-tunable microvortex platform for synthesising lipid-polymer nanoparticles with high reproducibility. At the same time, Sun et al. [46] promoted the HFF in a two-stage microfluidic device to accurately assembly monolayer or bilayer of lipid onto polymeric core. Different microfluidic flow patterns have been investigated for lipid-polymer NPs production. Great efforts are being made to study material interaction's role on biological entities, from cells to tissue. Nevertheless, their comprehension still needs to be elucidated entirely.

This thesis aims to understand how the complexation of material, lipid and polymer influences the stability of the carrier, impacting on its performance at multiple levels. The interaction of these materials has been investigated in their processing, employing one step microfluidic process that enables control in a predictable manner the fluid interfaces to guide the formation and stabilize the hybrid lipid-polymer nanoparticle (LiPoNs). To gain further insight into the solvent interdiffusion and their spatial distribution along the device, a Comsol simulation of the convective-diffusive mixing taking place in the cHFF was computed. In a preliminary model, we have rationalized the effect of fluid confinement on nanoparticle formation, surpassing the concept of pure diffusion of solvents in describing their formation. The structural integrity of the final carrier and its cargo in different biological environments was investigated. We studied the role of material in mediating cellular interactions and the effective delivery of a stable cargo to the cells, going beyond the chemotherapeutic agents to more sensible molecules such as microRNAs. Furthermore, we investigated the impact of the NPs-cell interface on enabling or limiting the cell machinery at the single cell level.

Recently, we have presented "coupled Hydrodynamic Flow Focusing (cHFF) to Engineer Lipid–Polymer Nanoparticles (LiPoNs) for Multimodal Imaging and Theranostic Applications", to obtain a hybrid vector, where a bilayer shell made of phosphatidylcholine and cholesterol is electrostatically anchored to a polymeric chitosan core, to integrate the advantages of individual material components[75]. Innovations with respect to the traditional microfluidic process are introduced by reverse way to obtain lipid-based NPs (lipids are injected in the side channels and antisolvent in the middle channel) to guide the mutual coupling of two thermodynamics occurring in HFF, the nanoprecipitation of polymer and the self-assembly of lipids. Indeed, both the mainstream and the lateral stream are involved in their thermodynamic process and mutually influence each other. In the coupled Hydrodynamic Flow Focusing, the influence of process parameters such as flow rates, solvent-nonsolvent ratio, and solute concentration was investigated to govern the competition mechanisms of precipitation and extraction, thus, identifying the microfluidic conditions that allow obtaining stable lipid-polymer complex. The LiPoNs, with an average size of about 100 nm and a slightly negative surface charge, show excellent physical stability in different environmental conditions due to the architectural advantage of polymer core loading. The ability of polymer-lipid NPs (LiPoNs) to stabilize the compounds' loading was tested with multiple active agents for both Multimodal Imaging (Gd-DTPA and Atto 633) and therapy (Irinotecan hydrochloride). Then, the capability of delivering stable compounds was proved by internalization studies as well as the cytotoxic effects on U87 MG glioma cell line upon treatments with theranostics LiPoNs.

To further elucidate the role of materials and their complexation on the stability of the cargo, we selected microRNAs, very challenging and potential biologics characterized by low intrinsic stability. microRNAs are defined as master gene regulators, and their dysregulations in cancer have proven their strong involvement in cancer progression[76-79]. The emerging number of nucleic acid strategies used to treat diseases by targeting

cells' genetic blueprints have demonstrated their therapeutics effects via gene inhibition or replacement[80, 81]. However, several challenges limit and reduce their therapeutic potentials, such as rapid degradation in blood, low cellular and intracellular delivery, undesired on and off-target effects, immune system activation[77, 81]. Various materials have been employed to improve nucleic acid delivery, to overcome the concept of simple mix and use, widely applied for nucleic acid transfection, with a more accurate design of the nanocarrier[81]. However, the delivery technologies capable of improving their stability, increasing cellular internalization and targeting affinity are still restrained and limit their clinical translation[82]. Furthermore, the conventional techniques for nanoparticle production limit their loading without comprising their functional integrity[83]. In this framework, the possibility of the microfluidic cHFF approach to guide the lipid-polymer complexation in one step was exploited and optimized for nucleic acid therapeutics. The idea is that the protonated amine groups of the chitosan that strongly interact with negatively charged nucleic acids could form a stable polyelectrolyte complex[84]. At the same time the lipid bilayer covering the polymer core could potentially improve the vehicle's delivery properties by enhancing the half-life, biocompatibility and bioavailability[11, 13]. Among microRNAs, miR-21 is significantly dysregulated in several cancers and is associated with processes essential to disease progressions, such as cell proliferation, cell death, metastasis and chemoresistance[85, 86]. Therefore, we entrapped antisense oligonucleotide, AntimiR-21, in LiPoNs to inhibit miR-21 downstream pathways and repristinates the expression of the tumour suppressor genes[77, 87]. Firstly, we analysed the impact of different processing parameters on AntimiR-21 and lipid properties, and optimized the microfluid conditions to produce nucleic acids loaded nanoparticles in which an MRI- Contrast Agent (CA) is co-entrapped. We validated the efficacy of these theranostic nanostructures on the gene regulation and cell migration of MDA-MB-231 human breast cancer cells. Considering the limited cellular uptake of negative charge microRNAs, the well-orchestrated expression of all genes of interest upon the treatment with nucleic acids-LiPoNs, highlights the crucial role of lipid components in the design of nano-architectures to assist the delivery of chitosan-nucleic acids complex to the target cells and improving their interaction with biological systems, nano-bio interactions.

Starting from these considerations, to gain more insight into the role of nanomaterial in guiding cellular internalization pathways, we interrogate single cells upon contact with LiPoNs with an innovative live imaging instrument. We analysed live cells' dynamics and monitored cell behaviour at single cell level for 48 hours. We reported the cellular response upon LiPoNs treatment regarding shape, proliferation, mitosis and motility. We initially observed cell state and functioning alterations due to LiPoNs nanoparticles. We hypothesized that this cellular alteration could be an attempt of the cell to face external stress, and this physical change could impact cell biology, maybe cellular metabolism. This interference of cellular physiology due to materials interactions shows the nanoparticles as active players in cellular interactions. We reported a lack of biological

knowledge that could lead to implications in drug delivery and material science, opening opportunities for cancer treatment.

Following this acquired knowledge on the synergic effects of materials on nucleic acids delivery and the microfluidics approach for their engineering, we applied it to one of the most aggressive breast cancer, Triple Negative Breast Cancer[88, 89]. Triple negative breast cancer (TNBC) is very aggressive disease with a poor prognosis due to the limited treatment options, mainly chemotherapy[90]. Following the evidence on miR-622 downregulation in breast cancer, we engineered miR-622 loaded LiPoNs to efficiently deliver miR-622 in cancer cells and restore its function in altered tumour molecular pathways[91]. Furthermore, to face the need for a more accurate diagnosis of TNBC in the early stage, we co-load with gadolinium diethylenetriamine penta-acetic acid (Gd-DTPA) contrast agent for multimodal imaging. We studied the cell behaviour upon the treatment with miR-622-Gd-DTPA-LiPoNs. We preliminary validate the capability of LiPoNs to reach the tumour environment in a preclinical model.

In this work, microfluidics plays an essential role in stabilizing the active cargo and the nanoparticles. Therefore, the microfluidics ability of guide nanoparticle formation was further analysed from the perspectives of fluid interfaces and convective-diffusive mixing in the coupled HFF process with a Comsol simulation. Indeed, the role of fluid interfaces, through the mixing of species and solvent exchange, in guiding simultaneous the nanoprecipitation of polymer and the self-assembly of lipids were not fully exploited. This study aims to quantify the solvents' interdiffusion and their spatial distribution along the device. We numerically study the effects on the components mixing of both the microfluidic geometry and the thinning of the diffusion mixing path, which could be adjusted by changing the volumetric flow rate ratio between the side- and the middle-phase. Thus, we identified the flow focusing confinement, represented as the confinement exerted by flow rates and the device geometry in the flow focusing region, as the crucial parameter in guiding the growth of nanoparticles. In this regard, we analysed the state of art and organized the data on nanoparticles synthesis in HFF for lipid-based and polymer-based material. Interestingly, we reported a correlation between NPs size and thinning of the flow focusing in the HFF. We discussed the critical parameter that guide the nanoparticle formation in a preliminary model to predict the NPs size.

We believe these findings could inspire new engineering strategies to take advantage of fluid interfaces to guide hybrid nanocarriers, exploiting both the nanoprecipitation and the self-assembly. Moreover, we reveal the need for a better understanding of the coupling between fluid dynamics and mechanism of nanoparticles formation in microfluidics devices to obtain stable complexes. Indeed, the current methods describing nucleation and growth of nanoparticles in solution, should be elucidated for confined microreactors, where more phenomena occur simultaneously. Furthermore, these process conditions directly influence on material properties and consequently mediate different biological responses. We reveal a correlation between lipid-polymer materials and cell physiological response,

which, could be used for therapeutics and science application if comprehended. As prospective, the acquired data on the effects of nanomaterials complexation in microfluidics for nucleic acids delivery could be used to increase the efficacy in designing new generation treatments and tools for their production, paying the way to nucleic acids to Clinics. Indeed, the microfluidics technology, through modular and continuous production set-up, allows the preservation of process control and parameters predictability even for large-scale production.

REFERENCES

[1] T.T.H. Thi, E.J.A. Suys, J.S. Lee, D.H. Nguyen, K.D. Park, N.P. Truong, Lipid-Based Nanoparticles in the Clinic and Clinical Trials: From Cancer Nanomedicine to COVID-19 Vaccines, Vaccines 9(4) (2021).

[2] G.Y. Chen, I. Roy, C.H. Yang, P.N. Prasad, Nanochemistry and Nanomedicine for Nanoparticle-based Diagnostics and Therapy, Chemical Reviews 116(5) (2016) 2826-2885.

[3] D. Bobo, K.J. Robinson, J. Islam, K.J. Thurecht, S.R. Corrie, Nanoparticle-Based Medicines: A Review of FDA-Approved Materials and Clinical Trials to Date, Pharmaceutical Research 33(10) (2016) 2373-2387.

[4] L. Capretto, D. Carugo, S. Mazzitelli, C. Nastruzzi, X.L. Zhang, Microfluidic and lab-on-a-chip preparation routes for organic nanoparticles and vesicular systems for nanomedicine applications, Advanced Drug Delivery Reviews 65(11-12) (2013) 1496-1532.

[5] R. Singh, J.W. Lillard, Nanoparticle-based targeted drug delivery, Experimental and Molecular Pathology 86(3) (2009) 215-223.

[6] M.J. Mitchell, M.M. Billingsley, R.M. Haley, M.E. Wechsler, N.A. Peppas, R. Langer, Engineering precision nanoparticles for drug delivery, Nature Reviews Drug Discovery 20(2) (2021) 101-124.

[7] A. Shukla, P. Maiti, Nanomedicine and versatile therapies for cancer treatment, Medcomm 3(3) (2022).

[8] L.A. Lane, Physics in nanomedicine: Phenomena governing the in vivo performance of nanoparticles, Applied Physics Reviews 7(1) (2020).

[9] B.Y. Kim, J.T. Rutka, W.C. Chan, Nanomedicine, N Engl J Med 363(25) (2010) 2434-43.

[10] S. Gavas, S. Quazi, T.M. Karpinski, Nanoparticles for Cancer Therapy: Current Progress and Challenges, Nanoscale Research Letters 16(1) (2021).

[11] K. Hadinoto, A. Sundaresan, W.S. Cheow, Lipid-polymer hybrid nanoparticles as a new generation therapeutic delivery platform: A review, European Journal of Pharmaceutics and Biopharmaceutics 85(3) (2013) 427-443.

[12] J.A. Kemp, Y.J. Kwon, Cancer nanotechnology: current status and perspectives, Nano Convergence 8(1) (2021).

[13] X.C. Hou, T. Zaks, R. Langer, Y.Z. Dong, Lipid nanoparticles for mRNA delivery, Nature Reviews Materials 6(12) (2021) 1078-1094.

[14] Y.P. Patil, S. Jadhav, Novel methods for liposome preparation, Chemistry and Physics of Lipids 177 (2014) 8-18.

[15] G. Pabst, N. Kučerka, M.-P. Nieh, J. Katsaras, Liposomes, lipid bilayers and model membranes : from basic research to application, CRC Press, Taylor & Francis Group, Boca Raton, Florida, 2014.
[16] J. Cao, D. Huang, N.A. Peppas, Advanced engineered nanoparticulate platforms to address key biological barriers for delivering chemotherapeutic agents to target sites, Advanced Drug Delivery Reviews 167 (2020) 170-188.
[17] A.D. Bangham, R.W. Horne, NEGATIVE STAINING OF PHOSPHOLIPIDS AND THEIR STRUCTURAL MODIFICATION BY SURFACE-ACTIVE AGENTS AS OBSERVED IN THE ELECTRON MICROSCOPE, J Mol Biol 8 (1964) 660-8.
[18] S. Palazzoloa, S. Bayda, M. Hadla, I. Caligiuri, G. Corona, G. Toffoli, F. Rizzolio, The Clinical Translation of Organic Nanomaterials for Cancer Therapy: A Focus on Polymeric Nanoparticles, Micelles, Liposomes and Exosomes, Current Medicinal Chemistry 25(34) (2018) 4224-4268.
[19] Y. Barenholz, Doxil (R) - The first FDA-approved nano-drug: Lessons learned, Journal of Controlled Release 160(2) (2012) 117-134.
[20] E.M. Kim, H.J. Jeong, Liposomes: Biomedical Applications, Chonnam Med J 57(1) (2021) 27-35.
[21] L.R. Baden, H.M. El Sahly, B. Essink, K. Kotloff, S. Frey, R. Novak, D. Diemert, S.A. Spector, N. Rouphael, C.B. Creech, J. McGettigan, S. Khetan, N. Segall, J. Solis, A. Brosz, C. Fierro, H. Schwartz, K. Neuzil, L. Corey, P. Gilbert, H. Janes, D. Follmann, M. Marovich, J. Mascola, L. Polakowski, J. Ledgerwood, B.S. Graham, H. Bennett, R. Pajon, C. Knightly, B. Leav, W.P. Deng, H.H. Zhou, S. Han, M. Ivarsson, J. Miller, T. Zaks, C.S. Grp, Efficacy and Safety of the mRNA-1273 SARS-CoV-2 Vaccine, New England Journal of Medicine 384(5) (2021) 403-416.
[22] F.P. Polack, S.J. Thomas, N. Kitchin, J. Absalon, A. Gurtman, S. Lockhart, J.L. Perez, G.P. Marc, E.D. Moreira, C. Zerbini, R. Bailey, K.A. Swanson, S. Roychoudhury, K. Koury, P. Li, W.V. Kalina, D. Cooper, R.W. Frenck, L.L. Hammitt, O. Tureci, H. Nell, A. Schaefer, S. Unal, D.B. Tresnan, S. Mather, P.R. Dormitzer, U. Sahin, K.U. Jansen, W.C. Gruber, C.C.T. Grp, Safety and Efficacy of the BNT162b2 mRNA Covid-19 Vaccine, New England Journal of Medicine 383(27) (2020) 2603-2615.
[23] S. Bochicchio, G. Lamberti, A.A. Barba, Polymer-Lipid Pharmaceutical Nanocarriers: Innovations by New Formulations and Production Technologies, Pharmaceutics 13(2) (2021).
[24] W.W. Gao, C.M.J. Hu, R.H. Fang, L.F. Zhang, Liposome-like nanostructures for drug delivery, Journal of Materials Chemistry B 1(48) (2013) 6569-6585.
[25] P. Nakhaei, R. Margiana, D.O. Bokov, W.K. Abdelbasset, M.A.J. Kouhbanani, R.S. Varma, F. Marofi, M. Jarahian, N. Beheshtkhoo, Liposomes: Structure, Biomedical Applications, and Stability Parameters With Emphasis on Cholesterol, Frontiers in Bioengineering and Biotechnology 9 (2021).
[26] J.Y. Yu, P. Chuesiang, G.H. Shin, H.J. Park, Post-Processing Techniques for the Improvement of Liposome Stability, Pharmaceutics 13(7) (2021).
[27] A.V. Yadav, M.S. Murthy, A.S. Shete, S. Sakhare, Stability Aspects of Liposomes, Indian Journal of Pharmaceutical Education and Research 45(4) (2011) 402-413.

[28] U. Fda, Liposome drug products chemistry, manufacturing, and controls; human pharmacokinetics and bioavailability; and labeling documentation, Guidance for Industry (2018).
[29] M. Anderson, A. Omri, The effect of different lipid components on the in vitro stability and release kinetics of liposome formulations, Drug Delivery 11(1) (2004) 33-39.
[30] M.H. Shi, M. Anantha, M. Wehbe, M.B. Bally, D. Fortin, L.O. Roy, G. Charest, M. Richer, B. Paquette, L. Sanche, Liposomal formulations of carboplatin injected by convection-enhanced delivery increases the median survival time of F98 glioma bearing rats, Journal of Nanobiotechnology 16 (2018).
[31] W. Poon, B.R. Kingston, B. Ouyang, W. Ngo, W.C.W. Chan, A framework for designing delivery systems, Nature Nanotechnology 15(10) (2020) 819-829.
[32] E. Blanco, H. Shen, M. Ferrari, Principles of nanoparticle design for overcoming biological barriers to drug delivery, Nature Biotechnology 33(9) (2015) 941-951.
[33] S. Tenzer, D. Docter, J. Kuharev, A. Musyanovych, V. Fetz, R. Hecht, F. Schlenk, D. Fischer, K. Kiouptsi, C. Reinhardt, K. Landfester, H. Schild, M. Maskos, S.K. Knauer, R.H. Stauber, Rapid formation of plasma protein corona critically affects nanoparticle pathophysiology, Nature Nanotechnology 8(10) (2013) 772-U1000.
[34] D. Walczyk, F.B. Bombelli, M.P. Monopoli, I. Lynch, K.A. Dawson, What the Cell "Sees" in Bionanoscience, Journal of the American Chemical Society 132(16) (2010) 5761-5768.
[35] M.P. Monopoli, C. Aberg, A. Salvati, K.A. Dawson, Biomolecular coronas provide the biological identity of nanosized materials, Nature Nanotechnology 7(12) (2012) 779-786.
[36] N. Onishchenko, D. Tretiakova, E. Vodovozova, Spotlight on the protein corona of liposomes, Acta Biomaterialia 134 (2021) 57-78.
[37] S.H. Jang, M.G. Wientjes, D. Lu, J.L.S. Au, Drug delivery and transport to solid tumors, Pharmaceutical Research 20(9) (2003) 1337-1350.
[38] P.A. Netti, D.A. Berk, M.A. Swartz, A.J. Grodzinsky, R.K. Jain, Role of extracellular matrix assembly in interstitial transport in solid tumors, Cancer Research 60(9) (2000) 2497-2503.
[39] E.A. Sykes, Q. Dai, C.D. Sarsons, J. Chen, J.V. Rocheleau, D.M. Hwang, G. Zheng, D.T. Cramb, K.D. Rinker, W.C.W. Chan, Tailoring nanoparticle designs to target cancer based on tumor pathophysiology, Proceedings of the National Academy of Sciences of the United States of America 113(9) (2016) E1142-E1151.
[40] S. Behzadi, V. Serpooshan, W. Tao, M.A. Hamaly, M.Y. Alkawareek, E.C. Dreaden, D. Brown, A.M. Alkilany, O.C. Farokhzad, M. Mahmoudi, Cellular uptake of nanoparticles: journey inside the cell, Chemical Society Reviews 46(14) (2017) 4218-4244.
[41] C. Allen, N. Dos Santos, R. Gallagher, G.N.C. Chiu, Y. Shu, W.M. Li, S.A. Johnstone, A.S. Janoff, L.D. Mayer, M.S. Webb, M.B. Bally, Controlling the physical behavior and biological performance of liposome formulations through use of surface grafted poly(ethylene glycol), Bioscience Reports 22(2) (2002) 225-250.
[42] S.M. Moghimi, J. Szebeni, Stealth liposomes and long circulating nanoparticles: critical issues in pharmacokinetics, opsonization and protein-binding properties, Progress in Lipid Research 42(6) (2003) 463-478.
[43] H. Shibata, H. Yoshida, K.I. Izutsu, Y. Haishima, T. Kawanishi, H. Okuda, Y. Goda, Interaction kinetics of serum proteins with liposomes and their effect on phospholipase-

induced liposomal drug release, International Journal of Pharmaceutics 495(2) (2015) 827-839.
[44] H.Y. Wu, M.R. Yu, Y.Q. Miao, S.F. He, Z. Dai, W.Y. Song, Y. Liu, S. Song, E. Ahmad, D.K. Wang, Y. Gan, Cholesterol-tuned liposomal membrane rigidity directs tumor penetration and anti-tumor effect, Acta Pharmaceutica Sinica B 9(4) (2019) 858-870.
[45] Y. Takechi-Haraya, Y. Goda, K. Sakai-Kato, Control of Liposomal Penetration into Three-Dimensional Multicellular Tumor Spheroids by Modulating Liposomal Membrane Rigidity, Molecular Pharmaceutics 14(6) (2017) 2158-2165.
[46] J.S. Sun, L. Zhang, J.L. Wang, Q. Feng, D.B. Liu, Q.F. Yin, D.Y. Xu, Y.J. Wei, B.Q. Ding, X.H. Shi, X.Y. Jiang, Tunable Rigidity of (Polymeric Core)-(Lipid Shell) Nanoparticles for Regulated Cellular Uptake, Advanced Materials 27(8) (2015) 1402-+.
[47] J. Bompard, A. Rosso, L. Brizuela, S. Mebarek, L.J. Blum, A.M. Trunfio-Sfarghiu, G. Lollo, T. Granjon, A. Girard-Egrot, O. Maniti, Membrane Fluidity as a New Means to Selectively Target Cancer Cells with Fusogenic Lipid Carriers, Langmuir 36(19) (2020) 5134-5144.
[48] J. Damen, J. Regts, G. Scherphof, Transfer and exchange of phospholipid between small unilamellar liposomes and rat plasma high density lipoproteins. Dependence on cholesterol content and phospholipid composition, Biochim Biophys Acta 665(3) (1981) 538-45.
[49] M.L. Immordino, F. Dosio, L. Cattel, Stealth liposomes: review of the basic science, rationale, and clinical applications, existing and potential, International Journal of Nanomedicine 1(3) (2006) 297-315.
[50] M. Sun, N. Northup, F. Marga, T. Huber, F.J. Byfield, I. Levitan, G. Forgacs, The effect of cellular cholesterol on membranecytoskeleton adhesion, Journal of Cell Science 120(13) (2007) 2223-2231.
[51] M. Ricci, R. Oliva, P. Del Vecchio, M. Paolantoni, A. Morresi, P. Sassi, DMSO-induced perturbation of thermotropic properties of cholesterol-containing DPPC liposomes, Biochimica Et Biophysica Acta-Biomembranes 1858(12) (2016) 3024-3031.
[52] P. Trucillo, R. Campardelli, E. Reverchon, Supercritical CO2 assisted liposomes formation: Optimization of the lipidic layer for an efficient hydrophilic drug loading, Journal of Co2 Utilization 18 (2017) 181-188.
[53] F.R.E. Curry, Redefining tumour vascular barriers, Nature Nanotechnology 11(6) (2016) 494-496.
[54] K.R. Levental, H.M. Yu, L. Kass, J.N. Lakins, M. Egeblad, J.T. Erler, S.F.T. Fong, K. Csiszar, A. Giaccia, W. Weninger, M. Yamauchi, D.L. Gasser, V.M. Weaver, Matrix Crosslinking Forces Tumor Progression by Enhancing Integrin Signaling, Cell 139(5) (2009) 891-906.
[55] A.T. Florence, "Targeting" nanoparticles: The constraints of physical laws and physical barriers, Journal of Controlled Release 164(2) (2012) 115-124.
[56] Y. Gao, M.G. Li, B. Chen, Z.C. Shen, P. Guo, M. GuillaumeWientjes, J.L.S. Au, Predictive Models of Diffusive Nanoparticle Transport in 3-Dimensional Tumor Cell Spheroids, Aaps Journal 15(3) (2013) 816-831.
[57] M.G. Wientjes, B.Z. Yeung, Z. Lu, J.L.S. Au, Predicting diffusive transport of cationic liposomes in 3-dimensional tumor spheroids, Journal of Controlled Release 192 (2014) 10-18.
[58] J.J. Tang, Q.T. Wang, Q.W. Yu, Y. Qiu, L. Mei, D.D. Wan, X.H. Wang, M. Li, Q. He, A stabilized retro-inverso peptide ligand of transferrin receptor for enhanced liposome-

based hepatocellular carcinoma-targeted drug delivery, Acta Biomaterialia 83 (2019) 379-389.
[59] M.A. Aghdam, R. Bagheri, J. Mosafer, B. Baradaran, M. Hashemzaei, A. Baghbanzadeh, M. de la Guardi, A. Mokhtarzadeh, Recent advances on thermosensitive and pH-sensitive liposomes employed in controlled release, Journal of Controlled Release 315 (2019) 1-22.
[60] A. Panariti, G. Miserocchi, I. Rivolta, The effect of nanoparticle uptake on cellular behavior: disrupting or enabling functions?, Nanotechnology Science and Applications 5 (2012) 87-100.
[61] I. Rivolta, A. Panariti, B. Lettiero, S. Sesana, P. Gasco, M.R. Gasco, M. Masserini, G. Miserocchi, CELLULAR UPTAKE OF COUMARIN-6 AS A MODEL DRUG LOADED IN SOLID LIPID NANOPARTICLES, Journal of Physiology and Pharmacology 62(1) (2011) 45-53.
[62] Y.H. Yao, Y.X. Zhou, L.H. Liu, Y.Y. Xu, Q. Chen, Y.L. Wang, S.J. Wu, Y.C. Deng, J.M. Zhang, A.W. Shao, Nanoparticle-Based Drug Delivery in Cancer Therapy and Its Role in Overcoming Drug Resistance, Frontiers in Molecular Biosciences 7 (2020).
[63] A. Mukherjee, A.K. Waters, P. Kalyan, A.S. Achrol, S. Kesari, V.M. Yenugonda, Lipid-polymer hybrid nanoparticles as a next-generation drug delivery platform: state of the art, emerging technologies, and perspectives, International Journal of Nanomedicine 14 (2019) 1937-1952.
[64] S. Shah, P. Famta, R.S. Raghuvanshi, S.B. Singh, S. Srivastava, Lipid polymer hybrid nanocarriers: Insights into synthesis aspects, characterization, release mechanisms, surface functionalization and potential implications, Colloid and Interface Science Communications 46 (2022).
[65] Y. Hui, X. Yi, F. Hou, D. Wibowo, F. Zhang, D.Y. Zhao, H.J. Gao, C.X. Zhao, Role of Nanoparticle Mechanical Properties in Cancer Drug Delivery, Acs Nano 13(7) (2019) 7410-7424.
[66] Y. Hui, D. Wibowo, Y. Liu, R. Ran, H.F. Wang, A. Seth, A.P.J. Middelberg, C.X. Zhao, Understanding the Effects of Nanocapsular Mechanical Property on Passive and Active Tumor Targeting, Acs Nano 12(3) (2018) 2846-2857.
[67] A.C. Anselmo, M.W. Zhang, S. Kumar, D.R. Vogus, S. Menegatti, M.E. Helgeson, S. Mitragotri, Elasticity of Nanopartides Influences Their Blood Circulation, Phagocytosis, Endocytosis, and Targeting, Acs Nano 9(3) (2015) 3169-3177.
[68] M.R. Yu, L. Xu, F.L. Tian, Q. Su, N. Zheng, Y.W. Yang, J.L. Wang, A.H. Wang, C.L. Zhu, S.Y. Guo, X.X. Zhang, Y. Gan, X.F. Shi, H.J. Gao, Rapid transport of deformation-tuned nanoparticles across biological hydrogels and cellular barriers, Nature Communications 9 (2018).
[69] P. Guo, D.X. Liu, K. Subramanyam, B.R. Wang, J. Yang, J. Huang, D.T. Auguste, M.A. Moses, Nanoparticle elasticity directs tumor uptake, Nature Communications 9 (2018).
[70] M.Q. Lu, A. Ozcelik, C.L. Grigsby, Y.H. Zhao, F. Guo, K.W. Leong, T.J. Huang, Microfluidic hydrodynamic focusing for synthesis of nanomaterials, Nano Today 11(6) (2016) 778-792.
[71] S.J. Shepherd, D. Issadore, M.J. Mitchell, Microfluidic formulation of nanoparticles for biomedical applications, Biomaterials 274 (2021).
[72] J.S. Hong, S.M. Stavis, S.H.D. Lacerda, L.E. Locascio, S.R. Raghavan, M. Gaitan, Microfluidic Directed Self-Assembly of Liposome-Hydrogel Hybrid Nanoparticles, Langmuir 26(13) (2010) 11581-11588.

[73] P.M. Valencia, P.A. Basto, L.F. Zhang, M. Rhee, R. Langer, O.C. Farokhzad, R. Karnik, Single-Step Assembly of Homogenous Lipid - Polymeric and Lipid - Quantum Dot Nanoparticles Enabled by Microfluidic Rapid Mixing, Acs Nano 4(3) (2010) 1671-1679.
[74] Y.T. Kim, B.L. Chung, M.M. Ma, W.J.M. Mulder, Z.A. Fayad, O.C. Farokhzad, R. Langer, Mass Production and Size Control of Lipid-Polymer Hybrid Nanoparticles through Controlled Microvortices, Nano Letters 12(7) (2012) 3587-3591.
[75] F. Roffo, A.M. Ponsiglione, P.A. Netti, E. Torino, coupled Hydrodynamic Flow Focusing (cHFF) to Engineer Lipid–Polymer Nanoparticles (LiPoNs) for Multimodal Imaging and Theranostic Applications %M doi:10.3390/biomedicines10020438 %U https://www.mdpi.com/2227-9059/10/2/438, Biomedicines %@ 2227-9059 10(2) (2022) 438.
[76] B.H. Zhang, X.P. Pan, G.P. Cobb, T.A. Anderson, microRNAs as oncogenes and tumor suppressors, Developmental Biology 302(1) (2007) 1-12.
[77] S.W.L. Lee, C. Paoletti, M. Campisi, T. Osaki, G. Adriani, R.D. Kamm, C. Mattu, V. Chiono, MicroRNA delivery through nanoparticles, Journal of Controlled Release 313 (2019) 80-95.
[78] C.Z. Chen, MicroRNAs as oncogenes and tumor suppressors, New England Journal of Medicine 353(17) (2005) 1768-1771.
[79] R. Singh, Y.Y. Mo, Role of microRNAs in breast cancer, Cancer Biology & Therapy 14(3) (2013) 201-212.
[80] J.A. Kulkarni, D. Witzigmann, S.B. Thomson, S. Chen, B.R. Leavitt, P.R. Cullis, R. van der Meel, The current landscape of nucleic acid therapeutics, Nature Nanotechnology 16(6) (2021) 630-643.
[81] Y.C. Chen, D.Y. Gao, L. Huang, In vivo delivery of miRNAs for cancer therapy: Challenges and strategies, Advanced Drug Delivery Reviews 81 (2015) 128-141.
[82] S.R. El Sayed, J. Cristante, L. Guyon, J. Denis, O. Chabre, N. Cherradi, MicroRNA Therapeutics in Cancer: Current Advances and Challenges, Cancers 13(11) (2021).
[83] M.S. Ali, N. Hooshmand, M. El-Sayed, H.I. Labouta, Microfluidics for Development of Lipid Nanoparticles: Paving the Way for Nucleic Acids to the Clinic, ACS Applied Bio Materials (2021).
[84] Y. Cao, Y.F. Tan, Y.S. Wong, M.W.J. Liew, S. Venkatraman, Recent Advances in Chitosan-Based Carriers for Gene Delivery, Marine Drugs 17(6) (2019).
[85] S.M. Zhu, H.L. Wu, F.T. Wu, D.T. Nie, S.J. Sheng, Y.Y. Mo, MicroRNA-21 targets tumor suppressor genes in invasion and metastasis, Cell Research 18(3) (2008) 350-359.
[86] D. Piasecka, M. Braun, R. Kordek, R. Sadej, H. Romanska, MicroRNAs in regulation of triple-negative breast cancer progression, Journal of Cancer Research and Clinical Oncology 144(8) (2018) 1401-1411.
[87] X.F. Sun, H.P. Xu, T. Huang, C.J. Zhang, J.Z. Wu, S.X. Luo, Simultaneous delivery of anti-miRNA and docetaxel with supramolecular self-assembled "chitosome" for improving chemosensitivity of triple negative breast cancer cells, Drug Delivery and Translational Research 11(1) (2021) 192-204.
[88] F. Bray, J. Ferlay, I. Soerjomataram, R.L. Siegel, L.A. Torre, A. Jemal, Global cancer statistics 2018: GLOBOCAN estimates of incidence and mortality worldwide for 36 cancers in 185 countries (vol 68, pg 394, 2018), Ca-a Cancer Journal for Clinicians 70(4) (2020) 313-313.

[89] K.M. Krizmanich-Conniff, C. Paramagul, S.K. Patterson, M.A. Helvie, M.A. Roubidoux, J.D. Myles, K. Jiang, M. Sabel, Triple Receptor-Negative Breast Cancer: Imaging and Clinical Characteristics, American Journal of Roentgenology 199(2) (2012) 458-464.
[90] N. Harbeck, F. Penault-Llorca, J. Cortes, M. Gnant, N. Houssami, P. Poortmans, K. Ruddy, J. Tsang, F. Cardoso, Breast cancer, Nature Reviews Disease Primers 5(1) (2019) 66.
[91] F.M. Orlandella, R.M. Mariniello, P. Mirabelli, A.E. De Stefano, P.L.C. Iervolino, V.A. Lasorsa, M. Capasso, R. Giannatiempo, M. Rongo, M. Incoronato, F. Messina, M. Salvatore, A. Soricelli, G. Salvatore, miR-622 is a novel potential biomarker of breast carcinoma and impairs motility of breast cancer cells through targeting NUAK1 kinase, British Journal of Cancer 123(3) (2020) 426-437.

I. CHAPTER I– OPTIMAL DESIGN TO ADRESS STABILITY

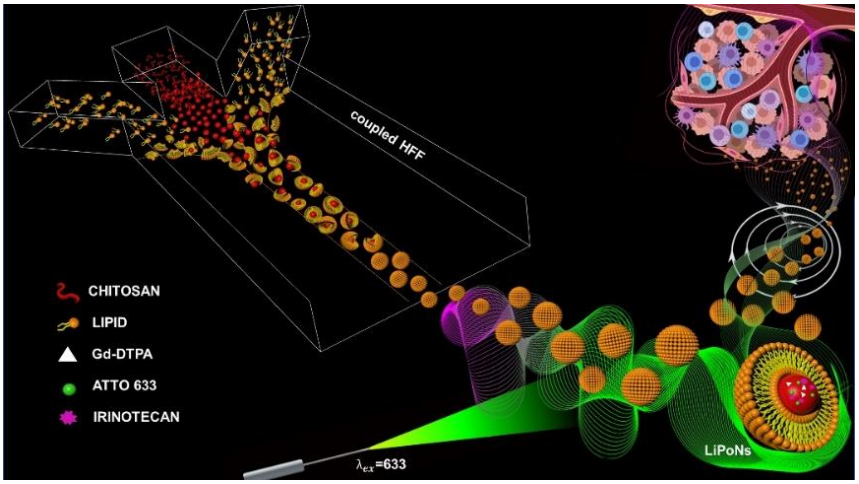

Graphical Abstract I. coupled Hydrodynamic Flow Focusing (cHFF) to Engineer Lipid–Polymer Nanoparticles (LiPoNs) for Multimodal Imaging and Theranostic Applications.

Abstract

Despite the potential offered by liposomes in the drug delivery field, several challenges mainly related to stability issues, limit their therapeutic efficacy. To overcome these drawbacks, we rationally designed lipid-polymer NPs, where a chitosan core is enveloped in a lipid bilayer, taking advantage of integrating both materials. To guide the formation of Lipid–Polymer NPs (LiPoNs), we developed a process named coupled Hydrodynamic Flow Focusing (cHFF) that controlled the time scales of solvent exchange and coupled the polymer nanoprecipitation with the lipid self-assembly simultaneously. We produced hybrid NPs with an average size of 100 nm with preserved structural integrity in different environmental conditions. The features of the hybrid NPs were exploited for the loading of contrast agents (Gd-DTPA), a fluorescent probe (Atto633) and chemotherapeutic drug (Irinotecan hydrochloride) for optical and theranostics purposes. Moreover, their toxicity and therapeutic efficacy were tested on U-87 MG cancer cells.

I.1 BACKGROUND

I.1.1 Introduction

Nanoparticles are promising vehicles for delivering of therapeutic and diagnostic probes to the disease site[1]. Two major classes of organic NPs, have been exploited for the drug delivery, polymer-based and lipid-based carriers[2, 3]. Polymeric nanoparticles have been widely used as they display high structural integrity, stability during storage, and controlled release behaviour[4]. In addition, they are also easy to prepare and functionalize for active targeted delivery[1]. Among them, nanogels are nano-sized three-dimensional cross-linked networks that offer high water content and excellent retention of compounds[5]. Liposomes with respect to polymer NPs, show superior biocompatibility, excellent biodegradability, low immunogenicity and non-toxic nature [5]. They are composed of one or multiple lipid bilayers enclosing an aqueous core, leading to the possibility of loading both hydrophilic and hydrophobic drugs[1]. Despite the advantages shown by liposomes formulation compare to free drugs, such as enhanced specific delivery, reduced off-target toxicity and improved therapeutic efficacy, they still suffer from limited circulation lifetime and poor tumour site targeting[5]. Liposomes on their own lack of structural integrity resulting in content leakage, large vesicles and altered morphologies, during storage and in biological context[6, 7].

Despite the huge effort made in manipulating the NPs properties to reach the tumour site, the majority of them still accumulate in off-target sites, with only 0.7 % of administered dose in tumour tissue[8, 9]. This unbalance is due to the interaction of NPs with tissue and organs, that filtered and sequestered them, during their in vivo journey[10].

These unsuccessful data reported for current NPs, stand out the need for developing of optimal design carriers. To address the limitations of the standalone carriers, hybrid NPs emerged as next generation vehicles offering unique properties from the integration of materials[4, 11]. Among these hybrid vectors, lipid-polymer NPs (LPNs), made up of a polymer core enveloped by the lipid component, offered multifaced properties such as boosted structural stability, high cargo loading, improved deformability, prolonged blood circulation and enhanced cell/tissue interaction[4, 5, 9, 11-13]. In detail, the polymer core allows the encapsulation and high-retention of therapeutic substances, while the lipid layer enveloping the polymer core minimizes the leakage of the cargo and confers biocompatibility to the polymer core[4, 12, 14].

These LPNs were conventionally produced by the two- or one-step method, with the latter being the more efficient technique[14]. Indeed, in two step-methods, the polymeric nanoparticles are mixed with preformed lipid vesicles and these vesicles are adsorbed on the polymeric NPs by electrostatic interactions. The polymeric NPs, typically produced by emulsification–solvent–evaporation [35], nanoprecipitation [39], or high-pressure homogenization[15], are added to a dried thin lipid film or alternatively added to preformed lipid vesicles prepared by thin film hydration technique. Afterwards, the LPNs are separated from the non-adsorbed lipid by centrifugation and are subjected to homogenization or extrusion steps to obtain monodisperse LPNs size[14]. In these

methods, the end-carrier features are dictated by several process parameters, such as the lipid-polymer ratio, the size and polydispersity of pre-formed NPs, the surface potential of the lipid shell and the ionic strength of the solution[16, 17]. In addition to these conventional methods, soft lithography and spray drying have been employed, with the latter technique that produce NPs with a size above 900 nm[18]. The cost, time and energy consumption of these two-step methods associated with low encapsulation and the request for post processing steps have led to the employment of other techniques[4, 19, 20].

Differently, in one-step method, either nanoprecipitation or emulsification– solvent–evaporation, the rapid mixing of polymer and lipid solutions direct the self-assembly to form lipid-polymer NPs. In the single or double emulsion technique, the polymer dissolved in oil-phase is added to a water lipid phase under sonication and stirring. Following solvent evaporation, the polymer precipitate and the lipid assemble[21, 22]. For the nanoprecipitation, the polymer and the active cargo are dissolved in a water-miscible organic solvent that is added dropwise to the aqueous lipid dispersion, prepared at a temperature beyond its gel-to-liquid transition temperature, under continuous stirring. Therefore, the polymer material precipitate in a coil and simultaneously the lipids, self-assemble, covering the polymer owing the hydrophobic interactions. Then, the LPNs are collected by centrifugation[14]. Several studies reported the lipid/polymer (L/P) ratio is the most influent parameter in the formation of stable LPNs in one-step-method. It influences the extent of lipid coating of polymeric NPs; thus it affects the LPNs morphology, encapsulation efficacy, loading capability and release kinetics. Briefly, higher L/P ratios result in the formation of liposomes in addition to the LPNs due to the excessive amount of lipids, whereas lower L/P ratios lead to LPNs aggregation due to the incomplete lipid coating[23-25].

Despite significant advancements in the batch field achieved so far, challenges remain in production LPNs, mainly related to the process efficacy in low control of NPs size, shape and encapsulation efficacy (EE%). Moreover, the inability to achieve reproducible and on-demanding properties of NPs strongly limits their performance in clinical translation[26]. To date, the main hurdles related to the clinical development of NPs are correlated to their optimal design to overcome biological barriers and the large-scale traditional manufacturing of complex synthesis procedures[9, 27].
On the contrary, the microfluidics, through the miniaturisation[28] and the parallelisation[29] of batch systems down to a few centimetre squares, allows a homogeneous reaction environment obtaining a fine-tuning of the process parameters to obtain NPs with well-defined properties[30-32]. The microfluidic ability to promote the ordered interaction among lipid and polymer materials was exploited to produce hybrid architectures[32, 33].

The complexity of guiding two mechanisms of NPs formation in microfluidics drove the development of several strategies for the synthesis of hybrid NPs. First, the on-chip production of liposomes was combined with off-chip polymerization of the interiors of lipid vesicles to obtain a hydrogel core[34]. Then, the hydrodynamic flow focusing in

combination with passive Tesla micromixer[35] was exploited for the production of PLGA NPs covered by lipid shell. A solution of lipid and lipid-PEG is dissolved in water and fed into side streams while the middle phase is a PLGA dissolved in acetonitrile. They studied the effect of PLGA: lipid ratio on final nanoparticle size, lipid coverage and stability of the carrier. They identified an optimal lipid-polymer ratio of 1:10 for the production of homogenous hybrid NPs, with uniform and complete coverage of lipids, resulting prolonged serum stability. Moreover, they implemented the same technology to synthesize NPs for imaging applications by entrapping quantum dots in lipid–PLGA NPs. Indeed, the microfluidic features and their operation conditions were exploited to enhance the controllability and homogeneity of active agent distribution with the NPs[32]. Sun et al.[36] developed a two-stage microfluidic chip for the synthesising mono-disperse lipid-poly (lactic-co-glycolic acid) NPs. The first stage of the device is a hydrodynamic flow focusing, while the second stage contains a central inlet and a spiral mixing channel. Changing the order of injection of lipid and polymer precursor inside the microfluidic device, it is possible to obtain two different lipid coverages with the same chemicals. For the lipid monolayer, a PLGA solution is injected in the first stage and a lipid-PEG solution in the second stage. On the contrary, if the lipid-PEG solution is fed in the first stage, an intermediate liposome structure is obtained that re-assembles on polymer precipitate injected in the second stage. They analysed the impact exerted by the lipid coverage in a monolayer or bilayer extent on the amount of water between polymeric core and the lipid shell on the rigidity of the NPs.

To improve the throughput of microfluidics, Kim et[37] al developed a pattern-tunable microvortex platform and they obtained small NPs (30-170 nm) at high productivity (∼3 g/hour) varying the flowrate ratio and consequently the Reynold number. Later, the same microvortex microfluidic platform was used to produce theranostic hybrid polymer–lipid NPs that load diagnostic nanocrystals and cytotoxic drug doxorubicin (DOX) in the PLGA core, while an anti-angiogenic drug Sorafenib (SRF) is placed in the lipidic layer[38].

I.1.2 Aim of chapter 1

Even though nanoparticles are designed with an optimal size, shape and surface charge to overcome the biological barriers encountered in the delivery to a solid tumour, less than 1% of NPs injected accumulate in the target site. Among nanocarriers, lipid-based NPs stand out for their low immunogenicity, improved fluidity and deformability[39, 40]. However, their therapeutic efficacy is still limited due to stability issues. To improve the carries stability and consequently refine their nano-bio interactions, we integrated a polymer component to a lipid one in the form of Lipid-Polymer NPs (LiPoNs). Through coupled Hydrodynamic Flow Focusing, we exploited the microfluidics to govern the solvent exchange and guide the production of hybrid Lipid-Polymer NPs (LiPoNs) with well-defined properties[41]. We studied the impact exerted by solvent-nonsolvent ratio, solute concentration, flow rate ratio and collection volume on the formation mechanism of hybrid NPs. The dual material nanostructure, where a lipid bilayer covers a chitosan core, was

exploited to co-entrap different cargos. Then, we assessed the capability of these hybrid vehicles to effectively deliver the cargo to cancer cells and induce a biological response.

I.2 CASE STUDY

I.2.1 Experimental section

I.2.1.1 Materials

L-α-Phosphatidylcholine from soybean ≥99% (SPC; lyophilised powder; storage temperature −20 °C; approximately Mw = 776 g/mol) and Cholesterol ≥99% (Chol; powder; storage temperature −20 °C; Empirical Formula $C_{27}H_{46}O$; Mw = 386.65 g/mol) have been purchased from Sigma-Aldrich (St. Louis, MO, USA). Chitosan (CH; powder; Low Mw = 50,000–190,000 Da; soluble in dilute aqueous acid); Diethylenetriaminepentaacetic acid gadolinium (III) dihydrogen salt hydrate (Gd-DTPA; Mw = 547.57 g/mol), Atto 633 (λex/em = 633/657 nm, Mw = 652 g/mol) and Atto 488 (λex/em = 480-515 nm, Mw = 804 g/mol) have been purchased from Sigma-Aldrich (St. Louis, MO, USA). Irinotecan HCl Trihydrate (IRI, Mw = 667.18 mg/mL, λabs = 368 nm) was purchased by Selleckchem Chemicals (Huston, USA,). As solvents, we used Acetic acid glacial (AcOH, ≥99.8%; Empirical formula CH_3COOH; Mw = 60.052 g/mol, ROMIL pure chemistry, Cambridge, UK), Ethanol (etOH, puriss. p.a., absolute, ≥99.8%GC; Empirical formula C_2H_5OH; MW: 46.07 g/mol; Carlo Erba Reagents, Italy) and filtered MilliQ water (Milli-Q Plus, Q-POD®, Merck KGaA, Darmstadt, Germany) for all the experiments. The phosphate-buffered saline (PBS, tablet) for dialysis, cell-culture and in vitro studies was purchased by Sigma-Aldrich (St. Louis, MO, USA). The Plasma Sigma-Aldrich (St. Louis, MO, USA). CellMask Orange Plasma membrane Stain (λex/em = 554/567 nm) was purchased from Thermofisher Scientific (Altrincham, UK). The human glioblastoma cell line U87 MG (passage 30–40) was purchased from ATCC (Manassas, VA, USA). For cell culture and in vitro studies, we have used Dulbecco Modified Eagle medium-high glucose (DMEM), foetal bovine serum (FBS), Dimethyl sulfoxide for molecular biology (DMSO), Thiazolyl Blue Tetrazolium Bromide soybean ≥97.5% (MTT) and Trypan Blue purchased from Sigma-Aldrich Co. (St. Louis, MO, USA), Antibiotic Solution 100× liquid purchased and L-glutamine (200 mM) from Himedia (Einhausen, Germany).

I.2.1.2 Microfluidic Set-up for coupled Flow Focusing Approach

A quartz microfluidic device (22.5 mm long × 15 mm wide × 4 mm thick) with 5 parallel inputs and one output purchased from Dolomite Centre Ltd. (Royston, UK) was used to perform all the experiments (Figure I-1a). The device consists of 5 parallel inlets converging and intersecting the corresponding end of the central channel at an angle of 45°at the junction, followed by a straight output channel. All channels have the same approximately circular cross-section of 160 μm × 150 μm. Only three of five inlets of the device are used for LiPoNs production. The chip is compatible with the H interface 7-way (Dolomite microfluidics, Royston, UK) for tubing connections (Figure I-1b). The device is connected to a glass middle syringe of 2.5 mL and glass side syringes of 5/10 mL (CETONI GmbH, Germany) with two FEP tubing segments (Outside diameter OD× Inside diameter ID-1/16''mm × 0.25 mm– 0.8 mm× 0.25 mm) controlled by a low-pressure syringe pump (Low-

Pressure Syringe Pump neMESYS 290 N, CETONI GmbH, Germany, Figure I-1c-d). Two-way in line ETFE valves, connecting syringes with the microfluidic device, make the automatic fill-in of the syringes feasible, thus allowing a continuous dispensing of reagents. A FEP outlet tube (OD × ID-0.8 mm × 0.25 mm), which starts from the output of the device, was employed to collect fluid in a glass vial containing water. The flow focusing behaviour on the microchannel was observed using an Optical Fluorescence Microscope (Olympus IX71) with a 4× scanning objective.

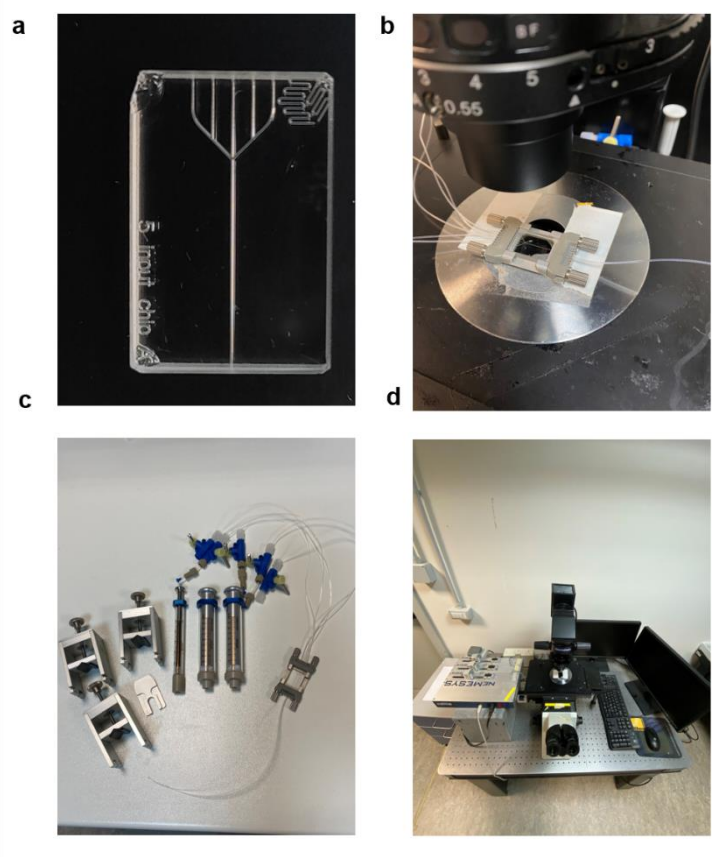

Figure I-1. Microfluidic experimental set-up. a) 5 inputs chip A 160 µm x 150 µm for Hydrodynamic flow focusing regime; **b**) 5 inputs chip A compatible with the H interface 7-way for fluidic connections under the transmission optical microscopy; **c**) Microfluidic components and **d**) microfluidic set-up for the implementation of coupled Hydrodynamic Flow Focusing.

I.2.1.3 One step HFF for Lipid Polymer Nanoparticles (LiPoNs) Production

A microfluidic process was used to produce a complex nanostructure named LiPoNs. The first step consisted of preparing the etOH/Water solution containing Lipids in mass ratio 8:1- SPC:Chol. It was kept under continuous stirring overnight and then injected through the side channels. In the feasibility study, the concentrations of reagents and solvents were

varied in order to understand their effect on LiPoNs morphologies. Firstly, the concentration of the lipid was varied from 0.016 to 0.0072 % w/v for a fixed etOH/Water solution (65/35% v/v) with pure water injected in the middle channel. By fixing the lipid concentration at 0.0072 % w/v, the effect of two etOH-Water mixture, (65/35% v/v-80/20% v/v) was observed. Keeping constant the concentration of lipids (0.0072 % w/v) dissolved in a fixed etOH-Water mixture (65/35% v/v), the effect of a mixture of AcOH-Water (1 % v/v and 10 % v/v of AcOH) injected in the middle channel was observed. Then, the water phase, injected in the middle channel, was made of an aqueous solution of 0.01%-0.03% w/v of CH and 1% v/v of AcOH. The volume of the collection was varied from 2 to 8 ml (2,3.5,8 ml). Finally, the flow rates of the middle and side streams were varied, as reported in Table I-1. These operative conditions are reported in Appendix VI.

Following this study, the conditions for producing LiPoNs were fixed as follows. The first step involved preparing the etOH/Water solution (65/35% v/v) containing 0.0072% w/v of Lipids (mass ratio 8:1- SPC:Chol). It was kept under continuous stirring overnight and then injected through the side channels. The water phase is aqueous solution of 0.01% w/v of CH and 1% v/v of AcOH. It was kept under continuous stirring for at least 1 h and then injected through the middle channel. To prepare Gd-DTPA-loaded LiPoNs, the contrast agent at a concentration of 0.4 % w/v was added to the acid solution containing chitosan (0.01% w/v). Atto 633, Atto 488 and Irinotecan co-encapsulation was achieved by dissolving the active agents in the acetic acid solution containing AcOH-CH-Gd-DTA (1% v/v–0.01% w/v–0.4% w/v). The Atto 633, Atto 488 and Irinotecan concentrations were 24 µg/mL, 32.2 µg/mL and 145 µg/mL, respectively. A Flow Rate Ratio FR^2 (0.073), defined as the ratio of the Volume Flow Rate of the middle channel (3 µL/min) and the Volume Flow Rate of the side channel (41 µL/min), was determined for all formulations. The microfluidic process was carried out for 40 min or its multiples, and the nanoparticles were collected in a vial glass containing 3.5 mL of water or its multiples. For large production of LiPoNs, the proportion was maintained by performing the process for 80 min in a collection of 7 ml of water. The suspension was stirred for 40 min at room temperature.

I.2.1.4 Purification and Concentration of NPs

Purification was performed by mild solvent gradient dialysis in PBS diluted in water (1:1). A sample volume of 5 ml was loaded in Spectra-Por Float-A-Lyzer G2, red (Molecular Weight Cut Off, MWCO = 20,000–50,000 Da, Sigma-Aldrich, St. Louis, MO, USA) or Spectra/Por™ 6 Dialysis Membrane Pre-wetted RC Tubing (Molecular Weight Cut Off, MWCO = 25,000–50,000 Da, Thermofisher, Altrincham, UK) with an external phase of ~ 16 ml. It was kept under continuous stirring at room temperature for at least one hour. LiPoNs were concentrated by Rotary Evaporator (BUCHI Italia s.r.l, Italy) at a vacuum pressure of 20 mbar at 25 °C until the desired concentration was achieved. In the case of the cell viability assay where a high concentration of material is required (Lipids concentration ≃ 1 mg/mL), additional dialysis by rotary evaporator, at the above-mentioned conditions, was performed to remove any residual solvent.

I.2.1.5 Characterisation of LiPoNs Nanoparticles

I.2.1.5.1 Physicochemical Characterisation

Dynamic light scattering (DLS) was used to determine nanoparticle size (Zeta sizer, Malvern Panalytical, UK). DLS measures the light scattered from a laser that passes through a colloidal solution, where the nanoparticles in the solution move under Brownian motion. Analysing the modulation of the scattered light intensity as a function of time, the hydrodynamic size of particles and particle agglomerates can be determined. The analysis of the intensity of fluctuations provides information on the diffusion coefficient of the particles. The diffusion coefficient D is then related to the radius R of the particles by means of the Stokes-Einstein Equation. The scattering angle used is 173°. The volume of the sample suitable for DLS analysis is 1 mL in a polystyrene cuvette (Optical Cuvette, Sarstedt, Italy). The measurement was performed after the stirring, and the appropriate solvent dispersant (etOH-26 % weight) was selected as the setting for the measurement. In DLS analysis, the z-Average value and the polydispersity index of the average of three measurements were collected. The DLS analyses were performed at 25 °C or 37 °C according to the aim of the analysis. Zeta potential measurements were also performed at 25 °C on a Zetasizer Nano ZS (Malvern Panalytical, UK), loading the high-concentration surface zeta potential cell (Malvern Panalytical, UK) with 1 mL of the NP suspension. Zeta potential measurements were performed at 25 °C by a Zetasizer Nano ZS (Malvern Panalytical, UK), loading Folded Capillary Zeta Cell (Malvern Panalytical, UK) with 1 mL of NPs suspension. The LiPoNs size was acquired with the DLS upon about 1 h of interaction with the plasma from humans (1:1) on stirring and diluted in milliQ water (1:9).

The hydrodynamic diameters and particle concentration were measured with a NanoSight NS300 (NTA version 3.4, Malvern Instruments Ltd, Camera sCMOS, Laser Blue488) at room temperature. The Nanotracking analysis (NTA) measures with a high resolution the particle size, and it provides count-based concentration and aggregation measurements. The scattered light by the particles, loaded into a sample chamber under a laser beam, is collected by the 20x microscope objective and captured by a camera. The motion of each particle is acquired and analysed to obtain the particle size. The camera allows the real-time monitoring of the sample. A manual shutter and gain adjustment are required for the measurement. The samples were diluted in water (dilution ranging from 10 to 200) in order to obtain better settings for the analysis. Particle size distribution and concentration were expressed as the average and standard error of the mean of three measurements.

I.2.1.5.2. LiPoNs Imaging

A Field Emission Scanning Electron Microscope (FE-SEM, Ultraplus Field Emission, Carl Zeiss, Oberkochen, Germany), Transmission Electron Microscope (TEM, FEI, Hillsboro, OR, USA) and confocal microscope (Leica Microsystems, Wetzlar, Germany) were used to characterize the morphology of nanosystem. The SEM observations were conducted by dropping 20 µL of the nanoparticle suspension on circular coverslips (22 mm), which were then air-dried overnight. To eliminate charging and improve contrast, nanoparticles are coated with 5 nm Au prior to the observation with 208HR High Resolution Sputter Coated

(Cressington). For the TEM analyses, the samples were prepared using Formvar/Carbon 200-mesh Cu Agar Scientific Ltd. (Stansted, UK) using 8 µL (two drops of 4 µL) of the suspended nanoparticles with and without staining. Negative staining is performed using a phosphotungstic acid solution (2% *w*/*v*) directly on the deposit for 45 s or using osmium tetroxide smoke (1% *w*/*w*) overnight. Then, the air-dried samples (overnight) were directly examined under the TEM. The nanoparticles were stained with CellMask Orange Plasma membrane Stain (dilution $1{:}10^4$) for a few minutes, and then 10 µL of that solution was dropped on 25 mm FluorDish. The stained and not-stained NPs were observed using a TCS SP5 Confocal Laser Microscope with a 60 × Oil objective. Lasers with different wavelengths were used for CellMask Orange Plasma membrane Stain, Atto 633 and Atto 488 dyes at 543 nm, 633 nm and 488 nm for the excitation and 610 nm, 657 nm and 515 nm for the emission, respectively.

I.2.1.5.3 In Vitro MRI

The relaxometric properties of blank nanoparticles (LiPoNs) and nanoparticles containing Gd-DTPA (Gd-DTPA LiPoNs, Atto 633-loaded LiPoNs (Atto633 LiPoNs), Atto 633 co-loaded Gd-DTPA LiPoNs (Atto633-Gd-DTPA LiPoNs), Irinotecan-Gd-DTPA co-loaded LiPoNs (IRI-Gd-DTPA LiPoNs)) were tested by in vitro MRI. The data were compared with Gd-DTPA calibration curves dispersed in water (Appendix, Figure VI-8a) ranging from 0 to 100 µM. A total of 300 µL of NPs and diluted NP suspension in water (1:1) were dropped in an NMR tube, and the changes in relaxation time (T1) were evaluated at 1.5 Tesla by a Minispec Bench Top Relaxometer (Bruker Corporation) at 37 °C. The Free Induction Decay sequence (FID) was used to evaluate the best value of the gain to control the saturation of the signal. Longitudinal relaxation times, T1, were determined by saturation and inversion recovery pulse sequence. The relaxation time distribution was obtained by CONTIN Algorithm.

I.2.1.5.4 Evaluation of Co-Encapsulation Efficiency

The Multiplate Reader Photometer Enspire Perkin-Elmer Inc (Waltham, MA, USA) was used to quantify the encapsulation efficiency (EE %) of Atto 633, Atto 488 and Irinotecan. The absorbance (λabs = 368 nm) of the IRI-Gd-DTPA LiPoNs was correlated to the IRI calibration curve at concentrations ranging from 0.5 to 100 uM (Appendix VI, Figure VI-8a). The fluorescence of Atto 633 (λex/em = 630/651 nm) from 25 ng/mL to 4 µg/mL for Atto 633 (Appendix VI-Figure VI-8b). Triplicates of each measurement were performed. The encapsulation efficiency of Gd-DTPA, the co-encapsulation of the fluorophores and Irinotecan (EE%) was calculated as:

$$\mathrm{EE\%} = \frac{\mathrm{C_M}}{\mathrm{C_T}} \times 100 \quad (1)$$

where $\mathrm{C_M}$ is the measured concentration of suspension, and $\mathrm{C_T}$ is the theoretical concentration used in the microfluidic process.

I.2.1.6 Cell Viability by MTT assay

Human brain glioblastoma astrocytoma cells, U87 MG, were cultured in Dulbecco's modified Eagle's medium (DMEM), containing FBS (10% *v*/*v*), L-glutamine (1% *v*/*v*) and penicillin-streptomycin (1% *v*/*v*), at 37 °C in water-saturated air supplemented with 5% CO2. For the cytotoxicity measurements, 2×10^4 U87 MG cells/well were plated in 96-well plates (Corning, Costar, Merck) for 24 h before the addition of the LiPoNs. Fresh medium, containing an increasing concentration of nanoparticles, was added to each well, and the cells were incubated for 24 h or 48 h according to the study. For the evaluation of LipoNs' biocompatibility, an increasing concentration of LiPoNs, Gd-DTPA LiPoNs and Atto633-Gd-DTPA LiPoNs (Lipid concentration: 2–42 µg/mL; chitosan concentration: 0.07–2.1 µg/mL; Gd-DTPA concentration: 3–105 µM; Atto 633 concentration: 0.01–0.3 µg/mL) was tested for 24 h. Conversely, for the evaluation of IRI-Gd-DTPA-loaded LiPoNs' effect on cell viability with respect to free drugs, 7.7 uM of Irinotecan in LipoNs (Lipid concentration: 0.4 mg/mL, Gd-DTPA concentration: 1.25 mM) and free IRI were tested for 24 h and 48 h on 1.5×10^4 U87 MG cells/well. To exclude any additional cytotoxic effects with respect to Irinotecan, the blank formulations in the same conditions (LipoNs-Lipid concentration: 0.4 mg/mL) were tested. At the end of the incubation time, the media were then removed, the cells were washed with PBS and a fresh medium containing MTT at a final concentration of 0.5 mg/mL was added to the cells. After 3 h of incubation, the medium was removed, and the insoluble formazan crystals synthesised by the live cells were dissolved in 200 µL of DMSO. After 30 min of incubation, the absorbance (λabs = 556 nm) of the solution was then recorded in triplicate using a Multiplate Reader Photometer Enspire from Perkin-Elmer Inc. (Waltham, MA, USA). The viability percentage of nanoparticle-treated cells was evaluated, with the cells not treated with nanoparticles or active agent considered as the control.

$$\text{Cell viability } \% = \frac{\text{AU of Cells tested with NPs}}{\text{AU of Untreated Control Cells}} \times 100 \quad (2)$$

where the AU is the measured Absorbance in triplicate.

I.2.1.7 Flow Cytometry Analysis

Prior to the addition of NPs, 5×10^4 U87 MG cells/well are seeded in a 48-well plate (Corning, Costar, Merck) and incubated for 24 h. Afterwards, cells were incubated with a culture medium containing an increasing concentration of Atto633-Gd-DTPA LiPoNs (Lipid concentration: 30–60–90 µg/mL, Gd-DTPA concentration: 75–150–225 µM, Atto 633 concentration: 0.2–0.4–0.6 µg/mL) for different time intervals according to the uptake study. The time intervals for the cellular uptake study with a Lipid concentration of 90 ug/mL in LiPoNs were set to 2 h, 4 h, 6 h, 8 h and 24 h, while for a comparative study of LiPoNs' uptake at different concentrations (30–60–90 µg/mL Lipid concentrations), the time intervals were 4 h, 8 h and 24 h. Negative controls were the complete medium condition without NPs. Then, the medium was removed, and the samples were washed three times with PBS (1×) to ensure particle removal from the outer cell membrane. Cells were then trypsinised for 5 min at 37 °C and transferred from the cell culture medium (without phenol red) to polystyrene round-bottomed tubes (Falcon round-bottom, Thermofisher, Altrincham, UK) on ice. The samples were analysed by flow cytometry using

a BD FACSCelesta Cell Analyzer (BD Biosciences, New Jersey, USA). A total of 10.000 events were recorded for each sample in triplicate, and the cells were gated using Forward Scattering Area (FSC) and Side Scattering Area (SSC). For the FI distribution, the cells were excited at 561 nm, and the fluorescence emitted by Atto 633 (PE_Cy5_A, Filter 688/33) was collected in the PE_CY5_A channel. The autofluorescence of the cell line was determined by untreated cells, which were used as a control. The data obtained by BD FACSCelesta Cell Analyzer were analysed with CytoFlow software (v1.1.1, Massachusetts Institute of Technology 2015–2018, Cambridge, MA, USA). The results are reported in Figures S8–S10 as the geometric mean of Fluorescence Intensity (FI), Side Scattering (SSC) and Forward Scattering (FSC), and the error bars are the standard deviations between the replicates. The raw flow cytometry data of U87 MG cells positive (orange) or not (blue) to a threshold gate for PE_ Cy5_A channel are reported in Appendix VI- Figure VI-12-14.

I.2.1.8 Cell Uptake Study by Confocal Imaging

The Atto633-Gd-DTPA LiPoNs cellular uptake was studied by confocal imaging. First, 5×10^4 U87 MG cells/well were seeded in µ-Slide 8-Well (Ibidi, Bayern, Germany) and cultured for 24 h. The medium was removed, and a fresh medium with Atto633-Gd-DTPA LiPoNs (Lipids:90 µg/mL, Gd-DTPA:225 uM, Atto 633:0.6 µg/mL) was added and incubated for 24 h. For the cell membrane staining, CellMask Orange Plasma membrane Stain (dilution $1{:}10^5$) was added to the cells for ≃15 min and then replaced with PBS for live acquisition. Live cells were observed with a Leica Microsystems TCS SP5 Laser Scanning Confocal Microscope (Wetzlar, Germany) with a 60×Oil objective. Atto633-Gd-DTPA-loaded LiPoNs were excited with the HeNe 633 nm laser, and a bight field was used to assess cell morphology. The Z-Stack videos were recorded by acquiring one image every 15 s for up to ≃8 min for cells exposed to Atto633-Gd-DTPA co-loaded LiPoNs.

I.2.2 Results and discussion

I.2.2.1 Rational design to address stability across biological barriers

The biological barriers play an important role in the therapeutic efficacy of NPs, as demonstrated by the poor clinical outcome of contemporary NPs[9]. Thus, a comprehensive understanding of the interactions between these barriers and nanoparticles is crucial for engineering advanced nanoparticles based platforms for cancer treatment[10]. Analysing these nano-bio interactions, general trends emerged in terms of the percentage of injected dose (ID) of NPs that reached the tumour site. Firstly, NPs characterized by a hydrodynamic diameter smaller than 100 nm show a higher delivery efficiency with an ID of 0.7 % with respect to larger particles (0.6%ID). Neutral charged NPs (0.7 % ID) with a zeta potential between −10 to +10 mV, tend to have a higher delivery efficacy, with respect to positive (>10mV, 0.6 % ID) or negative nanoparticles (<-10 mV, 0.5 % ID). Regarding the shape, rod-like nanostructure (1.1 % ID) reported a higher delivery efficacy with respect to spherical (0.7 % ID) and plate nanoparticles (0.6 % ID)[8]. Regarding the elasticity of NPs, no general conclusions can be stated due to the low and contradictory amount of data[11, 13, 36]. Given this fact, soft NPs or with moderate elasticity display longer circulation time and high tumour accumulation due to the reduction in macrophage uptake[42], high tumour penetration and cell interaction[11, 13].

Following these considerations, about the impact exerted by the size, shape, charge and elasticity on the *in vivo* performance of the carriers, among the vectors capable of acquiring controllable mechanical properties, we selected hybrid lipid-polymer nanoparticles[11, 36]. These carriers combined a lipid mixture with a polymer core to face the stability issues associated with lipid-based carriers[4, 14]. These structures, thanks to the combination of both materials, demonstrate high structural integrity, stability during storage, controlled release and improved nano-bio interactions[43, 44]. In our case, the Lipid-Polymer NPs (LiPoNs) are made of a core-shell structure, where a lipid bilayer surrounds the chitosan core. We selected as lipids a mixture of phosphatidylcholine (PC) and cholesterol to confer to nanoparticles improved stability, cellular delivery efficacy, prolonged blood circulation and fluidity[40]. The cholesterol addition had the aim of enhancing particle stability by modulating membrane integrity and rigidity[45-47]. The lipid layer masked the positive charge of chitosan and conferred a slightly negative charge to the vehicle reducing the elimination through MPS[10]. At a cellular level, the biomimetic nature of lipids improved the presentation of chitosan and the cargo to the cell membrane[48], while the sponge effect of positive charge chitosan pushed the delivery of the cargo in the cytoplasm, avoiding its degradation in late endosomes or lysosomes[49, 50]. In our case, we selected not to crosslink the core of the lipid-polymer to achieve a moderate elasticity to the carrier and improve its cellular interaction. Indeed, Guo et al.[13] reported improved cellular uptake of nanogels with a lower extent of the crosslinking core.

I.2.2.2 Coupled Hydrodynamic flow focusing to produce Lipid-Polymer NPs

A well-established technique for liposome production is thin-film hydration, which consists of swelling dry phospholipid films in excess water under vigorous shaking, inducing spontaneous vesicle self-assembly[51]. However, this spontaneous bulk process is unable to control the physical properties of the final products[30]. Recently, microfluidic systems, outdoing the mentioned limitation, offer control over the confinement microenvironment with a dimension of the nanoparticle itself[52]. In these systems, the formation of specific nanostructures is achieved by the Hydrodynamic Flow Focusing (HFF), where the nonsolvent phase, flowing through two side channels, focuses the solvent phase in the middle channel[53].

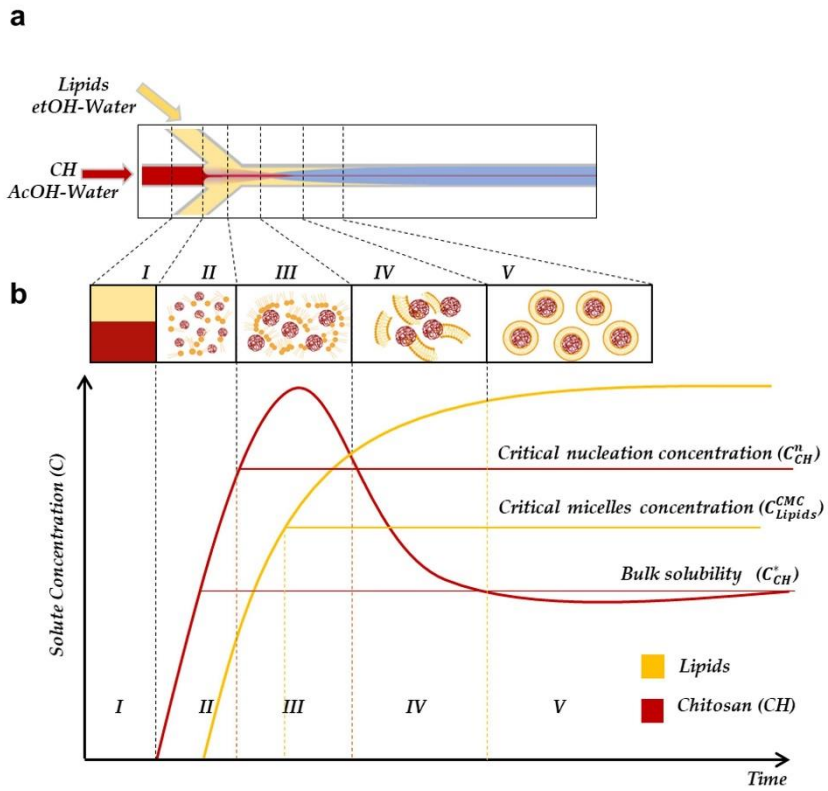

Figure I-2. Schematic illustration of nanoprecipitation and self-assembly processes implemented in microfluidics. a) Sketch of coupled Hydrodynamic Flow Focusing (cHFF), implemented by injecting Lipids dissolved in Ethanol/Water (etOH/Water, yellow stream) in the side channels and chitosan in Acetic Acid/Water (AcOH/Water, red stream) in middle one, for Lipid–Polymer Nanoparticles' (LiPoNs) production (blue stream). **b**) Schematic diagram of LiPoNs forming process in the cHFF: (I) Chitosan and Lipids dissolved in solvent mixture injected into the microfluidic channels; (II) Chitosan supersaturation and Lipid monomers formation; (III) Chitosan Nuclei and Lipid micellization; (IV) Chitosan intermediate and bilayer fragments formation; (V) Lipid–chitosan nanocomplex production.

Here, coupled Hydrodynamic Flow Focusing (cHFF), as schematised in Figure I-2, is proposed for the first time to produce a complex lipid–polymer nanosystem named LiPoNs. The ability to manage two thermodynamic processes is obtained simultaneously by controlling the time scales of solvent exchange[30, 54], to induce the polymer precipitation and the self-assembly of bilayer fragments that coat the NPs' surface. The peculiarity of the proposed approach for the synthesis of LiPoNs (Figure I-2a,b, region I) relies on the injection of two lateral lipid streams, dissolved in a variable ethanol–water (etOH/Water) ratio, that squeeze the chitosan (CH), dissolved in an acetic acid (AcOH) solution, injected into the middle channel. On the contrary, in the literature, the formation of liposomes is

typically performed by injecting the lipid solution into the main channel [8,37,38]. The cHFF features govern the competition of two solvent extractions and therefore coordinate the relative kinetics of nuclei and the growth of two phenomena: nanoprecipitation and self-assembly. The steps of cHFF involve a rapid nucleation rate of chitosan, self-assembly of lipids in bilayer fragments and, finally, the coupling of chitosan with the bent bilayer fragments. Consequently, the rapid chitosan precipitation mediates the bilayer fragments' enclosure. Indeed, the designed cHFF leverages rapid acetic acid (AcOH) extraction that promotes fast nucleation, leading to almost monodisperse chitosan nanoprecipitate (Figure I-2a,b, region II). Simultaneously, once the lateral solution comes in contact with the middle flow, the lipids are no longer solubilised and begin to assemble in bilayer fragments due to the organic solvent extraction (Figure I-2a,b, region III–IV). Then, the already formed bilayer fragments (slightly negatively charged) diffuse to the polymer nuclei nanoparticles (positively charged), covering their surface and inhibiting the further growth of chitosan nuclei, finally stabilising the LiPoNs complex. (Figure I-2a,b, region V).

I.2.2.3 Successful conditions to produce LiPoNs in coupled Hydrodynamic Flow focusing

We investigated the process parameters in terms of fine-tuning the flow rates, solvent–nonsolvent ratio, solute concentration and FR^2, which govern the coupling time of thermodynamic phenomena: nucleation of chitosan particles, self-assembly of lipid fragments and final interaction of these intermediate structures. In this work, FR^2 is defined as follows:

$$FR^2 = \frac{\text{Volume Flow Rate of AcOH/Water solution (Middle phase)}}{\text{Volume Flow Rate of etOH/ Water solution(Side phase)}} \quad (3)$$

A preliminary study was performed (Table I-1) evaluating the effect of solvent-non solvent ratio (etOH/Water: 80/20%v/v and 65/35% v/v; AcOH/Water: 1/99% v/v and 10/90% v/v) and the concentration of the reagents (Lipids: 0.016% w/v and 0.0072% w/v; chitosan: 0.01% w/v and 0.0375% w/v) for a proper interaction of both Lipids and chitosan components. Then, the effect of the FR^2 on the morphology of LiPoNs was assessed. A feasibility study was conducted by ranging FR^2 from 0.024 to 0.68, which was obtained by keeping the lateral flow rate at 41µL/min and increasing the middle one from 1 to 28 µL/min. Finally, the effect of the collection volume was also analysed by considering a collection volume of 2, 3.5 and 8 mL. Detailed results of the entire experimental campaign analysed by TEM and DLS are reported in Table I-1 and Appendix-Figure IV-1-5.

Table I-1. Range of process parameters performed in the preliminary experimental study in terms of average size and polydispersity index (PDI).

SPC:Chol Mass ratio	Lipids (% w/v)	etOH/Water ratio (% v/v)	AcOH/Water ratio (% v/v)	CH (% w/v)	Collection Volume (mL)	FR^2	Middle Flow: Side Flow (µL/min)	Average Size (nm)	PDI
8:1	0.016	64/36	/	/	4	0.51	21:41	/	/
	0.0072	80/20	/	/	2			177.2	0.503
		65/35	/	/				126.9	0.401
			10/90	/				204.3	0.283
			1/99	/				225	0.394
				0.0375				242.8	0.569
				0.01				131	0.554
						0.68	28:41	186.7	0.534
						0.34	14:41	199.7	0.367
						0.17	7:41	134.1	0.491
						0.073	3:41	66.79	0.269
						0.024	1:41	100.2	0.349
					3.5	0.17	7:41	87.14	0.150
						0.12	5:41	88.22	0.148
						0.073	3:41	77.45	0.218
						0.024	1:41	110.5	0.157
					8	0.073	3:1	308.7	0.337

Notes: Ethanol (etOH), Acetic Acid (AcOH), Soybean Phosphatidylcholine (SPC), Cholesterol (Chol), Lipids (mass ratio 8:1 SPC:Chol), chitosan (CH), FR^2 (Flow rate ratio).

The stability of the microfluidic process and the absence of massive precipitation combined with the evaluation of the morphologies guided the identification of the main operative conditions to obtain stable structures. As a result of optimisation studies for LiPoNs' synthesis, the value of FR2 equal to 0.073 (obtained at a middle flow rate of 3 µL/min, a side flow rate of 41 uL/min), a chitosan concentration of 0.01% w/v (dissolved in acetic solution 1 % v/v- middle phase) and a Lipid concentration of 0.0072 % w/v (dissolved in etOH/Water 65/35 % v/v- side phase), were proven to be the optimal conditions and were further used for all the experiments. The LiPoNs nanoparticles obtained directly from the device were measured by Dynamic Light Scattering instrument (DLS). The size distribution reported a peak at 94 nm with an average size of 77.4 nm. The NTA analysis for LiPoNs post dialysis procedure showed an average size of 119 nm with a mode of 73.3 nm. The lower size of LiPoNs measured by DLS could be linked to the ethanol residue that could have induced a shrinkage of the liposomes due to membrane undulation[55]. The TEM image of LiPoNS stained with osmium smoke and the SEM confirm the monodisperse population of LiPoNs (Figure I-3b). The staining with osmium smoke enhances contrast of lipid material making it darker. A TEM image without any staining of LiPoNs is reported to show the core-shell structures of NPs.

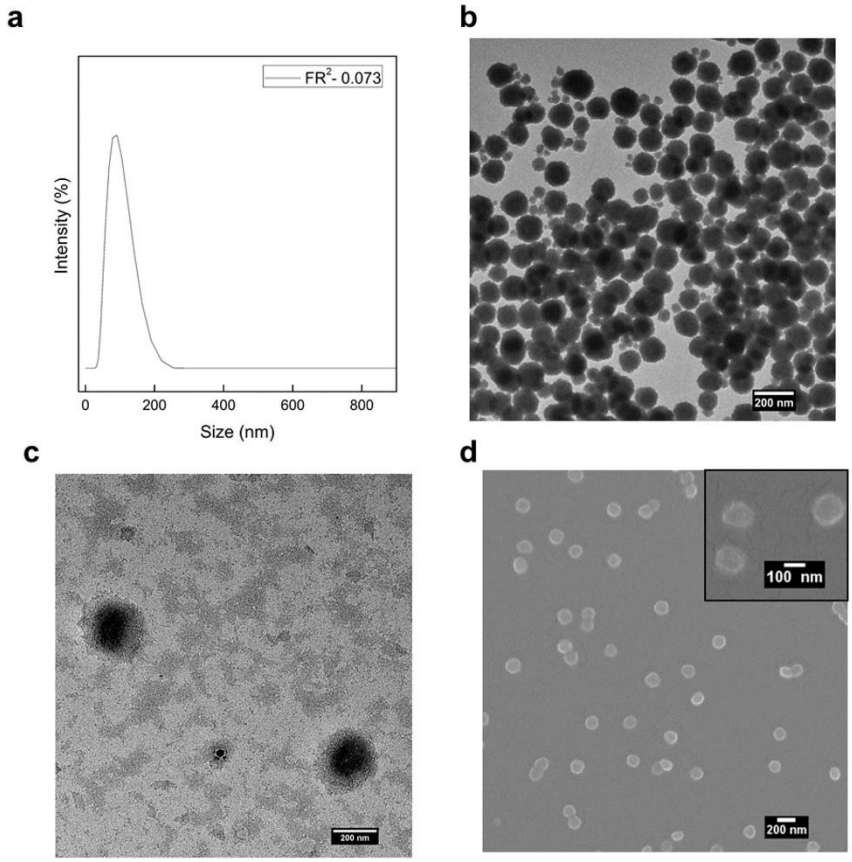

Figure I-3. **LiPoNs size distribution and morphological characterisation**. **a**) Particle size distribution, **b**)TEM image (stained with osmium smoke), **c**) TEM image and **d**) SEM image of LiPoNs performed at optimal conditions, with a Lipids concentration of 0.0072% w/v (mass ratio 8:1 SPC:Chol) dissolved in etOH/Water (65/35 % v/v) and a CH concentration of 0.01% w/v dissolved in acid solution (AcOH-1 % *v*/*v*) at FR^2 of 0.073.

Confocal images are also performed to support the morphological characterisation provided by TEM images. To confirm the presence of a lipid shell, we performed a staining of LiPoNs with CellMask Orange Plasma, which are amphipathic molecules mainly used for staining cell membrane. Red fluorescent spots are detected in AppendixVI-Figure VI-6. The Lipid-Polymer nanoparticles displayed a slightly negative charge -17.4 mV which may be attributed to the replacement of a phospholipid by cholesterol (mass ratio 8:1 of SPC:Chol). The slightly negative charge of LiPoNs combined with an average size lower around 100 nm strongly improve the nano-bio interactions these carriers will encounter during their transport across multiple barriers. Yamamoto et al.[56] reported a long circulation time and lower accumulation in the spleen and liver for neutral and anionic NPs, mainly due to lower absorption of serum proteins. Regarding the size, spherical nanoparticles with a size

smaller than 100 nm have higher delivery efficacy in tumour due to their long half-live which increased their probability to extravasate the fenestrations (380-700 nm) in the leaky vasculature[57]. Indeed, NPs with an average size of 100 nm may avoid renal clearance (<5nm) and accumulation in liver due to its vascular fenestrations (>150 nm)[57]. Moreover, the sizes of interendothelial cell slits are round 200-500 nm, leading to the retention of NPs > 200 nm, while particles larger than 2-5 µm accumulate within the capillaries of the lungs[10].

I.2.2.4 Stability Study of LiPoNs

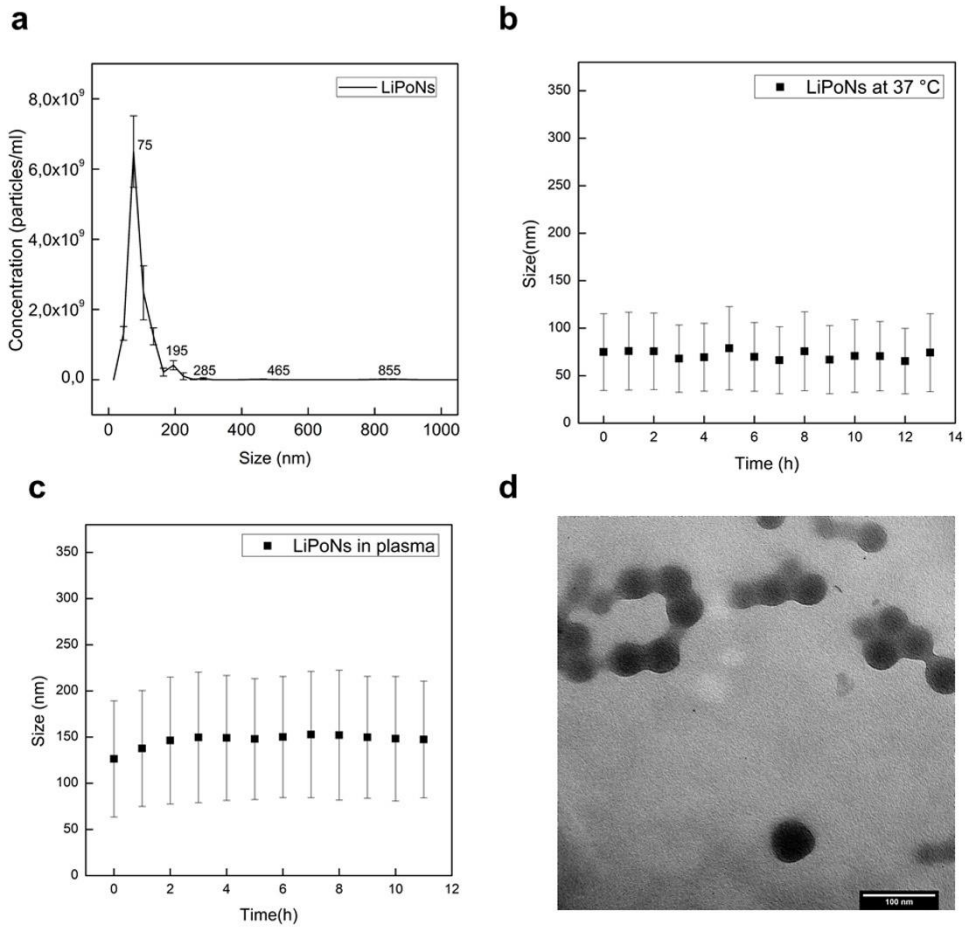

Figure I-4. Physical Stability Study of LiPoNs. **a**) particle size distribution is expressed as the average and standard error of the mean LiPoNs' concentration (particles/mL) evaluated in PBS (diluted 1:200) for five measurements. **b**) LiPoNs' average size and standard deviation observed at 37 °C for several time points (up to 13 h). **c**) LiPoNs' average size and standard deviation observed at 37 °C (diluted 1:9) for several time points (up to 11 h). **d**) TEM image of LiPoNs following the contact with the plasma.

Nanoparticle Tracking Analysis (NTA) measurement was performed to assess aggregation phenomena and stability of LiPoNs. It allowed a dynamic observation, counting and sizing of LiPoNs and a high-resolution of their distribution[58]. The NTA results of LiPoNs diluted in PBS 1:200 are shown in Figure I-4. The mean size and the mode of nanoparticle size are 94.7 nm and 79.7 nm, respectively, with 90% of the nanoparticles being <137.2± 6.1 nm (Appendix-Figure VI-7). The real-time visualisation (Appendix-Figure VI-7) of LiPoNs as individual particles confirmed their stability in PBS. The nanoparticle concentration is around 0.5-1 × e^{10} particles/mL.

When injected into the body, the rapid temperature increase at 37 °C could lead to some destabilization phenomena that alter the NPs features and consequently their performance *in vivo*[7]. Stress tests studies, on lipid-based NPs were highly encouraged by the FDA as reported in their guideline for liposome drug products addressed to the industry in 2008[59, 60]. Indeed, liposomes are prone to degradation due to the hydrolysis of saturated and unsaturated lipids. We evaluated their size distribution over time (up to 13 h) at 37 °C by DLS, and no significant increase in their average size and St.Dev was observed (Figure I-4b). Similar formulations to LiPoNs reported a decrease in plasma concentration within 11 post-injection (with a $T_{1/2}\alpha$ of 28.08 min and $T_{1/2}\beta$ of 297.05 min)[61]. In our case, the LiPoNs preserve the size over time, maybe due to electrostatic interaction between the chitosan entrapment and lipid bilayer that could reduce the phosphate group's motional freedom, increasing the stability[62].

The first biological barrier encountered by the NPs is the blood, where they interact with plasma proteins and blood cells[9]. The circulation time of NPs is affected by the composition and structure of protein corona[63]. The knowledge of how protein corona affects the biological performance of liposomes is not fully elucidated. Indeed, any changes in surface charge, size and lipid composition (including acyl chain length and saturation) of lipid-based carriers affect the protein bindings to the lipid-based NPs[64]. Therefore, to assess the LiPoNs stability in a more complex environments, such as plasma from the human. We reported an increase in the average size of LiPoNs in the first 2 h, from 126 nm to 146 nm, without any further significant variations (Figure I-4c). Even though the addition of proteins on LiPoNs may have increased the hydrodynamic diameter of NPs around 50 nm, no huge differences have been detected in size and aggregation phenomena. This limited increase in the binding of proteins could be related to the small size of the NPs that consequently display a low surface area and curvature available for absorption[65]. In addition, the slightly negative charge (-17.4 mV) and the cholesterol addition of LiPoNs could reduce interaction with the proteins[6, 56]. However, the TEM image reported a partial aggregation of NPs with the fusion of lipid bilayers, maybe due to some bilayer destabilizations or absorption of protein[66, 67]. Therefore, further investigations of phenomena involved in more realistic models where the contact with plasma proteins is evaluated in-flow, under shear stress conditions, are required[68-70].

I.2.2.5 Co-Encapsulation Efficacy of Multifunctional LiPoNs

The core-shell nanostructure of lipid-polymer NPs, made up of two different materials, is suitable for compound loading. The payload agents, Gd-DTPA, Atto633 and Irinotecan, are dissolved in chitosan solution and then injected into the middle channel, forcing their loading into the core of the LiPoNs' complex. The addition of Gd-DTPA to the polymer solution (mass ratio 1:40 of CH:Gd-DTPA) did not produce any instabilities at the flow focusing interface, however, higher precipitation along the device is observed. The loading of Gd-DTPA slightly increases the LiPoNs size to 95 nm (Table I-2). The morphology of LiPoNs slightly changed due to the entrapment of the compound, leading to a less stained core. The diagnostic properties of the carriers were measured at 37 °C and 1.5 T, reporting an *in vitro* longitudinal relaxation time T_1 of 1691 ms. The Encapsulation efficacy for the Gd-DTPA was around 78%, quantified from a calibration curve (Appendix- Figure IV-8) with the Minispec Bench Top Relaxometer (Bruker Corporation). A reduction of the negative charge to -11 mV was shown for Gd-DTPA LiPoNs.

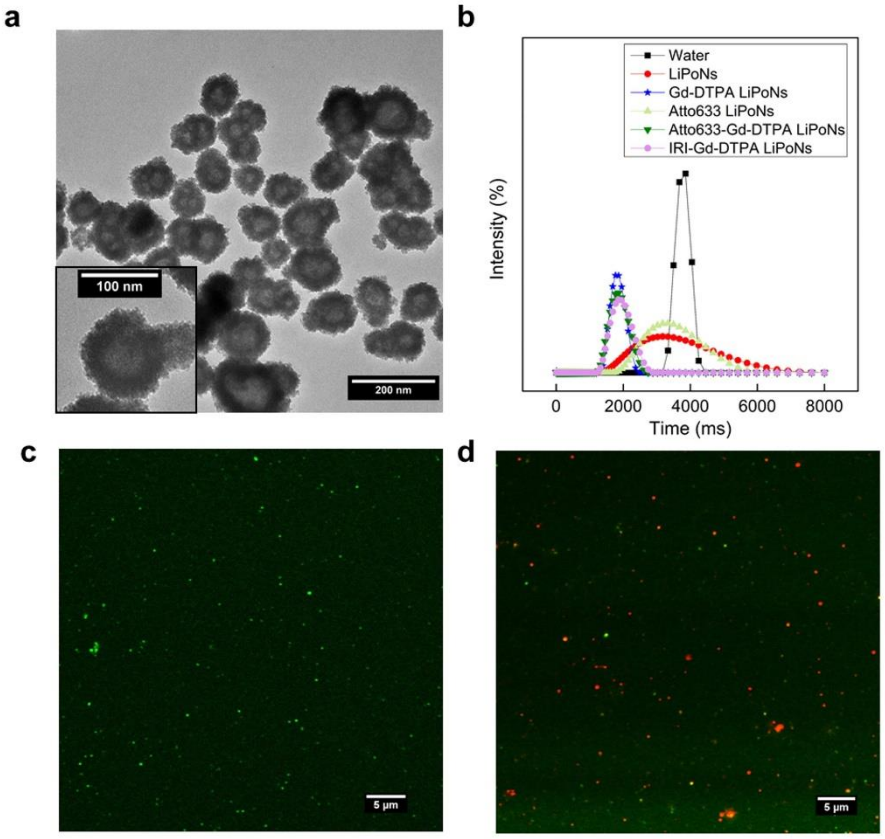

Figure I-5. Multimodal imaging properties of LiPoNs. a) TEM image of Gd-DTPA-loaded LiPoNs stained with osmium smoke; **b**) *in vitro MRI*. Comparison of longitudinal relaxation time distributions of water, LiPoNs, Gd-DTPA-loaded LiPoNs, Atto633-loaded LiPoNs, Atto633-Gd-DTPA co-loaded LiPoNs, IRI-Gd-DTPA co-loaded LiPoNs, **c**) optical imaging of Atto 488-loaded LiPoNs by confocal microscopy; **d**) merge fluorescent image of Atto 488 (green) and CellMask (red) of Atto 488-Gd-DTPA co-loaded LiPoNs stained with CellMask™ Orange Plasma membrane stain (dilution $1:10^4$).

We next examined the optical and theranostic properties of LiPoNs by simultaneous encapsulation of Gd-DTPA and active agents (Atto 633/Irinotecan) alternatively. In vitro longitudinal relaxation time T1 of different formulations of LiPoNs and water are shown in Figure I-5b. No changes in the longitudinal relaxation time were observed due to co-loading of Atto633/ Irinotecan. Indeed, the LiPoNs preserved the EE % around 67%. The amount of co-loaded Atto 633 and Irinotecan has been quantified through measurements with the Multiplate Reader Photometer starting from a calibration curve (Appendix-Figure VI-8). The co-EE% of Irinotecan was 36%, while the co-EE % of Atto 633 was 55%. The co-loading of Gd-DTPA did not affected the Atto633 loading. A further increase in the size of Gd-DTPA LiPoNs was observed for the loading of Irinotecan to 112.8 nm (Table I-2).

Table I-2. Table summary of average size, polydispersity index (PDI) and zeta potential for different LiPoNs formulations.

	FR^2	Average size (nm)	PDI	Zeta Potential (mV)
LiPoNs	0.073	77.4	0.22	-17.4
Gd-DTPA-LiPoNs		95.3	0.3	-11
Atto633- LiPoNs		/	/	-3.7
Atto633-Gd-DTPA-LiPoNs		/	/	-10.9
IRI-Gd-DTPA- LiPoNs		112.8	0.28	-14.2

The confocal observations confirmed the optical properties of LiPoNs, as shown in Figure I-5c and Appendix- Figure IV-9. To gain more insight into the structural properties of LiPoNs, we compared the loading of the fluorescent agent within the chitosan core and the CellMask Orange Plasma membrane staining of the lipid components using a confocal microscope. The overlapping of the CellMask Orange Plasma membrane stain and fluorescent spherical spots of Atto 488 and Atto 633, are shown in Figure I-d and Appendix-Figure VI-9, respectively.

I.2.2.6 In Vitro Cytotoxicity Study

Lipid-based NPs are usually considered pharmacologically inactive compounds as well as chitosan NPs [71]. As a reference, good biocompatibility of liposomes composed of Soy Lecithin and cholesterol with concentrations ranging from 0 to 500 ug/mL has already been reported[72]. Chitosan is a natural and biocompatible polymer, and it exhibits cytotoxicity at concentrations higher than 0.741 mg/ml[73]. However, any changes in materials compositions, surface charge, time and dose of exposure can lead to cytotoxic effects. Therefore, we tested LiPoNs formulation at increasing concentrations (lipids concentration 2–42 µg/mL; chitosan concentration 0.07–2.1 ug/mL) for 24 hours through MTT assay (Figure I-6). The MTT assay quantified the alteration of cell metabolism by the detecting of dehydrogenase activity in viable cells. No significant reduction in cell viability % for all tested formulations was detected.

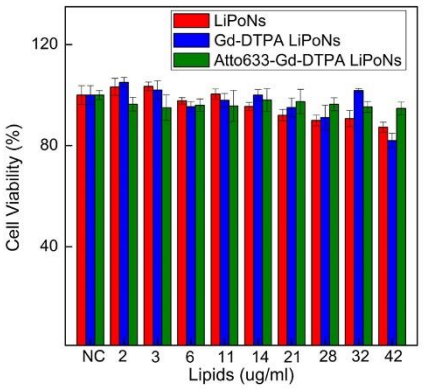

Figure I-6. In vitro citotoxicity. Cell viability % of U87 MG cells exposed to an increasing concentration of LiPoNs, Gd-DTPA-loaded LiPoNs and Atto 633-Gd-DTPA co-loaded LiPoNs (Lipid conc.: 2–42 µg/mL, chitosan conc.: 0.07–2.1 µg/mL, Gd-DTPA conc.: 3–105 µM, Atto 633 conc.: 0.01–0.3 µg/mL) for 24 h.

I.2.2.7 Evaluation of cellular uptake of multimodal imaging LiPoNs

A preliminary study of the cellular uptake kinetics of LiPoNs is performed by fluorescence-activated cell sorting (FACS) and confocal microscope imaging. U87 MG cells, upon incubation with Atto633-Gd-DTPA LiPoNs, at a lipid concentration of 90 µg/mL, were investigated individually for up to 24 h (Figure I-7a–c).

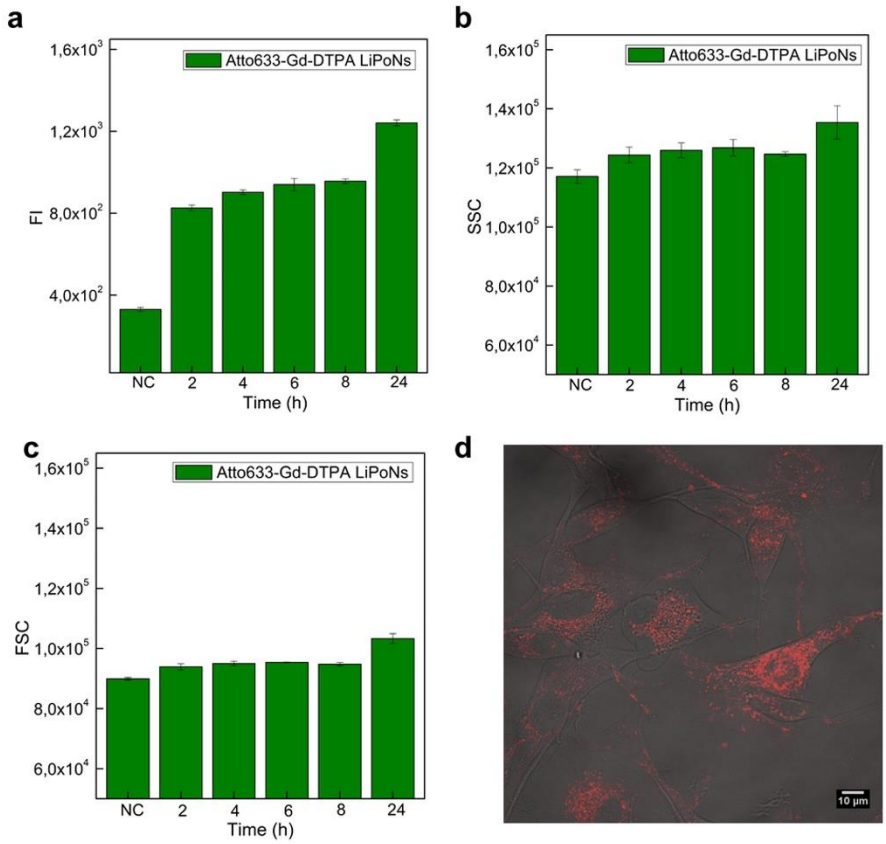

Figure I-7. Quantitative uptake of multimodal imaging LiPoNs by U87 MG cells. a) Fluorescent Intensity (FI); **b**) Side Scattering Area (SSC); **c**) Forward Scattering Area (FSC) of U87 MG cells exposed to Atto633-Gd-DTPA co-loaded LiPoNs (Lipids conc.: 90 µg/mL, Atto 633 conc.: 0.6 µg/mL, Gd-DTPA conc.: 225 µM) for different time points: 2 h, 4 h, 6 h, 8 h and 24 h. **d**) Merge image of the transmission and fluorescence (Atto633) images obtained by confocal microscopy of U87 MG cells treated for 24 h with the 90 µg/mL of Atto633-Gd-DTPA LipoNs.

The fluorescence intensity of cells (Figure I-7a) rises quickly (2 h) and pursues linearly over time (24 h). FACS was used for the analyses of the samples with the same concentration in terms of Forward Scattering (FSC) and Side Scattering (SSC) intensity after incubation of

Atto633-Gd-DTPA-loaded LiPoNs (Figure I-7b,c). The SSC signal is known to be related to the inner complexity or granulometry of the cells and the internalisation of NPs inside the cells[74]. Our data show an increase of SSC signal with longer times of incubation (Figure I-7b). The FSC is related to cell size and the cell death process[74]. In this case, no changes in FSC signal were reported, reiterating the high biocompatibility of LiPoNs nanosystems (Figure I-7c). These results match the FI signal already described (Figure I-7a) and confirm the LiPoNs uptake kinetics.

Analysing the fluorescence signal of the cells treated with an increasing concentration of LiPoNs (30–90 µg/mL) provides additional insights regarding their uptake kinetics (Figure VI-10). Further tests to evaluate the effect of the LiPoNs concentration, ranging from 30 to 90 µg/mL, on cell uptake are reported in Appendix-FigureVI-10. The results show a rise in the fluorescence signal in correlation with the increasing concentration of LiPoNs tested, but a more marked dose-dependent effect is observed over longer times. In the case of a lower LiPoNs concentration, the cell fluorescence increases within 4 h, and remains almost unchanged until 24 h. The results are coherent also with SSC and FSC acquisitions (Appendix-Figure VI-10).

Regarding uptake kinetics, all tested concentrations (Figures I-7a–c and VI–10) show a high uptake rate in the first 4 h of incubation, so we assume that LiPoNs uptake occurs mainly in the first 4 h. This linear increase in the mean fluorescence without any saturation phenomena at shorter periods was previously reported as energy-dependent uptake[75]. The raw flow cytometry data of U87 MG cells exposed to increasing concentrations of Atto -Gd-DTPA-loaded LiPoNs (Lipids conc.: 30–60–90 µg/mL) at different time points (4 h; 8 h; 24 h) are reported in Figure VI12–14.

We also establish the localisation of LiPoNs within the cells by imaging U87 MG cells treated with Atto633-Gd-DTPA LiPoNs, at a lipid concentration of 90 µg/mL, for 24 h with a confocal microscope (Figure I-7d and Figure VI-11). The Merge Z-stack video of the transmission and fluorescence (Atto 633) of the cell treated with LiPoNs shows the internalisation of NPs within the cells.

We can hypothesize that the increase in the mean fluorescence intensity at 24 h for a higher LiPoNs concentration is mainly due to the large number of NPs still available in the extracellular medium; therefore, their uptake is continuous over time. This latter statement is confirmed quantitatively by confocal Z-stack images where LiPoNs were localised near to cytoplasmic membrane of the minority of the cells even after 24 h.

This finding, in accordance with Daphne Montizaan et al.[76] which reported that the uptake of zwitterionic and negatively charged liposomes, is typical of an energy-dependent mechanism, particularly clathrin-mediated endocytosis. However, the liposome-cell interaction can also occur through three other mechanisms (adsorption, lipid exchange and fusion)[77, 78]. Therefore, the lipophilic interaction of LiPoNs with the cell membrane could induce a direct uptake by passive diffusion[79] in parallel to an energy-dependent mechanism. Indeed, Guo et al.[13] reported that the cell internalisation pathway shifts from fusion to endocytosis by altering the elasticity of particle nanolipogels, changing the

extent of crosslinking of the core material encapsulated in the liposome. In our case, the un-crosslinked core in LiPoNs could confer a moderate elasticity to nanoparticles mediating the cellular uptake of both: fusion and endocytosis pathways.

These behaviours required further investigation because differences in the nanoparticle formulation (head group of lipids, cholesterol addition, size, protein corona absorption), cell type and nanostructure elasticity, which can be controlled by microfluidics, strongly affect the NPs uptake behaviour[77, 78, 80].

I.2.2.8 In Vitro Assessment of Cytotoxicity Activity of Theranostic IRI Gd-DTPA-loaded LiPoNs

Irinotecan hydrochloride (IRI) is a semisynthetic of camptothecin used to inhibit topoisomerase-I (Topo I), producing DNA strand breaks and inducing cell death[81]. Indeed, in Phase I/II trials, Irinotecan has shown encouraging results for treating malignant glioma alone or in combination with other cytotoxic drugs[82]. To test the biological activity of theranostic Irinotecan Gd-DTPA co-loaded LiPoNs (IRI-Gd-DTPA LiPoNs) on human glioblastoma cells (U87 MG), a quantification of their cell cytotoxicity was performed. Therefore, the MTT assay on U87 MG glioblastoma cells was used to assess the improved efficacy of the IRI-Gd-DTPA LiPoNs formulation in comparison with free drug (Figure I-8) on cell survival and growth.

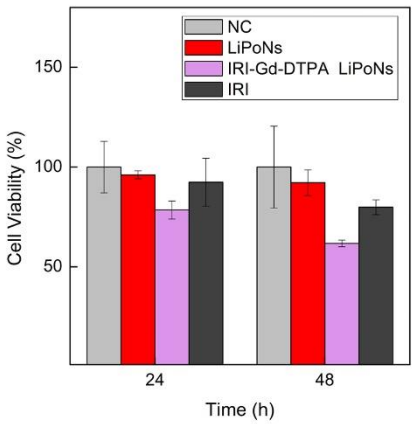

Figure I-8. Viability of U87 MG cells treated with theranostic LiPoNs. Comparison of cell viability % of U87 MG cells treated for 24 h and 48 h with 7.7 µM of free Irinotecan and in IRI-Gd-DTPA co-loaded LiPoNs formulation (lipid conc.: 0.4 mg/mL, Gd-DTPA conc.: 1.25 mM). The cell viability % of U87 MG cells in the presence of blank LiPoNs at the same tested conditions of IRI-Gd-DTPA LipoNs is reported.

U87-MG cells were treated with 7.7µM of free Irinotecan alone and loaded in LiPoNs (IRI-Gd-DTPA LiPoNs) for different time intervals (24 h and 48 h) (Figure I-8). Blank LiPoNs were tested in the same conditions as a control.

At 24 h, in the case of IRI-Gd-DTPA-loaded LiPoNs, a reduction in cell viability down to 78.5% ± 5 was detected. Moreover, the results at 48 h show a cell survival decreased from 100 to 61.7% ±2 and 79.9% ±4 when the cells were incubated with IRI-Gd-DTPA LiPoNs and free IRI, respectively. The most pronounced difference between the LiPoNs' formulation and free drug on the cell viability reduction was observed and highlighted at a longer incubation time of 48 h.This effect is in line with the pharmacodynamics of Irinotecan, which is a topoisomerase inhibitor, acting on cell division mainly completed up to 48 h[83].

These findings are in agreement with Casado et al.[84], who reported a different uptake mechanism for Irinotecan-loaded liposomes (mainly endocytic process) and free drugs (passive diffusion). Moreover, they highlighted the increase in the therapeutic index of Irinotecan using a liposomal formulation.

Comparing the data shown in Figure 8 with the bibliographic reference[81], LiPoNs seem to act as efficient theranostic carriers (≃61% U87 MG cells) for a lower dose (7.7 µM) at equal exposure time (48 h). It was also reported that the entrapment of Irinotecan within a liposome core at a low pH improves the stability of the lactone, the active form of the drug, avoiding its hydrolysis at a physiological pH[84, 85]. The acid chitosan core loads and preserves the IRI in lactone form, while the lipid counterpart mediates its cellular delivery, improving its efficacy. Finally, we also proved that the designed one-step cHFF enables a higher IRI encapsulation thanks to a microfluidic environment condition that locks the IRI in its active form within the architecture of LiPoNs.

I.3 CONCLUSIONS

Effective targeting and biological outcome of newly synthesized nanovectors are mainly determined by the dynamic and complex interplay between the heterogeneous biological microenvironment and the nanocarrier itself, defined as nano−bio interactions. We rationally selected materials of hybrid Lipid-Polymer NPs (LiPoNs) to improve the structural integrity of liposomes and consequently address the stability across the biological barriers. Lipid–Polymer Nanoparticles (LiPoNs) combined a chitosan core to a lipid bilayer, to acquire new functionalities and performances at nano–bio interactions. We designed an innovative one-step process that coupled thermodynamics, lipid self-assembly and polymer nanoprecipitation to produce LiPoNs. We studied the influence of solvent-nonsolvent ratio, concentration and flow rate ratio on the coupling kinetics. We identified the process conditions to produce lipid-polymer NPs with an average size of 100 nm and a slightly negative charge. These multifunctional nanostructures have shown structural stability in different environmental conditions, the ability to entrap multiple cargos and the capability to deliver them to the cells. Indeed, the chitosan core of LiPoNs, acting as a reservoir, enabled the high co-loading of the Gd-DTPA and Atto 633 for multimodal imaging applications. The LiPoNs showed a higher cell internalization in the first 4 hours. The theranostic effects of Irinotecan and Gd-DTPA co-loaded LiPoNs were validated on U87 MG cells upon 48 h of treatment, showing competition between the free IRI and the delivered one, speeding up the uptake and enhancing cytotoxicity at a reduced concentration. The high cellular uptake and the biological response of active agents co-loaded LiPoNs can be

connected to the peculiar elasticity and fluidity that characterised these hybrid systems. We proved that through the microfluidic approach cHFF, it is possible to achieve further control of the selected composition, triggering cell internalisation pathways, and subsequently to enhanced NPs–tissue interactions.

I.4 REFERENCES

[1] G.Y. Chen, I. Roy, C.H. Yang, P.N. Prasad, Nanochemistry and Nanomedicine for Nanoparticle-based Diagnostics and Therapy, Chemical Reviews 116(5) (2016) 2826-2885.
[2] D. Peer, J.M. Karp, S. Hong, O.C. FaroKhzad, R. Margalit, R. Langer, Nanocarriers as an emerging platform for cancer therapy, Nature Nanotechnology 2(12) (2007) 751-760.
[3] V. Wagner, A. Dullaart, A.K. Bock, A. Zweck, The emerging nanomedicine landscape, Nature Biotechnology 24(10) (2006) 1211-1217.
[4] K. Hadinoto, A. Sundaresan, W.S. Cheow, Lipid-polymer hybrid nanoparticles as a new generation therapeutic delivery platform: A review, European Journal of Pharmaceutics and Biopharmaceutics 85(3) (2013) 427-443.
[5] J. Cao, D. Huang, N.A. Peppas, Advanced engineered nanoparticulate platforms to address key biological barriers for delivering chemotherapeutic agents to target sites, Advanced Drug Delivery Reviews 167 (2020) 170-188.
[6] P. Nakhaei, R. Margiana, D.O. Bokov, W.K. Abdelbasset, M.A.J. Kouhbanani, R.S. Varma, F. Marofi, M. Jarahian, N. Beheshtkhoo, Liposomes: Structure, Biomedical Applications, and Stability Parameters With Emphasis on Cholesterol, Frontiers in Bioengineering and Biotechnology 9 (2021).
[7] M. Anderson, A. Omri, The effect of different lipid components on the in vitro stability and release kinetics of liposome formulations, Drug Delivery 11(1) (2004) 33-39.
[8] S. Wilhelm, A.J. Tavares, Q. Dai, S. Ohta, J. Audet, H.F. Dvorak, W.C.W. Chan, Analysis of nanoparticle delivery to tumours, Nature Reviews Materials 1(5) (2016).
[9] W. Poon, B.R. Kingston, B. Ouyang, W. Ngo, W.C.W. Chan, A framework for designing delivery systems, Nature Nanotechnology 15(10) (2020) 819-829.
[10] E. Blanco, H. Shen, M. Ferrari, Principles of nanoparticle design for overcoming biological barriers to drug delivery, Nature Biotechnology 33(9) (2015) 941-951.
[11] Y. Hui, X. Yi, F. Hou, D. Wibowo, F. Zhang, D.Y. Zhao, H.J. Gao, C.X. Zhao, Role of Nanoparticle Mechanical Properties in Cancer Drug Delivery, Acs Nano 13(7) (2019) 7410-7424.
[12] B. Mandal, H. Bhattacharjee, N. Mittal, H. Sah, P. Balabathula, L.A. Thoma, G.C. Wood, Core-shell-type lipid-polymer hybrid nanoparticles as a drug delivery platform, Nanomedicine-Nanotechnology Biology and Medicine 9(4) (2013) 474-491.

[13] P. Guo, D.X. Liu, K. Subramanyam, B.R. Wang, J. Yang, J. Huang, D.T. Auguste, M.A. Moses, Nanoparticle elasticity directs tumor uptake, Nature Communications 9 (2018).
[14] A. Mukherjee, A.K. Waters, P. Kalyan, A.S. Achrol, S. Kesari, V.M. Yenugonda, Lipid-polymer hybrid nanoparticles as a next-generation drug delivery platform: state of the art, emerging technologies, and perspectives, International Journal of Nanomedicine 14 (2019) 1937-1952.
[15] L. Fenart, A. Casanova, B. Dehouck, C. Duhem, S. Slupek, R. Cecchelli, D. Betbeder, Evaluation of effect of charge and lipid coating on ability of 60-nm nanoparticles to cross an in vitro model of the blood-brain barrier, Journal of Pharmacology and Experimental Therapeutics 291(3) (1999) 1017-1022.
[16] A.L. Troutier, T. Delair, C. Pichot, C. Ladaviere, Physicochemical and interfacial investigation of lipid/polymer particle assemblies, Langmuir 21(4) (2005) 1305-1313.
[17] J. Thevenot, A.L. Troutier, L. David, T. Delair, C. Ladaviere, Steric stabilization of lipid/polymer particle assemblies by poly(ethylene glycol)-lipids, Biomacromolecules 8(11) (2007) 3651-3660.
[18] C.J. Hitzman, W.F. Elmquist, L.W. Wattenberg, T.S. Wiedmann, Development of a respirable, sustained release microcarrier for 5-fluorouracil I: In vitro assessment of liposomes, microspheres, and lipid coated nanoparticles, Journal of Pharmaceutical Sciences 95(5) (2006) 1114-1126.
[19] A. Mahzabin, B. Das, A REVIEW OF LIPID-POLYMER HYBRID NANOPARTICLES AS A NEW GENERATION DRUG DELIVERY SYSTEM, International Journal of Pharmaceutical Sciences and Research 12(1) (2021) 65-75.
[20] D. Guimaraes, J. Noro, A. Loureiro, F. Lager, G. Renault, A. Cavaco-Paulo, E. Nogueira, Increased Encapsulation Efficiency of Methotrexate in Liposomes for Rheumatoid Arthritis Therapy, Biomedicines 8(12) (2020).
[21] A. Bershteyn, J. Chaparro, R. Yau, M. Kim, E. Reinherz, L. Ferreira-Moita, D.J. Irvine, Polymer-supported lipid shells, onions, and flowers, Soft Matter 4(9) (2008) 1787-1791.
[22] W.S. Cheow, K. Hadinoto, Factors affecting drug encapsulation and stability of lipid-polymer hybrid nanoparticles, Colloids and Surfaces B-Biointerfaces 85(2) (2011) 214-220.
[23] L.F. Zhang, J.M. Chan, F.X. Gu, J.W. Rhee, A.Z. Wang, A.F. Radovic-Moreno, F. Alexis, R. Langer, O.C. Farokhzad, Self-assembled lipid-polymer hybrid nanoparticles: A robust drug delivery platform, Acs Nano 2(8) (2008) 1696-1702.
[24] J.M. Chan, L.F. Zhang, K.P. Yuet, G. Liao, J.W. Rhee, R. Langer, O.C. Farokhzad, PLGA-lecithin-PEG core-shell nanoparticles for controlled drug delivery, Biomaterials 30(8) (2009) 1627-1634.
[25] X.Z. Yang, S. Dou, Y.C. Wang, H.Y. Long, M.H. Xiong, C.Q. Mao, Y.D. Yao, J. Wang, Single-Step Assembly of Cationic Lipid-Polymer Hybrid Nanoparticles for Systemic Delivery of siRNA, Acs Nano 6(6) (2012) 4955-4965.
[26] M.A. Younis, H.M. Tawfeek, A.A.H. Abdellatif, J.A. Abdel-Aleem, H. Harashima, Clinical translation of nanomedicines: Challenges, opportunities, and keys, Advanced Drug Delivery Reviews 181 (2022) 114083.
[27] S. Hua, M.B.C. de Matos, J.M. Metselaar, G. Storm, Current Trends and Challenges in the Clinical Translation of Nanoparticulate Nanomedicines: Pathways for Translational Development and Commercialization, Frontiers in Pharmacology 9 (2018).

[28] P. Tabeling, Introduction to microfluidics, OUP Oxford2005.
[29] P.M. Valencia, O.C. Farokhzad, R. Karnik, R. Langer, Microfluidic technologies for accelerating the clinical translation of nanoparticles, Nature Nanotechnology 7(10) (2012) 623-629.
[30] L. Capretto, D. Carugo, S. Mazzitelli, C. Nastruzzi, X.L. Zhang, Microfluidic and lab-on-a-chip preparation routes for organic nanoparticles and vesicular systems for nanomedicine applications, Advanced Drug Delivery Reviews 65(11-12) (2013) 1496-1532.
[31] R. Ferrari, M. Sponchioni, M. Morbidelli, D. Moscatelli, Polymer nanoparticles for the intravenous delivery of anticancer drugs: the checkpoints on the road from the synthesis to clinical translation, Nanoscale 10(48) (2018) 22701-22719.
[32] L. Zhang, Q.H. Chen, Y. Ma, J.S. Sun, Microfluidic Methods for Fabrication and Engineering of Nanoparticle Drug Delivery Systems, Acs Applied Bio Materials 3(1) (2020) 107-120.
[33] Q. Feng, L. Zhang, C. Liu, X.Y. Li, G.Q. Hu, J.S. Sun, X.Y. Jiang, Microfluidic based high throughput synthesis of lipid-polymer hybrid nanoparticles with tunable diameters, Biomicrofluidics 9(5) (2015).
[34] J.S. Hong, S.M. Stavis, S.H.D. Lacerda, L.E. Locascio, S.R. Raghavan, M. Gaitan, Microfluidic Directed Self-Assembly of Liposome-Hydrogel Hybrid Nanoparticles, Langmuir 26(13) (2010) 11581-11588.
[35] P.M. Valencia, P.A. Basto, L.F. Zhang, M. Rhee, R. Langer, O.C. Farokhzad, R. Karnik, Single-Step Assembly of Homogenous Lipid - Polymeric and Lipid - Quantum Dot Nanoparticles Enabled by Microfluidic Rapid Mixing, Acs Nano 4(3) (2010) 1671-1679.
[36] J.S. Sun, L. Zhang, J.L. Wang, Q. Feng, D.B. Liu, Q.F. Yin, D.Y. Xu, Y.J. Wei, B.Q. Ding, X.H. Shi, X.Y. Jiang, Tunable Rigidity of (Polymeric Core)-(Lipid Shell) Nanoparticles for Regulated Cellular Uptake, Advanced Materials 27(8) (2015) 1402-+.
[37] Y.T. Kim, B.L. Chung, M.M. Ma, W.J.M. Mulder, Z.A. Fayad, O.C. Farokhzad, R. Langer, Mass Production and Size Control of Lipid-Polymer Hybrid Nanoparticles through Controlled Microvortices, Nano Letters 12(7) (2012) 3587-3591.
[38] A.J. Mieszawska, Y. Kim, A. Gianella, I. van Rooy, B. Priem, M.P. Labarre, C. Ozcan, D.P. Cormode, A. Petrov, R. Langer, O.C. Farokhzad, Z.A. Fayad, W.J.M. Mulder, Synthesis of Polymer-Lipid Nanoparticles for Image-Guided Delivery of Dual Modality Therapy, Bioconjugate Chemistry 24(9) (2013) 1429-1434.
[39] T.T.H. Thi, E.J.A. Suys, J.S. Lee, D.H. Nguyen, K.D. Park, N.P. Truong, Lipid-Based Nanoparticles in the Clinic and Clinical Trials: From Cancer Nanomedicine to COVID-19 Vaccines, Vaccines 9(4) (2021).
[40] X.C. Hou, T. Zaks, R. Langer, Y.Z. Dong, Lipid nanoparticles for mRNA delivery, Nature Reviews Materials 6(12) (2021) 1078-1094.
[41] F. Roffo, A.M. Ponsiglione, P.A. Netti, E. Torino, coupled Hydrodynamic Flow Focusing (cHFF) to Engineer Lipid–Polymer Nanoparticles (LiPoNs) for Multimodal Imaging and Theranostic Applications %M doi:10.3390/biomedicines10020438 %U https://www.mdpi.com/2227-9059/10/2/438, Biomedicines %@ 2227-9059 10(2) (2022) 438.
[42] Y. Hui, X. Yi, D. Wibowo, G.Z. Yang, A.P.J. Middelberg, H.J. Gao, C.X. Zhao, Nanoparticle elasticity regulates phagocytosis and cancer cell uptake, Science Advances 6(16) (2020).

[43] A. Mohanty, S. Uthaman, I.K. Park, Utilization of Polymer-Lipid Hybrid Nanoparticles for Targeted Anti-Cancer Therapy, Molecules 25(19) (2020).
[44] S. Bochicchio, G. Lamberti, A.A. Barba, Polymer-Lipid Pharmaceutical Nanocarriers: Innovations by New Formulations and Production Technologies, Pharmaceutics 13(2) (2021).
[45] C.Y. Meng, Z. Chen, G. Li, T. Welte, H.F. Shen, Nanoplatforms for mRNA Therapeutics, Advanced Therapeutics 4(1) (2021).
[46] K.A. Hajj, K.A. Whitehead, Tools for translation: non-viral materials for therapeutic mRNA delivery, Nature Reviews Materials 2(10) (2017).
[47] J. Kim, Y. Eygeris, M. Gupta, G. Sahay, Self-assembled mRNA vaccines, Advanced Drug Delivery Reviews 170 (2021) 83-112.
[48] I. Rivolta, A. Panariti, B. Lettiero, S. Sesana, P. Gasco, M.R. Gasco, M. Masserini, G. Miserocchi, CELLULAR UPTAKE OF COUMARIN-6 AS A MODEL DRUG LOADED IN SOLID LIPID NANOPARTICLES, Journal of Physiology and Pharmacology 62(1) (2011) 45-53.
[49] Y. Cao, Y.F. Tan, Y.S. Wong, M.W.J. Liew, S. Venkatraman, Recent Advances in Chitosan-Based Carriers for Gene Delivery, Marine Drugs 17(6) (2019).
[50] Y.C. Chen, D.Y. Gao, L. Huang, In vivo delivery of miRNAs for cancer therapy: Challenges and strategies, Advanced Drug Delivery Reviews 81 (2015) 128-141.
[51] R.M. Reeves Jp Fau - Dowben, R.M. Dowben, Formation and properties of thin-walled phospholipid vesicles, (0021-9541 (Print)).
[52] A. Jahn, W.N. Vreeland, M. Gaitan, L.E. Locascio, Controlled vesicle self-assembly in microfluidic channels with hydrodynamic focusing, Journal of the American Chemical Society 126(9) (2004) 2674-2675.
[53] M.Q. Lu, A. Ozcelik, C.L. Grigsby, Y.H. Zhao, F. Guo, K.W. Leong, T.J. Huang, Microfluidic hydrodynamic focusing for synthesis of nanomaterials, Nano Today 11(6) (2016) 778-792.
[54] L. Capretto, W. Cheng, D. Carugo, O.L. Katsamenis, M. Hill, X.L. Zhang, Mechanism of co-nanoprecipitation of organic actives and block copolymers in a microfluidic environment, Nanotechnology 23(37) (2012).
[55] A. Pal, P. Sunthar, D.V. Khakhar, Effects of Ethanol Addition on the Size Distribution of Liposome Suspensions in Water, Industrial & Engineering Chemistry Research 58(18) (2019) 7511-7519.
[56] Y. Yamamoto, Y. Nagasaki, Y. Kato, Y. Sugiyama, K. Kataoka, Long-circulating poly(ethylene glycol)-poly(D,L-lactide) block copolymer micelles with modulated surface charge, Journal of Controlled Release 77(1-2) (2001) 27-38.
[57] H.S. Choi, W. Liu, P. Misra, E. Tanaka, J.P. Zimmer, B.I. Ipe, M.G. Bawendi, J.V. Frangioni, Renal clearance of quantum dots, Nature Biotechnology 25(10) (2007) 1165-1170.
[58] M. Wright, Nanoparticle tracking analysis for the multiparameter characterization and counting of nanoparticle suspensions, Methods Mol Biol 906 (2012) 511-24.
[59] U. Fda, Liposome drug products chemistry, manufacturing, and controls; human pharmacokinetics and bioavailability; and labeling documentation, Guidance for Industry (2018).
[60] C.T. Inglut, A.J. Sorrin, T. Kuruppu, S. Vig, J. Cicalo, H. Ahmad, H.C. Huang, Immunological and Toxicological Considerations for the Design of Liposomes, Nanomaterials 10(2) (2020).

[61] Y.Z. Huang, J.Q. Gao, W.Q. Lang, S. Nakagawa, Preparation and characterization of liposomes encapsulating chitosan nanoparticles, Biological & Pharmaceutical Bulletin 28(2) (2005) 387-390.
[62] M. Hasan, G. Ben Messaoud, F. Michaux, A. Tamayol, C.J.F. Kahn, N. Belhaj, M. Linder, E. Arab-Tehrany, Chitosan-coated liposomes encapsulating curcumin: study of lipid-polysaccharide interactions and nanovesicle behavior, Rsc Advances 6(51) (2016) 45290-45304.
[63] S. Tenzer, D. Docter, J. Kuharev, A. Musyanovych, V. Fetz, R. Hecht, F. Schlenk, D. Fischer, K. Kiouptsi, C. Reinhardt, K. Landfester, H. Schild, M. Maskos, S.K. Knauer, R.H. Stauber, Rapid formation of plasma protein corona critically affects nanoparticle pathophysiology, Nature Nanotechnology 8(10) (2013) 772-U1000.
[64] N. Onishchenko, D. Tretiakova, E. Vodovozova, Spotlight on the protein corona of liposomes, Acta Biomaterialia 134 (2021) 57-78.
[65] S.C. Semple, A. Chonn, P.R. Cullis, Interactions of liposomes and lipid-based carrier systems with blood proteins: Relation to clearance behaviour in vivo, Advanced Drug Delivery Reviews 32(1-2) (1998) 3-17.
[66] J. Pencer, G.F. White, F.R. Hallett, Osmotically induced shape changes of large unilamellar vesicles measured by dynamic light scattering, Biophysical Journal 81(5) (2001) 2716-2728.
[67] J. Wolfram, K. Suri, Y. Yang, J.L. Shen, C. Celia, M. Fresta, Y.L. Zhao, H.F. Shen, M. Ferrari, Shrinkage of pegylated and non-pegylated liposomes in serum, Colloids and Surfaces B-Biointerfaces 114 (2014) 294-300.
[68] O.K. Kari, J. Ndika, P. Parkkila, A. Louna, T. Lajunen, A. Puustinen, T. Viitala, H. Alenius, A. Urtti, In situ analysis of liposome hard and soft protein corona structure and composition in a single label-free workflow, Nanoscale 12(3) (2020) 1728-1741.
[69] S. Palchetti, D. Pozzi, A.L. Capriottic, G. La Barbera, R.Z. Chiozzi, L. Digiacomo, G. Peruzzi, G. Caracciolo, A. Lagana, Influence of dynamic flow environment on nanoparticle-protein corona: From protein patterns to uptake in cancer cells, Colloids and Surfaces B-Biointerfaces 153 (2017) 263-271.
[70] D. Pozzi, G. Caracciolo, L. Digiacomo, V. Colapicchioni, S. Palchetti, A.L. Capriotti, C. Cavaliere, R.Z. Chiozzi, A. Puglisi, A. Lagana, The biomolecular corona of nanoparticles in circulating biological media, Nanoscale 7(33) (2015) 13958-13966.
[71] B. Drasler, P. Sayre, K.G. Steinhauser, A. Petri-Fink, B. Rothen-Rutishauser, In vitro approaches to assess the hazard of nanomaterials (vol 8, pg 99, 2017), Nanoimpact 9 (2018) 51-51.
[72] T.L. Nguyen, T.H. Nguyen, D.H. Nguyen, Development and In Vitro Evaluation of Liposomes Using Soy Lecithin to Encapsulate Paclitaxel, International Journal of Biomaterials 2017 (2017).
[73] M. Huang, E. Khor, L.Y. Lim, Uptake and cytotoxicity of chitosan molecules and nanoparticles: Effects of molecular weight and degree of deacetylation, Pharmaceutical Research 21(2) (2004) 344-353.
[74] S.Y. Choi, N. Yang, S.K. Jeon, T.H. Yoon, Semi-quantitative Estimation of Cellular SiO2 Nanoparticles Using Flow Cytometry Combined with X-ray Fluorescence Measurements, Cytometry Part A 85A(9) (2014) 771-780.

[75] A. Salvati, C. Aberg, T. dos Santos, J. Varela, P. Pinto, I. Lynch, K.A. Dawson, Experimental and theoretical comparison of intracellular import of polymeric nanoparticles and small molecules: toward models of uptake kinetics, Nanomedicine-Nanotechnology Biology and Medicine 7(6) (2011) 818-826.
[76] D. Montizaan, K.N. Yang, C. Reker-Smit, A. Salvati, Comparison of the uptake mechanisms of zwitterionic and negatively charged liposomes by HeLa cells', Nanomedicine-Nanotechnology Biology and Medicine 30 (2020).
[77] E. Ducat, B. Evrard, O. Peulen, G. Piel, Cellular uptake of liposomes monitored by confocal microscopy and flow cytometry, Journal of Drug Delivery Science and Technology 21(6) (2011) 469-477.
[78] S.S. Lichtenberg, O.V. Tsyusko, S.R. Palli, J.M. Unrine, Uptake and Bioactivity of Chitosan/Double-Stranded RNA Polyplex Nanoparticles in Caenorhabditis elegans, Environmental Science & Technology 53(7) (2019) 3832-3840.
[79] D. Manzanares, V. Cena, Endocytosis: The Nanoparticle and Submicron Nanocompounds Gateway into the Cell, Pharmaceutics 12(4) (2020).
[80] S. Behzadi, V. Serpooshan, W. Tao, M.A. Hamaly, M.Y. Alkawareek, E.C. Dreaden, D. Brown, A.M. Alkilany, O.C. Farokhzad, M. Mahmoudi, Cellular uptake of nanoparticles: journey inside the cell, Chemical Society Reviews 46(14) (2017) 4218-4244.
[81] A. Taghizadehghalehjoughi, A. Hacimuftuoglu, M. Cetin, A.B. Ugur, B. Galateanu, Y. Mezhuev, U. Okkay, N. Taspinar, M. Taspinar, A. Uyanik, B. Gundogdu, M. Mohammadzadeh, K.A. Nalci, P. Stivaktakis, A. Tsatsakis, T.W. Jung, J.H. Jeong, A.M. Abd El-Aty, Effect of metformin/irinotecan-loaded poly-lactic-co-glycolic acid nanoparticles on glioblastoma: in vitro and in vivo studies, Nanomedicine 13(13) (2018) 1595-1606.
[82] J.J. Vredenburgh, A. Desjardins, D.A. Reardon, H.S. Friedman, Experience with irinotecan for the treatment of malignant glioma, Neuro-Oncology 11(1) (2009) 80-91.
[83] A.C. di Polidoro, G. Zambito, J. Haeck, L. Mezzanotte, M. Lamfers, P.A. Netti, E. Torino, Theranostic Design of Angiopep-2 Conjugated Hyaluronic Acid Nanoparticles (Thera-ANG-cHANPs) for Dual Targeting and Boosted Imaging of Glioma Cells, Cancers 13(3) (2021).
[84] A. Casado, M. Mora, M.L. Sagrista, S. Rello-Varona, P. Acedo, J.C. Stockert, M. Canete, A. Villanueva, Improved selectivity and cytotoxic effects of irinotecan via liposomal delivery: A comparative study on Hs68 and HeLa cells, European Journal of Pharmaceutical Sciences 109 (2017) 65-77.
[85] T.G. Burke, D. Bom, Campthotecin Design and Delivery Approaches for Elevating Anti-Topoisomerase I Activities in Vivo, Annals of the New York Academy of Sciences 922(1) (2000) 36-45.

II. CHAPTER II–ROLE OF MATERIALS IN STABILING AND DELIVERY BIOLOGICS

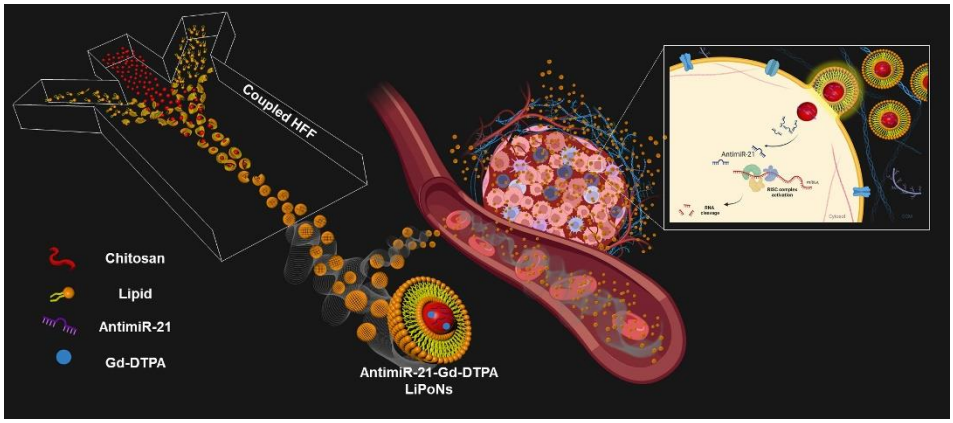

Graphical Abstract II. Lipid-Polymer Nanoparticles (LiPoNs) mediated Codelivery of AntimiR-21 and Gadolinium Chelate in Triple Negative Breast Cancer Theranostics.

Abstract

MicroRNAs have emerged as novel therapeutics regulating the expression of various genes involved in cellular functions. However, the low stability in blood circulation, limited transmembrane transport and degradation in endosomal/lysosomal vesicles of microRNAs limit their employment as therapeutics in cancer. Here, Lipid-Polymer Nanoparticles (LiPoNs) are proposed as theranostic vehicles for cancer treatment. The production of AntimiR-21-Gd-DTPA-LiPoNs is obtained in a one-step microfluidic process based on coupled Hydrodynamic Flow Focusing (cHFF), overcoming the drawbacks of simple mix and use, widely applied for microRNAs transfection. As a result, we obtained theranostic LiPoNs, co-loaded with gadolinium diethylenetriamine penta-acetic acid (Gd-DTPA) contrast agent, and validated the efficacy of microRNAs in acting on target genes in MDA-MB-231 cells by reporting a correlation between the induced miR-21 inhibition and a reduction of the cell migration ability.

II.1 BACKGROUND

II.1.1 miRNAs from master gene regulators to therapeutics in cancer

DNA is the genetic store of the cell, and it is transcribed into messenger RNA (mRNA). This mRNA is translated into a corresponding protein in the cytoplasm. The miRNAs are noncoding and non-messenger parts of RNA molecules [1]. These miRNAs are endogenous RNAs composed of short nucleotide sequences, 20-24 nucleotides, capable of binding mRNA without a perfect base pairing. They negatively regulate their targets through mRNA cleavage or translational regression[2]. A single miRNA can simultaneously regulate several genes, and several miRNAs can control a single miRNA target[3]. Therefore, they can act as master gene regulators manipulating several oncogenic pathways, such as cell cycle regulation (miR-15a/16 cluster, miR17/20 cluster, let-7 and miR-34), metabolism (miR-133, miR-33a/b, miR-29b), cell death (miRNA-221/222 cluster, miRNA-128) and metastasis (miR-200 family and miR-29 b) [1, 4]. In fact, their misexpression or dysfunction has been associated with tumour progression in two categories: oncogenic miRNAs and tumour suppressor miRNAs[5]. Oncogenic miRNAs are overexpressed in cancer and negatively regulate the tumor suppressor genes, consequently promoting cancer development. In contrast, tumour suppressor miRNAs are underexpressed in cancer and function by regulating oncogenes, consequently inhibiting cancer development[5]. According to the target miRNA expression, exogenous nucleic acids in forms of antisense oligonucleotides (AntimiR) and microRNAs (miRNAs) have been designed to inhibit and interfere with the mRNA[3]. In the former approach, miRNA antagonist-single strand oligonucleotides with RNA sequence complementary to mature miRNA, interrupt the miRNA processing and result in increased expression of the tumour suppressor genes. In the latter, the miRNA mimics in the form of replacement therapy have an identical sequence to exogenous mature miRNA restoring tumour suppressors miRNAs[3, 4]. For example, extensive studies reported the involvement of miR-21 in pathogenesis and all stages of carcinogenesis[6], especially in Triple Negative Breast Cancer (TNBC), where a reduction of the overall survival ratio of patients[7] has been associated with overexpression of miR-21. It was reported an increase in miR-21 expression due to TGFβ stimulation, which consequently leads to Epithelial-to-Mesenchymal Transition (EMT) process[7, 8]. In this context, antagonists–single-stranded oligonucleotides with miRNA complementary sequences (AntimiR-21) were exploited to interrupt the miRNAs processing and restabilise the expression of tumour suppressor genes. Through AKT and MAPK pathways, the miR-21 reversed the EMT phenotype and blocked angiogenesis in breast cancer[4]. Moreover, the same technology was exploited to target TNBC stem cells[9] and TNBC cells[10]. In both cases, the increased PTEN and PDCD4 suppressor gene expression inhibited tumour growth.

II.1.2 Stability challenges in miRNA delivery

Several concerns are related to the use of miRNA in therapy[11]. Firstly, they have low stability and integrity in blood circulation. They are rapidly cleared via renal excretion and degraded by the serum RNase A-type nucleases in the blood. Furthermore, poor blood perfusion, the high interstitial fluid pressure and the complex extracellular matrix of tumour tissue hindered their penetration[12]. Once reach the cancer cells, naked miRNAs are poorly taken up due to their negative charge and are prone to degradation in endosomal/lysosomal vesicles[3]. Moreover, their action in cells should be prolonged to ensure effective gene silencing through miRNAs. In addition, in some cancer cells, an insufficient or saturated miRNA processing enzyme (RISC complex) was observed making the therapeutic miRNAs ineffective [13, 14]. Due to their capability of targeting multiple pathways via imperfect matching, they may cause unwanted off-target and on-target effects [15]. Some undesired toxicity and immune system activation were reported upon the systemic miRNA delivery [16, 17]. They triggered the secretion of inflammatory cytokines and type I interferons (IFNs) through Toll-like receptors (TLRs). Through these TLRs, some miRNAs can induce neurotoxicity and neurodegeneration[4, 18, 19].

II.1.3 Strategies to improve the delivery of miRNA in cancer

Several strategies arise to solve the challenges linked to the systemic delivery of miRNAs, such as chemical modifications and viral and non-viral delivery. The chemical modifications performed on nucleic acids aim to increase their resistance to nuclease degradation. The modification of 2′-OH in the ribose ring, which is easily attacked by nuclease action, with an 2′-O-methyl (2′-OMe), 2′-O-methoxyethyl or 2′-fluoro oliglonucleotides has improved the stability, binding affinity and gene silencing of the microRNAs[20]. Promising results have also been reported for Locked nucleic acid (LNA) modifications. It consists in RNA analogues that introduce a 2′,4′ methylene bridge in the ribose to form a bicyclic nucleotide that strongly increases the affinity for complementary RNA[21, 22]. For mimics miRNA, modifications on the passenger stand such as nucleotide analogues, backbone modifications and terminal modifications (addition of inverted bases and biotin, alkyl groups) were performed[23, 24]. They enhance stability and reduce immunotoxicity of nucleic acids without acting on the guide strand[4].

Viral-based strategies employ lentiviruses, adenoviruses and adeno-associated viruses (AAVs) by substituting a part of viral genome with a therapeutic gene, in order to deliver vectors encoding the miRNAs[25-27]. Among them, the adenoviruses and AAVs, keeping their own genome in episomal form, are considered the safer strategies[28]. Recently, Pegtel et al.[29] have employed exosomes produced and released by virus-infected cells for encapsulating and delivering RNA therapeutics into the target cells. Even though viral vectors effectively deliver miRNAs in cells, their mutagenicity, immunogenicity, activation of oncogenic pathways and possibility of producing replicant component have limited their use in therapy[26, 27]. In addition, they are characterized by a challenging scale-up of manufacturing processes, which is an essential step for clinical translation[4].

With respect to viral-based strategies, non-viral approaches are characterized by a lower transfection efficacy and short duration of gene expression. However, the rational design of materials to guide miRNAs delivery has shown a relevant clinical impact.

As regards inorganic NPs, the iron oxide, silica and gold NPs are the widely employed. Shade et al.[30] developed streptavidin-coated magnetite (Fe3O4)-based NPs modified with biotin-bound miR-335/PEI complexes to knockdown the target gene in human mesenchymal stem cells (hMSCs)[3]. Moreover, the silica NPs, encapsulating miR-34a, conjugated with disialoganglioside GD2 antibodies have shown a delay of tumour growth, combined with an increase in the apoptosis and a reduction of vascularization of the tumour tissues [31]. Sukumar et al. reported the theranostic effects of polyfunctional gold-iron oxide nanoparticles (polyGIONs) surface loaded with miR-100 and antimiR-21 to treat the Glioblastoma in mice via intranasal administration[32]. Despite the possibility of using the inorganic NPs for theranostics purposes, major concerns in their use are related to their nanotoxicity, low loading capability, lack of cargo protection and inefficient endosomal escape.

As far as organic NPs for microRNAs delivery is concerned, they can be classified into two main classes the lipid-based and polymer-based NPs. Lipid-based NPs, thanks to their nature, easily interact with the cell membranes and promote the cellular uptake of their cargo[33]. Especially, cationic lipids having a head group with permanent positive charges, interact with both the negatively charged nucleic acids and cell membrane, improving the cellular delivery of nucleic acids [33-35]. However, some adverse effects have been associated to these positively charged lipids such as type I and type II interferon induction and liver toxicity[24, 36]. Furthermore, they can disrupt the cell membranes, induce vacuolization, reduce cell activity and interact with serum proteins, with the consequential elimination by the liver and spleen[4]. Even though neutral lipids have shown a lower loading ability and transfection efficacy than positive ones, they were used to replace the cationic ones to avoid these toxicity issues. Indeed, neutral lipid-based vehicles loaded with miR-34a effectively deliver miRNA in the tumour tissue and downregulate the target genes, without affecting the levels of cytokines and liver enzymes in the blood circulation[4, 37]. To reduce their positive charge, another strategy employed was the combination of neutral lipids, such as cholesterol (Chol), dioleoylphosphatidyl ethanolamine (DOPE) and phosphatidylcholine (PC), with the cation ones [3, 38]. Following the success of ionizable lipids for mRNA delivery, these lipids, capable of change their charge according to the buffer pH, have been used for microRNA delivery. They are protonated at low pH displaying a positive charge, while they are neutral charged at neutral pH. Therefore, they have shown high biocompatibility in vivo, reducing the interactions with anionic membrane of blood cells, and enhanced intracellular delivery, promoting the endosomal escape for the membrane destabilization at acid pH[33]. Gokita et al.[39] developed lipid nanoparticle (LNP), made up of ionizable lipids, to deliver miR-634 in cancer, that downregulate the target protein and reduce the tumour growth.

Synthetic polymer-based NPs, mainly in the form of polyplexes and polylactic-co-glycolic acid (PLGA) NPs, have been widely studied for miRNAs delivery due to their efficient cargo release in cytoplasm, undemanding functionalization with targeting moieties and easy manufacturing[3].
Poly(ethylene imine)s (PEIs) in a positively charged polymer allows strong electrostatic interactions with nucleic acids. It reduces the nuclease activity and protects miRNAs from endosome degradation due to its proton acceptor behaviour. In the endosomes, the acceptor nature of the PEI causes an influx of protons and water, that lead to the lysosomal lysis and sequential miRNAs release in the cytoplasm[3, 40]. In spite of their successful delivery of nucleic acids in different cancer models[41], the high positive charge and the low degradability strongly limit employment of PEI without any surface modification or blending with Polyethylene glycol (PEG) or Polyurethane (PU). For the delivery of miR-145, Zhang et al.[42] used branched PEI-PEG to treat prostate cancer, while Chiou et al.[43] developed PU short branch PEI nanocomplexes to inhibit stem cell niches in brain tumour. Both reported a successful transfection, knockdown and reduction of tumour growth.
The high colloidal stability, quick cellular uptake, low toxicity and controlled cargo release have made the Polycaprolactone (PCL) a promising polymer for nucleic acid delivery. Lin et al[44] achieved about 85% transfection efficiency in vitro with PEG-peptide-PCL[3].

Alternatively, the PLGA based NPs offer safety, biocompatibility, biodegradability and stable mechanical properties[45]. Devulapally et al.[10] loaded antisense-miR-21 and antisense-miR-10b in PLGA-b-PEG polymer NPs and evaluated the synchronous blocking of endogenous miR-21 and miR-10b function in TNBC cells in culture, and tumour xenografts in living animals. The NPs represented an efficient strategy for targeting metastasis and antiapoptosis in the treatment of metastatic cancer, showing substantial reduction in tumour growth at very low dose of microRNAs. To increase the microRNAs loading within the PLGA-NPs, the addition of polycationic polymer to the formulation is typically performed[46, 47].

Regarding natural polymers, chitosan represents an ideal material for the loading nucleic acids due to its protonated amino groups that rapidly interacts with opposite-charged molecules at acid pH. Gaur et al.[48] developed miR-34a loaded chitosan nanoparticle for metastatic prostate cancer, reporting a reduction of tumour growth in the bone, preserving its integrity. However, the strong interaction of chitosan with the nucleic acids may limit their intracellular release due to lack of unpacking of the complex in the cytoplasm[49]. For this reason, several materials, including lipid chains, bile acids or negatively charged polymers, have been integrated to chitosan to improve its release properties[50-52]. The chitosan polymer has shown enhanced retention of nucleic acids in PLGA NPs[47]. Sun et al[9] developed vesicular structures made from the self-assembly of amphiphilic grafted chitosan derivatives named chitosomes, to increase cellular transfection and stability against degradation by nuclease in serum. In the context of integration of materials to improve the delivering efficacy of nucleic acids, hyaluronic acid polymer has been widely used. It was added to cation polymer and lipids to mask their positive charge, reducing the

uptake by the MPS and increasing the NPs' circulation time[3, 4]. Deng et al.[53] co-loaded miR-34a and doxorubicin into hyaluronic acid (HA)-chitosan (CS) nanoparticles (NPs) for improving the effect of the drug on the breast cancer cells.
In this context, hybrid NPs, where the microRNA are complexed with a polymer and covered by a lipid bilayer, represent a promising strategy. Huang el al. presented miR-loaded transferrin-conjugated nanoparticles, where the miR-29b was loaded in the PEI polymer core, coated with DOPE/linoleic acid/DMG-PEG, for acute myeloid leukemia (AML) cells. They reported the downregulation of target gene and antileukemic activity[54].

II.1.4 From conventional methods to microfluidics for nucleic acids loaded NPs

The material and the nanoparticles' characteristics dictate the selection of the most appropriate preparation method[3]. Before the advent of microfluidics, the polymer NPs were mostly prepared via nanoprecipitation and emulsion techniques, while liposomes were through the thin film hydration technique.
The nanoprecipitation consists of the addition of polymer solution in nonsolvent phase, and as soon as the polymer-containing solvent has diffused into the dispersing medium (rapid desolvation of the polymer), the polymer precipitates forming nanoparticles[55].
In the single emulsion technique, for instance, oil-in-water emulsion, a polymer solution dissolved in an oil-phased is added into an external water phase containing surfactants. The mixture is processed using a high-speed homogenization or ultrasonication. The double-emulsion technique, typically used to encapsulate hydrophilic payloads, employs two emulsification steps to obtain water-in-oil-in-water (w/o/w) or oil-in water- in-oil (o/w/o) emulsions[3, 10, 56]. Historically, liposomes were mainly produced through a thin film hydration technique, that involved the addition of a dispersion medium to a thin film of lipid, that was pre-formed by the organic solvent removal. Spontaneously, multilamellar vesicles were formed. These heterogenous liposomes were sonicated or extruded to obtain the vesicles of desired size[57].
Even though some of these methods are still used for microRNA-loaded NPs, such as nanoprecipitation[47] and emulsion techniques[10], they are not recommended. Indeed, they are characterized by a low encapsulation efficacy and difficulty in scaling up the processes. In addition, the extrusion step requires large volumes of expensive material, like miRNAs, even at lab scale. Moreover, the sonication and the emulsion technique require post processing steps to remove lipids aggregate or free nucleic acids, such as centrifugation and filtration through a Sepharose gel column, which increase the change of degradation of miRNAs and sample contamination[58, 59].
With the advent of cation lipids, the stable nucleic acid lipid particle (SNALP) method was presented for producing the lipid-based NPs entrapping nucleic acids [60]. The stable nucleic acid lipid particle (SNALP) method, also known as ethanol dilution technique, was a prototype of a microfluidic device[61, 62]. The mixing of lipids stream dissolved in ethanol with a nucleic acid dissolved in buffer was performed in T-shaped mixer. Due to ethanol's rapid dilution, lipids assembly entrapped the nucleic acids. However, these lipid-based NPs do not have an aqueous core like liposomes, and they are a complexation of nucleic acids

and lipids[60]. This technique was used for the development of the first commercialized siRNA loaded LNPs, Onpattro[63]. Even though the T-Mixer devices were the first employed for the production of LNPs containing nucleic acids, they consume large volume of materials and have poor control over NPs features. Then, microfluidics was employed to overcome the several drawbacks of conventional production methods. For the development phase, the microfluidic devices consume small amount of raw materials and preserve the activity of nucleic acids. Moreover, device parallelisation allows achieving mass production without compromising the nanocarriers physiochemical properties. Thus, it fulfills the FDA requirements for drug approvals by offering precise control over particle size. Indeed, by controlling chip design, materials and solvents composition and liquid flow rate, a narrower particle size distribution could be achieved[64, 65].

The microfluidics for nucleic acids loaded lipid NPs mainly consists of fluxing two separate solutions, one containing the lipid mixture dissolved in organic solvent and the other nucleic acids dissolved in water, in a separate microchannels. At the intersection of these microchannels, due to the components' rapid mixing, the organic phase's polarity increases, which promotes the assembly of lipid-based NPs entrapping nucleic acids[66]. According to the flow patterns, the microfluidic device can be divided into single-phase continuous flow and multiphase segmented flow devices[67]. The single-phase continuous flow devices include the T-shaped and Hydrodynamic flow focusing devices (HFF). In HFF devices, the species are mixed via diffusion in laminar flow streams due to their low Reynolds number (<10). Krzysztoń et al. produced small (∼38 nm) monomolecular nucleic acid/lipid particles (mNALPs) in HFF device increasing the encapsulation efficacy, particle distribution and stability respect to bulk mixing. Taking advantage of the Hydrodynamic Flow Focusing geometry, NPs with size from 30-250 nm and with a high encapsulation efficacy are produced, however they are characterized by a high polydispersity[56, 68]. The same technology was exploited in the form of 3D HFF devices, in order to solve the problem of polydispersity and increase the throughput[69]. Nevertheless, large quantities of materials and post- processing steps are required to obtain the proper concentration for in vivo experiments[66].

To improve the mixing of species, the chaotic mixing was introduced to induce stretching or folding in the flow pathway, so reaching intermediate Reynold number (2-500). This class of devices includes Chaotic Mixers, Bifurcating mixer and Baffler mixer[70, 71]. Among Chaotic Mixer, the Staggered Herringbone micromixers (SHMs) stand out due to their ability to use low amount of materials and producing small NPs with low polydispersity and high encapsulation efficacy [72]. Chen et al.[73] for the first time employed the SHM device for the development of siRNA containing LNPs, producing small and homogenous NPs, saving reagents and allowing a more efficient screening of lipid structures. In the same year, Belliveau produced siRNA loaded LNPs with the size down to 20 nm and an encapsulation efficacy up to 95 %, reporting equal or superior efficacy of current gold standards cationic LNPs[66, 74].

However, in multiphase segmented flow devices with the high recirculation lead to the formation of small-sized droplets (segments) and channel clogging, that affect the process conditions and consequently increase the heterogeneity of NPs[67]. Morever, some

solvent incompatibilities may arise due to the materials that made up mixers, poly(dimethylsiloxane) or cyclic olefin copolymer[59].

II.1.4 Aim of chapter 2

microRNAs have gained ground as novel therapeutics capable of acting in the form of replacement or inhibition to restore the altered cellular pathways. However, microRNAs' low stability in blood circulation, limited transmembrane transport and degradation in endosomal/lysosomal vesicles limit their employment as therapeutics. Significant efforts have been made to stabilize the microRNAs using several strategies such as chemical modifications, viral-based and non-viral strategies. Nevertheless, the major obstacle in nucleic acid delivery is still to present a stable cargo in the cell cytoplasm. The role of material complexation on the performance of nucleic acids at nano-bio interactions has not been fully elucidated. This chapter aims to gain an understanding of how the design of materials impacts nucleic acids' stability and delivery at cellular and intracellular levels. To ascertain this influence, we rationally designed a hybrid nanostructure that integrated the properties of two materials, lipid and polymer. In these hybrid NPs, we entrapped an antisense oligonucleotide, AntimiR-21, to block the miR-21 processing. Indeed, the miR-21 is highly dysregulated in several cancers and acts as oncogenic microRNAs downregulating the tumour suppressor gene. A key role in material design was exerted by the microfluidics, which guided components interaction and preserved the activity of microRNAs. We validated the efficacy of lipid-polymer NPs in mediating the delivery of intact microRNAs to MDA-MB-231 human breast cancer cell line by evaluating the regulation of the target genes with respect to a common transfecting agent, Lipofectamine, and microRNA alone.

II.2 CASE STUDY

II.2.1 Experimental section

II.2.1.1 Materials

Materials used for the production of LiPoNs and Gd-DTPA LiPoNs were the same presented in Chapter 1. Sodium hydroxide (NaOH; pellets, ACS reagent, 97.0%, Mw = 40.00 g/mol) has been purchased from Sigma-Aldrich (St. Louis, MO, USA). Antisense miR-21 (AntimiR-21, sequence 5'-UCAACAUCAGUCUGAUAAGCUA-3', purification DESALT) was purchased by Merck (St. Louis, MO, USA). The human epithelial breast cancer cell line, MDA-MB-231, was obtained by Leibniz-Institute DSMZ-Deutsche Sammlung von Mikroorganismen und Zellkulturen GmbH (Braunschweig, Germany) and was cultured with Dulbecco Modified Eagle medium high glucose (DMEM, Sigma-Aldrich., St. Louis, MO, USA) supplemented with 4.5 g/ml of glucose, 10-20 % v/v fetal bovine serum (FBS, Sigma Aldrich, St. Louis, MO, USA), 2 mM L-glutamine and 1 % v/v Antibiotic Solution liquid (Thermo Fisher Scientific, Waltham, USA). The cells were incubated at 37° C with 5 % CO2 and harvested using Trypsin-EDTA. Dimethyl sulfoxide (DMSO) for molecular biology was purchased from Sigma-Aldrich Co. (St. Louis, MO, USA). Thiazolyl Blue Tetrazolium Bromide soybean 98 %

(MTT) and Lipofectamine 3000 (Lipo, Cat. Number L3000008) were purchased from Thermo Fisher Scientific, USA.

II.2.1.2 AntimiR-21 behaviour in CH-AcOH -Water ternary system

The stability of AntimiR-21 over time in different environmental conditions was evaluated experimentally. Firstly, a water solution of AntimiR-21 (26 µg/mL) was used as control and compared with a buffer solution containing AntimiR-21 (26 µg/mL) at room temperature and at 4 °C. The same experiment was performed at different pH (2.6-4.3). The buffer pH values ≃ 2.6 and 4.3 were obtained by adding 0.5 % v/v of acetic acid (AcOH) in a water solution, with and without 25 mM of NaOH, respectively. Different aliquots of AntimiR-21, one for each condition tested, were prepared and the degradation of microRNA in time (from 1 to 4 h) was detected by Multiskan SkyHigh Microplate Spectrophotometer (Thermo Fisher, Scientific, Massachusetts, USA). µDrop Plate was used to quantify the RNA concentration (λabs= 260 nm) in different solutions. Then, the same experiments on AntimiR-21 stability were performed by putting in contact the microRNA with the solutions to be injected the middle channel into the microfluidic device. Indeed, 54 µg/mL of AntimiR-21 was dispersed in a solution of chitosan dissolved in acetic acid (CH, 0.01 % w/v, AcOH 1 % v/v) with and without the addition of Gd-DTPA (0.4 % w/v). For both of them, the pH was adjusted to around 4 with the addition of 50 mM of NaOH. The RNA stability was expressed as a percentage of RNA concentration detected upon the treatment over the RNA concentration of un-treated and initial AntimiR-21 solution used as control.

II.2.1.3 Formulations of AntimiR-21 loaded LiPoNs

The microfluidic set-up presented in chapter I.2.1.2 was used to produce Lipid-Polymer nanoparticles (LiPoNs), LiPoNs encapsulating AntimiR-21 (AntimiR-21- LipoNs) without and with Gd-DTPA (AntimiR-21- Gd-DTPA- LiPoNs). The first step consisted of preparing ethanol-water solution (65% v/v- 35 % v/v) containing 0.0072 % w/v of lipids (mass ratio 8:1- SPC/Chol), kept under continuous stirring overnight and then injecting through the side channels. The water phase was made of an aqueous solution of 0.01% w/v of CH and 1% v/v of AcOH and kept under continuous stirring for at least 1 h. Then NaOH was added to the solution at final concentration of 50 mM to regulate the pH value ≃4.1. To prepare AntimiR-21 loaded LiPoNs, AntimiR-21 was added to the polymer solution at final concentration of 11 µM and the solution was kept under stirring for ten minutes before injecting a solution in the middle channel. The GD-DTPA (0.4 % w/v) was added to the over-mentioned solution for AntimiR-21- Gd-DTPA- LiPoNs. The microfluidic process was performed at a Flow Rate Ratio FR2 of 0.073, defined as the volume flow rate ratio of the middle channel (3µL/min) and Volume Flow Rate of the side channel (41µL/min) for 80 min. LiPoNs were collected in a vial glass containing 7 mL of pure water. The suspension was stirred for 40 min at 25 °C. The purification was described as reported in chapter I.2.1.4.

II.2.1.4 Synthetic Identity of AntimiR-21- Gd-DTPA- LiPoNs

The hydrodynamic diameters and particle concentration were measured with a NanoSight NS300 (NTA version 3.4, Malvern Instruments Ltd, Camera sCMOS, Laser Blue488) at room temperature, with a dilution factor from 10 to 20. Zeta potential measurements in the monomodal analysis were performed at 25 °C by a Zetasizer Nano ZS (Malvern Panalytical,UK), loading Folded Capillary Zeta Cell (Malvern Panalytical,UK) with 1 mL of NPs suspension. A Field Emission Scanning Electron Microscope (FE-SEM, Ultraplus Field Emission, Carl Zeiss, Oberkochen, Germany), Transmission Electron Microscope (TEM, FEI,Hillsboro, OR, USA) were used to characterize the nanosystem morphologically as in chapter I.2.1.5.2. For further analysis, the grids already observed by TEM were detected with FE-SEM, and nanoparticles were coated with 5 nm Au before the observation. To quantify the EE % of Gd-DTPA, the NPs were compared with Gd-DTPA calibration curves dispersed in water ranging from 0 to 100 µM as reported in chapter I.2.1.5.4. Multiskan SkyHigh Microplate Spectrophotometer was used to quantify the encapsulation efficacy (EE %) of AntimiR-21 loaded LipoNs. The absorbance of bare LipoNs was used as a value for the quantification.

II.2.1.5 RNA extraction and q-RT-PCR

Purification of total RNA from MDA-MB-231 cells was obtained using TRIzol reagent (Thermo Fisher Scientific, Cat. Number 15596026) after 72 h of transfection. Measurements of RNA extracted were obtained using a Qubit 4 Fluorometer (Thermo Fisher Scientific).

For miR-21 detection, starting from 100 ng of total RNA, cDNA synthesis was obtained by miRCURY LNA RT Kit (Cat. Number: ID: 339340). Next, SYBR® Green-based detection (Cat. Number: 339371) was performed using miRCURY LNA miRNA Probe Assay specific for miR-21 (Cat. Number 339350/ GeneGlobe Id - ZP00000445). Normalization of miR-21 real-time PCR data was done using the Ct of the endogenous small nuclear RNA molecule (U6 snRNA/GeneGlobe Id - ZP00030496). All these reagents were purchased from Qiagen (Hilden, Germany).

For miR-21 target detections (PTEN and PDCD4), 1 µg of total RNA was reverted using SuperScriptTM III First–Strand Synthesis SuperMix kit (Cat. Number: 18080400; Thermo Fisher Scientific) according to the manufacturer's instructions, while q-RT-PCR was performed using iQ SYBR Green Supermix (Cat. Number: 1708882) purchased from Bio–Rad (Hercules, California, USA). Thermal cycling protocol on the C1000 Touch Thermal Cycler (Bio–Rad) instrument was inserted according to the protocol instruction. The data were analyzed using Bio-Rad CFX Maestro version 1.0 (Bio–Rad). The gene expression levels were calculated using the formula 2−(sample 1 ΔCt − control ΔCt) where the Ct values of each gene were normalized to the housekeeping mRNA β-ACTIN. Three independent experiments were performed in triplicate.

Oligonucleotides used for RT–qPCR were:

PTEN: fw 5' -ggggaagtaaggaccagagac-3'; rev 5' -tccagatgattctttaacaggtagc- 3';

PDCD4: fw 5'- tggaaagcgtaaagatagtgtgtg- 3'; rev 5' -ttctttcagcagcatatcaatctc- 3';

ACTIN: fw 5'- ccaaccgcgagaagatga-3'; rev 5' - ccagaggcgtacagggatag- 3.

II.2.1.6 Wound closure

To analyze the migration ability of breast cancer cells silenced for miR-21 expression, wound healing was performed. Briefly, 1x105 MBA-MB-231 cells were seeded in a 12-well plate and, the day after, cells were treated with AntimiR-21- LiPoNs, LiPoNs or transfected using AntimiR-21 in combination with Lipofectamine 3000. 48 hours post-transfection, a scraped was introduced on the monolayer of cells with a tip, and cell migration was tracked and photographed (at 100 X magnification) using the automated time-lapse video microscopy (Celldiscoverer 7, Zeiss, Munich, Germany) enclosed in the incubator. In detail, three independent fields of each well were acquired every two hours and the Region Area expressed in pixel2 was obtained using the software ZEN 3.0 version (Zeiss). The migration ability was expressed as a percentage of wound closure.

II.2.1.7 Cell viability

For the cytotoxicity measurements, 1 X 10^4 MDA-MB-231 cells/well (passage $\simeq$ 20-40) were plated in 96-well plates for 24 h before adding the formulations. Fresh medium, containing AntimiR-21 alone and using Lipofectamine 3000, AntimiR-21- LipoNs or AntimiR-21- Gd-DTPA- LiPoNs (AntimiR-21conc. 33 nM, Lipids conc. 12 µg/ml and Gd-DTPA conc.:28 µM) was added to each well and the cells were incubated for 24 h and 48 h. Moreover, the LiPoNs and Gd-DTPA- LiPoNs were added in equal concentrations. At the end of the incubation time, the MTT assay was performed as reported in chapter I.2.1.6.

II.2.1.8 Statistical analysis

Results were analyzed by performing the Student's Unpaired t-test (two-tailed) using GraphPad Prism 9 software (La Jolla, CA, USA) and are shown as the mean ± standard error of the mean (SEM). Differences were considered significant when $p < 0.05$.

II.2.2 Results and discussion

II.2.2.1 Lipid-Polymer Nanoparticles for nucleic acids delivery

Here the rationale for materials selection to improve the delivery of microRNAs is reported. Cationic polymers have shown high transfection efficacy on different cancer cells. However, their application was strongly limited by their undesired toxicity and low degradation ability[3, 4]. Among natural polymers, chitosan stands out for its low immunogenicity, excellent biocompatibility, and high positive charge[49]. At acid pH, the amine groups of the chitosan are protonated and become cationic, making easy the complexation with genetic material[49]. The negatively charged nucleic acids establish strong electrostatic interactions with chitosan, producing a stable complex against nuclease degradation[75]. Different uptake mechanics characterized the chitosan NPs, but the most interesting feature of these carriers is their intracellular behaviour. Indeed in the acidified endosomes, where the NPs are mainly located upon internalization, the amine groups of the chitosan become protonated, leading to an influx of water and chloride ions to neutralize these charges[76]. All mentioned leads to an extensive osmotic swelling and, consequently a rapture of endosomes that release the cargo[40]. Thus, the role of chitosan

is to protect the nucleic acids from both extracellular and intracellular degradation. However, its positive charge causes several problems for NPs in the biological environment since the high interaction with blood proteins, albumin, glycosaminoglycans alters the blood circulation of the NPs[49]. Moreover, the proteins can compete with nucleic acids and promote their premature release[77, 78]. Following these considerations on the chitosan as a delivery vehicle, we decided to cover it with a lipid bilayer, made up of phosphatidylcholine and cholesterol, which provide a slightly negative charge to the NPs, and increase the NPs stability in a biological environment. Indeed, these lipids increase particle stability, delivery efficacy, tolerability and biodistribution[3, 38]. Moreover, due to its biomimetic nature, this lipidic bilayer enhances the cellular penetration of the chitosan complex. Another way of internalizing of the hybrid vector could be the release of the chitosan complex directly in the cytoplasm due to the lipid-based NPs' capability of merging with the cell membrane. Therefore, the lipid-polymer NPS (LiPoNs) were designed to form stable complexes with microRNAs, protect them from nuclease degradation, and promote cellular delivery and release in the cytoplasm.

II.2.2.2 Optimization of coupled Hydrodynamic Flow Focusing (cHFF) to produce AntimiR-21 Gd-DTPA Lipid-Polymer NPs

Starting from the results obtained in chapter I on the cHFF[79], with the aim of not compromising the activity of microRNAs, we adjusted the microfluidic process conditions to load them in the Hybrid Lipid-Polymer Nanoparticles (LiPoNs). We performed a preliminary bulk study to assess the chemical stability of microRNAs in the form of degradation. In particular, we evaluated in bulk the effect of the exogenous parameters [80], such as changes in temperature, pH, and polymer components, on AntimiR-21. These parameters were set according to the conditions performed in the microfluidic process.

Since our microfluidic process is conducted at room temperature, we first analysed temperature's impact on AntimiR-21. In detail, we studied the stability in a buffer of AntimiR-21 at 4 °C and room temperature [81]. No effects on AntimiR-21 stability were detected, even though after 4 h a slight decrease of about 11% and 19% for 25 °C and 4°C, was observed, respectively (Figure II-1a). This evidence was relevant to optimize the cHFF for the microRNA loading. Indeed, a change in process parameters, such as the temperature, could affect the solvent extraction during the cHFF and the relatively constant membrane elasticity modulus of the lipid bilayer self-assembly, both needed for LiPoNs formation[82]. Therefore, considering the short processing time of the experiments for the LiPoNs production, we selected 25°C as the constant temperature for AntimiR-21 LiPoNs production, reducing any dependence of these parameters on the output LiPoNs carrier and miRNA chemical stability.

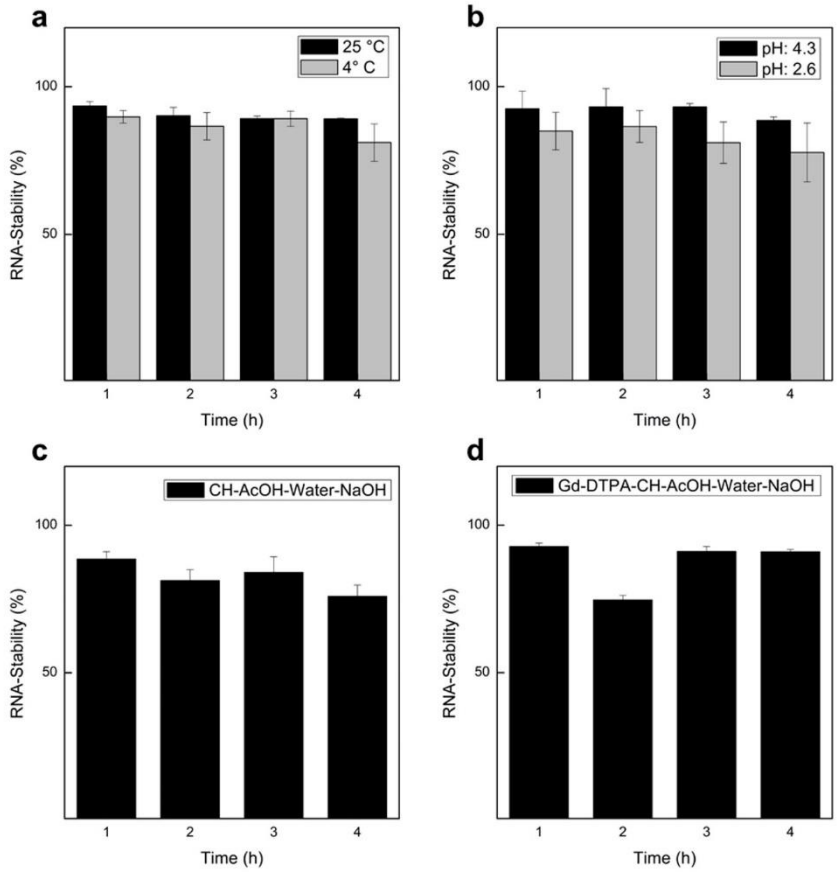

Figure II-1. Evaluation of AntimiR-21 stability up to 4 h: **a**) at room temperature (25°C) and 4°C and **b**) at pH of 4.3 and 2.6 by keeping constant the temperature at 25 °C. AntimiR-21 stability in the mixture CH-AcOH-Water at microfluidic process conditions: pH ~4 and at room temperature without **c**) and with the addition of Gd-DTPA **d**) up to 4 hr.

Successively, the impact of different pH conditions at room temperature was assessed. Indeed, for the loading of AntimiR-21 in LiPoNs, the active agent was dissolved in a chitosan solution, where acetic acid was added to solubilize the polymer.
For this reason, AntimiR-21 degradation for two different pH, 4.3 and 2.6, obtained for a water solution with 0.5 % of AcOH adjusted and not with 25 mM NaOH, respectively, was investigated at room temperature. Results showed a reduction of 12 % and 23 % of the signal of AntimiR-21 upon 4 h of contact with pH of 4.3 and 2.6, respectively (Figure II-1b). This instability was expected since naked miRNAs are made up of RNA molecules that are highly susceptible to degradation by hydrolysis at alkaline and extreme acid pH conditions [83, 84]. Furthermore, the selection of a mildly acid pH for the production process correlates with the consolidated manufacturing protocols for the siRNA-lipid nanoparticles reported by Wash [85].

Finally, the effect of the chitosan polymer dissolved in an acid solution on AntimiR-21 was evaluated. To the best of our knowledge, in literature, no data regarding the interaction and handling of AntimiR-21 in the quaternary system Chitosan-Acetic Acid-Water /Ch-AcOH-Water) overtime was reported. We studied the effect that a complex system (Ch-AcOH-Water) at pH around 4 has in time (from 1 to 4 h) on AntimiR-21 chemical stability. Results show no reduction of the AntimiR-21 signal in the first hour, but it decreases by 20 % in 4 h (Figure II-1c). The same preliminary study was performed by adding of Gd-DTPA to the over-mentioned system (Figure II-1d).

Following the studies reported on AntimiR-21 chemical stability in terms of degradation, all the experiments for the obtaining of the AntimiR-21- LiPoNs were conducted by dissolving for 10 min the AntimiR-21 in the polymer solution at pH ~4 prior to being injected in the microfluidic device, where the cHFF process was carried on at room temperature.

In the cHFF, a chitosan (0.01 % w/v) in acid solution (AcOH-NaOH/1% v/v-50 mM) containing microRNAs is injected in the middle channel, and it is sheeted by two side solution of lipids (0.0072 % w/v, 8:1 mass ratio SPC:Chol) dissolved in a mixture of etOH-Water (65%-35% v/v) (Figure II-2). For the production of theranostics microRNAs-Gd-DTPA LiPoNs, the Gd-DTPA (0.4 % w/v) is added to the central solution. The cHFF process is conducted at FR^2 of 0.073, by setting the side flow rate at 41 µL/min and the middle at 3 µL/min.

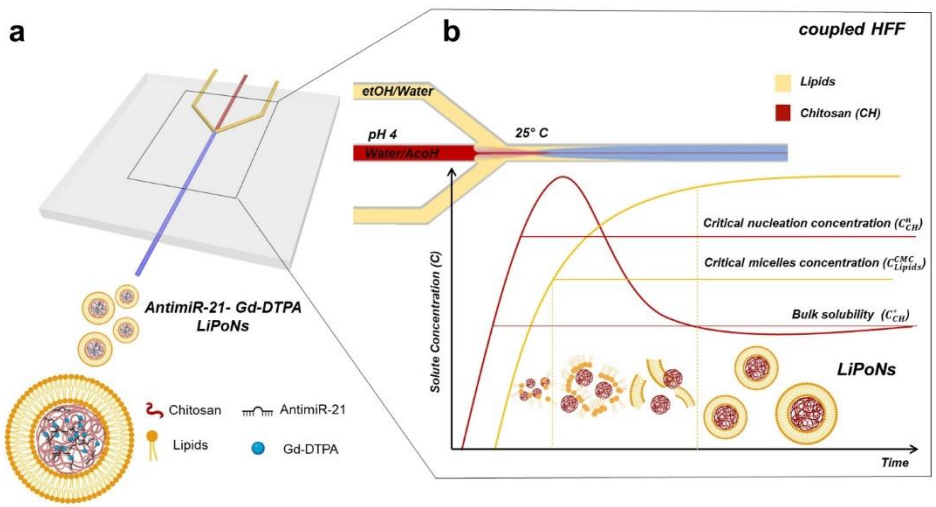

Figure II-2. Coupled Hydrodynamic Flow Focusing (cHFF) to produce AntimiR-21- Gd-DTPA-Lipid-polymer Nanoparticles (LiPoNs). **a**) Schematic representation of cHFF strategy and the LiPoNs structure. **b**) Schematic illustration of nanoprecipitation and self-assembly processes implemented in microfluidics for LiPoNs production. Some graphic elements of nanostructures in Figure II- 2, were created with BioRender.com, accessed on December 9th, 2022.

The nanoparticles were analyzed in terms of the mean and mode of NPs size, Standard Deviation (St.Dev) value and Zeta potential obtained by NanoSight NTA and Zetasizer Nano (Figure II-3, Table II-1).

Table II-1.
Table summary of nanoparticles mean size, mode, standard deviation (SD), zeta potential and concentration of different LiPoNs formulations.

	Mean size ± St. Error (nm)	**Mode ±St.Error (nm)**	**SD ± St. Error (nm)**	**Zeta Potential ± St. Error (mV)**	**Concentration (particles/mL)**
LiPoNs	155.8±0.8	140.8±4.9	84.8±1.5	-13.3± 1.0	$1.17*e^{10}$
Gd-DTPA- LiPoNs	149.9±2.6	107.6±6.1	81.0±3.7	-9.2± 1.1	$5.92*e^{9}$
AntimiR-21- LiPoNs	134.7±2.1	87.9±2.8	68.7±1.3	-8.7±0.5	$7.91*e^{9}$
AntimiR-21- Gd-DTPA-LiPoNs	124.7±3.2	88.5±3.7	62.4±6.1	-13.3±0.5	$5.09*e^{9}$

The direct and real-time visualization of AntimiR-21- LiPoNs by NTA (Figure II-3) showed a monodisperse population of NPs, confirming the high-resolution particle distribution (Figure II-3a) showing a peak at 134.7±2.1 nm with 90% of the particles being 200.6±6 nm. The mean size value of AntimiR-21- LipoNs (7.91*e9 particles/mL) correlated with the scanning and transmission electron images reported in Figure II-3b-c. A recognizable dark core within a lipid bilayer vesicle is shown in TEM image Figure II-3b. The clear resolution of the lipid bilayer can be associated with the enhanced electron contrast due to the ntimiR-21 located in the chitosan core of LiPoNs (EE~50 %).

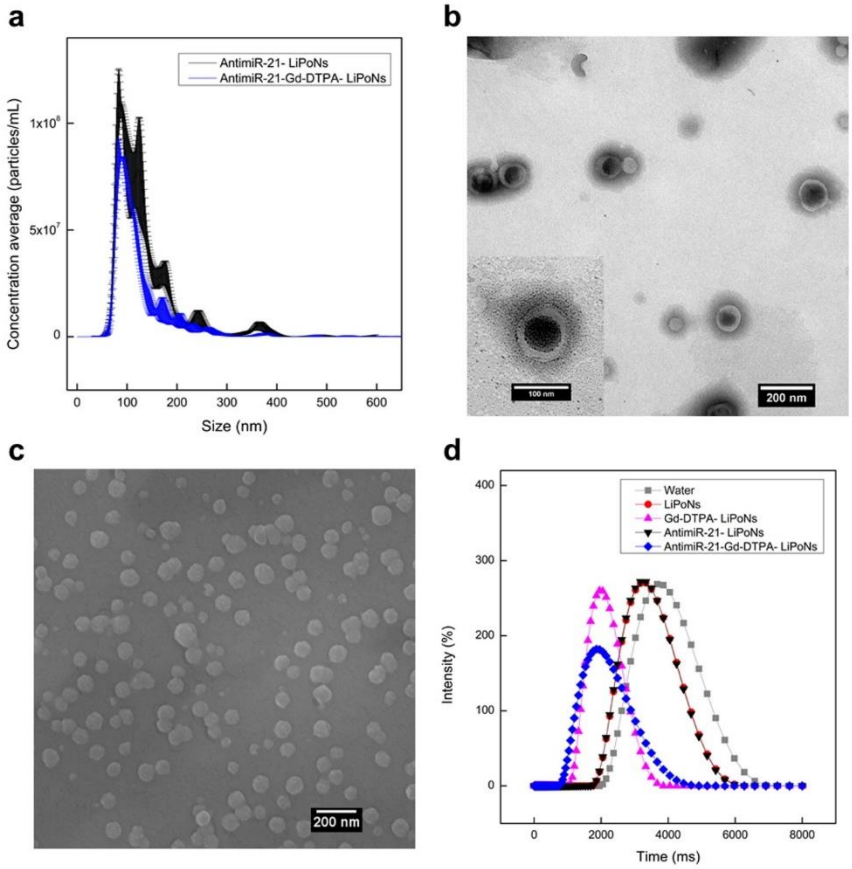

Figure II-3. LiPoNs morphological characterization and in vitro MRI. **a**) Size distribution of AntimiR-21- LiPoNs (black) and AntimiR-21- Gd-DTPA- LiPoNs (Blue) as a function of the mean nanoparticle concentration from the three measurements. **b**) TEM and **c**) SEM of AntimiR-21- LiPoNs. **d**) In vitro MRI comparison of longitudinal relaxation time distributions of water, LiPoNs, Gd-DTPA- LiPoNs, AntimiR-21-LiPoNs and AntimiR-21- Gd-DTPA- LiPoNs.

The longitudinal relaxation time distribution of AntimiR-21- Gd-DTPA- LiPoNs (T1=1830 ms) in Figure II-3d confirmed the loading of Gd-DTPA Contrast Agent (EE-62 %) within the LiPoNs nanostructures, that did not affect nanoparticles size of LiPoNs, as shown in Figure II- 3a and Table 1. Furthermore, the zeta potential data showed a slight increase of the negative charge from -8.7 to -13.3 mV for AntimiR-21 and AntimiR-21- Gd-DTPA- LiPoNs, respectively.

II.2.2.3 miR-21 silencing by AntimiR-21 loaded LiPoNs

As reported by The Cancer Genome Atlas (TCGA) Breast cancer (BRCA) database, the miR-21 high expression is correlated to a reduction of the overall survival ratio of patients under study [86, 87], and extensive studies show its involvement in tumour pathogenesis. MDA-MB-231, a human epithelial triple negative breast cancer cell line, expressed significant miR-21 levels with respect to other breast cancer cell lines (MCF-7 and SKBR3 cells) [87]. Therefore, the inhibition of miR-21, achieved with antisense miRNA, consisting of a single-stranded oligonucleotide with a complementary sequence to mature miRNA [10], could inhibit its role in carcinogenesis. To test the effects of AntimiR-21- LiPoNs in MDA-MB-231 cells, we analyzed the resulting expression of miR-21, its targets and, the underlying biological effects. The MDA-MB-231 cells were treated with AntimiR-21- LiPoNs, free AntimiR-21 and LiPoNs, for 72 h; the total RNA was extracted from the cells, and the miR-21 expression level was quantified by q-RT-PCR. The cells treated with LiPoNs were used as control (equal to 1). A reduction of miR-21 expression from 1 to 0.08 is reported for the cells treated with 33 nM of AntimiR-21- LiPoNs (Figure II-4a). This reduction in miR-21 expression using NPs formulation follows the previously reported cellular uptake of NPs encapsulated miRNAs due to the shielding of miRNA charge groups [3, 10]. In parallel, to compare commercially available transfection agents, the Lipofectamine 3000 (Lipo), and the newly designed hybrid vector, LiPoNs, the same experiment was performed at 72 h. Upon 72 h of treatment with AntimiR-21 Lipofectamine-mediate transfection (Lipo + AntimiR-21), the cells showed a miR-21 downregulation from 1 to 0.26 (Figure II- 4b).
This enhanced capability of AntimiR-21 to bind the miR-21 effectively and induce its silencing provides evidence of the stable and safe delivery to the cells by LiPoNs. Indeed, the chitosan-miRNA complex enveloped in a lipid shell provides higher protection for microRNA molecules to RNA nuclease in a medium containing 10 % of serum.

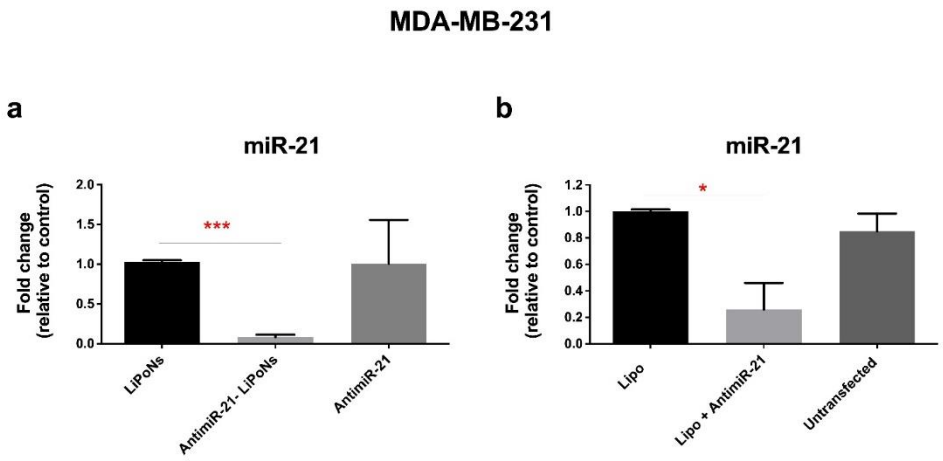

Figure II-4. The efficiency of miR-21 silencing by AntimiR-21- LiPoNs in MDA-MB-231 cells. **a**) MDA-MB-231 cells were treated with, LiPoNs (used as control), AntimiR-21- LiPoNs and

AntimiR-21. **b**) MDA-MB-231 cells were transfected with the only Lipofectamine 3000 reagent (Lipo, used as a control), AntimiR-21 together with Lipofectamine 3000 (Lipo + AntimiR-21) or Untransfected. After 72 h, total RNA was extracted and the expression level of miR-21 was evaluated by q-RT-PCR. The fold change of miR-21 was calculated by normalizing the absolute levels of miR-21 to those of internal control (U6 snRNA), and setting the value of LiPoNs (a) and of Lipo (b) equal to 1. The transfections were performed three times. Bar represents the mean ± SEM of three independent experiments (*$p < 0.05$; ***$p < 0.001$).

II.2.2.4 Downstream regulation of miR-21 target genes

The miR-21 targets many gene transcripts, such as Phosphatase and TENsin homolog deleted on chromosome 10 (PTEN) and Programmed cell death 4 (PDCD4), resulting in increased cancer cell transformation, invasion, and metastasis [88, 89]. In order to verify the bioactivity of AntimiR-21 on the expression level of downstream genes, the mRNA levels of target miR-21 genes were analyzed in MDA-MB-231 cells treated for 72 h with 33 nM of AntimiR-21 in the LiPoNs and Lipofectamine 3000 mediated transfection (Lipo + AntimiR-21). PTEN and PDCD4 gene levels were quantified by q-RT PCR and normalized to the housekeeping mRNA β-ACTIN. The results showed an upregulation of 4.77 of PTEN expression for the treatment with AntimiR-21- LiPoNs (Figure II-5a), while PDCD4 showed an up-regulation of 7.3 times with respect to the control LipoNs treated cells (Figure II- 5c). As outlined above, the AntimiR-21 delivered in combination with Lipofectamine 3000 confirmed the effect obtained for the AntimiR-21 entrapped in LiPoNs after 72 h of treatment (Figure II-5b-d).

No increase of both target genes is reported for free AntimiR-21, underlying the inefficient delivery of naked antisense miRNA.

The effective transfection of AntmiR-21 by LiPoNs guaranteed that, upon internalization, the chitosan-AntimiR-21 complex reduced the degradation of the cargo at low pH in the endosomal environment, releasing the intact AntimiR-21 in the cytoplasm. This effect was not usually reported with only lipid-based particles [38]. Indeed, we supposed that the acidified endosomal environment protonates the amine groups of chitosan progressively, increasing the amount and acidification of the positive charges, inducing a membrane instability [9, 90] or osmotic lysis of endosome through a pH-buffering effect [40]. Indeed, chitosomes' more substantial endosomal escape efficacy was already reported up to 8 h, with respect to free AntimiR-21 [9].

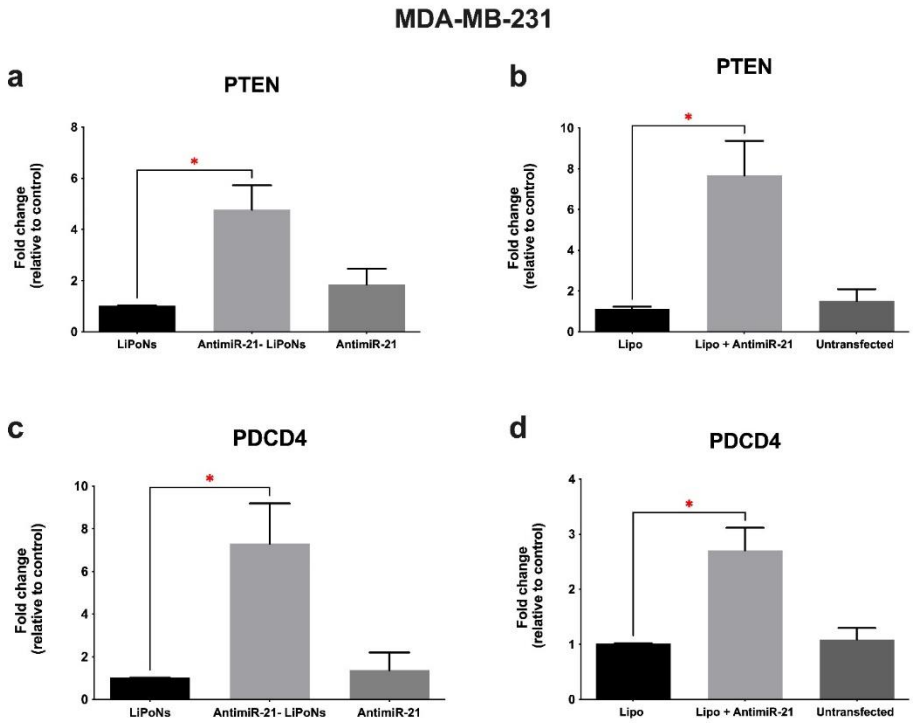

Figure II-5. The efficiency of AntimiR-21- LiPoNs in downregulating the miR-21 targets genes in MDA-MB-231 cells. **a**) Expression level of PTEN mRNA was analyzed, by q-RT-PCR, in MDA-MB-231 cells treated for 72 h with LiPoNs, AntimiR-21- LiPoNs or treated only with the AntimiR-21. **b**) Expression level of PTEN mRNA was analyzed by q-RT-PCR in MDA-MB-231 cells transfected for 72 h with AntimiR-21 using Lipofectamine 3000 (Lipo + AntimiR-21) or transfected only with Lipofectamine 3000 (Lipo, used as a control) or Untransfected. **c**) Expression level of PDCD4 in the cells transfected with LiPoNs, AntimiR-21- LiPoNs or treated only with the AntimiR-21. **d**) Expression level of PDCD4 mRNA in MDA-MB-231 cell line untransfected or transfected, for 72 h, with Lipofectamine 3000 reagent alone (Lipo) or in combination with the AntimiR-21 (Lipo + AntimiR-21). The fold change was calculated by normalizing the Ct of PTEN (a-b) and of PDCD4 (c-d) to the Ct of β-ACTIN used as an internal control. The value of PTEN and PDCD4 in LiPoNs (a and c) and Lipo (b and d) was set equal to 1. The transfections were performed three times, and the q-RT-PCR was performed in triplicate. Bars represent the mean ± SEM of three independent experiments (*$p < 0.05$).

II.2.2.5 Biological effect on MDA-MB-231 cells mediated by AntimiR-21-LiPoNs

miR-21 is associated with an increased migratory behaviour of human breast cancer cells [10, 87]. Indeed, its target genes, the PTEN and PDCD4, are related to several pathways

that lead to the acquisition of invasive abilities of the cells [88, 89]. Therefore, we studied the biological activity of AntimiR-21- LiPoNs, achieved through the inhibition of miR-21 with the AntimiR-21, on migration properties of MDA-MB-231 cells (Figure II- 6).

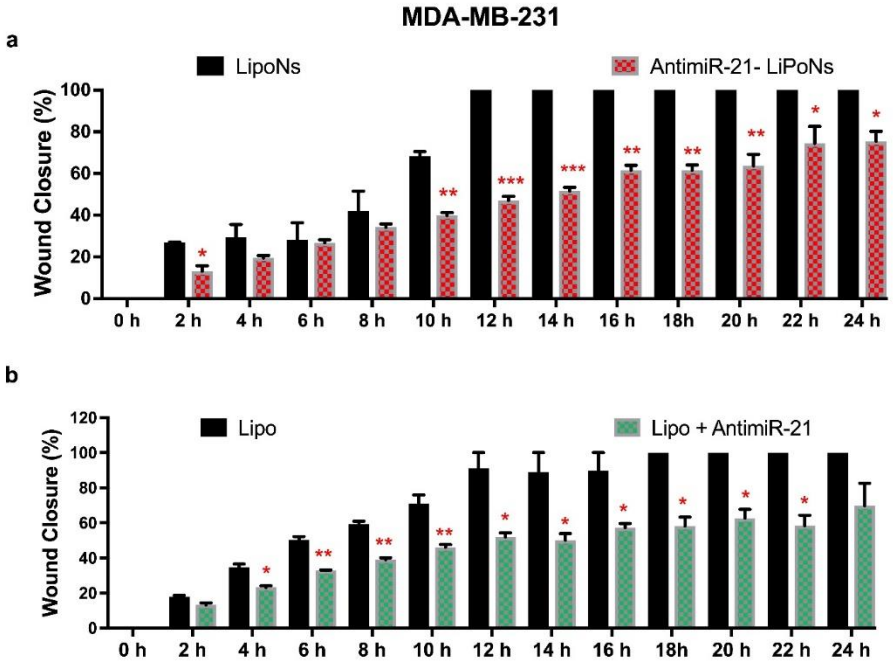

Figure II-6. Effects of the AntimiR-21 delivered by LiPoNs on migration ability of MDA-MD-231 cells. **a**) Cells were treated with AntimiR-21- LiPoNs, or LiPoNs. **b**) Cells were transfected with the AntimiR-21 using Lipofectamine 3000 (Lipo + AntimiR-21), while cells with Lipofectamine 3000 alone (Lipo) were used as control. (a-b). After 48 from transfection, a scraped wound was introduced and cell migration into the wound was recorded for 24 h using time-lapse microscopy. Wound closure was measured every two hours by calculating pixel densities in the wound area and expressed as a percentage of wound closure of triplicate areas ± SEM. *, $p < 0.05$; **, $p < 0.01$ ***, $p < 0.001$, Unpaired T- test.

Thus, we silenced miR-21 in the triple-negative breast cancer MDA-MB-231 cells using the AntimiR-21- LiPoNs (Figure II-6a) or combined with Lipofectamine 3000 (Lipo + AntimiR-21) at 33 nM (Figure II-6b).
In parallel, the cells were also treated with LiPoNs or Lipofectamine 3000 (Lipo) alone as controls as the previous cell treatments.
After 48 h from transfection, a scraped wound was introduced on the confluent monolayers. Then the migration ability was monitored by time-lapse microscopy for 24 h and expressed as a percentage of wound closure. Quantitative measures of the wound

closure at different time points showed that the silencing of miR-21 impaired cell migration of MDA-MB-231 cells using both the LiPoNs as vehicle and Lipofectamine 3000 reagent.
Indeed, after 12 h, cells treated with LiPoNs presented a closure of 100%, while cells treated with AntimiR-21- LiPoNs presented a closure of 47% (Figure II-6a).
Simultaneously, as reported in Figure II-6b, a closure of 51.9 % and of 91% was observed in cells transfected with AntimiR-21 using Lipofectamine and in cells transfected with Lipofectamine alone, respectively.
The reductions of cell migration obtained by AntimiR-21- LipoNs and Lipo+ Anti miR-21 were observed at all the time points studied for up to 24 hours (Figure II-6 a-b).
The good correlation between the data obtained with LiPoNs nanoparticles and the standard protocol, Lipofectamine transfection reagent, confirmed the effectiveness of AntimiR-21- LiPoNs treatment in reducing the migratory properties of human breast cancer cells.
To test the cell viability of on MDA-MB-231 cells treated with different AntimiR-21 formulations, the MTT assay was performed at 24 h and 48 h (Figure II-7). The treatment with AntimiR-21 alone, in both LiPoNs formulations and mediated with Lipofectamine produced no significant reductions in cell viability compared to control groups. These data were consistent with the cytotoxicity test results reported by Devulapally et al. [10], even at higher AntimiR-21 concentrations.

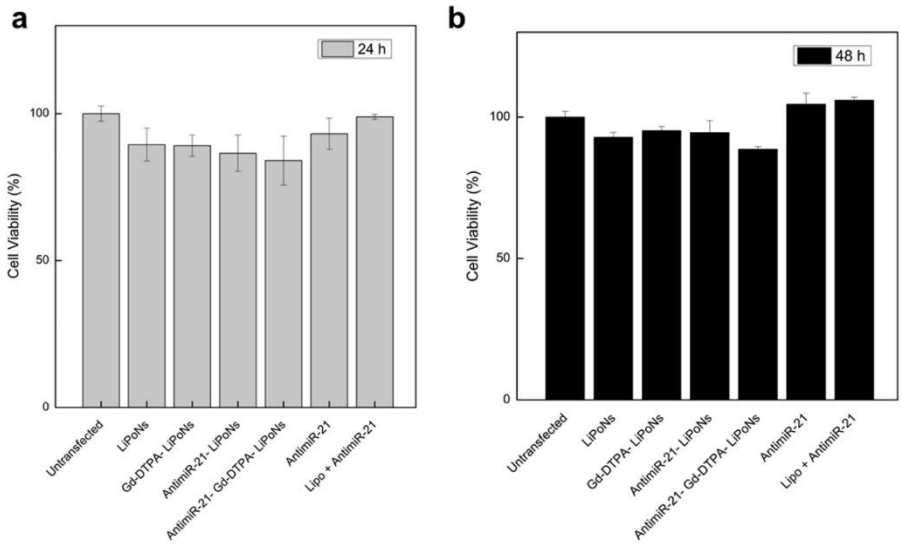

Figure II-7. Cell viability % of MDA-MB-231 cells transfected with the AntimiR-21 alone and together with Lipofectamine 3000 reagent (AntimiR-21 conc. 33 nM), with AntimiR-21 LiPoNs and AntimiR21- Gd-DTPA LiPoNs, and LiPoNs and Gd-DTPA LiPoNs (AntimiR-21conc. 33 nM, Lipids conc. 12 µg/ml and Gd-DTPA conc.:28 µM) for **a**) 24 h and **b**) 48 h.

II.3 CONCLUSIONS

The integrity and stability of microRNAs in blood circulation is the major obstacle to their employment as a drug in cancer therapy. In this regard, several strategies, including chemical modifications of microRNA, have been exploited. Moreover, microRNA's size and negative charge also limit their transmembrane transport.

In this study, we used Lipid-polymer hybrid nanoparticles LiPoNs to enhance the stability of AntimiR-21, to increase its cellular uptake and improve its endosomal escape. In particular, we exploited the coupled Hydrodynamic Flow Focusing (cHFF) by sheeting a middle chitosan solution containing the microRNAs with two lipids streams injected from the side channel, forcing the entrapment of the microRNAs in the hybrid Lipid-Polymer NPs. This hybrid architecture of a polymer core entrapped in a lipid-cholesterol bilayer also offers many advantages to respect the traditional LNPs, by integrating the advantage of different materials in the same structure to improve the miRNA delivery.

These theranostic LiPoNs, co-loaded with Gd-DTPA, were validated as an effective shuttle for AntimiR-21 to MDA-MB-231 cells by comparing the bioactivity of the cargo with respect to its naked version and its delivery mediated by a common transfection agent.

The enhanced blockage of miR-21, promoted by the AntimiR-21- LiPoNs, prevented its binding to target mRNA and consequently induced the upregulation of its targeted genes, PTEN and PDCD4. As a result, the MDA-MB-231 cells transfected with the AntimiR-21-LiPoNs reduced their motility and invasion ability. Considering the limited cellular uptake of negative charge microRNAs, the well-orchestrated expression of all genes of interest upon the treatment with microRNAs loaded LiPoNs, highlights the crucial role of lipid components in the design of nano-architectures to assist the delivery of chitosan-microRNAs complex to the target cells.

II.4 REFERENCES

[1] R. Singh, Y.Y. Mo, Role of microRNAs in breast cancer, Cancer Biology & Therapy 14(3) (2013) 201-212.
[2] A. Esquela-Kerscher, F.J. Slack, Oncomirs - microRNAs with a role in cancer, Nature Reviews Cancer 6(4) (2006) 259-269.
[3] S.W.L. Lee, C. Paoletti, M. Campisi, T. Osaki, G. Adriani, R.D. Kamm, C. Mattu, V. Chiono, MicroRNA delivery through nanoparticles, Journal of Controlled Release 313 (2019) 80-95.
[4] Y.C. Chen, D.Y. Gao, L. Huang, In vivo delivery of miRNAs for cancer therapy: Challenges and strategies, Advanced Drug Delivery Reviews 81 (2015) 128-141.
[5] C.Z. Chen, MicroRNAs as oncogenes and tumor suppressors, New England Journal of Medicine 353(17) (2005) 1768-1771.
[6] J. Zhao, Y.S. Zhang, G.H. Zhao, Emerging role of microRNA-21 in colorectal cancer, Cancer Biomarkers 15(3) (2015) 219-226.
[7] D. Piasecka, M. Braun, R. Kordek, R. Sadej, H. Romanska, MicroRNAs in regulation of triple-negative breast cancer progression, Journal of Cancer Research and Clinical Oncology 144(8) (2018) 1401-1411.
[8] A. Ghosh, N. Ranjan, L.W. Jiang, A.H. Ansari, N. Degyatoreva, S. Ahluwalia, D.P. Arya, S. Maiti, Fine-tuning miR-21 expression and inhibition of EMT in breast cancer cells using aromatic-neomycin derivatives, Molecular Therapy-Nucleic Acids 27 (2022) 685-698.
[9] X.F. Sun, H.P. Xu, T. Huang, C.J. Zhang, J.Z. Wu, S.X. Luo, Simultaneous delivery of anti-miRNA and docetaxel with supramolecular self-assembled "chitosome" for improving chemosensitivity of triple negative breast cancer cells, Drug Delivery and Translational Research 11(1) (2021) 192-204.
[10] R. Devulapally, N.M. Sekar, T.V. Sekar, K. Foygel, T.F. Massoud, J.K. Willmann, R. Paulmurugan, Polymer Nanoparticles Mediated Codelivery of AntimiR-10b and AntimiR-21 for Achieving Triple Negative Breast Cancer Therapy, Acs Nano 9(3) (2015) 2290-2302.
[11] K. Raemdonck, R.E. Vandenbroucke, J. Demeester, N.N. Sanders, S.C. De Smedt, Maintaining the silence: reflections on long-term RNAi, Drug Discovery Today 13(21-22) (2008) 917-931.
[12] T. Stylianopoulos, R.K. Jain, Combining two strategies to improve perfusion and drug delivery in solid tumors, Proceedings of the National Academy of Sciences of the United States of America 110(46) (2013) 18632-18637.
[13] J.J.D. Ho, J.L. Metcalf, M.S. Yan, P.J. Turgeon, J.J. Wang, M. Chalsev, T.N. Petruzziello-Pellegrini, A.K.Y. Tsui, J.Z. He, H. Dhamko, H.S.J. Man, G.B. Robb, B.T. Teh, M. Ohh, P.A. Marsden, Functional Importance of Dicer Protein in the Adaptive Cellular Response to Hypoxia, Journal of Biological Chemistry 287(34) (2012) 29003-29020.
[14] S. Sarkar, G. Horn, K. Moulton, A. Oza, S. Byler, S. Kokolus, M. Longacre, Cancer Development, Progression, and Therapy: An Epigenetic Overview, International Journal of Molecular Sciences 14(10) (2013) 21087-21113.
[15] S. van Dongen, C. Abreu-Goodger, A.J. Enright, Detecting microRNA binding and siRNA off-target effects from expression data, Nature Methods 5(12) (2008) 1023-1025.

[16] A.I. Villanueva, R.R. Kulkarni, S. Sharif, Synthetic double-stranded RNA oligonucleotides are immunostimulatory for chicken spleen cells, Developmental and Comparative Immunology 35(1) (2011) 28-34.
[17] M. Fabbri, A. Paone, F. Calore, R. Galli, E. Gaudio, R. Santhanam, F. Lovat, P. Fadda, C. Mao, G.J. Nuovo, N. Zanesi, M. Crawford, G.H. Ozer, D. Wernicke, H. Alder, M.A. Caligiuri, P. Nana-Sinkam, D. Perrotti, C.M. Croce, MicroRNAs bind to Toll-like receptors to induce prometastatic inflammatory response, Proceedings of the National Academy of Sciences of the United States of America 109(31) (2012) E2110-E2116.
[18] T.O. Kabilova, M.I. Meschaninova, A.G. Venyaminova, V.P. Nikolin, M.A. Zenkova, V.V. Vlassov, E.L. Chernolovskaya, Short Double-Stranded RNA with Immunostimulatory Activity: Sequence Dependence, Nucleic Acid Therapeutics 22(3) (2012) 196-204.
[19] A.D. Judge, V. Sood, J.R. Shaw, D. Fang, K. McClintock, I. MacLachlan, Sequence-dependent stimulation of the mammalian innate immune response by synthetic siRNA, Nature Biotechnology 23(4) (2005) 457-462.
[20] S. Davis, B. Lollo, S. Freier, C. Esau, Improved targeting of miRNA with antisense oligonucleotides, Nucleic Acids Research 34(8) (2006) 2294-2304.
[21] Y. Fu, J. Chen, Z. Huang, Recent progress in microRNA-based delivery systems for the treatment of human disease, ExRNA 1(1) (2019) 24.
[22] J. Elmen, M. Lindow, A. Silahtaroglu, M. Bak, M. Christensen, A. Lind-Thomsen, M. Hedtjarn, J.B. Hansen, H.F. Hansen, E.M. Straarup, K. McCullagh, P. Kearney, S. Kauppinen, Antagonism of microRNA-122 in mice by systemically administered LNA-antimiR leads to up-regulation of a large set of predicted target mRNAs in the liver, Nucleic Acids Research 36(4) (2008) 1153-1162.
[23] J.C. Henry, A.C.P. Azevedo-Pouly, T.D. Schmittgen, microRNA Replacement Therapy for Cancer, Pharmaceutical Research 28(12) (2011) 3030-3042.
[24] D.M. Pereira, P.M. Rodrigues, P.M. Borralho, C.M.P. Rodrigues, Delivering the promise of miRNA cancer therapeutics, Drug Discovery Today 18(5-6) (2013) 282-289.
[25] M.T. Cai, Z.Z. Wu, Y. Li, J. Cao, Y.W. Chen, X.L. Luo, Bioinspired mimics: Self-assembly of redox-activated phosphorylcholine based biodegradable copolymers for enhancing antitumor efficiency, Materials Science & Engineering C-Materials for Biological Applications 89 (2018) 401-412.
[26] D.S. Anson, The use of retroviral vectors for gene therapy-what are the risks? A review of retroviral pathogenesis and its relevance to retroviral vector-mediated gene delivery, Genet Vaccines Ther 2(1) (2004) 9.
[27] F.C. Moraes, C. Pichon, D. Letourneur, F. Chaubet, miRNA Delivery by Nanosystems: State of the Art and Perspectives, Pharmaceutics 13(11) (2021).
[28] J. Kota, R.R. Chivukula, K.A. O'Donnell, E.A. Wentzel, C.L. Montgomery, H.W. Hwang, T.C. Chang, P. Vivekanandan, M. Torbenson, K.R. Clark, J.R. Mendell, J.T. Mendell, Therapeutic microRNA Delivery Suppresses Tumorigenesis in a Murine Liver Cancer Model, Cell 137(6) (2009) 1005-1017.
[29] D.M. Pegtel, K. Cosmopoulos, D.A. Thorley-Lawson, M.A.J. van Eijndhoven, E.S. Hopmans, J.L. Lindenberg, T.D. de Gruijl, T. Wurdinger, J.M. Middeldorp, Functional delivery of viral miRNAs via exosomes, Proceedings of the National Academy of Sciences of the United States of America 107(14) (2010) 6328-6333.

[30] A. Schade, E. Delyagina, D. Scharfenberg, A. Skorska, C. Lux, R. David, G. Steinhoff, Innovative Strategy for MicroRNA Delivery in Human Mesenchymal Stem Cells via Magnetic Nanoparticles, International Journal of Molecular Sciences 14(6) (2013) 10710-10726.
[31] A. Tivnan, W.S. Orr, V. Gubala, R. Nooney, D.E. Williams, C. McDonagh, S. Prenter, H. Harvey, R. Domingo-Fernandez, I.M. Bray, O. Piskareva, C.Y. Ng, H.N. Lode, A.M. Davidoff, R.L. Stallings, Inhibition of Neuroblastoma Tumor Growth by Targeted Delivery of MicroRNA-34a Using Anti-Disialoganglioside GD(2) Coated Nanoparticles, Plos One 7(5) (2012).
[32] U.K. Sukumar, R.J.C. Bose, M. Malhotra, H.A. Babikir, R. Afjei, E. Robinson, Y.T. Zeng, E. Chang, F. Habte, R. Sinclair, S.S. Gambhir, T.F. Massoud, R. Paulmurugan, Intranasal delivery of targeted polyfunctional gold-iron oxide nanoparticles loaded with therapeutic microRNAs for combined theranostic multimodality imaging and presensitization of glioblastoma to temozolomide, Biomaterials 218 (2019).
[33] X.C. Hou, T. Zaks, R. Langer, Y.Z. Dong, Lipid nanoparticles for mRNA delivery, Nature Reviews Materials 6(12) (2021) 1078-1094.
[34] S.H. Hsu, B. Yu, X.M. Wang, Y.Z. Lu, C.R. Schmidt, R.J. Lee, L.J. Lee, S.T. Jacob, K. Ghoshal, Cationic lipid nanoparticles for therapeutic delivery of siRNA and miRNA to murine liver tumor, Nanomedicine-Nanotechnology Biology and Medicine 9(8) (2013) 1169-1180.
[35] Y. Wu, M. Crawford, B. Yu, Y.C. Mao, S.P. Nana-Sinkam, L.J. Lee, MicroRNA Delivery by Cationic Lipoplexes for Lung Cancer Therapy, Molecular Pharmaceutics 8(4) (2011) 1381-1389.
[36] C.V. Pecot, G.A. Calin, R.L. Coleman, G. Lopez-Berestein, A.K. Sood, RNA interference in the clinic: challenges and future directions, Nature Reviews Cancer 11(1) (2011) 59-67.
[37] J.F. Wiggins, L. Ruffino, K. Kelnar, M. Omotola, L. Patrawala, D. Brown, A.G. Bader, Development of a Lung Cancer Therapeutic Based on the Tumor Suppressor MicroRNA-34, Cancer Research 70(14) (2010) 5923-5930.
[38] X.C. Hou, T. Zaks, R. Langer, Y.Z. Dong, Lipid nanoparticles for mRNA delivery, Nature Reviews Materials.
[39] K. Gokita, J. Inoue, H. Ishihara, K. Kojima, J. Inazawa, Therapeutic Potential of LNP-Mediated Delivery of miR-634 for Cancer Therapy, Molecular Therapy-Nucleic Acids 19 (2020) 330-338.
[40] A. Parodi, C. Corbo, A. Cevenini, R. Molinaro, R. Palomba, L. Pandolfi, M. Agostini, F. Salvatore, E. Tasciotti, Enabling cytoplasmic delivery and organelle targeting by surface modification of nanocarriers, Nanomedicine 10(12) (2015) 1923-1940.
[41] O. Boussif, F. Lezoualch, M.A. Zanta, M.D. Mergny, D. Scherman, B. Demeneix, J.P. Behr, A VERSATILE VECTOR FOR GENE AND OLIGONUCLEOTIDE TRANSFER INTO CELLS IN CULTURE AND IN-VIVO - POLYETHYLENIMINE, Proceedings of the National Academy of Sciences of the United States of America 92(16) (1995) 7297-7301.
[42] T.T. Zhang, X. Xue, D.L. He, J.T. Hsieh, A prostate cancer-targeted polyarginine-disulfide linked PEI nanocarrier for delivery of microRNA, Cancer Letters 365(2) (2015) 156-165.
[43] G.Y. Chiou, J.Y. Cherng, H.S. Hsu, M.L. Wang, C.M. Tsai, K.H. Lu, Y. Chien, S.C. Hung, Y.W. Chen, C.I. Wong, L.M. Tseng, P.I. Huang, C.C. Yu, W.H. Hsu, S.H. Chiou, Cationic polyurethanes-short branch PEI-mediated delivery of Mir145 inhibited epithelial-

mesenchymal transdifferentiation and cancer stem-like properties and in lung adenocarcinoma, Journal of Controlled Release 159(2) (2012) 240-250.
[44] Q. Lin, R.T. Li, H.Q. Qian, J. Wei, L. Xie, J. Shen, M. Yang, X.P. Qian, L.X. Yu, X.Q. Jiang, B.R. Liu, Targeted delivery of miR-200c/DOC to inhibit cancer stem cells and cancer cells by the gelatinases-stimuli nanoparticles, Biomaterials 34(29) (2013) 7191-7203.
[45] J. Panyam, V. Labhasetwar, Biodegradable nanoparticles for drug and gene delivery to cells and tissue, Advanced Drug Delivery Reviews 64 (2012) 61-71.
[46] I. Dasgupta, A. Chatterjee, Recent Advances in miRNA Delivery Systems, Methods and Protocols 4(1) (2021).
[47] D. Cosco, F. Cilurzo, J. Maiuolo, C. Federico, M. Di Martino, M.C. Cristiano, P. Tassone, M. Fresta, D. Paolino, Delivery of miR-34a by chitosan/PLGA nanoplexes for the anticancer treatment of multiple myeloma, Scientific Reports 5 (2015).
[48] S. Gaur, Y.F. Wen, J.H. Song, N.U. Parikh, L.S. Mangala, A.M. Blessing, C. Ivan, S.Y. Wu, A. Varkaris, Y. Shi, G. Lopez-Berestein, D.E. Frigo, A.K. Sood, G.E. Gallick, Chitosan nanoparticle-mediated delivery of miRNA-34a decreases prostate tumor growth in the bone and its expression induces non-canonical autophagy, Oncotarget 6(30) (2015) 29161-29177.
[49] Y. Cao, Y.F. Tan, Y.S. Wong, M.W.J. Liew, S. Venkatraman, Recent Advances in Chitosan-Based Carriers for Gene Delivery, Marine Drugs 17(6) (2019).
[50] B. Layek, J. Singh, N-hexanoyl, N-octanoyl and N-decanoyl chitosans: Binding affinity, cell uptake, and transfection, Carbohydrate Polymers 89(2) (2012) 403-410.
[51] S.Y. Chae, S. Son, M. Lee, M.K. Jang, J.W. Nah, Deoxycholic acid-conjugated chitosan oligosaccharide nanoparticles for efficient gene carrier, Journal of Controlled Release 109(1-3) (2005) 330-344.
[52] R. Mandke, J. Singh, Effect of acyl chain length and unsaturation on physicochemical properties and transfection efficiency of N-acyl-substituted low-molecular-weight chitosan, Journal of Pharmaceutical Sciences 101(1) (2012) 268-282.
[53] X.W. Deng, M.J. Cao, J.K. Zhang, K.L. Hu, Z.X. Yin, Z.X. Zhou, X.Q. Xiao, Y.S. Yang, W. Sheng, Y. Wu, Y. Zeng, Hyaluronic acid-chitosan nanoparticles for co-delivery of M1R-34a and doxorubicin in therapy against triple negative breast cancer, Biomaterials 35(14) (2014) 4333-4344.
[54] X.M. Huang, S. Schwind, B. Yu, R. Santhanam, H.Y. Wang, P. Hoellerbauer, A. Mims, R. Klisovic, A.R. Walker, K.K. Chan, W. Blum, D. Perrotti, J.C. Byrd, C.D. Bloomfield, M.A. Caligiuri, R.J. Lee, R. Garzon, N. Muthusamy, L.J. Lee, G. Marcucci, Targeted Delivery of microRNA-29b by Transferrin-Conjugated Anionic Lipopolyplex Nanoparticles: A Novel Therapeutic Strategy in Acute Myeloid Leukemia, Clinical Cancer Research 19(9) (2013) 2355-2367.
[55] U. Bilati, E. Allemann, E. Doelker, Development of a nanoprecipitation method intended for the entrapment of hydrophilic drugs into nanoparticles, European Journal of Pharmaceutical Sciences 24(1) (2005) 67-75.
[56] J. Yang, H.M. Liu, X. Zhang, Design, preparation and application of nucleic acid delivery carriers, Biotechnology Advances 32(4) (2014) 804-817.
[57] H.W. Zhang, Thin-Film Hydration Followed by Extrusion Method for Liposome Preparation, Liposomes: Methods and Protocols, 2nd Edition 1522 (2017) 17-22.

[58] M.S. Ali, N. Hooshmand, M. El-Sayed, H.I. Labouta, Microfluidics for Development of Lipid Nanoparticles: Paving the Way for Nucleic Acids to the Clinic, ACS Applied Bio Materials (2021).
[59] M.J.W. Evers, J.A. Kulkarni, R. van der Meel, P.R. Cullis, P. Vader, R.M. Schiffelers, State-of-the-Art Design and Rapid-Mixing Production Techniques of Lipid Nanoparticles for Nucleic Acid Delivery, Small Methods 2(9) (2018).
[60] E. Samaridou, J. Heyes, P. Lutwyche, Lipid nanoparticles for nucleic acid delivery: Current perspectives, Advanced Drug Delivery Reviews 154 (2020) 37-63.
[61] L.B. Jeffs, L.R. Palmer, E.G. Ambegia, C. Giesbrecht, S. Ewanick, I. MacLachlan, A scalable, extrusion-free method for efficient liposomal encapsulation of plasmid DNA, Pharmaceutical Research 22(3) (2005) 362-372.
[62] S.C. Semple, S.K. Klimuk, T.O. Harasym, N. Dos Santos, S.M. Ansell, K.F. Wong, N. Maurer, H. Stark, P.R. Cullis, M.J. Hope, P. Scherrer, Efficient encapsulation of antisense oligonucleotides in lipid vesicles using ionizable aminolipids: formation of novel small multilamellar vesicle structures, Biochimica Et Biophysica Acta-Biomembranes 1510(1-2) (2001) 152-166.
[63] S.M. Hoy, Patisiran: First Global Approval, Drugs 78(15) (2018) 1625-1631.
[64] S. Krishnadasan, R.J.C. Brown, A.J. deMello, J.C. deMello, Intelligent routes to the controlled synthesis of nanoparticles, Lab on a Chip 7(11) (2007) 1434-1441.
[65] N. Kimura, M. Maeki, M. Tokeshi, Microfabrication and microfluidic devices for drug delivery, Microfluidics for Pharmaceutical Applications: from Nano/Micro Systems Fabrication to Controlled Drug Delivery (2019) 123-136.
[66] S.J. Shepherd, D. Issadore, M.J. Mitchell, Microfluidic formulation of nanoparticles for biomedical applications, Biomaterials 274 (2021).
[67] J.P. Ma, S.M.Y. Lee, C.Q. Yi, C.W. Li, Controllable synthesis of functional nanoparticles by microfluidic platforms for biomedical applications - a review, Lab on a Chip 17(2) (2017) 209-226.
[68] A. Jahn, W.N. Vreeland, M. Gaitan, L.E. Locascio, Controlled vesicle self-assembly in microfluidic channels with hydrodynamic focusing, Journal of the American Chemical Society 126(9) (2004) 2674-2675.
[69] R.R. Hood, D.L. DeVoe, High-Throughput Continuous Flow Production of Nanoscale Liposomes by Microfluidic Vertical Flow Focusing, Small 11(43) (2015) 5790-5799.
[70] A.D. Stroock, S.K.W. Dertinger, A. Ajdari, I. Mezic, H.A. Stone, G.M. Whitesides, Chaotic mixer for microchannels, Science 295(5555) (2002) 647-651.
[71] C.Y. Lee, W.T. Wang, C.C. Liu, L.M. Fu, Passive mixers in microfluidic systems: A review, Chemical Engineering Journal 288 (2016) 146-160.
[72] M. Maeki, T. Saito, Y. Sato, T. Yasui, N. Kaji, A. Ishida, H. Tani, Y. Baba, H. Harashima, M. Tokeshi, A strategy for synthesis of lipid nanoparticles using microfluidic devices with a mixer structure, Rsc Advances 5(57) (2015) 46181-46185.
[73] D.L. Chen, K.T. Love, Y. Chen, A.A. Eltoukhy, C. Kastrup, G. Sahay, A. Jeon, Y.Z. Dong, K.A. Whitehead, D.G. Anderson, Rapid Discovery of Potent siRNA-Containing Lipid Nanoparticles Enabled by Controlled Microfluidic Formulation, Journal of the American Chemical Society 134(16) (2012) 6948-6951.

[74] N.M. Belliveau, J. Huft, P.J.C. Lin, S. Chen, A.K.K. Leung, T.J. Leaver, A.W. Wild, J.B. Lee, R.J. Taylor, Y.K. Tam, C.L. Hansen, P.R. Cullis, Microfluidic Synthesis of Highly Potent Limit-size Lipid Nanoparticles for In Vivo Delivery of siRNA, Molecular Therapy-Nucleic Acids 1 (2012).
[75] M. Malhotra, C. Tomaro-Duchesneau, S. Saha, I. Kahouli, S. Prakash, Development and characterization of chitosan-PEG-TAT nanoparticles for the intracellular delivery of siRNA, International Journal of Nanomedicine 8 (2013).
[76] N. Aibani, R. Rai, P. Patel, G. Cuddihy, E.K. Wasan, Chitosan Nanoparticles at the Biological Interface: Implications for Drug Delivery, Pharmaceutics 13(10) (2021).
[77] K. Buyens, S.C. De Smedt, K. Braeckmans, J. Demeester, L. Peeters, L.A. van Grunsven, X.D. du Jeu, R. Sawant, V. Torchilin, K. Farkasova, M. Ogris, N.N. Sanders, Liposome based systems for systemic siRNA delivery: Stability in blood sets the requirements for optimal carrier design, Journal of Controlled Release 158(3) (2012) 362-370.
[78] S. Danielsen, S. Strand, C.D. Davies, B.T. Stokke, Glycosaminoglycan destabilization of DNA-chitosan polyplexes for gene delivery depends on chitosan chain length and GAG properties, Biochimica Et Biophysica Acta-General Subjects 1721(1-3) (2005) 44-54.
[79] F. Roffo, A.M. Ponsiglione, P.A. Netti, E. Torino, coupled Hydrodynamic Flow Focusing (cHFF) to Engineer Lipid–Polymer Nanoparticles (LiPoNs) for Multimodal Imaging and Theranostic Applications %M doi:10.3390/biomedicines10020438 %U https://www.mdpi.com/2227-9059/10/2/438, Biomedicines %@ 2227-9059 10(2) (2022) 438.
[80] D. Pogocki, C. Schoneich, Chemical stability of nucleic acid-derived drugs, Journal of Pharmaceutical Sciences 89(4) (2000) 443-456.
[81] T. Wang, E.G. Hammond, W.R. Fehr, Neutral and polar lipid phase transition of soybeans with various saturated fatty acid contents, Journal of the American Oil Chemists Society 78(11) (2001) 1139-1144.
[82] J.M. Zook, W.N. Vreeland, Effects of temperature, acyl chain length, and flow-rate ratio on liposome formation and size in a microfluidic hydrodynamic focusing device, Soft Matter 6(6) (2010) 1352-1360.
[83] H.S. Bernhardt, W.P. Tate, Primordial soup or vinaigrette: did the RNA world evolve at acidic pH?, Biology Direct 7 (2012).
[84] M. Oivanen, S. Kuusela, H. Lonnberg, Kinetics and mechanisms for the cleavage and isomerization of the phosphodiester bonds of RNA by Bronsted acids and bases, Chemical Reviews 98(3) (1998) 961-990.
[85] C. Walsh, K. Ou, N.M. Belliveau, T.J. Leaver, A.W. Wild, J. Huft, P.J. Lin, S. Chen, A.K. Leung, J.B. Lee, C.L. Hansen, R.J. Taylor, E.C. Ramsay, P.R. Cullis, Microfluidic-Based Manufacture of siRNA-Lipid Nanoparticles for Therapeutic Applications, Drug Delivery System, 2nd Edition 1141 (2014) 109-120.
[86] M.J. Goldman, B. Craft, M. Hastie, K. Repecka, F. McDade, A. Kamath, A. Banerjee, Y.H. Luo, D. Rogers, A.N. Brooks, J.C. Zhu, D. Haussler, Visualizing and interpreting cancer genomics data via the Xena platform, Nature Biotechnology 38(6) (2020) 675-678.
[87] E.D. Arisan, O. Rencuzogullari, C. Cieza-Borrella, F.M. Arenas, M. Dwek, S. Lange, P. Uysal-Onganer, MiR-21 Is Required for the Epithelial-Mesenchymal Transition in MDA-MB-231 Breast Cancer Cells, International Journal of Molecular Sciences 22(4) (2021).

[88] M.B. Brito, E. Goulielmaki, E.A. Papakonstanti, Focus on PTEN regulation, Frontiers in Oncology 5 (2015).
[89] S. Matsuhashi, M. Manirujjaman, H. Hamajima, I. Ozaki, Control Mechanisms of the Tumor Suppressor PDCD4: Expression and Functions, International Journal of Molecular Sciences 20(9) (2019).
[90] S.R. Mao, W. Sun, T. Kissel, Chitosan-based formulations for delivery of DNA and siRNA, Advanced Drug Delivery Reviews 62(1) (2010) 12-27.

III. CHAPTER III–CELL DYNAMICS AT NANO-INTERACTIONS

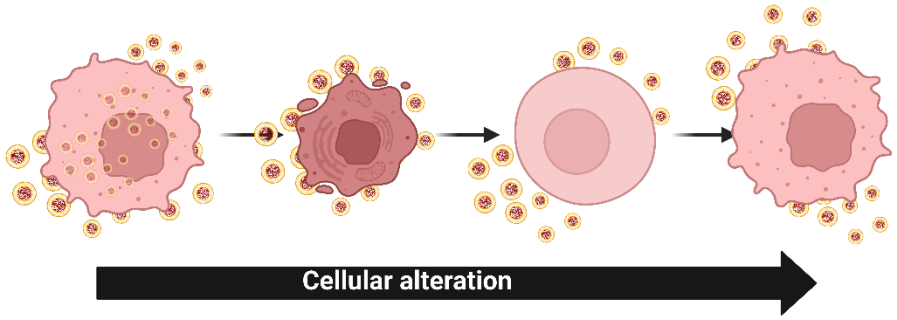

Graphical Abstract III. Cellular alterations upon interaction with Lipid-Polymer NPs.

Abstract

The study of nano-bio interactions is an emerging topic that aims to identify the interaction between nanomaterials and biological systems. However, the scientific community has been mainly focused on identifying the potential toxicological response of cells to these nano-bio interactions, while their biological effects on cell functioning have been less investigated. Overcoming the cytotoxicity concept, the cell mechanobiological response, the inflammatory reaction and the biological alterations upon NPs interaction and uptake, could open new possibilities for cancer treatment. In this context, the increase or the reduction of the operational level of the cellular machinery induced by the NPs, is leveraged as a tool to enable new cellular functions instead of disrupting them. In this perspective, the results of morphological and behavioural modifications of cells following exposure to LiPoNs, are reported. The cellular morphological alterations, the slowdown of cellular proliferation and the increase in cell motility become favourable conditions for designing new therapeutic strategies for drug delivery.

III.1 BACKGROUND

III.1.1 Introduction

The cell membrane (CM), made up of a bilayer assembly of phospholipids, not only protects intracellular components from the surrounding environment but guarantees the cell homeostasis and ion concentration gradients. Moreover, it provides structural support and controls the exchange of molecules and nutrients[1, 2]. The cell employs two mechanisms for the exchange of substances. The first transport is along the concentration gradient and it is in the absence of energy, while the second is against the concentration gradient with energy consumption (active transport), called endocytosis[3].

In the endocytosis process, the substances from extracellular space are internalized in the cells with a cellular membrane invagination and buds off, leading to membrane-bounded vesicles known as endosomes. According to the size of this endocytotic vesicle, it is possible to classify the endocytosis as phagocytosis, where the vesicles is around 250 nm, and the pinocytosis, which involves the internalization of fluids with small material in the range of few to hundreds of nanometer. The latter can be further categorized as clathrin-mediated endocytosis, caveoleae-mediated endocytosis, clathrin- and caveoleae-indipendent endocytosis and macropinocytosis[2].
The chemical and physical properties of the nanomaterials, including size, shape, charge, texture, and elasticity, are of the foremost importance in cellular interactions[4].
Chitosan NPs as charged biomolecules mainly enter the cells via endocytosis[5], but lipid-based nanoparticles due to their strong affinity and similarity with the CM can also undergo a non-energy dependent mechanism, known as cell fusion[6, 7]. It is worth mentioning that any change in the liposomal composition, such as head group of the lipids, cholesterol addition, the degree of lipid chain saturation and their length, affects the cellular fate of the lipid-based carrier[8, 9]. Abumanhal-Masarweh et al.[9] made extensive studies on how the lipid tails affected the magnitude of cellular uptake, reporting that longer acyl chains improved the liposomal cellular uptake compared to shorter tails, while keeping the same lipid tail length, unsaturated lipids offered higher internalization than saturated one.

Following the observations on the intracellular pathways and dimensions of their vesicles, the size of NPs emerges as determining factor in guiding the endocytic mechanisms. Large NPs (200-1500 nm) mainly enter through phagocytosis, while small NPs (<100 nm) adhere to clathrin or caveoleae proteins and get in through pinocytosis[2]. Several studies reported the improved ability of NPs to enter in the cell by reducing their size, with the identification of 50 nm as the optimal size. Undeniably, smaller particles (15-30 nm) and large particles (70-240 nm) show a reduced binding tendency to cell receptors and a subsequently limited receptor-mediated endocytosis[10-12]. As regards the chitosan NPs, the effect of the size on their uptake varying according to the cell lines and experimental conditions[5]. Tahara et al.[13] reported a higher cellular uptake for PLGA NPs coated with chitosan with a size up to 200 nm, rather than 1000 nm, in A549 cells, suggesting as uptake mechanism an energy-dependent clathrin-mediated endocytic process. Tammam et al.[14] reported that small chitosan NPs in the 25 nm range could enter into L929 fibroblast cells by passive

diffusion, whereas the uptake of larger NPs of up to 150 nm was more energy-dependent mechanism.

The impact of the electrostatic interactions occurring at the interface of NPs and CM has to be considered in the cellular fate of NPs[10]. Indeed, Jiang et al[15] reported that the uptake of gold NPs was both size- and charge- dependent. They observed that the cellular uptake of anionic particles decreased by increasing the size. On contrary it increased for cationic ones. Due to the negative charge carried by the CM, positive NPs have better thermodynamical interaction with the CM, that consequently enhances the membrane engulfing process[16-18]. These NPs are mainly internalized via macropinocytosis. Inversely, the production of a local disorder in contact with the CM upon interaction with the negatively charged NPs reduces their uptake that preferentially enters by caveolin and or/clathrin-mediated endocytosis[19]. In accordance, Yue et al.[20] studied the impact of the surface charge of chitosan NPs on cellular uptake on eight cell lines. They observed a higher and faster internalization for positive chitosan NPs (39.25 mV) compared to neutral and negative ones.
As regards to liposomes, Kang et al.[21] investigated the effect of surface charge of liposome with a similar size (around 115 nm) by live cell imaging. They reported a difference in cellular uptake mechanism between glioblastoma U87MG cells and fibroblast NIH/3T3 cells. In the former, the cationic and anionic liposomes were mainly taken up via macropinocytosis, while the neutral liposomes mainly via caveolae-mediated endocytosis. In the latter, all the formulations entered via clathrin mediated endocytosis. Then, Montizaan et al.[8] compared the cellular uptake of zwitterionic and negatively charged liposomes of comparable size by HeLa cells, reporting a strongly decrease in the uptake of negatively charged liposome (-41 mV) by blocking clathrin-mediated endocytosis and actin polymerization. This reduction was not observed for zwitterionic liposomes (-6 mV). Moreover, the authors underlined that a key role in the different uptake behaviours could be determined by the nature and amounts of the proteins adsorbed on liposome surface according to their different charge. Indeed, both formulations converged to the same value of surface charge in presence of serum.
Upon contact with biological fluids, the surface of NPs becomes dramatically modified by the adsorption of biomolecules, including proteins. Therefore, the cells are not seeing the pristine surfaces of the particles but the corona-coated surfaces, and this makes these nano-bio interactions more complex and dynamic[2]. Apart from nanoparticles physiochemical characteristics, the cell-nano bio interactions depend on several factors such as cell lines, cell size, incubation time, NPs concentration and protein absorption, making their understanding more complex[10].

The area of contact between the NPs and CM acts on cell internalization as shown by the different uptake mechanisms that mediate differently shaped nanomaterial[22, 23]. Despite the contradictory results on how differently shaped nanomaterials interact with cells[24, 25], it is briefly reported that sphere-shape material shows an uptake 3 to 5 times more than nanorods on human breast cancer cells, mainly due to the longer time needed

for nanorods for cell membrane wrapping[26]. However, the reduction in the aspect to the ratio of material drastically improves the uptake of nanorods.

NPs elasticity or rigidity has recently been identified as significant factor in the entry pathways. The difference in the rigidity of NPs has been correlated to different uptake mechanisms[27]. Indeed. Guo et al.[28] reported that soft liposomes (∼160 nm, 45 kPa) were internalized in MDA-MB-231, and MCF-7 cancer cells via both endocytosis (inferior) and membrane fusion(predominant), whereas the uptake of stiff hydrogel lipid NPs (∼160 nm, 19 MPa) occurred through endocytosis. Lately, many studies underlined the higher internalization of soft nanoparticles by cancer cells, as observed by Sun et al.[29] on Hela cells, who reported a higher specific uptake by soft (0.76 GPa) PEGylated polymer–lipid NPs (∼40 nm) compared to stiff ones (1.2 GPa). However, Anselmo et al.[30] al reported no difference in the uptake of stiff and soft NPs at short time points (≤4 h), while the stiff NPs were only bound to cells or internalized by 4T1 cells greater than their soft counterparts at 8 and 12 h[30]. These findings were supported by MD simulations that revealed that soft NPs were less internalized due to their easy deformation during internalization, which raised the energy level for complete their cell membrane wrapping[29].
Although mechanical properties of NPs have a crucial role in modulating cancer cell uptake, it remains challenging to clarify and rationalize the role of elasticity of NPs in their interactions with cells[27].

The phenomena occurring at the nanomaterial-cell interface mainly modulate cell structure and fate, induce mutations and initiate cell-cell communication[2]. A review by Panariti in 2012 provided a detailed overview of cell mechanisms and functioning that may be perturbed by cell–NP interaction[6]. The inflammatory reaction is one of the first cellular responses induced by the NPs uptake and it is highly interconnected with the cell mechanics[31, 32]. Indeed, the increase in the ROS production and the cell apoptosis sensitivity were related to the cytoskeleton dysfunction or decrease of actin dynamics [33]. On the other hand, the reduction in mitochondrial activity, as a consequence ATP reduction, could lead to a reduction in cell motility and intracellular trafficking[6].
The cytoskeleton guides many cellular functions, such as maintenance of the cell structure, movement, division, cells communication, connection with the microenvironment and anchoring of organelles. Thus, its reorganization alters the cytoskeleton-associated proteins and induces multiple cellular dysfunctions[10, 34]. Among them, the impairment of the cell proliferation, the detachment, the induction of cell rounding and the deposit of massive dense filaments close to nucleus, can be mentioned[35-38]. Regarding intracellular trafficking, NPs move within the cells for diffusive motion guided by thermal motion or active movement of the microtubules [39]. Indeed, the localization of the NPs mainly in the perinuclear region of the cell[40, 41], against the diffusion gradient, could be due to local energy consumption generated by the cytoskeleton[6, 42]. In this sense, evidences of the interaction of NPs and the cytoskeleton proteins even within vesicles, endosomes or lysosomes, were found[10, 38, 43, 44]. Up to now, the interplay between the cytoskeleton and the intracellular trafficking of NPs is still not completely clarified. Indeed, upon NPs internalization, several morphologic alterations in cell actin networks were reported for

inorganic NPs[45, 46]. As regards organic NPs, less studies on the changes in the cytoskeleton following their uptake are published[47]. Ruenraroengsak et al.[48] reported the interaction of sixth-generation cationic dendrimer with actin filament of acelluar systems in vitro. Moreover, they observed a retarding or acceleration of actin polymerization for a high or lower NPs concentration, respectively.
Incubation with cation NPs, zinc oxide, and cerium, has been reported to compromise the homeostatic mechanism that guarantees low calcium levels within the cell, leading to its abnormal increase[49-51]. The free Ca^{2+} alters intracellular signalling of the cells trough the activation of protein kinase C and promotes physiological defence mechanisms known as autophagy and mitophagy[52, 53].
Another aspect to accounting for is the influence of tangential forces on the plasma membrane that act directly to the cell cytoskeleton, which can potentially act on ion channels[6, 54]. The impact of polystyrene NPs on ionic current across the cell was reported by McCarthy et al.[55]. They demonstrated that polystyrene NPs direct activation of CFTR channels in a monolayer of Calu-3, a human airway submucosal cell line, acting as modulators of ion-channel function in human airway epithelial cells.
Interestingly, an alteration of cell proliferation upon liposome uptake depending on length of carbon chain was outlined[9]. Following the treatment with phospholipids (5 mM) having 18 or 16-carbon-long tails (HSPC and DPPC, respectively), it was observed an increase in cell proliferation. Differently, cells treated with 14- or 12- carbon-long lipids (DMPC and DLPC) have decreased the proliferation maybe due to a membrane destabilization. Furthermore, the addition of cholesterol to the formulation with DMPC cancelled this effect on cell membrane.

III.1.2 Aim of chapter 3

Tremendous improvements in characterizing the cytotoxicity of NPs have been made. However, less effort has been made to clarify the changes in cell physiology upon nanoparticle interactions. The aim of this chapter is to gain an understanding of the morphological and biological response of cells following the interaction with LiPoNs. Taking advantage of a new generation of live imaging instruments that acquire a unique phenotypic fingerprint for each cell without altering their behaviour with the examination, we monitored individual cells every 18 min for 48 hours upon interaction with LiPoNs. We quantified their behavioural characteristics, and gained information on their morphology, proliferation, mitosis and random motility. The results showthat Lipid-Polymer Nanoparticles are not passive shuttles of compounds, but they have an active role in the cell biology. Indeed, they seem to alter the cell functioning inducing a transient cellular state for several hours that has a impact on cell machinery in terms of cell proliferation, mitosis and motility. To elucidate the role of nanomaterial features in guiding cellular pathways, we conducted a preliminary comparative study on cellular response upon the interactions with LiPoNs and Polystyrene NPs.

III.2 CASE STUDY

III.2.1 Experimental section

III.2.1.1 Materials

Materials used to produce the LiPoNs formulations were the same presented in Chapter II.

III.2.1.2 Cell culture

The MDA-MB-231 were cultured, as reported in Chapter II. $2X10^3$ MDA-MB-231 cells/well were plated in 96-well plates for 24 h before adding the formulations. Fresh medium containing LiPoNs formulations was added to each well prior to quantification. For AntimiR-21 formulations, AntimiR-21 alone and using Lipofectamine 3000, AntimiR-21- LiPoNs or AntimiR-21- Gd-DTPA- LiPoNs (AntimiR-21conc. 33 nM, Lipids conc. 12 µg/ml and Gd-DTPA conc.:28 µM) were added in triplicate. Moreover, LiPoNs, Gd-DTPA-LiPoNs and Lipofectamine alone at the same concentration were tested in triplicate.

III.2.1.3 Livecyte cell imaging

The Livecyte of Phasefocus (Alfatest, Milan, Italy) exploits Ptychography, a form of Quantitative Phase Imaging (QPI) – imaging technique that retrieves phase-delay of light passing through a cell. This technique generates high-contrast images of cells that appear as bright objects on a dark background. The sample is illuminated with low power (<1 mW) 650 nm laser allowing the prolonged observation of cells without perturbation. The detector collects a series of diffraction patterns.

High-contrast quantitative phase images were automatically captured using the Livecyte Kinetic Cytometer. Cells were imaged with an Olympus PLN 10X objective and 750µm x 750µm field of view (FOV) per well for 48 hours at 18-minute intervals. Cells were maintained inside an environmental chamber at 37°C with 5% CO2 and 95% humidity.

III.2.1.4 Analysis

The Livecyte instrument contains automated tracking software that monitors single cells. Following image processing, automated cell segmentation and tracking, a plethora of phenotypic metrics are produced. They provide information on both the morphological parameters and the kinetic behaviour of the cells. Single-cell metrics were extracted, and Livecyte automatically produced interactive Cell Dashboards sorted into Morphology, Proliferation, Mitosis and Random Motility.

From the Morphology Dashboards, the data about the median cell sphericity, median cell area, median cell thickness, median length-to-width ratio and median cell dry mass were extracted for each well, and then the average of the three wells was evaluated. The outputs were formatted using a smooth signal processing known as savitzky–Golay filter using Origin8.5. This method performs a local polynomial regression around each point and creates a new, smoothed value for each data point. To increase the smoothness of the result, the number of data points used in each local regression was 10 with a polynomial of the second order.

From the Proliferation Dashboards, the data about cell count normalised, total dry mass normalised and doubling time were extracted for each well, and then the average of the three wells was performed. For the cell count and total dry mass, the values were normalized with respect to the value obtained in the first acquisition. For the outputs of cell count normalised and total dry mass normalised, the signal processing was performed with the same method reported for data on the cell morphology.
From the Mitosis Dashboard, the mitotic index was ordered by treatment group and extracted. The mitotic index was processed with a savitzky-Golay filter.
From Random motility Dashboard, the data across multiple wells are ordered by treatment group, and cell migration metrics are generated in the form of average cell speed, average instantaneous and mean velocity, confinement ratio and displacement.

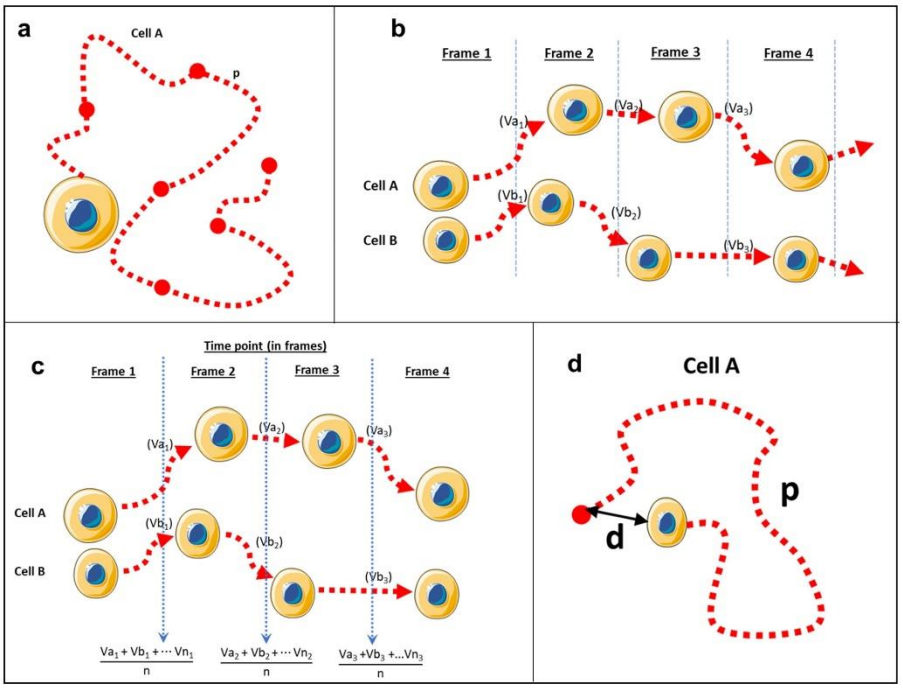

Figure III-1. Graphical explanation of the analysis of random mobility data: **a**)Track Speed, **b)**Average instantaneous velocity, **c**)mean velocity and **d**)confinement ratio.

The Track speed of the cells is reported as a distribution plot where the speed is calculated by dividing the total distance travelled by the lifetime of the track:

$$\text{Track speed} = \frac{p}{t} \quad (1)$$

Where p is the pathlength travelled by the cell and t is the lifetime of a track (Figure III-1a).

The average instantaneous velocity of cells is reported as a distribution plot and shows the velocity of a cell from one frame to the next for a population of cells. By taking into consideration only one cell A (Figure III-1b), its instantaneous velocity is computed as:

$$Cell\ A\ instantaneous\ velocity = \frac{v_{a1}+v_{a2}+v_{a2}+\cdots v_{an}}{n} \quad (2)$$

Where v_{an} is the velocity of cell A in the transition of each frame and n is the number of transitions between frames (Figure III-1b). Differently, the mean velocity is plotted as a line graph of the mean of the instantaneous velocities of all cells in a frame. In each frame, the velocity is computed as:

$$\frac{v_{a1}+v_{b1}+v_{a2}+\cdots v_{k1}}{k} \quad (3)$$

Where v is the velocity of the cell and K is the number of cells (Figure III-1c). Due to the calculation method, the first frame has a velocity of 0. The extracted data were processed using a Savitzky-Golay filter.
The Confinement Ratio is reported as a distribution plot of the track averaged confinement ratio of each track and is defined as:

$$\text{Confinement ratio } = \frac{d}{p} \times \sqrt{t} \quad (4)$$

Where d is displacement between the initial and final point (Figure III-1d).
The displacement is reported as a spider graph of up to the first 50 tracks of a data series, where the position is plotted on the X-Y Axis. The first track is defined as the track whose first feature is the earliest in the experiment.

III.2.2 Results and discussion

The cell physiologically adapts to changes in the microenvironment, mainly by varying its shape. The shape of the cells is usually a measure of their state in terms of cell growth, cycle and metabolism[56]. To gain insight into the cellular interactions of Lipid-Polymer NPs, we interrogated cell population and single cell for 48 h in contact with LiPoNs formulations with the live imaging instrument.

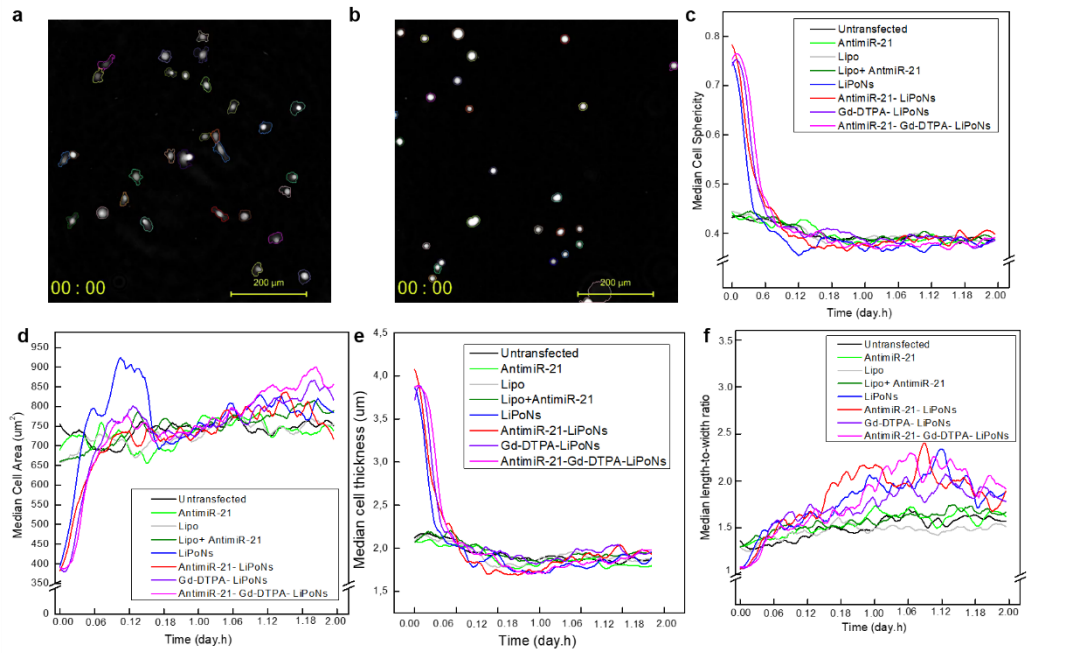

Figure III-2. Analysis of the morphology of MDA-MB-231 cells for 48 h. The MDA-MB-231 cells were treated with different LiPoNs (lipids conc. 12ug/mL), AntimiR-21, Lipofectamine (Lipo), AntimiR-21 mediated transfection with Lipofectamine (Lipo+AntimiR-21). The image of (**a**) untrasfected and (**b**) treated cells with AntimiR-21-LiPoNs at initial timepoint. The cells were imaged every 18 min in Quantitative Phase Imaging (QPI) and segmented automatically to quantify the median cell sphericity (**c**), median cell area (**d**), median cell thickness (**e**) and median length-to-width ratio (**f**).

Figure III-2 displays extracted segmented images of untransfected cells(Figure III-2a) and cells treated with AntimiR-21-LiPoNs formulation (Figure III-2b) from the Quantitative Phase Imaging modality. There is visual evidence of morphological changes in treated cells with respect to control cells (untransfected) upon interaction with AntimiR-21-LiPoNs (t=0). This rounding was mainly observed in the first hours of treatment and it was quantified in terms of median cell sphericity in Figure III-2c. This cell sphericity was almost doubled for treated cells compared to the control at intial time (t=0), and it progressively disappeared in 6 hours (Figure III-2c). This change in cell morphology was detected for all the LiPoNs formulations. Differently, the AntimiR-21 alone and transfected with the Lipofectamine ((Lipo+AntimiR-21) did not induce any alterations in cell shape. In this transitory phase (first few hours) for LiPoNs formulations, the area of treated cells is lower than untransfected cells, whiletheir thickness is greater as reported in figure III-2d,e. The rise in cell thickness could be linked to the detachment of cell protrusions. Upon changes in the microenvironment for the LiPoNs treatment, the cytoskeleton could be fluidized to reduce the stiffness of cells. Indeed, a cell's deformability and integrity are mainly controlled by the actin filaments of the cytoskeleton, which could be interested at several levels [38, 44]. Evidences of NPs interaction with structural components of cells were already reported,

but it is still unclear how role the intracellular trafficking of the NPs plays within this interaction [2], especially for organic NPs[10]. Despite the NPs' transport from the microenvironment to the cellular compartment, being encapsulated inside endosomes and lysosomes, there is evidence of their interaction with cytoskeletal protein[10]. Qin et al.[46] reported a reduction in the number and length of filipodia of breast cancer cells upon the interaction with fullerenol NPs. In accordance, Subbiah et al.[45] observed a morphological change in cell morphology, becoming more rounded, upon the interaction of PVA-coated hybrid NPs. Furthermore, Devendran et al.[57] reported an alteration of cell morphology upon treatment with acoustic fields that was likely linked to metabolic alteration. They hypothesized that cells actively exerted resistance by increasing structural stiffness, consequently increasing their metabolic activity. Recently, the effects of DMPC(1,2-dimyristoyl-sn-glycero-3-phosphocholine) liposomes on the destabilization of cell membrane were reported[9], demostring the impact of tunning of lipid composition on cellular interface.

Interestingly, the cells treated with LiPoNs formulations appeared to acquire a more elongated shape in time as reported by the length-to-width ratio graph (Figure III-2f) and this phenomenon was mostly evident after 1 day of contact with NPs. Maybe this cell behaviour could be linked to the dynamic nature of the cells, which convert an external stimuli, like microenvironmental changes, into biological response[10] such as the reduction of cell divisions leading to a sustained cellular spreading over time.

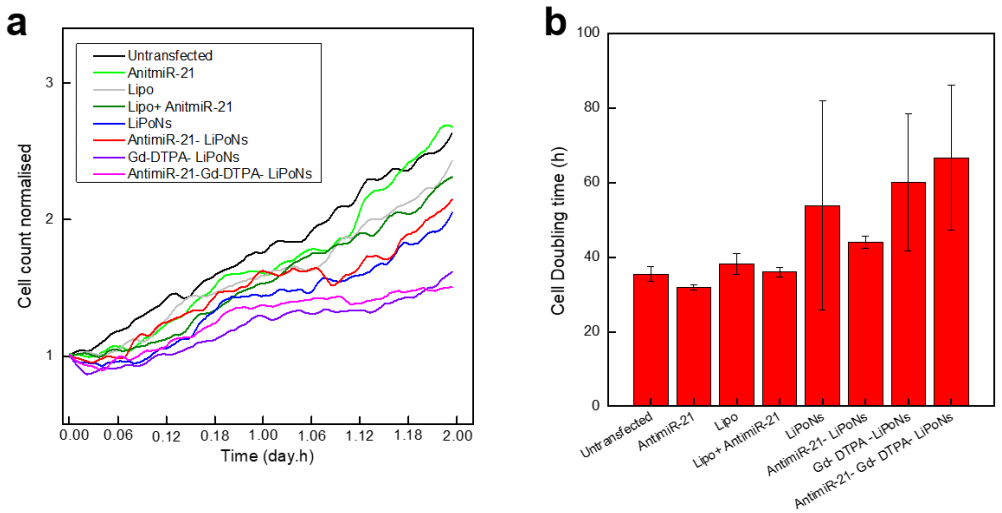

Figure III-3. Analysis of the proliferation of MDA-MB-231 cells. The MDA-MB-231 cells were treated with different LiPoNs (lipids conc. 12ug/mL), AntimiR-21, Lipofectamine, AntimiR-21 mediated transfection with Lipofectamine (Lipo+AntimiR-21). The cells were imaged every 18 min in Quantitative Phase Imaging (QPI) and segmented automatically to quantify cell count normalised (**a**) and the cell doubling time (**b**).

Considering the direct interplay that occurs between cellular structures and their biological function, the proliferation of cells upon NPs treatment was investigated in terms of normalised cell count, cell doubling, mitotic index and mitotic time (Figure III-3-4). Figure III-3a,b shows that the LiPoNs treatment had reduced the cell proliferation rate and increased the cell doubling time. In contrast to the linear increase over time of the normalised cell count for untransfected cells, the cells treated with LiPoNs formulations reported a discontinuous increase in the cell count showing a burst increase between 18 h and 24 h, followed by a more plateau-like profile (figure III-3a). It increased again almost after 48 h. In fact, by analysing the time needed to double the cell population, and cell doubling time, the untransfected cells needed 35 ± 2 h, while cells treated with LiPoNs required 53 ± 28 h. The cells treated with AntimiR-21-LiPoNs and AntimiR-Gd-DTPA-LiPoNs reported a doubling time of 42 h± 5 h and 67± 19 h, respectively. These results confirmed the hypothesis of a reduction in cell proliferation for cells treated with LiPoNs.

However, the mitotic index, that records the percentage of cells within the population undergoing mitosis, and the mitotic time, remained almost constant for a treat and untreated cells (Figure III-4a,b). For the mitotic time, a little increase is reported for the cells treated with Lipofectamine, AntimiR-21 transfection mediated with Lipofectamine and AntimiR-21-Gd-DTPA-LiPoNs. The maximum value for the mitotic index for cells treated with LiPoNs was reported at t=0, because the instrument identified as a mitotic event the rounding up of cells in the first few hours. To sum up, the LiPoNs interaction with cells seemed to slow down the cell functions but did not affect the cell capability of undergoing a mitotic event.

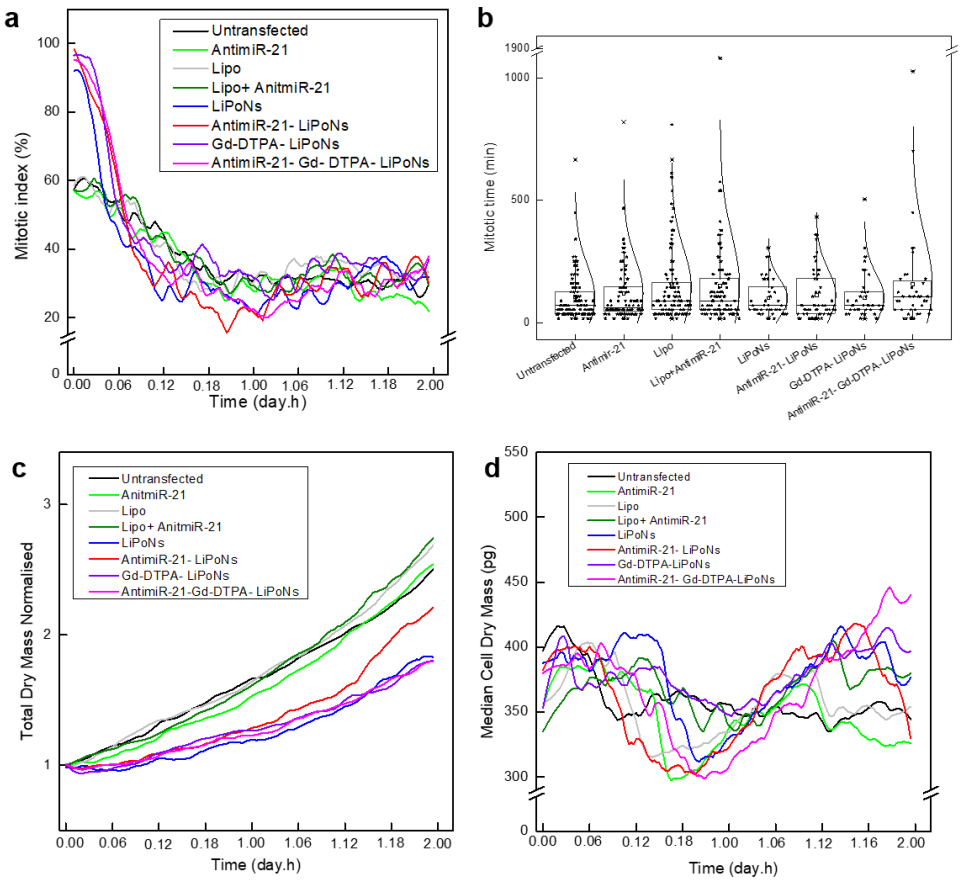

Figure III-4. Analysis of the mitosis of MDA-MB-231 cells treated with LiPoNs. The MDA-MB-231 cells were treated with different LiPoNs (lipids conc. 12ug/mL), AntimiR-21, Lipofectamine, AntimiR-21 mediated transfection with Lipofectamine (Lipo+AntimiR-21). The cells were imaged every 18 min in Quantitative Phase Imaging (QPI) and segmented automatically to quantify the mitotic index(**a**), mitotic time(**b**), total dry mass normalised (**c**) and median cell dry mass (**d**).

Different from cell proliferation, that is the increase in the number of cells over time due to cell division, cell growth is the process by which cells accumulate mass[58]. The cellular dry mas is a metric unique to QPI and represents the total mass of all cellular components, including proteins, lipids, carbohydrates and DNA, but excluding water[59]. The cell dry-mass changes could be described as the sum of biosynthesis, degradation, uptake or secretion of components[56, 60]. The interactions between cell proliferation and cell growth pathways are complex, but these processes can operate independently under certain conditions. Indeed, abnormal accumulation of cell dry mass has been associated to the development of diseases [61] while hyperproliferation has a role on progression of cancers[62]. In the case of muscle cell hypertrophy, the cells grow without dividing, differently during an embryo cleavage, the cells can proliferate without growing. The total

dry mass of all cells in a field of view is the sum of the effects of individual cell growth, divisions and proliferation of the entire population of cells (Figure III-4 c).

In order to quantify the rate of cell death or proliferation, the normalized dry mass (normalised to total dry mass at first acquisition) of the population was calculated at each time point (Figure III-4c). Treating the cells with LiPoNs resulted in an increase in relative normalised dry mass of 1.2 at 24 hours and 1.8 at 48 hours, whereas in the untreated cells an increase is observed of 1.6 at 24 h and 2.5 at 48 h. Noteworthy, the normalised dry mass doubled following the overmentioned doubling time for untransfected and treated cells, reporting a delay in cells upon LiPoNs treatment. The cells treated with AntimiR-21 alone or mediated-transfection did not display any difference in cell normalised dry mass (Figure III-4c).

Generally, during a cell cycle, the dry mass of single cell increases in time during cell growth and suddenly decreases upon the mitosis event, where a single cell becomes two daughter cells. Conversely, during cell death, the dry mass does not increase, but once the membrane is compromised, the cell loses mass. This dry mass evolution linked to cell entry in mitosis explains the rapid exchange in median cell dry mass evolution for both treated and untreated cells (Figure III-4c). Recently, Miettinen et al[60]. monitored the dry mass of L1210 cells throughout multiple cell cycle and reported a cellular loss of dry mass following the entry in mitotic entry. This loss in dry mass of cells, ranging from 4%-8%, is a transitory phase in early mitosis, followed by a rapid recovery. It is partially dependent on exocytosis of lysosomes and acts as a restartfor daughter cells having less useless contents[60]. Even if no relevant changes in the cell dry mass for both treated and untreated cells were detached, a zoom on median cell dry mass evolution in time showed two distinctive profiles for control and treated cells. In detail, the untransfected cells showed a decrease in mdian the cells' dry mass after 10 hours (Figure III-4d). Differently, the cells treated with LiPoNs formulations showed the minimum with different intensities after 18 hours. This delay could be linked to the transitory phase affecting the cells in the first hours(Figure III-4d). However, this detectable difference in the profile minimum of treated cells with respect to the untrasfected cells could be explained as an overall cell divisions process that the cells were undergoing. The hypothesis that the reduction of the cells' dry mass is due to a collective cell division is supported by the comparison between the data of the reduction of cell area, the increase of cell count and the maximum for the mitotic index, for cells treated with LiPoNs formulations,in period of interest (18-24 h). In accordance, the data with the total dry mass of the cell population over time, (Figure III-4d) reported an overall decrease of total cell dry mass normalized between 12-18 h, followed by an almost linear increase in the next hours. Moreover, a significant degree of non-genetic cell-to-cell variability in cell regulation of mitotic cell mass, that is not related to unsuccessful cell division, was already reported by Miettinen et al.[60]. Also the cells treated with lipofectamine, AntimiR-21 alone and with the lipofectamine reported this decrease in the cell dry mass. Therefore, the change in the cells' dry mass could not be directly linked to NPs uptake but to cell synchronization.

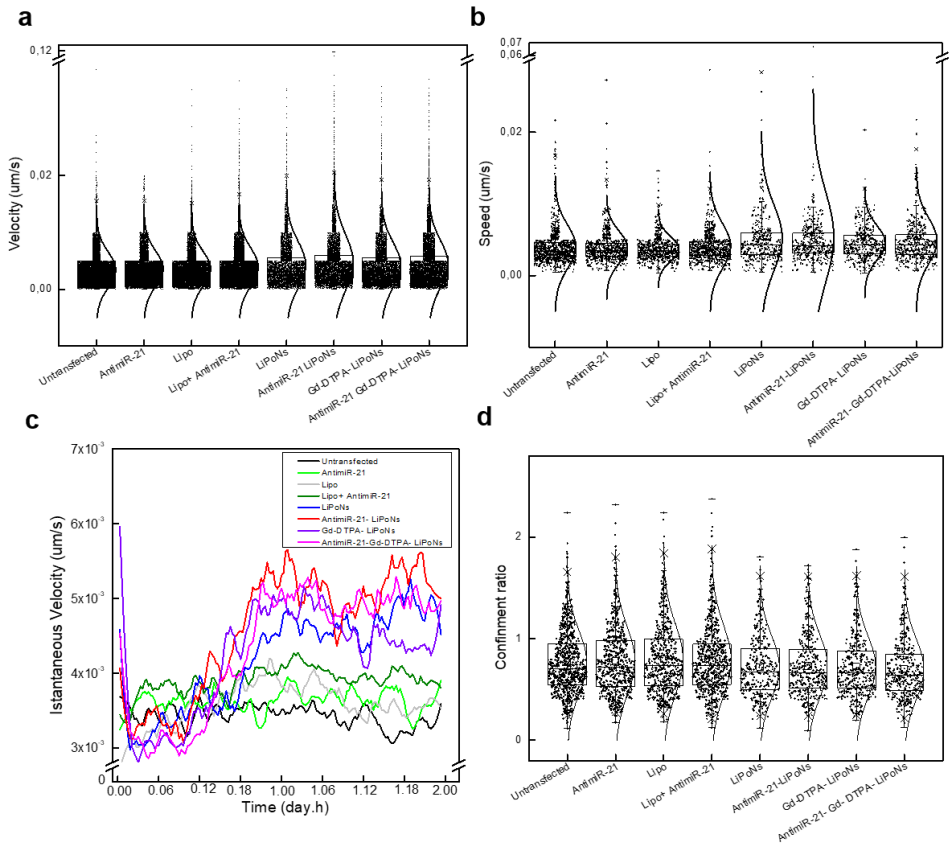

Figure III-5. Analysis of the motility of MDA-MB-231 cells treated with LiPoNs. The MDA-MB-231 cells were treated with different LiPoNs (lipids conc. 12ug/mL), AntimiR-21, Lipofectamine, AntimiR-21 mediated transfection with Lipofectamine (Lipo+AntimiR-21). The cells were imaged every 18 min in Quantitative Phase Imaging (QPI) and segmented automatically to quantify the track speed(**a**), velocity (**b**), instantaneous velocity (**e**) and confinement ratio(**d**).

In cells the cytoskeleton, particularly microtubules and microfilaments have dual functions, dynamically maintaining cell shape and enabling cell motility. We analysed the possible random cell motility in terms of average velocity, instantaneous velocity, track speed and confinement ratio following the observation of rounding of cells upon NPs treatment (Figure III-5). Figure III-5a shows the velocity of a cell from one frame to the next for a population of cells in a distribution plot. In detail, the velocity for each cell is computed as the sum of velocity from one frame to the other (18 min) over *n,* that is the number of transitions between frames in the cell timeline. No evident difference between untransfected and treated cells was observed. A slight increase in the cell speed was observed, as reported in the distribution plot Figure III- 5b, where the track speed is calculated by dividing the total distance travelled by the lifetime of the track. By computing the line graph of the mean of the instantaneous velocities of all cells in a frame, we

observed that the velocity in the first hours was almost zero due to the transitory phase affecting the cells, followed by a rapid increase in cell velocity at 24 hours for cells treated with LiPoNs formulations with respect to untransfected ones or the ones treated with AntimiR-21 alone and in combination with Lipofectamine. Interestingly, in the same time frame, the length-to-width ratio increased upon the treatment with LiPoNs formulations (Figure III-3f). This behaviour could be linked to delay in the cell divisions, as confirmed by the plateau in the cell count normalised and median cell dry mass, so leading the cells to the possibility to endure as single cells, preserve the cell shape and not reduce their velocity for the cellular division. In accordance with this velocity increase, the cells appeared slightly less confined as indicated by the distribution plot of the confinement ratio (Figure III- 5d). The cell's confinement represents the distance of a cell migration with respect to its point of origin, while the displacement graph considers the degree to which a cell meanders from its starting and end point. The spider graph reports up to the first 50 tracks of a data series on the position on the X-Y Axis of the cell, showing no directionality in displacement for both untransfected and treated cells (Figure III- 6). The cytoskeleton, the changes in cell adhesion and the expression of cell-migration-related proteins mainly control the motility of cells. Several studies reported a reduction in cell motility and invasion after the exposure to NPs[63, 64]. On the contrary, few studies[65] showed the opposite effect of gold NPs on cell invasion, mainly linked to an increase in the metalloproteinase9 upon NPs cell interaction. In any case, alteration to cell motility could be linked to a change in cell stiffness[10], but it is not clear why the cells treated with LiPoNs increased their average velocity.

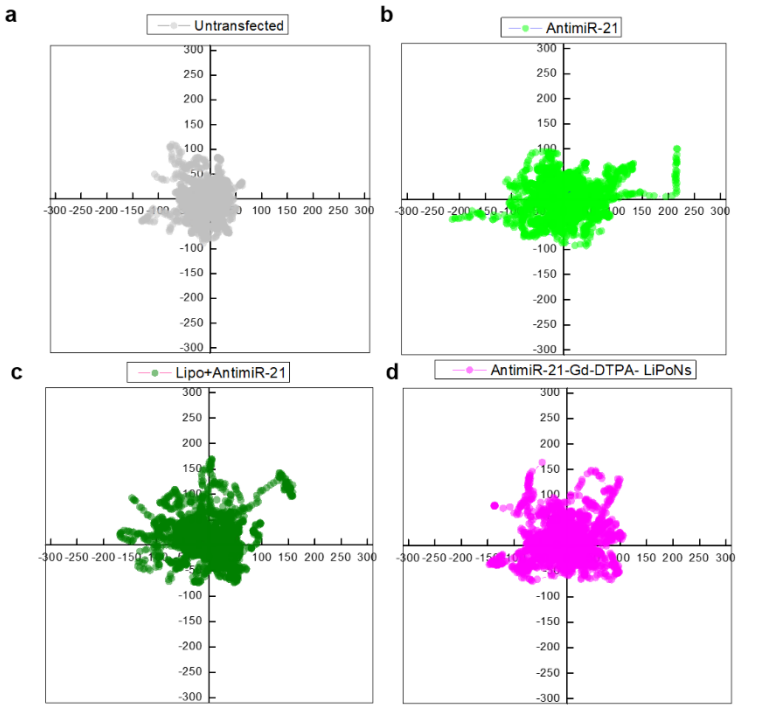

Figure III-6. Analysis of the displacement of MDA-MB-231 cells treated with LiPoNs. The MDA-MB-231 cells were treated with (**a**) Untrasfected cells and cells treated with AntimiR-21 (**b**), AntimiR-21 transfection mediated with Lipofectamine(**c**) and AntimiR-21-Gd-DTPa-LiPoNs (**d**).

The AntimiR-21 loaded LiPoNs reported a different cell behaviour with respect to untransfected cells and cells transfected with Lipofectamine. Nevertheless, it was impossible to distinguish the effect of LiPoNs-mediated delivery of AnitimiR-21 with respect to the blank LiPoNs. We observed a similar cellular behaviour, in terms of cell morphology, proliferation and motility, among all the LiPoNs formulations, with no changes reported for the AntimiR-21-LiPoNs. However, the cells were observed for 48 h, differently, the data on gene relations upon microRNA treatments were performed after 72 h of contact (Chapter II). Maybe the difference could be observed for a longer time. No changes in cell proliferation were reported by MTT assay in previous chapters, confirming the lack of cytotoxicity of LiPoNs. Recently, a similar effect on the cell behaviour of MSCs, MG63, and HaCaT cells, was reported by Devendran and co-workers[57]. Upon acoustic exposure, they observed that the cells prevented cell adhesion and changed their morphology with no differences in live/dead assays. They linked these changes to increased cell resistance to the external stimuli, maybe correlated to cell metabolism. In our case, the cells may alter their stiffness upon interactions with LiPoNs leading to an alteration of cellular biological response. However, Devendran et al. reported a huge variability in this correlation between cell lines and exposure conditions. Therefore, further investigations are required to understand the cell-LiPoNs interaction and the reason for this cellular response.

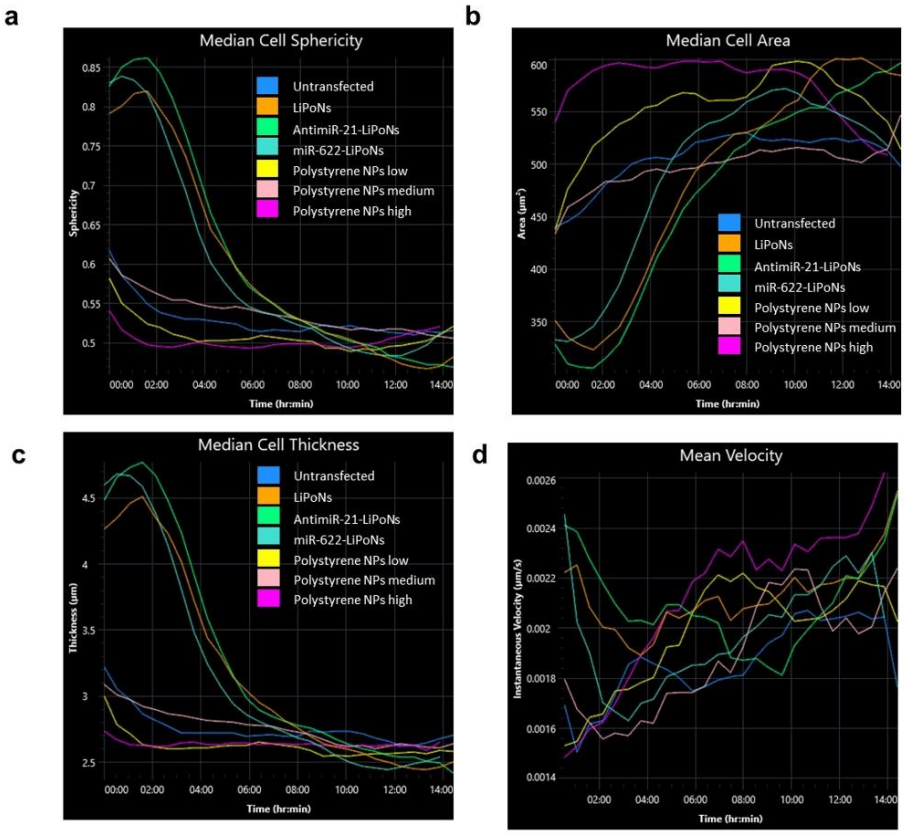

Figure III-7. Analysis of the morphology of MDA-MB-231 cells for 14 h. The MDA-MB-231 cells were treated with different LiPoNs formulations (lipids conc. 12ug/mL) and three different polystyrene NPs concentration. The cells were imaged in Quantitative Phase Imaging (QPI) and segmented automatically to quantify the median cell sphericity (**a**), median cell area (**b**), median cell thickness (**c)** and instantaneous velocity (**d**).

We reported how any changes in cell morphology, proliferation and motility could be induced by the nano-bio interactions of LiPoNs. To verify the active role of LiPoNs in mediating these cellular alterations, we performed a comparative study with commercially available NPs, like polystyrene. Indeed, polystyrene NPs are commercial NPs widely used as model NPs to study the NP-cell interactions. We tested three different concentrations of polystyrene NPs of 100 nm around at 1 $*10^7$ (low), $2*10^7$ (high) and $3*10^7$ NPs/mL (high) compared to LiPoNs (around $3*10^8$ NPs/mL). We studied the cell median sphericity, area, thickness and instantaneous velocity for 14 h (Figure III-7). The results confirmed the abovementioned findings about the cells' morphological changes upon LiPoNs interactions. Differently, the cells treated with Polystyrene NPs did not report any alteration in median cell sphericity, area or thickness, confirming the role of materials in altering the cell response (Figure III-7a-c). We observed an increase in the instantaneous velocity around 14 h for the LiPoNs and for a high concentration of polystyrene NPs (Figure III-7d). However, the limited observation window (14 h) did not allow to follow a complete increase in the

instantaneous velocity of the cells. Indeed, in Figure III-5c, the cells displayed an average velocity of around $5*10^{-3}$ um/s upon 20 hours of incubations with LiPoNs. Therefore, the 14 h of observations were insufficient to observe the cell behaviour regarding motility for both the LiPoNs and Polystyrene NPsWe reported how any changes of cell morphology, proliferation and motility could be induced by the nano-bio interactions of LiPoNs.

III.3 CONCLUSIONS

Massive efforts have been made to find a relationship between NPs' synthetic properties, including size, charge, shape, rigidity and surface coating, and cell internalization pathways[2, 9, 10]. Many researchers have limited their attention to evaluating of these internalization mechanisms on cell biological response, mainly as cytotoxicity. However, the capability of these NP-cell interactions to impact and alter cell physiology emerged in several studies [4]. In the same direction, the results on alteration of cell morphology, motility and proliferation upon interaction with LiPoNs, display the nanomaterials impact on cell machinery. To summarize, it was observed that LiPoNs induced a spherical morphology in cells at t=0 that progressively disappeared in time. Cell rounding was associated with increased cell thickness, maybe due to cell detachment. Downstream to this transitory phase, the cells had a similar morphology to the untransfected cells, except for the width-to-length ratio. As a consequence of this transitory phase, the cells reduced the rates of growth and proliferation, as shown by the increase in doubling time, reduction in cell count and slow increase in the total dry mass. However, they did not lose the capability of undergoing mitotic events. Indeed, a huge difference in mitotic index between the treated and untreated cells is not reported. Interestingly, the cells increased random motility in terms of average instantaneous velocity over a longer time. Finally, the cells treated with LiPoNs changed their morphology and seemed to slow down their functions, but the negative or positive effect of this alteration in the treatment of the cells is not clear. Interestingly, these cellular alterations were not detected for standard NPs, like polystyrene NPs, confirming that were specific cellular pathways induced by the materials in the form of LiPoNs.

This void of knowledge could have unexplored beneficial effects. A transient condition of cells could be exploited to design and open new possibilities in drug delivery, improving cargo internalization. He et al.[66] reported an increase in cellular uptake of EGFP-R8 and dextran following disruption of actin organisation in skin epithelial cells.

III.4 REFERENCES

[1] Y. Shi, M.J. Cai, L.L. Zhou, H.D. Wang, The structure and function of cell membranes studied by atomic force microscopy, Seminars in Cell & Developmental Biology 73 (2018) 31-44.
[2] S. Behzadi, V. Serpooshan, W. Tao, M.A. Hamaly, M.Y. Alkawareek, E.C. Dreaden, D. Brown, A.M. Alkilany, O.C. Farokhzad, M. Mahmoudi, Cellular uptake of nanoparticles: journey inside the cell, Chemical Society Reviews 46(14) (2017) 4218-4244.
[3] K. Sugano, M. Kansy, P. Artursson, A. Avdeef, S. Bendels, L. Di, G.F. Ecker, B. Faller, H. Fischer, G. Gerebtzoff, H. Lennernaes, F. Senner, Coexistence of passive and carrier-mediated processes in drug transport, Nature Reviews Drug Discovery 9(8) (2010) 597-614.
[4] R. Augustine, A. Hasan, R. Primavera, R.J. Wilson, A.S. Thakor, B.D. Kevadiya, Cellular uptake and retention of nanoparticles: Insights on particle properties and interaction with cellular components, Materials Today Communications 25 (2020).
[5] N. Aibani, R. Rai, P. Patel, G. Cuddihy, E.K. Wasan, Chitosan Nanoparticles at the Biological Interface: Implications for Drug Delivery, Pharmaceutics 13(10) (2021).
[6] A. Panariti, G. Miserocchi, I. Rivolta, The effect of nanoparticle uptake on cellular behavior: disrupting or enabling functions?, Nanotechnology Science and Applications 5 (2012) 87-100.
[7] I. Rivolta, A. Panariti, B. Lettiero, S. Sesana, P. Gasco, M.R. Gasco, M. Masserini, G. Miserocchi, CELLULAR UPTAKE OF COUMARIN-6 AS A MODEL DRUG LOADED IN SOLID LIPID NANOPARTICLES, Journal of Physiology and Pharmacology 62(1) (2011) 45-53.
[8] D. Montizaan, K.N. Yang, C. Reker-Smit, A. Salvati, Comparison of the uptake mechanisms of zwitterionic and negatively charged liposomes by HeLa cells', Nanomedicine-Nanotechnology Biology and Medicine 30 (2020).
[9] H. Abumanhal-Masarweh, D. da Silva, M. Poley, A. Zinger, E. Goldman, N. Krinsky, R. Kleiner, G. Shenbach, J.E. Schroeder, J. Shklover, J. Shainsky-Roitman, A. Schroeder, Tailoring the lipid composition of nanoparticles modulates their cellular uptake and affects the viability of triple negative breast cancer cells, Journal of Controlled Release 307 (2019) 331-341.
[10] A.S. Kashani, M. Packirisamy, Cancer-Nano-Interaction: From Cellular Uptake to Mechanobiological Responses, International Journal of Molecular Sciences 22(17) (2021).
[11] P. Foroozandeh, A.A. Aziz, Insight into Cellular Uptake and Intracellular Trafficking of Nanoparticles, Nanoscale Research Letters 13 (2018).
[12] S. Mayor, R.E. Pagano, Pathways of clathrin-independent endocytosis, Nature Reviews Molecular Cell Biology 8(8) (2007) 603-612.
[13] K. Tahara, H. Yamamoto, N. Hirashima, Y. Kawashima, Chitosan-modified poly(D,L-lactide-co-glycolide) nanospheres for improving siRNA delivery and gene-silencing effects, European Journal of Pharmaceutics and Biopharmaceutics 74(3) (2010) 421-426.
[14] S.N. Tammam, H.M.E. Azzazy, H.G. Breitinger, A. Lamprecht, Chitosan Nanoparticles for Nuclear Targeting: The Effect of Nanoparticle Size and Nuclear Localization Sequence Density, Molecular Pharmaceutics 12(12) (2015) 4277-4289.

[15] Y. Jiang, S.D. Huo, T. Mizuhara, R. Das, Y.W. Lee, S. Hou, D.F. Moyano, B. Duncan, X.J. Liang, V.M. Rotello, The Interplay of Size and Surface Functionality on the Cellular Uptake of Sub-10 nm Gold Nanoparticles, Acs Nano 9(10) (2015) 9986-9993.
[16] S. Jeon, J. Clavadetscher, D.K. Lee, S.V. Chankeshwara, M. Bradley, W.S. Cho, Surface Charge-Dependent Cellular Uptake of Polystyrene Nanoparticles, Nanomaterials 8(12) (2018).
[17] Y. Li, N. Gu, Thermodynamics of Charged Nanoparticle Adsorption on Charge-Neutral Membranes: A Simulation Study, Journal of Physical Chemistry B 114(8) (2010) 2749-2754.
[18] M.T. Zhu, G.J. Nie, H. Meng, T. Xia, A. Nel, Y.L. Zhao, Physicochemical Properties Determine Nanomaterial Cellular Uptake, Transport, and Fate, Accounts of Chemical Research 46(3) (2013) 622-631.
[19] J. Dausend, A. Musyanovych, M. Dass, P. Walther, H. Schrezenmeier, K. Landfester, V. Mailander, Uptake Mechanism of Oppositely Charged Fluorescent Nanoparticles in HeLa Cells, Macromolecular Bioscience 8(12) (2008) 1135-1143.
[20] Z.G. Yue, W. Wei, P.P. Lv, H. Yue, L.Y. Wang, Z.G. Su, G.H. Ma, Surface Charge Affects Cellular Uptake and Intracellular Trafficking of Chitosan-Based Nanoparticles, Biomacromolecules 12(7) (2011) 2440-2446.
[21] J.H. Kang, W.Y. Jang, Y.T. Ko, The Effect of Surface Charges on the Cellular Uptake of Liposomes Investigated by Live Cell Imaging, Pharmaceutical Research 34(4) (2017) 704-717.
[22] X.P. Xie, J.F. Liao, X.R. Shao, Q.S. Li, Y.F. Lin, The Effect of shape on Cellular Uptake of Gold Nanoparticles in the forms of Stars, Rods, and Triangles, Scientific Reports 7 (2017).
[23] H. Herd, N. Daum, A.T. Jones, H. Huwer, H. Ghandehari, C.M. Lehr, Nanoparticle Geometry and Surface Orientation Influence Mode of Cellular Uptake, Acs Nano 7(3) (2013) 1961-1973.
[24] S.E.A. Gratton, P.A. Ropp, P.D. Pohlhaus, J.C. Luft, V.J. Madden, M.E. Napier, J.M. DeSimone, The effect of particle design on cellular internalization pathways, Proceedings of the National Academy of Sciences of the United States of America 105(33) (2008) 11613-11618.
[25] B.D. Chithrani, W.C.W. Chan, Elucidating the mechanism of cellular uptake and removal of protein-coated gold nanoparticles of different sizes and shapes, Nano Letters 7(6) (2007) 1542-1550.
[26] B.D. Chithrani, A.A. Ghazani, W.C.W. Chan, Determining the size and shape dependence of gold nanoparticle uptake into mammalian cells, Nano Letters 6(4) (2006) 662-668.
[27] Y. Hui, X. Yi, F. Hou, D. Wibowo, F. Zhang, D.Y. Zhao, H.J. Gao, C.X. Zhao, Role of Nanoparticle Mechanical Properties in Cancer Drug Delivery, Acs Nano 13(7) (2019) 7410-7424.
[28] P. Guo, D.X. Liu, K. Subramanyam, B.R. Wang, J. Yang, J. Huang, D.T. Auguste, M.A. Moses, Nanoparticle elasticity directs tumor uptake, Nature Communications 9 (2018).
[29] J.S. Sun, L. Zhang, J.L. Wang, Q. Feng, D.B. Liu, Q.F. Yin, D.Y. Xu, Y.J. Wei, B.Q. Ding, X.H. Shi, X.Y. Jiang, Tunable Rigidity of (Polymeric Core)-(Lipid Shell) Nanoparticles for Regulated Cellular Uptake, Advanced Materials 27(8) (2015) 1402-+.

[30] A.C. Anselmo, M.W. Zhang, S. Kumar, D.R. Vogus, S. Menegatti, M.E. Helgeson, S. Mitragotri, Elasticity of Nanopartides Influences Their Blood Circulation, Phagocytosis, Endocytosis, and Targeting, Acs Nano 9(3) (2015) 3169-3177.
[31] M. Ghasemi, T. Turnbull, S. Sebastian, I. Kempson, The MTT Assay: Utility, Limitations, Pitfalls, and Interpretation in Bulk and Single-Cell Analysis, International Journal of Molecular Sciences 22(23) (2021).
[32] B. Drasler, P. Sayre, K.G. Steinhauser, A. Petri-Fink, B. Rothen-Rutishauser, In vitro approaches to assess the hazard of nanomaterials, Nanoimpact 8 (2017) 99-116.
[33] C.W. Gourlay, K.R. Ayscough, The actin cytoskeleton: a key regulator of apoptosis and ageing?, Nature Reviews Molecular Cell Biology 6(7) (2005) 583-U5.
[34] D.A. Fletcher, D. Mullins, Cell mechanics and the cytoskeleton, Nature 463(7280) (2010) 485-492.
[35] X.Y. Wu, Y.B. Tan, H. Mao, M.M. Zhang, Toxic effects of iron oxide nanoparticles on human umbilical vein endothelial cells, International Journal of Nanomedicine 5 (2010) 385-399.
[36] N. Singh, G.J.S. Jenkins, R. Asadi, S.H. Doak, Potential toxicity of superparamagnetic iron oxide nanoparticles (SPION), Nano Reviews & Experiments 1(1) (2010).
[37] M.R.K. Ali, Y. Wu, Y. Tang, H.P. Xiao, K.C. Chen, T.G. Han, N. Fang, R.H. Wu, M.A. El-Sayed, Targeting cancer cell integrins using gold nanorods in photothermal therapy inhibits migration through affecting cytoskeletal proteins, Proceedings of the National Academy of Sciences of the United States of America 114(28) (2017) E5655-E5663.
[38] H.K. Patra, S. Banerjee, U. Chaudhuri, P. Lahiri, A.K. Dasgupta, Cell selective response to gold nanoparticles, Nanomedicine-Nanotechnology Biology and Medicine 3(2) (2007) 111-119.
[39] C.P. Brangwynne, G.H. Koenderink, F.C. MacKintosh, D.A. Weitz, Intracellular transport by active diffusion, Trends in Cell Biology 19(9) (2009) 423-427.
[40] S.K. Chakraborty, J.A.J. Fitzpatrick, J.A. Phillippi, S. Andreko, A.S. Waggoner, M.P. Bruchez, B. Ballou, Cholera toxin B conjugated quantum dots for live cell Labeling, Nano Letters 7(9) (2007) 2618-2626.
[41] S.K. Lai, K. Hida, C. Chen, J. Hanes, Characterization of the intracellular dynamics of a non-degradative pathway accessed by polymer nanoparticles, Journal of Controlled Release 125(2) (2008) 107-111.
[42] I. Rivolta, A. Panariti, M. Collini, B. Lettiero, L. D'Alfonso, L. Sironi, G. Miserocchi, G. Chirico, A biophysical model of intracellular distribution and perinuclear accumulation of particulate matter, Biophysical Chemistry 158(2-3) (2011) 134-140.
[43] M. Lundqvist, J. Stigler, T. Cedervall, T. Berggard, M.B. Flanagan, I. Lynch, G. Elia, K. Dawson, The Evolution of the Protein Corona around Nanoparticles: A Test Study, Acs Nano 5(9) (2011) 7503-7509.
[44] K. Kralovec, L. Melounkova, M. Slovakova, N. Mannova, M. Sedlak, J. Bartacek, R. Havelek, Disruption of Cell Adhesion and Cytoskeletal Networks by Thiol-Functionalized Silica-Coated Iron Oxide Nanoparticles, International Journal of Molecular Sciences 21(24) (2020).

[45] R. Subbiah, S. Ramasundaram, P. Du, K. Hyojin, D. Sung, K. Park, N.E. Lee, K. Yun, K.J. Choi, Evaluation of cytotoxicity, biophysics and biomechanics of cells treated with functionalized hybrid nanomaterials, Journal of the Royal Society Interface 10(88) (2013).
[46] Y.X. Qin, K. Chen, W.H. Gu, X.H. Dong, R.H. Lei, Y.N. Chang, X. Bai, S.B. Xia, L. Zeng, J.X. Zhang, S.H. Ma, J. Li, S. Li, G.M. Xing, Small size fullerenol nanoparticles suppress lung metastasis of breast cancer cell by disrupting actin dynamics, Journal of Nanobiotechnology 16 (2018).
[47] O. Ispanixtlahuatl-Meraz, R.P.F. Schins, Y.I. Chirino, Cell type specific cytoskeleton disruption induced by engineered nanoparticles, Environmental Science-Nano 5(2) (2018) 228-245.
[48] P. Ruenraroengsak, A.T. Florence, Biphasic interactions between a cationic dendrimer and actin, Journal of Drug Targeting 18(10) (2010) 803-811.
[49] A.M. Scherbart, J. Langer, A. Bushmelev, D. van Berlo, P. Haberzettl, F.J. van Schooten, A.M. Schmidt, C.R. Rose, R.P.F. Schins, C. Albrecht, Contrasting macrophage activation by fine and ultrafine titanium dioxide particles is associated with different uptake mechanisms, Particle and Fibre Toxicology 8 (2011).
[50] H.J. Wang, A.C. Growcock, T.H. Tang, J. O'Hara, Y.W. Huang, R.S. Aronstam, Zinc oxide nanoparticle disruption of store-operated calcium entry in a muscarinic receptor signaling pathway, Toxicology in Vitro 24(7) (2010) 1953-1961.
[51] R.R. Arvizo, O.R. Miranda, M.A. Thompson, C.M. Pabelick, R. Bhattacharya, J.D. Robertson, V.M. Rotello, Y.S. Prakash, P. Mukherjee, Effect of Nanoparticle Surface Charge at the Plasma Membrane and Beyond, Nano Letters 10(7) (2010) 2543-2548.
[52] J.P. Decuypere, G. Bultynck, J.B. Parys, A dual role for Ca2+ in autophagy regulation, Cell Calcium 50(3) (2011) 242-250.
[53] D.N. Johnson-Lyles, K. Peifley, S. Lockett, B.W. Neun, M. Hansen, J. Clogston, S.T. Stern, S.E. McNeil, Fullerenol cytotoxicity in kidney cells is associated with cytoskeleton disruption, autophagic vacuole accumulation, and mitochondrial dysfunction, Toxicology and Applied Pharmacology 248(3) (2010) 249-258.
[54] S. Hughes, A.J. El Haj, J. Dobson, Magnetic micro- and nanoparticle mediated activation of mechanosensitive ion channels, Medical Engineering & Physics 27(9) (2005) 754-762.
[55] J. McCarthy, X. Gong, D. Nahirney, M. Duszyk, M.W. Radomski, Polystyrene nanoparticles activate ion transport in human airway epithelial cells, International Journal of Nanomedicine 6 (2011) 1343-1356.
[56] X.L. Liu, S. Oh, M.W. Kirschner, The uniformity and stability of cellular mass density in mammalian cell culture, Frontiers in Cell and Developmental Biology 10 (2022).
[57] C. Devendran, J. Carthew, J.E. Frith, A. Neild, Cell Adhesion, Morphology, and Metabolism Variation via Acoustic Exposure within Microfluidic Cell Handling Systems, Advanced Science 6(24) (2019).
[58] A.C. Lloyd, The Regulation of Cell Size, Cell 154(6) (2013) 1194-1205.
[59] S. Aknoun, J. Savatier, P. Bon, F. Galland, L. Abdeladim, B. Wattellier, S. Monneret, Living cell dry mass measurement using quantitative phase imaging with quadriwave lateral shearing interferometry: an accuracy and sensitivity discussion, Journal of Biomedical Optics 20(12) (2015).

[60] T.P. Miettinen, K.S. Ly, A. Lam, S.R. Manalis, Single-cell monitoring of dry mass and dry mass density reveals exocytosis of cellular dry contents in mitosis, Elife 11 (2022).
[61] P.B. Crino, mTOR Signaling in Epilepsy: Insights from Malformations of Cortical Development, Cold Spring Harbor Perspectives in Medicine 5(4) (2015).
[62] A.S. Alvarado, Cellular Hyperproliferation and Cancer as Evolutionary Variables, Current Biology 22(17) (2012) R772-R778.
[63] T. Zhou, M.F. Yu, B. Zhang, L.M. Wang, X.C. Wu, H.J. Zhou, Y.P. Du, J.F. Hao, Y.P. Tu, C.Y. Chen, T.T. Wei, Inhibition of Cancer Cell Migration by Gold Nanorods: Molecular Mechanisms and Implications for Cancer Therapy, Advanced Functional Materials 24(44) (2014) 6922-6932.
[64] Y.H. Hou, K.Y. Cai, J.H. Li, X.Y. Chen, M. Lai, Y. Hu, Z. Luo, X.W. Ding, D.W. Xu, Effects of titanium nanoparticles on adhesion, migration, proliferation, and differentiation of mesenchymal stem cells, International Journal of Nanomedicine 8 (2013) 3619-3630.
[65] Z.X. Liu, Y.C. Wu, Z.R. Guo, Y. Liu, Y.J. Shen, P. Zhou, X. Lu, Effects of Internalized Gold Nanoparticles with Respect to Cytotoxicity and Invasion Activity in Lung Cancer Cells, Plos One 9(6) (2014).
[66] L. He, E.J. Sayers, P. Watson, A.T. Jones, Contrasting roles for actin in the cellular uptake of cell penetrating peptide conjugates, Scientific Reports 8 (2018).

IV. CHAPTER IV– PRELIMINARY RESULTS OF IN VIVO DELIVERY OF LiPoNs LOADING miRNA

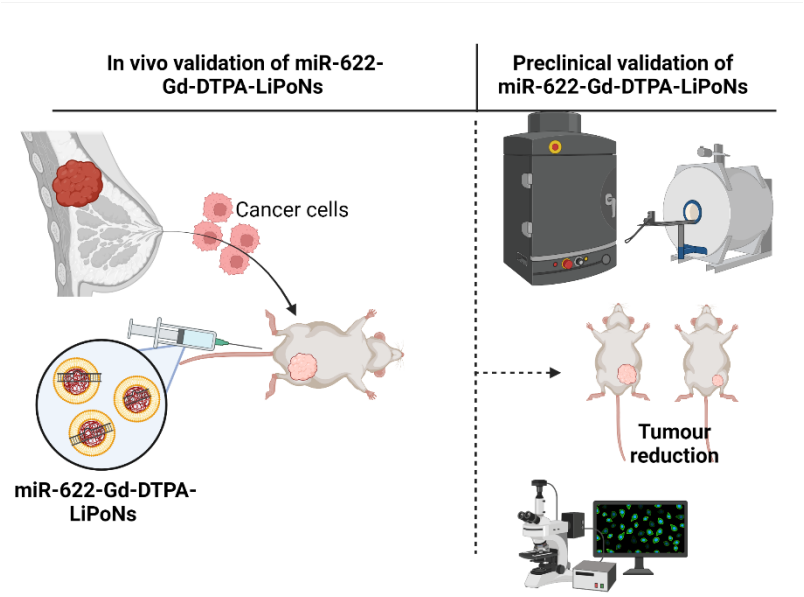

Graphical Abstract IV. In vivo validation of miR-622-Gd-DTPA-LiPoNs for Multimodal Imaging and Theranostic Applications

Abstract

The delivery of the therapeutic or diagnostic agents to the tumour site is a fundamental and crucial aspect of asses in new nanoformulations for cancer treatment. Indeed, upon intravenous administration, the sequential biological barriers encountered by NPs hinder a site-specific delivery of the cargo, limiting the therapeutic potential of the vectors. Here, we developed miR-622-Gd-DTPA-LiPoNs through the coupled Hydrodynamic flow focusing on treating and diagnosing Triple Negative Breast Cancer. We preliminary evaluated the ability of LiPoNs to target the tumour site and we estimated their antitumoral efficacy.

IV.1 BACKGROUND

IV.1.1 Introduction

Breast cancer is a malignant tumour that occurs due to abnormal proliferation of cells or tissue in or around the breast tissue, mainly in the mammary ducts and glands[1]. According to the Global Cancer Project 2018 (GLOBOCAN 2018), female breast cancer ranked as the second most commonly diagnosed cancer and the second leading cause of cancer-related death among woman (American society of cancer) [2].

The breast cancer is characterized by a high intertumoral and intratumoural heterogeneity. Currently, it is classified by six intrinsic molecular subtypes: luminal A, luminal B, normal-like, tumour enriched with human epidermal growth factor receptor 2 (Her2), basal-like and claudin-low subtype[3-5].
The luminal A is the most common subtype (50-60 % of total breast cancer type) characterized by the expression of estrogen receptor (ER), progesterone receptor (PR), Bcl-2 and absence of Her2[5, 6]. The above mentioned receptors (ER, PR and absence of Her2) characterize also the luminal B subtype, that can be distinguished from the luminal A subtype based on high Ki67 staining[7]. The treatments for both luminal A and luminal B subtypes target the ER signalling and consist in adjuvant endocrine therapy (tamoxifen and aromatase inhibitors). A similar clinical outcome to basal like and luminal A subtype characterizes the Normal-like subtype (only 5–10% of all breast carcinomas), which expresses ER, Her2 and PR receptors. The expression of Her2 gene distinguished the Her2 positive subtype (15–20% of all breast cancer). This breast cancer subtype is treated with trastuzumab and an antibody against Her2. However, a poor overall prognosis characterizes them. Basal-like breast cancer (10–20% of all breast carcinoma) does not express any of the three markers (ER, PR and Her) while Claudin-low breast cancer subtype (12–14 % of breast carciroma) shows low expression of claudin- 3, 4, 7, occluodin and E-cadherin with cancer stem like features[3, 8]. Both of them show a poor diagnosis and form the majority of triple-negative breast cancers (TNBCs)[9].

The TNBC accounts for 15 % of all breast tumours[10] and it is often distinguished by high histologic grade with central necrotic zones, pushing borders and fibrous cellular proliferation[11, 12]. Moreover, it is marked by blood vessels with variable size, perilobular lymphocytic infiltrate close to tumour tissue and lymphocytic inflammatory infiltrate in the tissue [13].

A breast cancer diagnosis is based on a triple test comprising the needle biopsy and clinical examination, usually mammography and/or ultrasonography and under specific conditions Magnetic Resonance Imaging- MRI is added[14]. In the initial mammography the TNBC is not detected in 18 % of cases despite its large size. On mammography, the TNBC is generally presented as circumscribed area without calcifications. To support the screening of patients at high risk, the ultrasonography imaging modality, characterized by an high sensitivity for TNBC (around 92-100 %) is combined to the mammography imaging[15]. At ultrasonography, the lesions appeared as mass with distinct margins and posterior acoustic

enhancement. MRI imaging is used when conventional imaging tests have been equivocal, for high risk patients and for treatments follow-up. On MRI imaging, the rim enhancement characterizes the TNBC lesions in the majority of cases (76%). The combination of the three techniques increases the sensitivity in detecting breast cancers, however there are still false-positive findings. [16]. Indeed most of TNBC are still detected for the pain of patients or as palpable masses and not detected early via imaging [17].

Patients with TNBC do not benefit from therapies that are designed to target the hormone receptors and HER-2 receptor-positive cancers, such as the estrogen receptor antagonist (Tamoxifen) and anti-HER-2 antibodies (Trastuzumab and Pertuzumab). Indeed, the TNBC is characterized by the exclusion of the expression and/or amplification of three biomarkers (estrogen receptor [ER], progesterone receptor [PR], and human epidermal growth factor receptor 2 [HER2], that make hormone therapy and HER2 drugs do not work.
The chemotherapy represents the standard of care for the treatment of TNBC with the selection of the therapeutic regimen according to the patient and disease related factors[18]. Currently, taxane, anthracycline, cyclophosphamide, cisplatin and fluorouracil-based combination chemotherapies are recommended for treating TNBC patients[19]. In early breast cancer, the chemotherapy is preferred in neoadjuvant setting, followed by surgery. If a complete pathological response (pCR) is not achieved, systemic therapy can be escalated by using adjuvant capecitabine. In advance cancer, for BRCA- associated TNBC, PARP inhibitor (olaparib or talazoparib) compared with monochemotherapy has reported promising results in terms of quality of life of patients. Differently, if the BRCA mutations are not present, the chemotherapy is still the suggested treatment[19]. Both in early and advanced stage of TNBC, the platinum drugs could be added to chemotherapy treatments[14, 20]. Moreover, these conventional treatments can be combined with capecitabine chemotherapy, bevacizumab and anti-VEGF monoclonal antibody bevacizumab[14, 21]. Among the promising strategies developed, poly-ADP ribose polymerase-1 inhibitors and immune checkpoints inhibitors can be mentioned[22, 23].
However, the intratumoral heterogeneity and histologic heterogeneity within an individual tumour pose a diagnostic dilemma and a therapeutic challenge when evaluating metastatic lesions[20, 23]. Therefore, the limited and unspecific treatments options for TNBC demonstrate an urgent clinical need to develop more personalized medicine.

A crucial role in tumour initiation and progression is exerted by the tumour microenvironment (TME), where abnormal vessels in structure and functions lead to hypo-perfusion conditions that ultimately create hypoxia. The hypoxia mediates the cancer metastasis, immune suppression and drug resistance. In the TME, to meet the oxygen and nutrients requests [24], there is the sprouting of new blood vessels (angiogenesis) combined with the growth of cancer cells around pre-existing vessels (co-option). The former vessels are characterized by high irregular architecture, not heterogenous spatial distribution (dilated and tortuous)[25], avascular spaces and large intracellular and intercellular openings (2 μm)[26]. This disorganized and tortuous vasculature network results in a plasma leakage into the interstitial space, increasing the viscous resistance to

blood flow. This effect combined with the geometrical resistance exerted by the abnormal vasculature, reduces the blood velocity of one order of magnitude in microvessels respect to ones in the normal tissue. In addition, the proliferating cells compress the blood and lymphatic vessels, that leads to an abnormal extracellular matrix (ECM) production[27, 28]. Typical elastic modulus of human breast cancer lesions is one order of magnitude higher than the one of normal breast (3.25 kPa/24.37 mmHg), measured in the range of 10.0–42.0 kPa (75.0–315.0 mmHg)[25, 29]. The dysfunctional lymphatic system, the plasma leakage, and the dense ECM cause the percolation of the plasma in the surrounding tissue and as a consequence there is the increase of the extravascular hydrostatic pressure in the tumour. Unlike normal breast, where the interstitial fluid pressure (IFP) is close to zero the IFP in breast carcinoma rise to 10–20 mmHg in breast cancer[30].These abnormalities, in the flow patterns and blood pressure, drive the development of hypo-perfusion, hypoxia and low extracellular pH in the tumour microenvironment[25, 31]. Hypoxia is known to be a key trigger in tumour progression and metastasis by inducing genetic instability and microRNA alterations. The cells adapt to this hypoxia condition through a specific heterodimeric protein that consists of two proteins, hypoxia-induced factor (HIF)-1α and HIF-1β, which together constitute HIF-1[32]. The upregulation of hypoxia-inducible factors has been associated to the Epithelial to mesenchymal transitions (EMT) via overexpression of ZEB1/2 and protection of SNAIL from degradation [33, 34].

Among the significantly dysregulated microRNAs in breast cancer, several have been associated with processes essential to disease progression, such as EMT and acquisition of stem-like properties by cancer cells (CSCs)[3, 35]. During the EMT, epithelial cells lose contact with the basement membrane and neighbouring cells acquire mesenchymal traits (expression of N-cadherin and Vimentin) increased motility, and resistance to induction of apoptotic cell death[1]. The epithelial–mesenchymal switch involves changes in several pathways, including TGF-β, WNT, HIF1/2, NOTCH, NF-κB and RAS-ERK1/2. In the case of TNBC, miR-21, miR-200 and miR-221 are highly dysregulated and correlated to low patient survival. The miR-200 family has been identified as hypoxia microRNAs and its overexpression is associated to HIF-1[32], which acts as suppressor of EMT, especially targeting ZEB1/2[35]. In accordance, the upregulation miR-21 was related to the Hypoxia-inducible factors and to the acquisition of breast cancer stem cells (BCSCs) phenotype[35]. The cancer progression is associated to the formation of self-renewing cancer stem cells (CSCs), that make it more resistant to chemo- and radiotherapy. The let-7, miR-16, miR-107 e miR-128 have been recognized as miRNAs downregulated in BCSC-enriched population [3]. Both the EMT and CSCs are prerequisites for metastasis[35] and development of chemoresistance. In this sense, several microRNAs have been identified as modulators of critical genes involved in breast cancer therapy resistance[3]. The action of miR-451 and miR-298 on MDR1 genes has been associated to developing resistance to doxorubicin in MCF-7 and MDA-MB-231 cells[36, 37]. Moreover, the overexpression of MRP-1 has been correlated to VP-16 resistant MCF-7 cell line. By restoring the miR-326 overexpression, the VP-16 resistant MCF-7 cell lines have become again sensitive to VP-16 and doxorubicin treatment, confirming the miRNA involvement in therapy resistance[38]. Recently, Orlandella et al.[39] provided evidences that miR-622 is downregulated in the plasma and

tissue samples of breast cancer patients. Moreover, they showed its action as a tumour suppressor by targeting the NUAK1 kinase. NUAK1 is a serine/threonine kinase involved in cell adhesion, polarity and in epithelial-mesenchymal transition. NUAK1 overexpression is correlated with poor clinical outcome in various types of cancers.

IV.1.2 Aim of chapter 4

We have proved the ability of both the coupled Hydrodynamic flow focusing and LiPoNs nanostructure in stabilizing biologics, in particular microRNAs. Moreover, the microRNAs delivered with LiPoNs showed promising cellular results in orchestrating the genes involved in tumour progression. Going beyond the cellular delivery, several challenges to microRNAs action arise in the tumour microenvironment, where the high interstitial fluid pressure and the complex extracellular matrix, hindered their penetration. To understand the role exerted by the material complexation in preserving stability of both the vector it-self and the biologics in a more complex biological environment, we studied the behaviour of LiPoNs in a preclinical model.

We selected one of the most aggressive breast cancer types, triple negative breast cancer (TNBC), characterized by fewer treatment options, mainly chemotherapy. Therefore, the TNBC represents the ideal candidate for testing the selectivity and specificity of microRNAs therapeutics. Taking advantage of the recent evidence on the downregulation of miR-622 in breast cancer, we entrapped a mimics microRNAs, miR-622, in LiPoNs to restore its tumour suppressor function in the cells. Despite these multiple efforts in clinical examination to detect TNBC in early stage, the current imaging-based screens are still partially effective. To address this issue, we co-entrap the Gd-DTPA as Gadolinium-based Contrast agents (CAs) for MRI imaging. miR-622-Gd-loaded LiPoNs could potentially provide tissue specificity for delivery of microRNAs to the target cells and for enhancing the detection of the lesion, at the same time reduce nephrotoxicity, transmetalation and abnormal brain deposition of free Gd-based contrast agents.

IV.2 CASE STUDY

IV.2.1 Experimental section

Materials used for miR-622 preparation were the same presented in Chapter II.2.1.1. The has-miR-622 MISSION microRNA Mimic (mature sequence ACAGUCUGCUGAGGUUGGAGC) and Atto700 were purchased by Merck (St. Louis, MO, USA). These LiPoNs formulations were produced in a quartz microfluidic device (22.5mm long x 15mm wide x 4mm thick, Dolomite Centre Ltd, Royston, UK) through the coupled Hydrodynamic Flow Focusing (cHFF) process as reported in chapter I.2.1.2. The same microfluidic process conditions used in Chapter II.2.1.3 were exploited to prepare miR-622 loaded LiPoNs formulations. In the cHFF, two side streams of Lipids (0.0072 % w/v, 8:1 mass ratio SPC:Chol) dissolved in etOH-Water (65%-35% v/v) mixture sheeted an acid solution (AcOH-NaOH/1% v/v-50 mM) containing the chitosan (0.01 % w/v) and the miR-622 (2uM). To produce Gd-DTPA LiPoNs

and miR-622-Gd-DTPA-LiPoNs, the Gd-DTPA compound was added to the middle solution (0.4 % w/v). The microfluidic cHFF process was conducted by setting the side flow rate at 41 µL/min, while the middle one at 3 µL/min for a flow rate ratio (FR^2) of 0.073. The synthetic identities of miR-622 were computed as described in Chapter II.2.1.4. The Atto700 is dissolved in the chitosan solution at 24 ug/ml before being injected into the device's middle channel.

The live cell imaging experiment was performed as in Chapter III. For miR-622 formulations, mir-622 alone and using Lipofectamine 3000, miR622- LiPoNs or miR622- Gd-DTPA- LiPoNs (miR-622 conc. 6 nM, Lipids conc. 12 µg/ml and Gd-DTPA conc.:28 µM) were added in triplicate. Moreover, LiPoNs, Gd-DTPA-LiPoNs and Lipofectamine alone at the same concentration were tested in triplicate.

IV.2.2 Results and discussion

IV.2.2.1 Synthetic Identity of miR-622- Gd-DTPA- LiPoNs

This study exploited the Hybrid Lipid-Polymer Nanoparticles (LiPoNs) to make the miR-622 more stable in systemic circulation and improve its cellular/tissue uptake. The miR-622 was entrapped in a chitosan core, aimed to protect and improve the intracellular delivery of the complex, covered by a lipid shell, made up of phosphatidylcholine and cholesterol, to enhance the cellular uptake. Once administered into the body, NPs delivery potency will depend on the interactions between the nanomaterials and biological systems (nano-biointeractions)[40]. Indeed, the synthetic identities of miR-622- LiPoNs formulations were analyzed in terms of the mean and mode of the size, Standard Error (St.Error) and Zeta potential by NanoSight (NTA) and Zetasizer Nano (Figure IV-1a,b). The Nanoparticle tracking analysis of the miR-622 loaded LiPoNs formulations showed a mode size range from 105.1 nm to 112.2nm (Figure IV-1a), with an average size values of 123.7 nm and 135.1 nm for miR-622-LiPoNs and miR-622-Gd-DTPA-LiPoNs, respectively (Figure IV-1a). The zeta potential was in the range of -6.28 to -15.9 mV, with an increase of the negative charge for the addition of miR-622 in LiPoNs, from -15.9 to -19.8 mV (Figure IV-1b). Differently, the Gd-DTPA addition to LiPoNs formulations reduced their negative charge, making them more neutral from -19.8 mV to - 6.81 mV. The morphology of miR-622-LiPoNs is observed by TEM (Figure IV-1c). Therefore, the LiPoNs are small enough to avoid massive accumulation in off-target organs and could prolong their circulation lifetimes on account of their slightly negative charge [41]. The longitudinal relaxation time distributions of miR-622-Gd-DTPA-LiPoNs (T1=1690 ms) in Figure IV-1d confirmed the loading of Gd-DTPA Contrast Agent (EE: 62 %) within the LiPoNs nanostructures.

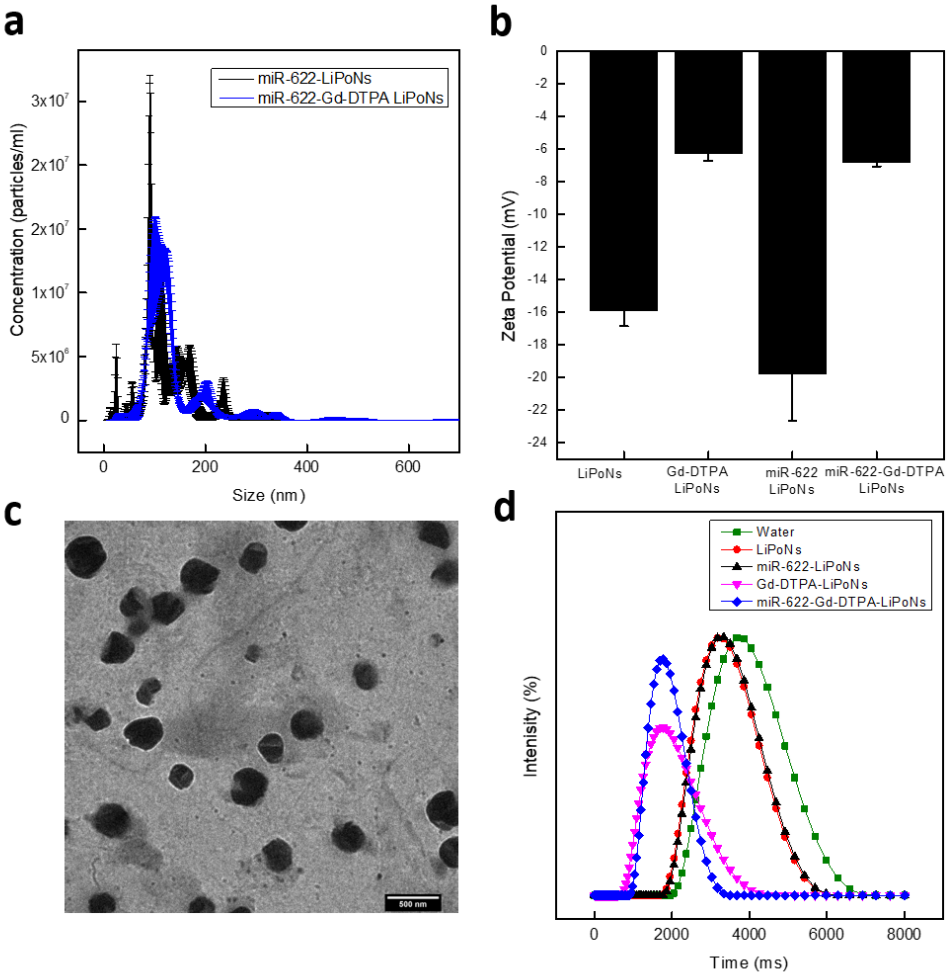

Figure IV-1. Morphological characterization and in vitro MRI. (a) Size distributions of miR-622 LiPoNs (black) and miR-622- Gd-DTPA- LiPoNs (blue) as a function of the mean nanoparticle concentration; (b) Zeta potential values of LiPoNs, Gd-DTPA LiPoNs, miR-622-LiPoNs, miR-622-Gd-DTPA- LiPoNs; (c) TEM image of miR-622-LipoNs; (d) In vitro comparison of longitudinal relaxation time distributions of water, LiPoNs, Gd-DTPA-LiPoNs, miR-622-LiPoNs, miR-622-Gd-DTPA-LiPoNs.

IV.2.2.2 Cellular interaction of miR-622- Gd-DTPA- LiPoNs

Recently, Orlandella et al.[39] have demonstrated the role of the miR-622 in inducing a reduction of NUAK1 expression in the MDA-MB-231 cells, that through the AHT signalling, enhances the invasive and metastatic potential of the cells. To restore the miR-622 action as a tumour suppressor, we provided an additional source of miR-622 to the MDA-MB-231 cells with the LiPoNs mediated delivery.

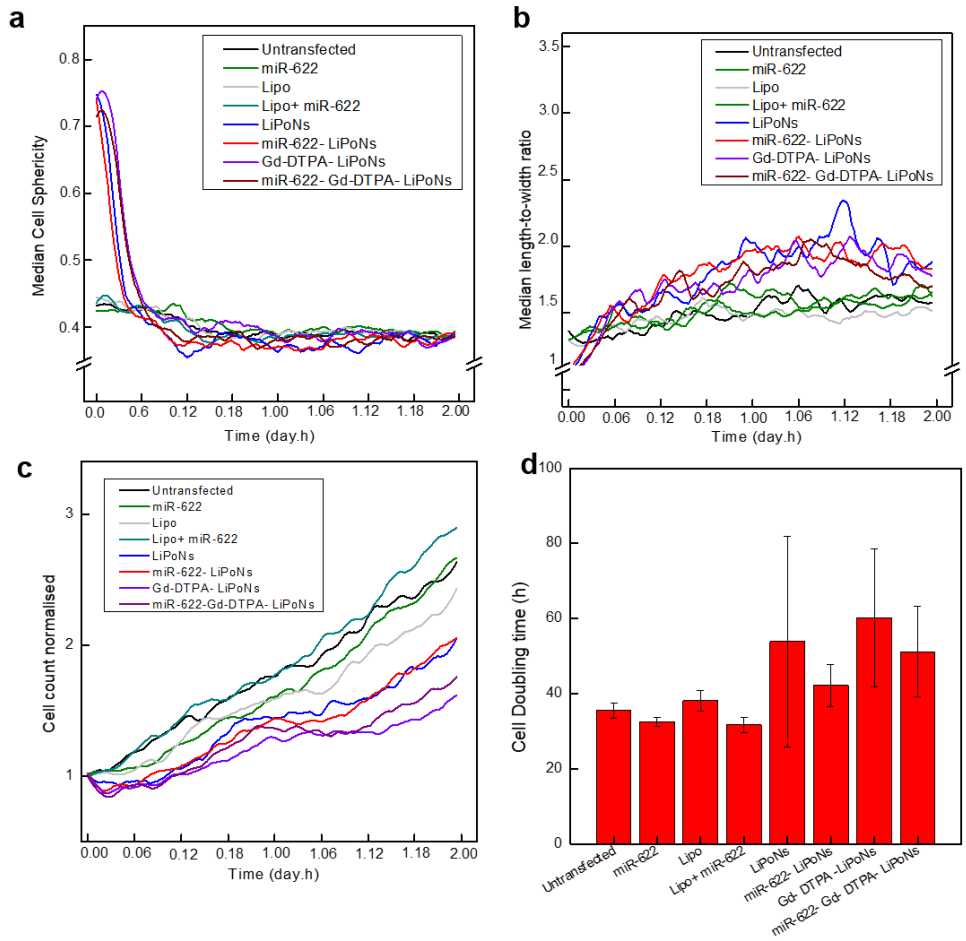

Figure IV-2. Analysis of the proliferation of MDA-MB-231 cells. The MDA-MB-231 cells were treated with different LiPoNs (lipids conc. 12ug/mL), miR-622, Lipofectamine and miR-622 mediated transfection with Lipofectamine (Lipo+miR-622). The cells were imaged every 18 min in Quantitative Phase Imaging (QPI) and segmented automatically to quantify **a**) median cell sphericity, **b**) median length-to-width ratio, **c**) cell count normalised and **d**) the cell doubling time.

We tested the miR-622-Gd-DTPA-LiPoNs on MDA-MB-231 cells and we quantified their effects on the behavioural characteristics of the cells with automated live cell imaging. We gained information on the cell population's morphology, proliferation, mitosis and random motility every 18 min for 48 h. The cells were treated with miR-622 alone and in combinations with the Lipofectamine as a comparison. As controls, blank LiPoNs formulations and lipofectamine alone were tested. The results on cell morphology, such as sphericity, area, thickness and length-to-with ratio, confirmed the findings already

reported in chapter III. Indeed, a change in the cell morphology was detected upon incubating with miR-622-LiPoNs that progressively disappeared in 6 hours. After 6 hours, the cells increased their length-to-with ratio as reported in Figure IV-2. This morphological change could be linked to a cellular biological response. Indeed, following this transitory phase, the cells seemed to reduce the proliferation rate, as reported by the plate-like curve around 24 h-1 day in Figure IV-2c. This reduction in the cell count normalised matched with the increase in cell doubling time reported for the miR-622-LiPoNs formulations. In particular, the miR-622- LiPoNs and miR-622-Gd-DTPA-LiPoNs showed an increase of the doubling time up to 42± 5 h and 51± 11h, respectively (Figure IV-2d).

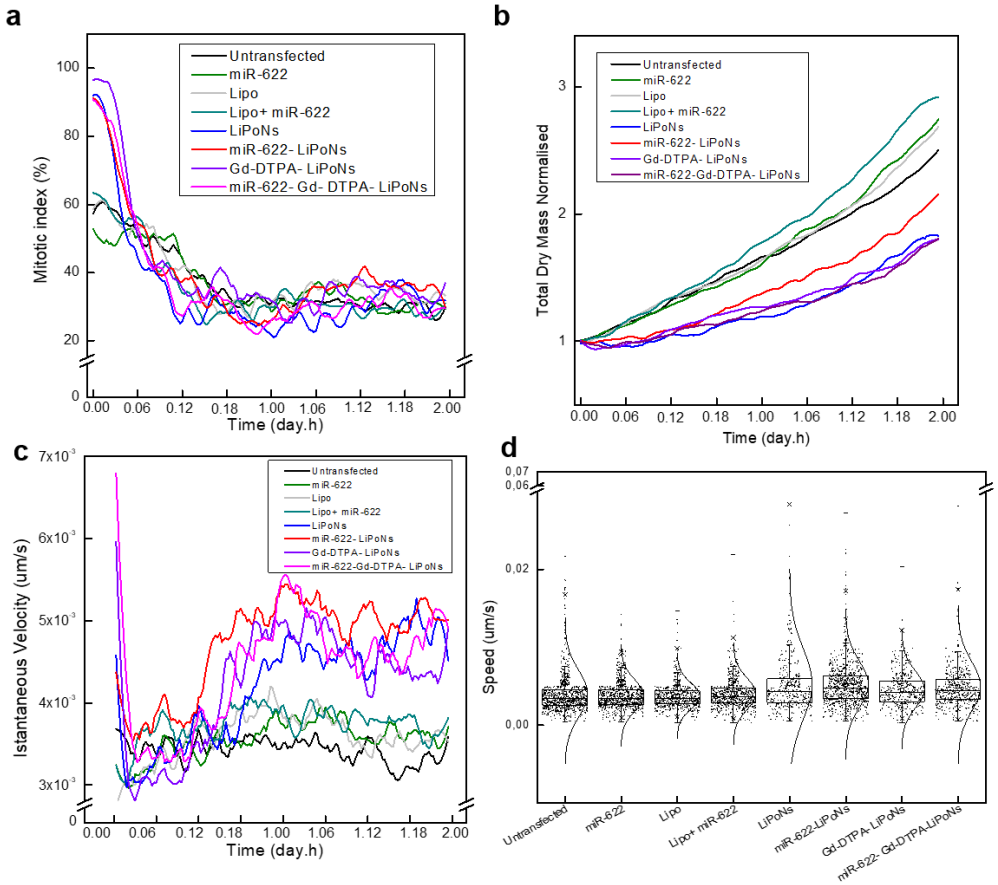

Figure IV-3. Livecyte analysis of the proliferation of MDA-MB-231 cells. The MDA-MB-231 cells were treated with different LiPoNs (lipids conc. 12ug/mL), miR-622, Lipofectamine and miR-622 mediated transfection with Lipofectamine (Lipo+miR-622). The cells were imaged every 18 min in Quantitative Phase Imaging (QPI) and segmented automatically to quantify **a**) mitotic index, **b**) total dry mass normalised, **c**) instantaneous velocity and **d**) the cell track speed.

As already reported in Chapter III, the mitotic index did not significantly differ among all the conditions tested. Therefore, the miR-622-LiPoNs formulations decreased the proliferation rate of the cells but did not induce their arrest. However, this reduction in the cell activity reduced the cell duplications and consequently the total cell dry mass (Figure IV-3d).

The line graph of the mean of the instantaneous velocities of all cells in a frame reported a rise in the cell random motility after 18 h of contact with LiPoNs formulations (Figure IV-3c). This behaviour could be linked to the reduction of cell doublings, allowing to the cells to preserve their cell shape for a longer time, with respect to untransfected cells. In accordance with the increase of cell instantaneous velocity, a slight increase in the cell speed is reported (Figure IV-3d). The speed of the cells is evaluated by dividing the total distance travelled by the lifetime of the track.

A difference between the miR-622 alone and mediated transfection is detected; however, this change cannot be linked to the delivery of miR-622 mediated by the LiPoNs formulations but to LiPoNs carriers.

IV.2.2.3 Preliminary in vivo data of LiPoNs

We preliminary validated the ability of LiPoNs to target the tumour site by exploiting the passive targeting via the EPR (Enhanced Permeability Retention) effect. The LiPoNs were loaded with Atto700 (~1200 nM) and Gd-DTPA (~250 uM) to be tracked *in vivo*. In collaboration with CEINGE-Biotecnologie avanzate, CNR IBB – Istituto di Biostrutture e Bioimmagini and University Parthenope, the LiPoNs have been injected in an orthotopic syngeneic murine model of breast cancer (4t1 cells inoculated into the breast). The LiPoNs biodistribution was acquired *in vivo* and *ex vivo* with the fluorescence-mediated tomography (FMT). For the *ex vivo* analysis, the muscle tissue was used to normalize the fluorescence value. Following the last acquisition at 24 h, the mice have been sacrificed, the organs have been explanted and acquired in FMT (Figure IV-4).

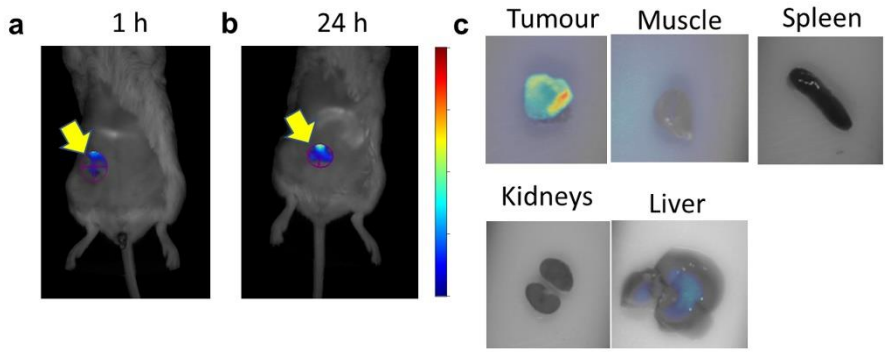

Figure IV-4. In vivo and ex-vivo fluorescence imaging and organ distribution of the Atto700-Gd-DTPA-LiPoNs in an orthotopic syngeneic murine model of breast cancer. Representative fluorescence images for in vivo distribution of Atto700-Gd-DTPA-LiPoNs at (a) 1h and (b) 24 h post i.v. injection; (c) Ex-vivo distribution of Atto700-Gd-DTPA-LiPoNs examined at 24 h post injection.

The LiPoNs did not cause major adverse effects, and no changes in respiratory frequency or signs of suffering during and upon the injection were detected. The LiPoNs showed an accumulation in the tumour tissue at 24 h post injection (Figure IV-4). The ex vivo results reported a moderate accumulation in the liver, possibly due to the hepatobiliary excretion (Figure IV-4c). On the other hand, the signal at the splenic and renal level was absent, likely proving the lack of sequestration of the LiPoNs by the reticuloendothelial system and the preferential excretion by the hepato-biliary route, instead of the renal excretion. Therefore, the LiPoNs mainly reached the tumour with a moderate off-target accumulation.

Following these biodistribution studies, the antitumoral activity of miR-622-Gd-DTPA-Atto700 loaded LiPoNs was evaluated. We monitored the tumour progression upon intratumoral administration of miR-622 loaded LiPoNs. Preliminary results have shown an inhibition of the tumour growth for the delivery of miR-622 mediated by LiPoNs with respect to the untreated one. We do not have additional available data since the experiments are in progress.

The dual material nanostructure of Lipid-Polymer NPs seems to take advantage of the EPR effect to target the tumour site effectively and to exploit the material design to deliver a stable microRNAs cargo in the TME. However, to confirm these results, further in vivo studies are required.

IV.3 CONCLUSIONS

We have proven the role of the LiPoNs in effectively delivering stable microRNAs to the cells, overcoming the low cellular uptake and intracellular release of microRNAs alone. Nevertheless, the tumour microenvironment poses further challenges to microRNA delivery in cancer. Indeed, the poor blood perfusion, the high interstitial fluid pressure and the complex extracellular matrix of the tumour tissue hindered their penetration.
We verified the cellular interactions of miR-622-Gd-DTPA-LiPoNs on MDA-MB-231 cells with a high throughput cell scanning instrument. Here, the coupled Hydrodynamic flow focusing is exploited to co-load the miR-622 and the Gd-DTPA agent in LiPoNs. These LiPoNs showed both therapeutic and diagnostic properties. We preliminary reported the capability of LiPoNs to target the tumour site. This preferential tumour accumulation indicates a limited or reduced uptake of LiPoNs by the RES system. Furthermore, the preliminary results on reducing tumour growth in mice at a low dose of nucleic acid delivery through LiPoNs, confirm their therapeutic potential.

IV.4 REFERENCES

[1] H.Y. Loh, B.P. Norman, K.S. Lai, N. Abd Rahman, N.B.M. Alitheen, M.A. Osman, The Regulatory Role of MicroRNAs in Breast Cancer, International Journal of Molecular Sciences 20(19) (2019).

[2] F. Bray, J. Ferlay, I. Soerjomataram, R.L. Siegel, L.A. Torre, A. Jemal, Global cancer statistics 2018: GLOBOCAN estimates of incidence and mortality worldwide for 36 cancers in 185 countries (vol 68, pg 394, 2018), Ca-a Cancer Journal for Clinicians 70(4) (2020) 313-313.

[3] R. Singh, Y.Y. Mo, Role of microRNAs in breast cancer, Cancer Biology & Therapy 14(3) (2013) 201-212.

[4] T. Sorlie, C.M. Perou, R. Tibshirani, T. Aas, S. Geisler, H. Johnsen, T. Hastie, M.B. Eisen, M. van de Rijn, S.S. Jeffrey, T. Thorsen, H. Quist, J.C. Matese, P.O. Brown, D. Botstein, P.E. Lonning, A.L. Borresen-Dale, Gene expression patterns of breast carcinomas distinguish tumor subclasses with clinical implications, Proceedings of the National Academy of Sciences of the United States of America 98(19) (2001) 10869-10874.

[5] T. Sorlie, R. Tibshirani, J. Parker, T. Hastie, J.S. Marron, A. Nobel, S. Deng, H. Johnsen, R. Pesich, S. Geisler, J. Demeter, C.M. Perou, P.E. Lonning, P.O. Brown, A.L. Borresen-Dale, D. Botstein, Repeated observation of breast tumor subtypes in independent gene expression data sets, Proceedings of the National Academy of Sciences of the United States of America 100(14) (2003) 8418-8423.

[6] C.M. Perou, T. Sorlie, M.B. Eisen, M. van de Rijn, S.S. Jeffrey, C.A. Rees, J.R. Pollack, D.T. Ross, H. Johnsen, L.A. Akslen, O. Fluge, A. Pergamenschikov, C. Williams, S.X. Zhu, P.E. Lonning, A.L. Borresen-Dale, P.O. Brown, D. Botstein, Molecular portraits of human breast tumours, Nature 406(6797) (2000) 747-752.

[7] M.C.U. Cheang, S.K. Chia, D. Voduc, D.X. Gao, S. Leung, J. Snider, M. Watson, S. Davies, P.S. Bernard, J.S. Parker, C.M. Perou, M.J. Ellis, T.O. Nielsen, Ki67 Index, HER2 Status, and Prognosis of Patients With Luminal B Breast Cancer, Jnci-Journal of the National Cancer Institute 101(10) (2009) 736-750.

[8] A. Prat, J.S. Parker, O. Karginova, C. Fan, C. Livasy, J.I. Herschkowitz, X.P. He, C.M. Perou, Phenotypic and molecular characterization of the claudin-low intrinsic subtype of breast cancer, Breast Cancer Research 12(5) (2010).

[9] R.M. Pommier, A. Sanlaville, L. Tonon, J. Kielbassa, E. Thomas, A. Ferrari, A.S. Sertier, F. Hollande, P. Martinez, A. Tissier, A.P. Morel, M. Ouzounova, A. Puisieux, Comprehensive characterization of claudin-low breast tumors reflects the impact of the cell-of-origin on cancer evolution, Nature Communications 11(1) (2020).

[10] A.C. Garrido-Castro, N.U. Lin, K. Polyak, Insights into Molecular Classifications of Triple-Negative Breast Cancer: Improving Patient Selection for Treatment, Cancer Discovery 9(2) (2019) 176-198.

[11] C.A. Livasy, G. Karaca, R. Nanda, M.S. Tretiakova, O.I. Olopade, D.T. Moore, C.M. Perou, Phenotypic evaluation of the basal-like subtype of invasive breast carcinoma, Modern Pathology 19(2) (2006) 264-271.

[12] Abstracts and Case Studies From the College of American Pathologists 2012 Annual Meeting (CAP '12), Archives of Pathology & Laboratory Medicine 136(9) (2012) 1005-1162.

[13] R. Schmadeka, B.E. Harmon, M. Singh, Triple-Negative Breast Carcinoma Current and Emerging Concepts, American Journal of Clinical Pathology 141(4) (2014) 462-477.
[14] N. Harbeck, F. Penault-Llorca, J. Cortes, M. Gnant, N. Houssami, P. Poortmans, K. Ruddy, J. Tsang, F. Cardoso, Breast cancer, Nature Reviews Disease Primers 5(1) (2019) 66.
[15] B.E. Dogan, L.W. Turnbull, Imaging of triple-negative breast cancer, Annals of Oncology 23 (2012) 23-29.
[16] W.A. Berg, Z. Zhang, D. Lehrer, R.A. Jong, E.D. Pisano, R.G. Barr, M. Bohm-Velez, M.C. Mahoney, W.P. Evans, L.H. Larsen, M.J. Morton, E.B. Mendelson, D.M. Farria, J.B. Cormack, H.S. Marques, A. Adams, N.M. Yeh, G. Gabrielli, A. Investigators, Detection of Breast Cancer With Addition of Annual Screening Ultrasound or a Single Screening MRI to Mammography in Women With Elevated Breast Cancer Risk, Jama-Journal of the American Medical Association 307(13) (2012) 1394-1404.
[17] K.M. Krizmanich-Conniff, C. Paramagul, S.K. Patterson, M.A. Helvie, M.A. Roubidoux, J.D. Myles, K. Jiang, M. Sabel, Triple Receptor-Negative Breast Cancer: Imaging and Clinical Characteristics, American Journal of Roentgenology 199(2) (2012) 458-464.
[18] H. Yao, G. He, S. Yan, C. Chen, L. Song, T.J. Rosol, X. Deng, Triple-negative breast cancer: is there a treatment on the horizon?, Oncotarget 8(1) (2017) 1913-1924.
[19] L. Yin, J.J. Duan, X.W. Bian, S.C. Yu, Triple-negative breast cancer molecular subtyping and treatment progress, Breast Cancer Research 22(1) (2020).
[20] G. Bianchini, J.M. Balko, I.A. Mayer, M.E. Sanders, L. Gianni, Triple-negative breast cancer: challenges and opportunities of a heterogeneous disease, Nature Reviews Clinical Oncology 13(11) (2016) 674-690.
[21] N. Berrada, S. Delaloge, F. Andre, Treatment of triple-negative metastatic breast cancer: toward individualized targeted treatments or chemosensitization?, Annals of Oncology 21 (2010) 30-35.
[22] M.L. Telli, W.J. Gradishar, J.H. Ward, NCCN Guidelines Updates: Breast Cancer, Journal of the National Comprehensive Cancer Network 17(5) (2019) 552-555.
[23] G. Bianchini, C. De Angelis, L. Licata, L. Gianni, Treatment landscape of triple-negative breast cancer - expanded options, evolving needs, Nature Reviews Clinical Oncology 19(2) (2022) 91-113.
[24] P. Carmeliet, R.K. Jain, Angiogenesis in cancer and other diseases, Nature 407(6801) (2000) 249-257.
[25] T. Stylianopoulos, L.L. Munn, R.K. Jain, Reengineering the Physical Microenvironment of Tumors to Improve Drug Delivery and Efficacy: From Mathematical Modeling to Bench to Bedside, Trends in Cancer 4(4) (2018) 292-319.
[26] H. Hashizume, P. Baluk, S. Morikawa, J.W. McLean, G. Thurston, S. Roberge, R.K. Jain, D.M. McDonald, Openings between defective endothelial cells explain tumor vessel leakiness, American Journal of Pathology 156(4) (2000) 1363-1380.
[27] T. Stylianopoulos, J.D. Martin, M. Snuderl, F. Mpekris, S.R. Jain, R.K. Jain, Coevolution of Solid Stress and Interstitial Fluid Pressure in Tumors During Progression: Implications for Vascular Collapse, Cancer Research 73(13) (2013) 3833-3841.
[28] T.P. Padera, B.R. Stoll, J.B. Tooredman, D. Capen, E. di Tomaso, R.K. Jain, Cancer cells compress intratumour vessels, Nature 427(6976) (2004) 695-695.

[29] A. Samani, J. Zubovits, D. Plewes, Elastic moduli of normal and pathological human breast tissues: an inversion-technique-based investigation of 169 samples, Physics in Medicine and Biology 52(6) (2007) 1565-1576.
[30] Y. Boucher, J.M. Kirkwood, D. Opacic, M. Desantis, R.K. Jain, INTERSTITIAL HYPERTENSION IN SUPERFICIAL METASTATIC MELANOMAS IN HUMANS, Cancer Research 51(24) (1991) 6691-6694.
[31] R.K. Jain, R.T. Tong, L.L. Munn, Effect of vascular normalization, by antiangiogenic therapy on interstitial hypertension, peritumor edema, and lymphatic metastasis: Insights from a mathematical model, Cancer Research 67(6) (2007) 2729-2735.
[32] A. Birbrair, Tumor Microenvironment Molecular Players - Part B Preface, Tumor Microenvironment: Molecular Players, Pt B 1277 (2020) VII-VIII.
[33] K.G.K. Deepak, R. Vempati, G.P. Nagaraju, V.R. Dasari, S. Nagini, D.N. Rao, R.R. Malla, Tumor microenvironment: Challenges and opportunities in targeting metastasis of triple negative breast cancer, Pharmacological Research 153 (2020).
[34] S. Lamouille, D. Subramanyam, R. Blelloch, R. Derynck, Regulation of epithelial-mesenchymal and mesenchymal-epithelial transitions by microRNAs, Current Opinion in Cell Biology 25(2) (2013) 200-207.
[35] D. Piasecka, M. Braun, R. Kordek, R. Sadej, H. Romanska, MicroRNAs in regulation of triple-negative breast cancer progression, Journal of Cancer Research and Clinical Oncology 144(8) (2018) 1401-1411.
[36] O. Kovalchuk, J. Filkowski, J. Meservy, Y. Iinytskyy, V.P. Tryndyak, V.F. Chekhun, I.P. Pogribny, Involvement of microRNA-451 in resistance of the MCF-7 breast cancer cells to chemotherapeutic drug doxorubicin, Molecular Cancer Therapeutics 7(7) (2008) 2152-2159.
[37] L.L. Bao, S. Hazari, S. Mehra, D. Kaushal, K. Moroz, S. Dash, Increased Expression of P-Glycoprotein and Doxorubicin Chemoresistance of Metastatic Breast Cancer Is Regulated by miR-298, American Journal of Pathology 180(6) (2012) 2490-2503.
[38] Z.X. Liang, H. Wu, J. Xia, Y.H. Li, Y.W. Zhang, K. Huang, N. Wagar, Y. Yoon, H.T. Cho, S. Scala, H. Shim, Involvement of miR-326 in chemotherapy resistance of breast cancer through modulating expression of multidrug resistance-associated protein 1, Biochemical Pharmacology 79(6) (2010) 817-824.
[39] F.M. Orlandella, R.M. Mariniello, P. Mirabelli, A.E. De Stefano, P.L.C. Iervolino, V.A. Lasorsa, M. Capasso, R. Giannatiempo, M. Rongo, M. Incoronato, F. Messina, M. Salvatore, A. Soricelli, G. Salvatore, miR-622 is a novel potential biomarker of breast carcinoma and impairs motility of breast cancer cells through targeting NUAK1 kinase, British Journal of Cancer.
[40] W. Poon, B.R. Kingston, B. Ouyang, W. Ngo, W.C.W. Chan, A framework for designing delivery systems, Nature Nanotechnology 15(10) (2020) 819-829.
[41] E. Blanco, H. Shen, M. Ferrari, Principles of nanoparticle design for overcoming biological barriers to drug delivery, Nature Biotechnology 33(9) (2015) 941-951.

V. CHAPTER V– INSIGHT INTO FLUID INTERFACES FOR STABILIZING NANOPARTICLES FORMATION

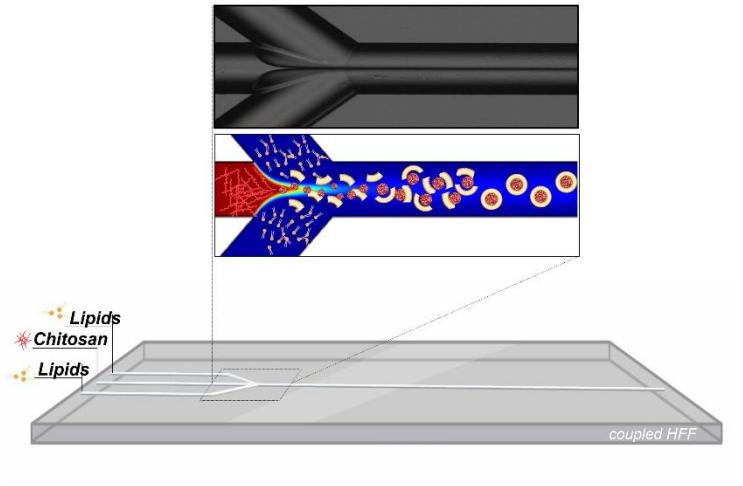

Graphical Abstract V. Insight on the coupled Hydrodynamic Flow focusing from perspective of fluid interfaces.

Abstract

The coupled Hydrodynamic flow focusing (cHFF), is analysed in terms of fluid interfaces and their impact on mechanism of NPs formation. Firstly, the solvent displacement in the coupled HFF process is studied using computational fluid dynamics simulation (CFD) and it is compared to experimental results to acquire knowledge on the coupling between two simultaneously mechanisms of formation: self-assembly and nanoprecipitation. Then, the impact of the HFF features in confining the species in a thin reaction zone was investigated and elucidated by analysing several HFF processes for the synthesis of NPswith different materials. A preliminary correlation between the confinement exerted in the HFF device and the size of NPs is reported.

V.1 BACKGROUND

V.1.1 Introduction

The liposomes formation is described as two-step process[1, 2], while the mechanism of polymer nanoparticle formation includes several steps, such as nucleation, growth and aggregation. The polymer nanoparticles distribution depends on each step's rate [3].

The phospholipids, they are amphiphilic molecules made up of a hydrophilic head group and double long hydrophobic tails, which make them poorly soluble in water unless they self-assemble into bilayers [4]. The formation of a vesicle can be described as a two-step self-assembly process: the aggregation of amphiphiles in bilayer fragments and then its closure into a vesicle [1].
For the aggregation of lipids, Marsh reported that the standard free energy of the lipid monomer transformation from water into a micelle of size m is given by[5, 6]:

$$\Delta G^0_{tr,m} = \mu^0_{mic,m} - \mu^0_w = RTInX_w - \frac{RT}{m} In\left(\frac{X_m}{m}\right) \qquad (1)$$

where X_w and X_m are the mole fractions of a lipid (with respect to water) in the monomer and micellar states, respectively; R is the ideal gas constant; and T is the absolute temperature. The simplest assumption is to consider the micelles monodisperse with a unique size m equal to the aggregation number of lipids (n_{agg}), so $m = n_{agg}$. For large micelles or extended bilayers (i.e $n_{agg} \rightarrow \infty$), the standard free energy of the transfer can be related to the critical micelle concentration, CMC, by:

$$\Delta G^0_{tr} = RT\ InX_{CMC} \qquad (2)$$

where CMC (in mole fraction units) is the critical micelle concentration of the lipid monomer in mole fraction units with respect to water[5, 7]. $\Delta G^0_{tr,m}$ is a negative free energy term (CMC < 1), underlying that micelle formation is a spontaneous process. The CMC is the concentration above which a further addition of solute molecules results in the formation of more aggregates while leaving the monomer concentration unchanged[8]. It is possible to predict this finite shape of amphiphiles' self-assembly by determining the molecular packing parameter associated with their structural features. The molecular packing parameter is defined as:

$$CPP = \frac{v_0}{al_0} \qquad (3)$$

where v_0 and l_0 are the volume and length of the amphiphile's tail and a is the surface area of the hydrophobic core of the aggregate [9]. Then, these small aggregates' spontaneous growth through coalescence in disk-like bilayer structures according to the kinetic model of a micelle–vesicle transition[1, 10-12]. Generally, as the bilayer structures grow, they tend to minimize the overall line energy initially by curving themselves into a spherical cup and then, to reduce the line energy further by closing themselves into a spherical vesicle[13].

For many years, the nucleation and growth of polymer nanoparticles have been described through the LaMer burst nucleation[14]. The nanoprecipitation begins at the onset of supersaturation, generated by the sudden change in concentration, to reduce the system's free energy (ΔG). The newly formed nuclei grow by aggregation of molecular species until a critical size (r_c), stable upon dissolution, is achieved. The nucleation rate is defined by the Arrhenius relationship as:

$$B = K_1 \exp\left(-\frac{\Delta G_{cr}}{KT}\right) = K_1 \exp\left(-\frac{16\pi\gamma^3 v^2}{3k^3T^3[\ln(S_r)]^2}\right) \quad (4)$$

Here, K_1 is a constant, K is Boltzmann's constant, T is the absolute temperature, S_r is the local supersaturation at particle surface and ΔG_{cr} is the critical free energy for nucleation[15]. Hence, the local supersaturation (S) controls the nucleation kinetics that in the case of solvent-exchange precipitation or rapid mixing is defined as[15, 16]:

$$S \equiv \frac{C}{C^*} \quad (5)$$

where C is the real-time concentration and C^* represents the saturation solubility[16]. For the rapid mixing, the solute concentration continues to rise to the saturation concentration $C > C^*$ and reaches the critical nuclei concentration C^n, where the nanoprecipitation process is triggered and almost monodisperse polymer nuclei are formed[2, 16]. In this stage the nuclei are formed by molecules condensation until a stable size against dissolution is obtained. This nucleation phase proceeds until the solute concentration felt down to critical nucleation concentration C^n, where new nuclei cannot be formed. Then, these existing nuclei grow to add or capture the remaining dissolved solute until the concentration of still-dissolved material fell to saturation solubility or bulk solubility C^*. The relative kinetics of the nucleation and growth dictate the nanoparticle size and distribution[2, 15, 17].

Lince et al.[3] described the molecular growth of NPs, the attachment of molecules to the surface of particle, in the case of diffusion-controlled growth rate as:

$$G = \frac{2k_m M_w C}{\rho}(S-1) \quad (6)$$

Where k_m is the mass transfer coefficient, M_w is the molecular weight of the polymer and ρ is the density.

The nanoparticles' sizes are described by a third step, that determines the size distribution of the final nanoparticles. The aggregation depends on the frequency of collision of NPs and their stability, consequently, it is proportional to the number density (i.e., concentration) and aggregation frequency (aggregation kernel). Then, the aggregation frequency is dictated by the size of the particles and the mechanism of collision, Brownian motions (perikinetic aggregation) or fluid motions (orthokinetic aggregation)[3].

A key determinant of nanoparticle size and distribution is the nucleation rate, which is controlled by the fluid dynamics and mixing rate. Generally, fast mixing results in a high

nucleation rate and large population of small particles, while poor mixing results low nucleation rate and, consequently, the formation of larger particles[3].

Microfluidics, with respect to other conventional manufacturing methods for the production of NPs, offers unique control of fluid dynamics and mixing among species. Indeed, microfluidics, flowing minute amount (nano-picoliters) in the micrometre scale, leverages the physical characteristics of mass and fluid transfer. Indeed, in a miniaturized system, the Reynolds number is lower than 100 due to the predominance role exerted by viscous forces, resulting in laminar flow. Thus, the mass transfer is governed by passive molecular diffusion and advection. For small scale, the mixing between species is enhanced, since the time required for species to diffuse scale quadratically with the distance covered[2]. Among all continuous flow microfluidic geometries, the hydrodynamic flow focusing (HFF), where a middle flow is sheathed by two side flows, reduces the inner sample stream and consequently results in faster mixing. The possibility of fine tuning the hydrodynamic flow focusing width by varying the volumetric flowrate ratio between the inner and side flows was exploited to control the displacement and mixing times of solvents to trigger the nanoprecipitation mechanism. Among all continuous flow microfluidic geometries, the hydrodynamic flow focusing (HFF) [18, 19].

In the 2004, Jahn and co-workers[20] firstly synthesized liposome in a trapezoidal cross-section microfluidic device where a lipid stream dissolved in isopropyl alcohol (IPA) was hydrodynamically sheathed between two buffer streams at an angle of 90 °. The liposomes formation was controlled by the mass transfer at the fluid interface, where the increase in aqueous solution triggers the formation of lipid vesicles. The reduction of the radius of the liposomes, with the increase in the flow rate ratio, was associated with an increase in the shear stress exerted on liposomes during their self-assembly[20]. Later, they studied the change in the liposomes size manipulating the flow rate in HFF device characterized by multiple inlets at 45 ° and with a higher aspect ratio. Differently from previous findings, they reported that the absolute magnitude of the shear forces between the streams had limited impact on liposome size [21], at the same time the flow rate ratio guided the phenomenon of assembly, because it changed the dynamics of mass transfer across the streams[22]. To deeply investigate the role of the device geometry on liposome formation, they compared the liposomes formation in two device geometry, characterized by a different intersection angle and aspect ratio, reporting no differences of device geometry on liposome mechanism of formation[2, 23].

Back in the 2008, Karnik et al.[24] applied the HFF technology to the production of material with size ranging in the nanometres scale. In their method, a poly(lactide-co-glycolide)-b-poly(ethylene glycol) PLGA-PEG block copolymer, dissolved in acetonitrile, was hydrodynamic focused by two lateral nonsolvent water phases inducing the mutual diffusion of all solvents and ultimately resulting in precipitate formation. They reported a decrease in nanoparticle size to 20 nm for lower flow ratio and consequently reduction of mixing time.

Afterwards, several microfluidic platforms were fabricated for the synthesis of nanocarriers based on chitosan[25], hyaluronic acid[26] and PLGA-PEG[27]. In further studies, the microfluidic ability to promote the ordered interaction among different materials was exploited to produce hybrid nanoparticles[28-30].

V.1.2 Aim of chapter 5

Working in a micro-confined domain, microfluidics leverages the physical characteristics of mass and fluid transfer, makes the microfluidic devices not only a miniaturised version of a micromixers. The hydrodynamic flow focusing devices (HFF), was exploited to guide the nucleation and growth of lipid-based and polymer-based nanoparticles, separately. However, the role of the HFF in controlling the formation of coupled phenomena simultaneously, self-assembly of liposomes and nanoprecipitation of polymer, was not explored. To study the interplay between the fluid dynamics and mechanism of hybrid nanoparticles' formation, we used the coupled Hydrodynamic flow focusing process as confined microreactors with highly controllable fluid interfaces. The rationale was to create controllable fluid interfaces where the mixing between components drives the mutual solvent extraction. For this scope, a Comsol simulation of the convective-diffusive mixing in the cHFF was computed to quantify the solvent interdiffusion and their spatial distribution along the device. This, in turn, was aimed at having insight into the kinetics of the assembly and growth of both the lipids and the polymer precipitate to identify the main parameters that guide the stabilization of the complex. Then, we analysed the current state of the art to find a relationship between interfacial phenomena occurring in the HFF and nanoparticle formation. We preliminary reported a correlation between NPs size and the flow focusing width in the HFF. We discussed the critical parameters that guide the nanoparticle formation in a preliminary model that predicts the NPs size.

V.2 CASE STUDY

V.2.1 Experimental section

V.2.1.1 Materials

Materials used for the production were the same as presented in Chapter I.
Sulforhodamine B has been purchased from Sigma-Aldrich (St. Louis, MO, USA).

V.2.1.2 LiPoNs production

The LiPoNs were produced and characterized as reported in Chapter I. Aiming to analyse different fluid-dynamic regimes, different flow rate ratio (FR^2) conditions were tested. The flow rate ratio FR^2 was defined in Chapter I. Five selected values for the FR^2 were 0.02, 0.07, 0.12, 0.17, 0.22, obtained by keeping constant the side flow rates at 41 µl/min and letting vary the middle one among 1, 3, 5, 7, 9 µl/min, respectively. For the fluorescent study, the Sulforhodamine B at 0.01 % w/v was added to a water solution and injected in the central channel, while mixtures of etOH/water (65/35 % v/v) were injected in the side ones.

V.2.1.3 Numerical simulation

The simulations of the process were run in the computational environment that we built on the xy plane of the working window of COMSOL Multiphysics 5.4 (COMSOL Inc., Burlington, MA, USA, Figure V-1). Further details on the designed chip are in Appendix-Table VI-1

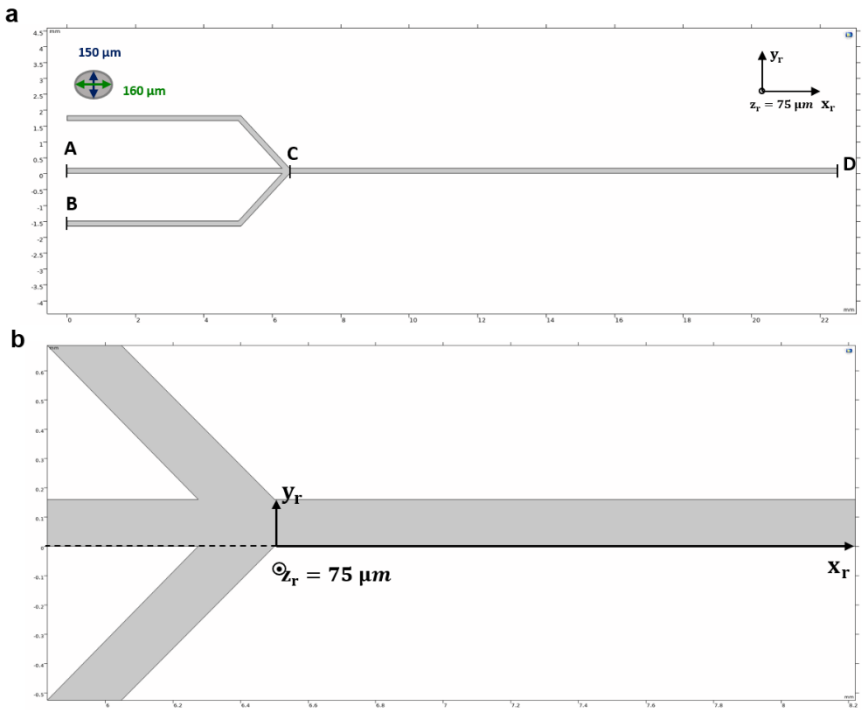

Figure V-1. **a**) Bidimensional device geometry built on Comsol Multiphysics 5.4 for simulating the 2D HFF. **b**) Schematization of the reference system set for running simulations.

In figure V-1 the reference system for the simulation study is reported, where the origin of reference is placed at the end of the junction that connects side and central channels (in the actual position of x = 6.5 mm) in the downer channel wall ($z_{\frac{1}{2}}$ = 75 µm, with the 2D xy plane centered at xr = 0, yr = 0, Figure V-1).

For the side streams, we selected as initial material an ethanol solution with density of 0.88 X 10^3 kg/m^3 and a dynamic viscosity of 1.66 X 10^{-3} Pa*s to reproduce the ethanol/water volumetric ratio of 65/35 % v/v[31]. The same solution was set as initial material for the main channel, downstream the channel junction. For the central stream, an acetic acid solution with a density of 0.99 X 10^3 kg/m^3 and a dynamic viscosity of 0.89 X 10^{-3} Pa*s was set as initial material to reproduce the acOH/Water volumetric ratio 1/99 % v/v[32], as reported in the Appendix VI- TableVI-2.

The Laminar Flow interface was selected to compute the velocity and pressure fields for the flow of the single-phase fluid in the laminar flow regime and the stationary steady state, whose governing equations were the Navier-Stokes for conservation of momentum (7) and the continuity law for conservation of mass (9), namely:

$$\rho(u \cdot \nabla)u = \nabla \cdot [-pI + K] + F \quad (7)$$

$$K = \mu(\nabla u + (\nabla u)^T) \quad (8)$$

$$\rho\nabla \cdot (u) = 0 \quad (9)$$

where u is the flow velocity, ρ is the fluid density, p is the pressure, μ is the dynamic viscosity and F represents outer forces. They were coupled with the boundary conditions of incompressible fluid flow, no slip at walls, fully developed flows and suppressed backflow at the outlet (pressure equal to 0 Pa).

The driving forces for mass transport were diffusion by Fick's law, driven by concentration gradients, and convection, also contributing to the flux of chemical species by bulk fluid motion. The combined effect of them was included in our model through the "Transport of diluted species", whose determining equations in the stationary case were:

$$\nabla \cdot J_i + u \cdot \nabla c_i = R_i \quad (10)$$

$$J_i = -D_i \nabla c_i \quad (11)$$

where c_i is the species concentration (mol/m^3), J_i is the molar flux (1/m^{2}s^1), R_i is a net volumetric source for the species concentration, such that R>0 assumes that a chemical reaction is creating more of the species, and R<0 that a chemical reaction is destroying the species. D_i is the mutual diffusion coefficient of the species (m^2/s). The Multiphysics coupling of all the physics declared was selected.

Different flow focusing regimes were explored by modulating the flow rate ratio FR^2 in a range from 0.02 up to 0.22, by keeping the side flow rate (FR) constant while manipulating the middle one. These flow rates were set for each channel in the simulation as average velocity in the fully developed flows (Table V-1).

Table V-1. Table of the average velocity used for the CFD simulation.

FR²	**Side Stream**	**Middle Stream**
0.02	Side Flow rate =41 ul/min Average velocity = 36.27 mm/s	Middle Flow rate =1 ul/min Average velocity = 0.88 mm/s
0.07	Side Flow rate =41 ul/min Average velocity = 36.27 mm/s	Middle Flow rate =3 ul/min Average velocity = 2.65 mm/s
0.12	Side Flow rate =41 ul/min Average velocity = 36.27 mm/s	Middle Flow rate =5 ul/min Average velocity = 4.42 mm/s
0.17	Side Flow rate =41 ul/min Average velocity = 36.27 mm/s	Middle Flow rate =7 ul/min Average velocity = 6.19 mm/s
0.22	Side Flow rate =41 ul/min Average velocity = 36.27 mm/s	Middle Flow rate =9 ul/min Average velocity = 7.96 mm/s

The mesh was user-controlled mesh, with a high number of nodes located in the Y junction built. It was built in accordance with the parameters reported by Amrani et al. [33], that optimized the mesh for a HFF geometry in order to have a correspondence between calculated and theoretical values of the flow focusing width (converge towards the same value). The parameters used for the mesh are reported in AppendixVI-TableVI-3

For quantitatively purposes, 2D Cut lines were stated in the Data Sets of the Results Panel with a line entry method based on the declaration of their coordinates. According to our reference system, the main channel was investigated by spanning from x_r =-200 µm, defined through a vertical cut line with coordinates (x_1=6.3 mm, y1=0 mm) and (x_2=6.3 mm, y_2=0.16 mm), to x_r =15000 µm (x_1=21.5 mm, y_1=0 mm - x_2=21.5 mm, y_2=0.16 mm) as reported in Appendix-IV-Figure VI-15-17. Whereas, for detecting changes along the main channel width of 160 µm, horizontal cutlines were defined along the entire device from y_r = 0 µm (x_1=0 mm, y_1=0 mm - x_2=22.5 mm, y_2=0 mm) to the centre of the channel at y_r=80 µm (x_1=0 mm, y_1=0.08 mm - x_2=22.5 mm, y_2=0.08 mm) see Appendix VI-Figure VI-18.

V.2.2 Results and Discussion

IV.2.2.1 Rational of numerical simulation

The hydrodynamic flow focusing is typically performed by injecting a nonsolvent phase from the side channel focusing a solvent phase containing a polymer or lipid solution in the main channel, promoting the solvent/ nonsolvent extraction and inducing the NPs precipitation and the formation of polymer NPs or liposomes. The main driver for both mechanisms of NPs formation is the mutual solvent interdiffusion at fluid interfaces. To take advantage of this mutual solvent extraction, we designed a coupled Hydrodynamic Flow Focusing, where two lipids' streams sheeted a polymer solution in the main channel. Thus, at the fluid interface, both the mainstream and the side streams are involved in their thermodynamic process and mutually influence each other. In detail, the Lipids streams (SPC, 0.0072 % w/v), dissolved in a mixture of ethanol/water (EtOH/Water, 65/35 % v/v) are injected in the side streams while chitosan (CH, 0.01 % w/v), dissolved in acetic acid (AcOH) solution (AcOH, 1 % v/v), is injected in the middle one.

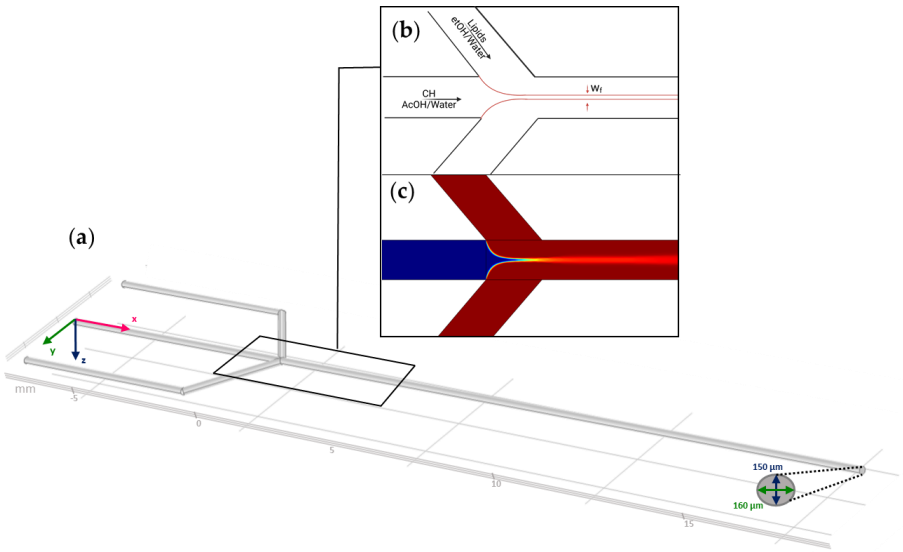

Figure V-2. a) Microfluidic device geometry with the respective 3D dimensions to produce Lipid-Polymer NPs (LiPoNs); **b**) Schematic representation of cHFF width and **c**) 2D comsol simulation.

The HFF feature enables to exert a control on this mutual interface by adjusting the width of the flow focusing, which can be varied by changing the volumetric flow rate ratio between the middle and side streams. In our case, we controlled the flow focusing width by modulating the flow rate ratio FR^2, from 0.02 to 0.22. Thus, we fixed the side channels at a flow rate (FR) equal to 41 µL/min, and changed the middle channel's FR from 1 to 9 µL/min, with a constant step of 2 µL/min.

Based on HFF simulations already reported in literature [33-35], a simulative framework for numerical studies of the cHFF was realized on COMSOL Multiphysics (5.4 software) to assess the mixing of solvents and antisolvents that is governed by the Navier-Stokes equations for incompressible flow plus the convection-diffusion equation.

We are aware that the three-dimensional characteristics of the cylindrical shape device lead to nonuniform diffusion of the focused stream across the vertical midplane, due to the no-slip boundary conditions at the top and bottom walls. The bidimensional representation of the device architecture was realized in the reference system centered at xr = 0, yr = 0, that was supposed to lie on the half of z-axis, therefore at $z_{\frac{1}{2}}$ = 75 µm, because the most salient features of the cHFF features in the x-y plane [36] and to have better visualization of fluid interfaces. Moreover, it required less extensive processing and computing resources and less time to compute.
With this configuration, a first study was carried out to analyse how the flow focusing modulates the development of solvent concentration profiles along the channel width at relevant locations along the main channel length (Figure V-3,4). Then, to investigate the interference phenomenon happening at the microfluidic junction, a second study was

carried out by spanning the entire channel length at selected locations along the channel width, more precisely by moving from the lower wall to the centre of the channel (Figure V-5,6).

IV.2.2.2 Quantitative study about the FR^2 impact on mutual solvent interdiffusion in a cHFF

The use of numerical simulation realized through the interface Transport of Diluted Species on Comsol Multiphysics, gave us access to the analysis of the development of fluid interfaces along the length of the device. We were primarily interested in the studying the impact of flow focusing modulation on the mixing two species, ethanol-water and acetic acid-water. Indeed, the change in microenvironment polarity, and decrease of ethanol content induce and mediate the self-assembly of the liposome. Differently, the reduction of acetic acid leads to the nanoprecipitation of chitosan.

To span the entire microfluidic environment from the start of the junction until the end of the device, we selected reference positions (xr) equal to -200, -100, 0, 100, 5000, 10000, 15000 µm (Appendix VI-Figure VI-16-17). However, we reported relevant positions identified at xr=-100, 0, 100, µm to emphasize the progression of the mixing around the junction (FigureV-3,4). Then, the position at xr=5000 µm (that corresponds to the device length of 11.5 mm) was chosen to investigate the achievement of the steady state condition. All the other plots are collected and reported in Appendix VI-Figure VI-16-17.

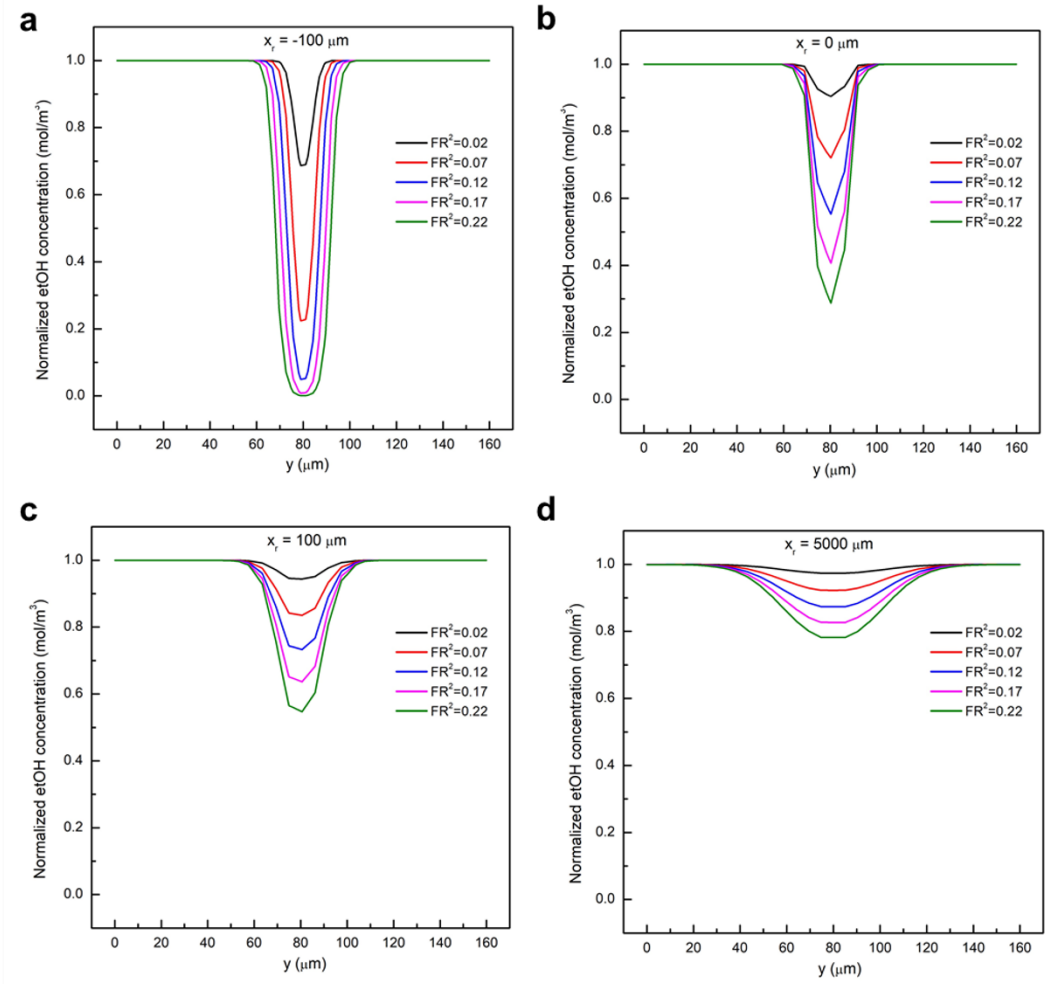

Figure V-3: The impact of FR^2(0.02-0.22) on the ethanol interdiffusion in terms of normalized ethanol (etOH) concentration in the main channel width (0-160 µm) at different locations (x_r) along the channel length (0-22.5 mm) evaluated with 2D comsol simulation: **a**) x_r:-100 µm, **b**) x_r: 0 µm, **c**) x_r: 100 µm, **d**) x_r: 5000 µm

As reasonably expected from the implementation of a reverse HFF set-up, the ethanol concentration profiles (Appendix VI-Figure VI-16a) display maximum values at the channel walls from which the component comes and minimum ones in the middle of the mainstream due to the intercept with the acetic acid solution. With the aid of the simulations, these values could be measured for each of the reference positions selected, and an average value in the minimum interval is computed for reference. Starting from Figure V-3a, it is found a minimum value for the normalized ethanol concentration equal to 0.68 mol/m^3 for the flow rate of 1 µl/min, that decrease to 0.22, 0.04, 0.08x10^{-1} and 0.01x10^{-1} for the middle flow rates of 3, 5, 7 and 9 µl/min, respectively.

The set of curves pertaining to xr=0 µm are of great relevance since they display a linear convergence towards a minimum point (FigureV-3b) by representing the thinning of the focusing region due to the gradual extinguishing of the phenomena involved. Minimum points were measured equal to 0.9-0.28 mol/m^3 for the middle FR values from 1 to 9 µl/min.

The same trend can be observed when moving along the channel length (switching to the next location at xr=100 µm), however, an increase of the minimal values to 0.94-0.54 mol/m^3, for FR^2 ranging from 0.2-0.22 is reported. This increase in normalized values is confirmed by the overall shortening of the curves and widening of the curves.

The steady state condition is achieved at the ethanol concentration value of 0.97 and 0.78 for the lower and higher FR^2, respectively. However, a steady state condition is not yet achieved at the reference position of xr=5000 µm (corresponding to 16.5 mm), since small changes from the flattened curves can still be recognized, as even more evident for the higher FR^2 in Figure V-d. Only at the lower FR^2 tested (0.02) is a steady state already achieved at xr=5000 µm.

We can conclude that the rise of the FR^2 slows down the achievement of a steady state condition. The resulting increase of the reaction zone width induces the spatial shifting of the mixing degree, directly impacting on the process progression and establishing a steady state condition that happens downstream along the channel.

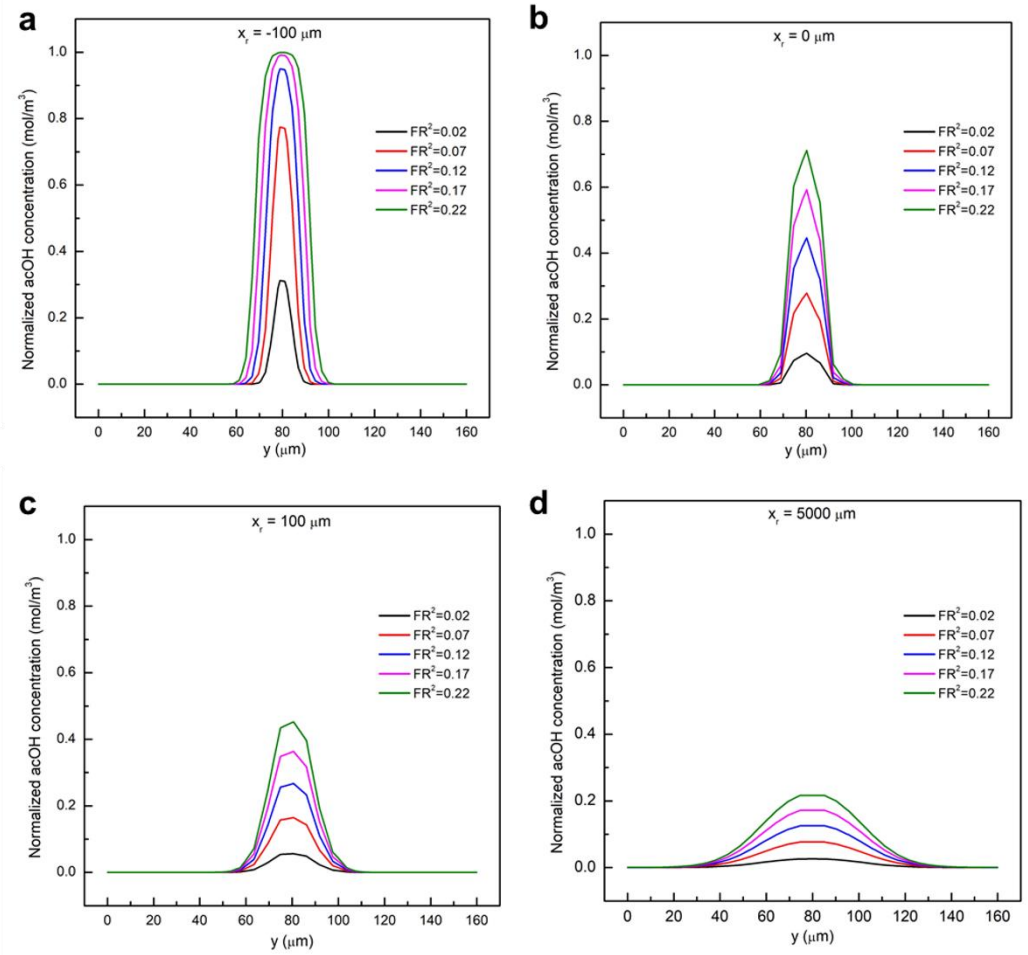

Figure V-4. The impact of FR^2(0.02-0.22) on the acetic acid interdiffusion in terms of normalized acetic acid (acOH) concentration in the main channel width (0-160 µm) at different locations (x_r) along the channel length (0-22.5 mm) evaluated with 2D comsol simulation: **a**) x_r:-100 µm, **b**) x_r: 0 µm, **c**) x_r: 100 µm, **d**) x_r: 5000 µm.

Switching from the normalized ethanol concentration profiles to the acetic acid ones immediately stands out as the perfect mirroring between the plots obtained at all the examined conditions, demonstrating that a mutual interdiffusion occurs globally (Figure V-4). Despite the trends of curves appear to overlap, big differences can be recognized from the normalized values of acetic acid obtained at each location, thus opposite considerations can be done with respect to the previous case.

From FigureV-4a to figure V-4d, it is possible to recognize the expected concentration gradient profile from a usual HFF, with the development of gaussian curves converging to maximum values [37, 38]. Figure V-4a shows the profile established at the centre of the junction connecting inputs in the reference position of xr=-100 µm. The effects of the

massive invasion of the alcoholic solution from side channels can be recognized in the rapid reduction of the acOH concentration from the initial nominal value down to values in the range of 0.30-0.99 mol/m^3 according to the FR^2. As in the previous case, the global trend of curves is maintained when switching from x=-100 µm to x=0 µm (Figure V-4b), however, it is shown the lowering of the averaged maximum values achieved in the focusing region. Quantified values go from 0.30-0.99 mol/m^3 to 0.09-0.71 mol/m^3 for the FR^2 of 0.02-0.22, respectively. When the characteristic curves are established at x=100 µm, these averaged maximum values converge to maximum points achieved at normalized concentration values in the range of 0.05- 0.45 by raising the FR^2 from 0.02 to 0.22.

Also in this case, the increase in the focusing width is brought about by raising the central flow rate ratio up to 0.22, with a consequent slower and more gradual concentration gradient established, that mostly consumes the mixing at the initial section of the flow focusing. When moving along the channel, the evolution of the mixing process can be acknowledged in the significant changes in the curve shapes and the lowering of the maximum values achieved at the centre of the channel. Finally, the system further evolves achieving a steady state condition. At x=5000 µm the steady state is almost ascertained for lower FR^2. A concentration value of 0.02 mol/m^3 for FR^2 equal to 0.02 is obtained (Figure V-4d). For the other conditions, the interdiffusion of components still takes place for longer distances, with a different magnitude according to the FR^2 and steady state conditions are achieved with final values of 0.07-0.21 mol/m^3 for FR2=0.07-0.22, respectively.

The comparison of the curves pertaining to each FR^2 tested, which is evaluated moving along the channel length from x=-100 µm to x=5000 µm gives more insight into the impact of the junction geometry on the gradual evolution of the flow focusing on the mainstream, that drives the mutual interdiffusion of solvents and antisolvents. By looking at the two extreme conditions tested of FR^2 of 0.02 and 0.22, it is possible to detect for the ethanol concentration a minimum change from 0.68 to 0.97 mol/m^3 and from 0.01x10^{-1} to 0.78 mol/m^3 when moving along the channel. Differently, the acetic acid concentration shows a change of maximum value from 0.3 to 0.02 mol/m^3 and from 0.99 to 0.2 mol/m^3 for FR^2 of 0.02 and 0.22, respectively.

By a global comparison of the plots on the variation of fluid interfaces according to the FR^2 tested, the absolute minimum or maximum values depending on whether ethanol or acetic acid is considered, are recorded at the position of xr=-100 µm, namely the location in the middle of the flow focusing junction. Going away, both the reduction of ethanol and acetic acid concentrations occurs along the fluid interfaces with a concentration gradient dependent of FR^2.

IV.2.2.3 Role of Flow focusing junction on modulation of the fluid interfaces

To gain insight into the impact of the expansion of flow focusing region on the modulation of fluid interfaces and the increase of surface area for their mixing, we investigated it along the length of the device for different flow rate ratios.

Due to the symmetry between the two halves of the geometry, just one of them was considered. In particular, we were interested in investigating changes in the normalised

concentration profiles of ethanol (Figure V-5) and acetic acid (Figure V-6) that develop in the entire geometry length (0- 22.5 mm) at different channel widths, starting from the lower wall at yr=0 µm up to the centre at yr=80 µm. To display the development of the normalized concentration profiles along the entire device length, four locations out of the five identified by moving from the lower wall to the centre with a step of 20 µm, were selected in Figure V-5 and Figure V-6.

The effect of the mixing on the normalized ethanol concentration at the selected reference positions yr=20 µm, yr=40 µm, yr=60 µm, yr=80µm, is reported in Figure V-5.

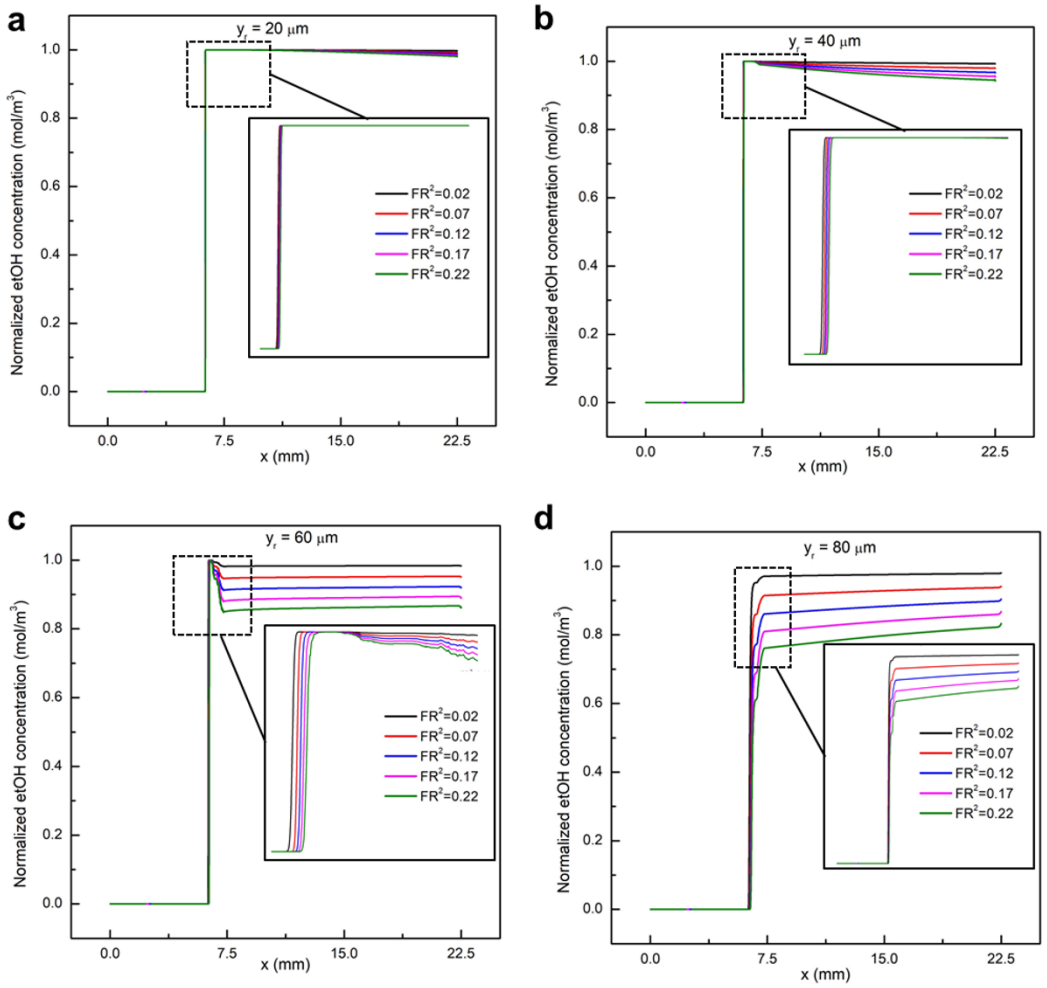

Figure V-5. Impact of FR^2(0.02-0.22) on the development of ethanol normalized concentration profile across the whole channel at different positions along the channel width (y_r) evaluated with 2D comsol simulation: **a**) y_r: 20 µm, **b**) y_r: 40 µm, **c**) y_r: 60 µm, **d**) y_r: 80 µm.

At yr=20 µm and 40 µm close to channel walls (Figure V-5a) the system is so far from the area of components exchange that is only partially affected by the mixing and almost all the device length is required to observed minimal changes. The position yr=60 µm from the walls is interested in components exchange with an amplitude that increases when the central FR rises, as observed from the enlargement of the curves (Figure V-5 c). Moreover, a spatial shift of the mixing along the channel length (x direction) is observed in Figure V-5c. At the centre of the mainstream (yr=80 µm) , it is observed the establishment of an increase of ethanol component as a function of FR^2 (Figure V-5d). The gradual increase in the presence of ethanol at yr=80 µm confirms that the process happens at the interface between the fluids (yr=80-60 µm) and gradually expands to the central stream.

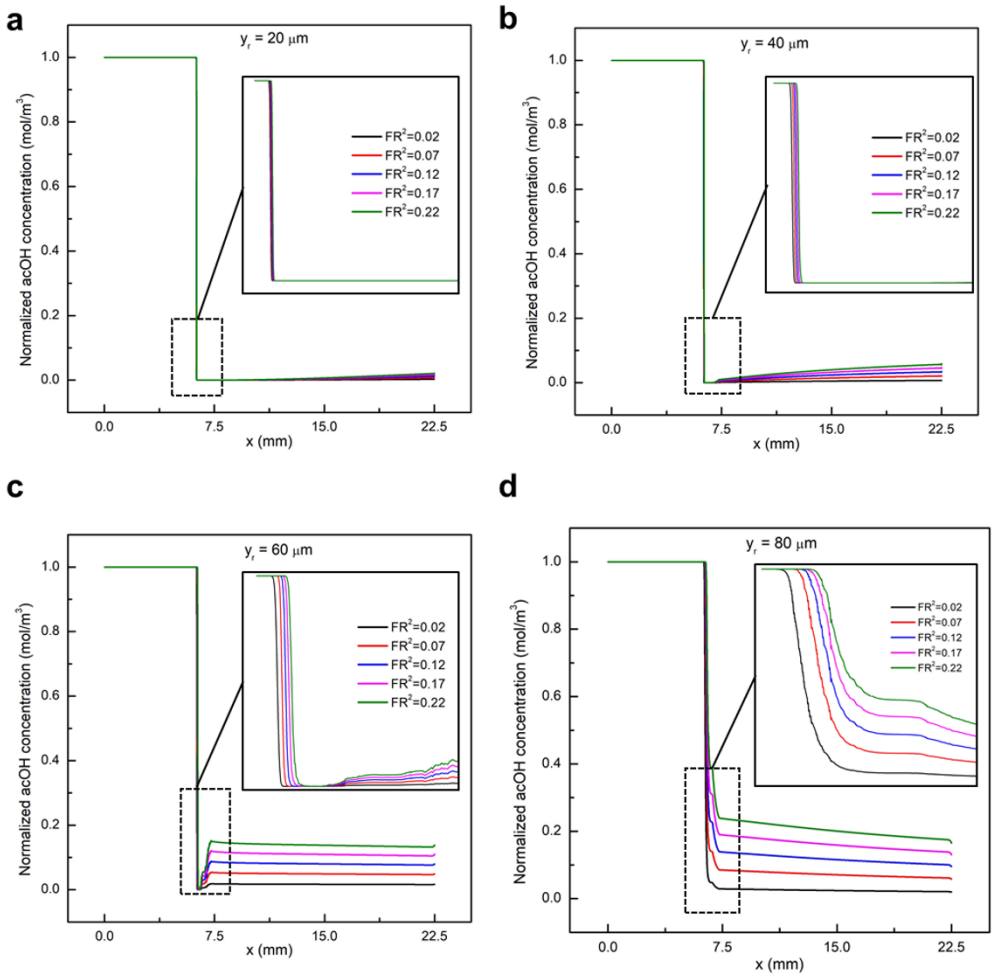

Figure V-6: The impact of FR^2(0.02-0.22) on the development of acetic acid normalized concentration profile across the whole channel at different positions along the channel width evaluated with 2D comsol simulation: **a**) y_r: 20 µm, **b**) y_r: 40 µm, **c**) y_r: 60 µm, **d**) y_r: 80 µm.

The same trend, although opposite, is obtained for the acOH, as shown in Figure V-6. A similar trend can be recognized for the normalised function representing the development of the acOH concentration profile along the entire channel length. However, while the etOH move from null to maximum values since it comes from side channels, the acOH normalised values move from the unit to the minimal ones. From the zoom figures, for both solvents, the wider focusing width caused by the rise of the FR^2 results in a delay in the process extinction that induces the spatial and temporal shifting of the steady state condition.

The channel width interested by the mixing phenomena with a different amplitude according to FR^2 is around 40 um, as reported in Figure V-6. Consequently, a confinement microenvironment for the solvent mixing is established in the device, due to the geometrical choice that puts side channels at 45° with respect to the middle one. With this configuration, side inputs first leverage the solvent extractions and then sheet and envelope the middle stream by driving the solvent extraction and mixing components within a confined stream. Indeed, as already demonstrated by Kunstmann-Olsen et al.[36], the junction's local geometry can modulate the hydrodynamic focusing and, consequently, the long-range divergence of the sample stream.

IV.2.2.4 Role of flow focusing confinement on LiPoNs formation

Figure V-7 shows the comparison of numerical simulations, optical microscopy images and fluorescence images for different FR^2, from 0.02 to 0.22, confirming the results obtained with the simulation regarding the mixing of species. Lower FR^2 resulted in a fluidic configuration in which the middle stream is more squeezed by the side streams, and the area for components exchange was mthinner, so that vanished before the end of the device for the fast mixing among species. Alternatively, by raising the FR^2, the focusing width increased, and a sustained flow focusing profile carried on along the all-channel length.

Following all these comparative studies, we can ascertain that the geometrical design and the flow rate ratio have a significant impact on the gradual progression of the mixing process. Both features can be incorporated in one parameter (f), which is the ratio between the flow focusing width (w_f) and the width of the main channel (w). It gave a measure of the confinement exerted by both the device geometry and flow rate ratio on the mixing of species. As reported by Kunstmann-Olsen[36], who applied a theoretical model of Lee et al.[39] there is a relationship between the device geometry in terms of the sheath angle (θ) and this parameter f, defined as

$$f = \frac{w_f}{w} = \sqrt{\frac{1}{1+3\,r^2+2\,r^2 sin\theta^2}} \qquad (13)$$

where r is the ratio between the one volumetric side flowrate and the middle one.
This model was built considering the change in momentum undergone by the sheath fluid as it turns the corner into the exit channel. It is considered valid under these assumptions: a) Fluids are Newtonian, b) they have equal density and viscosity, c) all the channels of the device have the same cross-sections and d) it is verified under laminar flow conditions. Even though this model was built for square cross-section and neglects 3D effects and velocity

profiles across the flows, we applied this model to our system since almost all the conditions are verified. In our case, the ethanol and water are Newtonian fluids with similar density (water-997 kg/m³and ethanol-789 kg/m³) and viscosity (~1 mPas). We are working under laminar flow conditions as confirmed by the low Reynolds number, around 6.78.

$$Re = \frac{\rho v w}{\mu} = \frac{880 * 0.08 * 160 * 10^{-6}}{1.66 * 10^{-3}} = 6.78 \quad (14)$$

To compute the Reynolds number the density and the viscosity for the ethanol-water mixture (65-35 % v/v) were set to 880 kg/m^3 and 1.66 X 10^{-3} Pa*s, respectively. The mean velocity in the main channel is 0.08 m/s and the width of the devices is 160 µm.

We computed the value f in our experimental conditions with the angle of 45 ° between the channels as reported in table V-2.

Table V-2. Table shows the obtained values for the parameter f and the width of the focused stream W_f with the corresponding Flow rate (ul/min), FR^2 and parameter r.

Middle Flow rate (ul/min)	Side Flow rate (ul/min)	FR^2	r	f	w_f (µm)
1	41	0.02	41.00	0.01	1.95
3	41	0.07	13.67	0.04	5.85
5	41	0.12	8.20	0.06	9.74
7	41	0.17	5.86	0.09	13.61
9	41	0.22	4.56	0.11	17.46

The values of the flow focusing widths obtained with the model mentioned above were confirmed by the comparison with other theoretical models that evaluated the width of the focused stream[22, 24]. Moving from low to high f parameter, there is an extension of the arrowhead-shaped focusing region (from 2 to 17 µm) which influences the relative amounts of convective-diffusion mixing[40] and spatially shifts the complete mixing over the focusing region. This shift impacts the competition between the chitosan precipitation and liposome self-assembly.

As was first reported by Karnik et al.[24], the formation of polymer NPs is mainly controlled by the level of supersaturation of the solute that has to be precipitated. The chitosan nanoprecipitation mainly occurs upon rapid solvent extraction in two stages: the nuclei formation, consisting of a coil of several polymer chains, and its growth for the addition of more polymer chains through a diffusion limited process. In the latter phase, solvent mixing should be complete to avoid further addition of polymer chains. In the cHFF, the chitosan polymer, already at its solubility limit (1 % v/v-AcOH/water), experiences a rapid reduction of acetic acid, leading to its nanoprecipitation. The size of this precipitate is controlled by the growth phase, that in turn is dependent on rate of solvent exchange. From the normalized AcOH concentration profiles, it is possible to distinguish the role of FR^2 in the mixing of components.

Lower focusing width, resulting from lower FR^2, reduces the diffusion length, a higher diffusive mixing and a steep concentration gradient. For lower *f*, in the middle of the cHFF junction, the acetic acid rapidly decreases (see Figure V-4). This fast solvent extraction provides a high level of supersaturation of the species, leading to nucleation and diffusion-limited aggregation of precipitates. Moreover, for lower FR^2, obtained by reducing the middle flow rate, the chitosan material processed in the device is lower with respect to higher FR^2 (increasing *f* value), leading to a reduction in chitosan entrapment within the LiPoNs complex. As a result, we observed a size reduction of the chitosan nuclei formation inside LiPoNs, as reported in Figure V-8 a,b. This finding was also confirmed by the small size around 170 nm and the negative zeta potential (around -10 mV) observed for the *f* values in the range of 0.01-0.04 (Figure V-8e).

Differently, for high *f* (higher FR^2), a higher amount of chitosan is being processed in the device, and a more gradual depletion of acetic acid is reported. Consequently, a significant fraction of chitosan chains remains available to be added to the chitosan precipitate, leading to a big chitosan precipitate within the LiPoNs core (Figure V-8 c). The LiPoNs size increased up to 400.7 nm for *f* value equals 0.09. The zeta potential increased up to 6.2 mv for an *f* value of 0.09 (FR^2 of 0.17) due to the loading of a large chitosan precipitate.

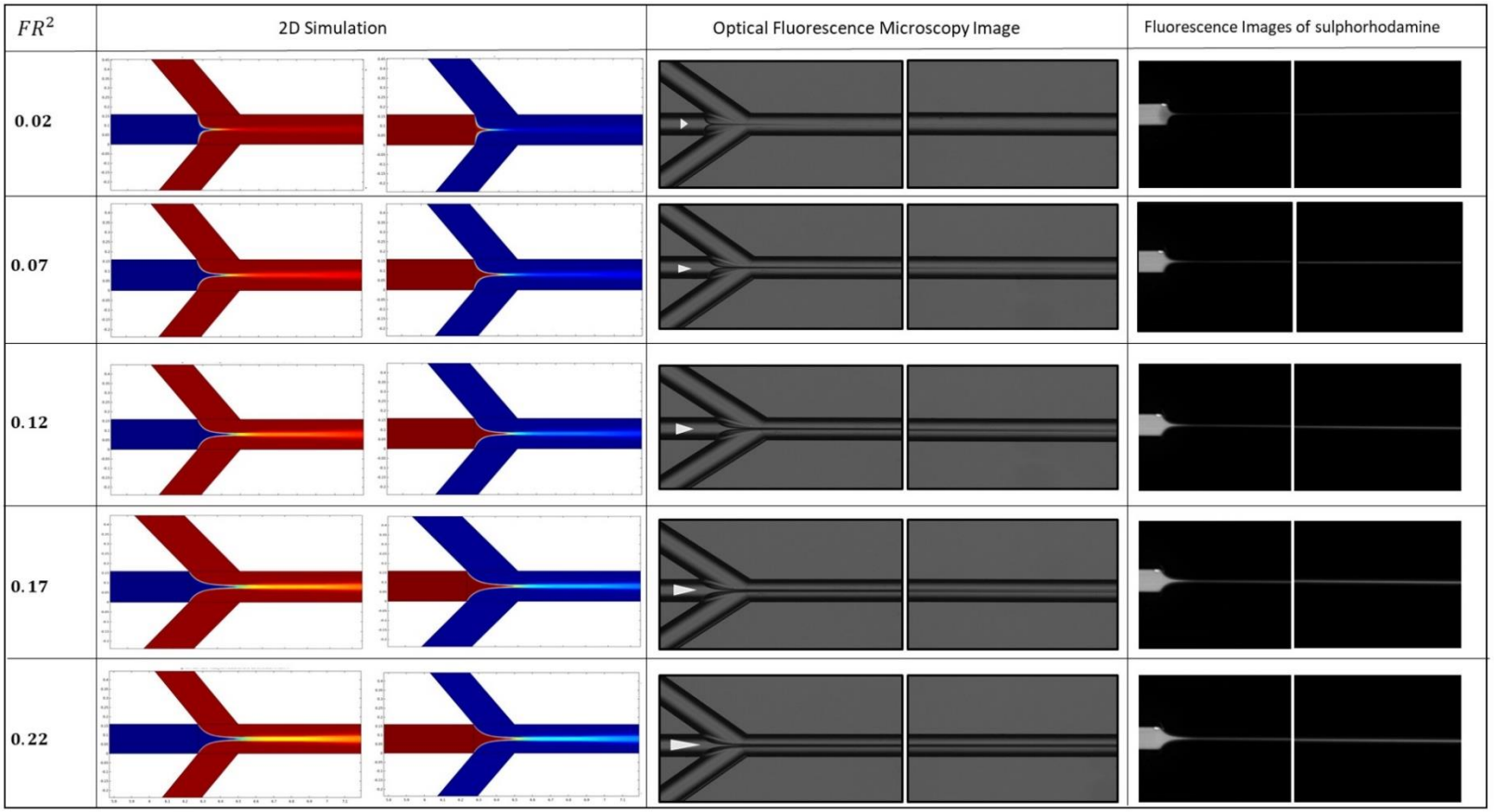

Figure V-7. 2D simulations, optical Fluorescence Microscopy images of flow focusing pattern and fluorescence images of Sulphorhodamine injected in the middle stream at different FR^2.

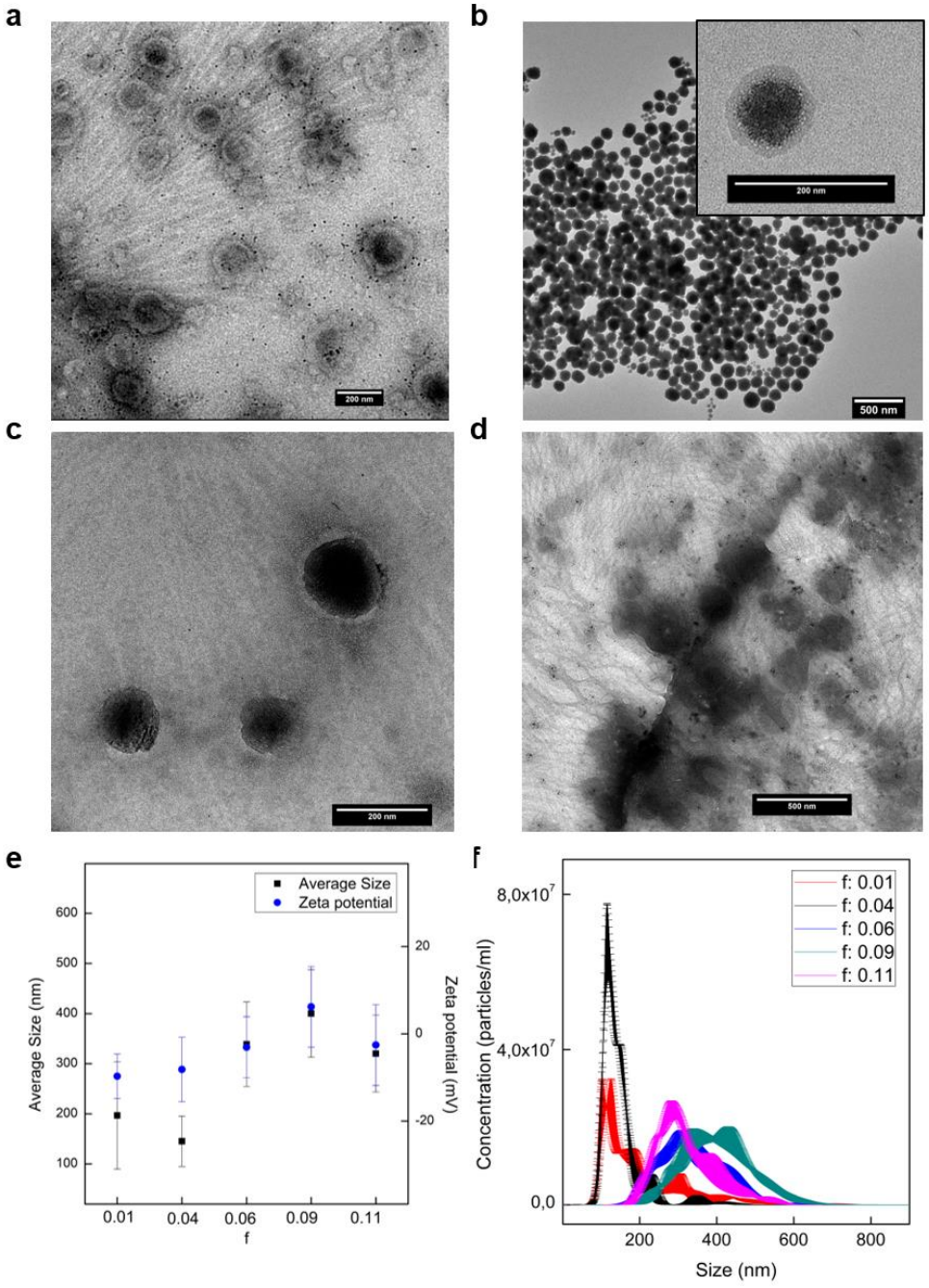

Figure V-8. Morphological characterisation of LiPoNS at different f values. TEM images at different volumetric f values tested: **a**) *f* of 0.01, **b**) *f* of 0.04, **c**) *f* of 0.09, **d**) *f* of 0.11. **e**) Study of the effect of *f* value on the nanoparticle's average size and zeta potential, (**f**) particle size distribution is expressed as the average and standard error of the mean LiPoNs' concentration (particles/mL) evaluated of three measurements for different *f* values.

On the other hand, the self-assembly of liposomes is controlled by the ethanol concentration and microenvironment polarity. In cHFF, the lipid molecules are injected in the side streams encountered the water stream at the junction of the device, where a rapid change in the microenvironmental polarity leads to the formation of lipid fragments. These lipid fragments located at the two-phase interface detect a massive reduction of alcoholic content that induces thermodynamic instabilities at the edge of bilayer fragments, determining their closure into micellar structures [4, 13, 34].

By increasing the *f* value corresponding to an increase of f value up to 0.11 (FR^2 of 0.22), the central aqueous stream induces a steep growth of surrounding microenvironmental polarity resulting in a rapid reduction of organic solvent (Figure V-3), which could impact lipids solubility, compromising a homogenous control of the self-assembly [41]. Therefore, an excess of lipidic material and the formation of chitosan precipitates as uncontrolled morphologies were identified in Figure V-8d.

By decreasing the *f* and consequently the FR^2, the ethanol amount that occupied the device is increasing, however, the microenvironmental polarity at fluid interfaces seems to be enough to induce the self-assembly process. In accordance, Jahn et al.[42] investigating the formation of lipid structures in the microfluidic chip with immediate immobilization of the process, observing that shallow alcohol concentration gradient could promote liposome formation. Therefore, we concluded that for *f* value between 0.01-0.09, obtained at a middle channel flow rate of 1-7 µl/min and side channel flow rate of 41 µL/min, the extraction time was adequate for lipid fragments to aggregate [42] and cover the polymer structures. Therefore, we identified an operative window where the coupling between nanoprecipitation and self-assembly is guaranteed. However, by changing the flow focusing confinement and the extraction time, the extent of lipid coverage and polymer precipitate varied, as reported by the TEM images, NTA analysis and zeta potential. In figure V-8a-d, it is possible to observe a different size of the chitosan core and lipid extent by varying the *f* values.

IV.2.2.5 Model to predict the nanoparticle size in HFF

We followed the considerations on the flow focusing confinement and its impact on the nanoparticle mechanism of formation. In collaboration with Professor Patrick Tabeling of ESPCI University in Paris, we analysed the literature regarding nanoparticle formation, aiming to generalize the effect of fluid patterns on the stability of NPs. In particular, we explored these mechanisms from the perspectives of fluid interfaces and convective-diffusive mixing in the HFF process. Furthermore, we collected data on device geometry and implemented flow rates to rationalize the contribution of the flow focusing width on NPs formation. In particular, we elaborated the data in function of this parameter *f*, described above, that incorporates the geometric contribution of the devices and the flow rate ratio. This parameter allowed the organization of the microfluidic process conditions

with respect to the interfacial phenomena among all the different device geometries. Indeed, by considering the ratio of flow focusing on the device's width, we could compare different microfluidic processes.

A pioneering study of liposomes formation in HFF was conducted in 2004, with the work of Jahn et al. [20]. They guided the self-assembly of liposomes through a two-dimensional flow focusing approach (2D HFF) in a cross-junction device. Lately, they investigated the formation of liposomes in HFF implemented in two microfluidic devices. They used the same species, a mixture of DMPC, DCP, and Cholesterol, in two devices, X- and Y- Junction chips, with different channel dimensions and geometrical scaling[23]. We collected data about the device geometries, the flow rate ratio tested and the diameter of liposomes obtained. The data were plotted in the f parameter function and processed with a linear fitting, as shown in Figure V-9, Table VI-4.

Interestingly, a linear correlation between the liposome size and the *f* parameter emerged, underlying the direct relationship between the flow focusing and the mechanism of NPs formation. This finding was confirmed by the same linear trend observed among different devices (X-Y-Junctions) that processed the same chemicals. For the X-junction device, the intercept is 28.2, with a slope of 786 (Figure V-9a). Similarly, for the Y-junction device, an intercept of 28.1 and a slope of 1273 is reported (Figure V-9b). These trends were both related to the self-assembly of liposomes. Therefore, the good correlation between the curves,especially for low f values, has demonstrated the capability of the parameter *f* to compare and study the mechanism of formation in different devices.

From this knowledge of lipid self-assembly in microfluidics, we interrogated diverse materials and, consequently, other mechanisms of nanoparticle formation in HFF. In this perspective, Karnik et al.[24] in 2008 synthesized PLGA-PEG nanoparticles (NPs) utilizing the assembly of the amphiphilic block-copolymers during nanoprecipitation. The collected data were analysed as reported in figure V-9c, Table VI-4. For PLGA-PEG the relationship reported was almost linear, characterized by a lower slope of 96.8 and an intercept of 17.8 (Figure V-9c).

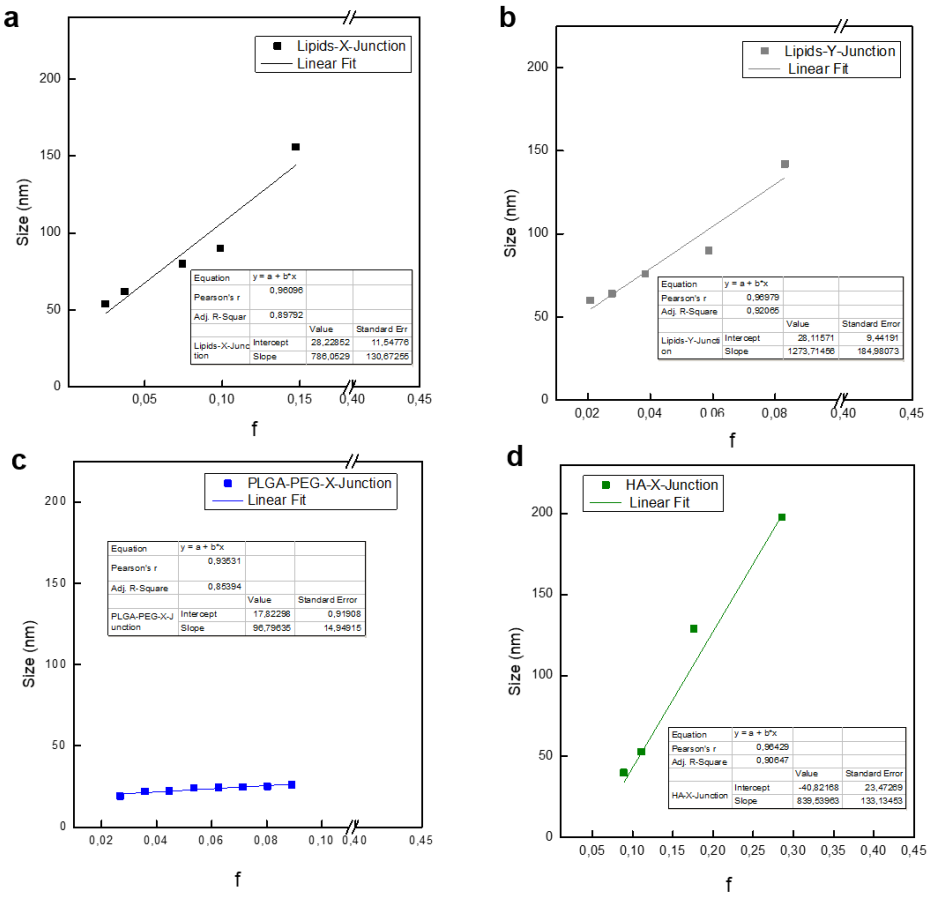

Figure V-9. Linear fitting of nanoparticles size as function of parameter f for different materials in HFF devices. a) Linear fitting of liposomes size in function of the parameter *f* from the data of Jahn and co-workers[23] in X-Junction and b) Y-Junction; c) Linear fitting of polymer nanoparticles (PLGA-PEG) size in function of *f* parameter from the data of Karnik et al.[24] and d) Linear fitting of polymer nanoparticles (HA) size in function of *f* parameter from the data of Russo et al.[26] .

We collected and fitted data on polymer nanoprecipitation to further elucidate this relationship. We selected Hyaluronic acids (HA) as the model polymer. Russo et al.[26] made an extensive study on hyaluronic acid precipitation through HFF in X-junction for the synthesis of crosslinked Hyaluronic Acid Nanoparticles (cHANPs) (Figure V-9d, Table VI-4). As previously reported a correlation between the f parameter and NPs size is observed, with an intercept of -40.8 and slope of 839.5 (Figure V-9d).

Looking to the reported curve (Figure V-9), a linear relation emerged in the form of

$$D = D_0 + A\,f$$

where D represents the nanoparticle diameter and D_0 could be the minimum diameter achieved to have a stable complex. By comparing the linear fitting, for the lipid self-assembly the D_0 is around 28 nm, while for polymer for PLGA-PEG micellization and HA precipitation is around 18 nm and 41 nm, respectively. The value of D_0 varies in the range of 20-30 nm, except for HA polymer that reachs the value of 41 nm. The D_0 could be varied in agreement with the mechanism of formation of NPs.
Regarding the D_0,Kotouček et al.[13] compared the published theoretical and experimental data on the sizes of liposomes composed of EPC, SOPC, and DMPC in different processes. They reported a diameter in the range of 14 to 22 nm, which is in accordance with our proposal on the meaning of D_0. The lower value for D_0, around 17 nm,is reported for PLGA-PEG micellization, where further addition of more unimers to the particles is difficult due to the formation of a polymer brush layer on surface[24]. For the HA nanoprecipitation, the minimum obtained value is 41 nm, where the addition of material is only diffusion-limited, and the polymer chains are more elongated.

Moreover, this increase in the size of HA NPs could be linked to post-processing step rather than to the microfluidic process conditions. Indeed, the purification procedure of cHANPs , crosslinked Hyaluronic Acid Nanoparticles, is the solvent gradient dialysis and involves the use of a large volume of solvent exchange, mainly water. The high affinity of HA polymer with the water could lead an increase in the NPs size. Indeed, the HA polymer is the only material with a negative value for the intercept. In this sense, we are performing new experiments to evaluate the Hyaluronic acid nanoparticle size right after the synthesis in the microfluidic device.
Above these considerations, we hypothesized that nanoparticles' growth is controlled by the addition of other chains to a stable complex D_0 in a linear form. This growth will be dependent on parameter A and the portion of the channel occupied by the flow focusing width (*f*). A reduction in particle size is obtained for the low values of *f* parameter.
Different from the previous model, which relates the nanoparticle size to the mixing of species, where the complete exchange of solvent stabilizes the NPs for further addition[24], here this parameter f is linked to the velocity of species moving in the device and the confinement of molecules.
For laminar flow and fully developed flow, the velocity distribution in the main channel is parabolic, as reported according to Poiseuille flow. The speed gradient, close to the symmetry axis, at a distance w_f from it, is on the order of $\frac{U}{w^2} w_f = \frac{U}{w} f$. Due to the parabolic velocity profile, the f parameter represents the locations in the main channel where the velocity displays higher values, close to the centerline. Considering this aspect, NPs size could depend on velocity streamlines where species are located. The growth of nanoparticles is described by a diffusion limited process, so the location and velocity of species within the devices guide their addition on the surface of NPs. We assume that polymer chains are added to stable ones by a kinematical process, where the flux of species added is linked to the difference in velocity between the two complexes. In this theory, the residence time of NPs within the device becomes relevant because it represents the time available for adding material.

Following these considerations, a key role is exerted by the amount of material available to the growth (number density) and the distance between this material and the stable complex (path length, l). This path length could represent the distance the molecules travel to join the stable complex, which will depend on the number density of material (related to the concentration of species injected in the device, C) and the material properties (polymer or lipid density, ρ).
In this sense, a big difference in nanoparticle growth arises from the conformation and affinity between the solvent and polymer available for the addition, represented in a parameter ε. As previously introduced[43], the interaction between the material to be precipitated and the solvent/nonsolvent composition affects the composition phase and impacts on the properties of the final NPs. In this sense, few studies investigated the impact of polymer/solvent/nonsolvent on the nanoprecipitation process of NPs[44, 45]. Costa Souza Bicudo et al.[46] reported this interaction in continuous processes for the production of Hyaluronic acid NPs. In particular, the lower affinity between the solvent and nonsolvent phase led to a longer molecule persistence at their interfaces, consequently slowing down the supersaturation. As a result, larger particles were obtained. On the contrary, a higher affinity promoted the formation of small NPs.
Therefore, we hypothesized that parameter A could incorporate several process conditions such as the chip length, where the formation is occurring, the path length that the molecules have to travel and the material-solvent affinity. The path length should be associated with the concentration of material available for the growth and the material properties, such as density and molecular weight.

$$D = D_0 + A\,[L, \mathrm{l}(C, \rho), \varepsilon] * f$$

Following all these comparative studies, we can confirm a correlation between NPs size and the confinement of solvents within the device, in the form of hydrodynamic flow focusing. We identified a linear relationship that describes the formation of the nanoparticles within the device. We also assumed that the parameters of this relationship are dependent on the material properties and the process conditions spanning to residence time, distance between species, confinement of material and their conformation.

V.3 SECOND CASE STUDY
Exosomes produced by engineered MDA-MB-231 cells

V.3.1 Introduction

To improve the tumour targeting of lipid-based formulations, the nanomedicine community conducts fundamental and technical research investigating their behaviour in living organisms. To gain insight into the role of lipid material in complex biological environments such as preclinical models, I have been hosted as visiting PhD student in the Genetic Engineering for Multimodality Imaging laboratory at Erasmus University Medical Center (The Netherlands), where I did experimental work on labeled lipid-based nanoparticle for Optical and Nuclear Imaging applications.

The acquired knowledge of lipid-based materials in microfluidics has been applied to the engineering nanosized lipid bilayer vesicles released by the cells, known as extracellular vesicles (EVs). Exosomes are phospholipid-based particles with a size ranging in the nanometer scale, and they represent a homogenous population of vesicles released from cells[47]. They showed significant therapeutic effects in several disease models due to their enhanced stability, low immunogenicity and dosage flexibility. However, several studies reported their off-target distribution in organs rich in blood vessels or associated with the reticuloendothelial system[48]. The complex composition and short half-life of EVs make them challenging to study and evaluate their *in vivo* distribution [49]. To understand the lipid part's contribution in guiding the carriers' fate in the preclinical model, the exosomes have been engineered to be tracked in living organisms. We exploited the bioluminescence of EVs using NanoLuc technology, where the combination of a reporter probe with a reporter protein induces the accumulation of specific signals that can be detected in living subjects[50, 51].

In the case of exosomes, the loading of reporter proteins on exosomes allows tracking the EVs *in vivo* without losing information of unlabelled dye or cargo leakage. Several technologies have been exploited to follow EVs in vivo such as labelling with lipophilic fluorescent dyes[52, 53], radioisotopes[54, 55] and MRI contrast agents[56, 57].

Among them, bioluminescent strategies for EV labelling have gained increased attention[50] due to the high sensitivity of the bioluminescence imaging (BLI) in the preclinical model. Indeed, it is an imaging modality in preclinical research used for small animals that surpass all the others in terms of sensitivity for the absence of background signal. BLI relays on converting chemical energy into light by using enzymes known as luciferases or photoproteins and combining them with luciferins, the substrates[58]. Therefore, the BLI imaging modality requires the genetic engineering of a luciferase gene-based reporter construct, the administration of a luciferin substrate and a detection system for the emitted light[59].

Firstly, Takahashi et al.[60] isolated exosomes from the B16-BL6 murine melanoma cells transfected with a plasmid expressing fusion protein, consisting of Gaussia luciferase and a truncated lactadherin, gLuc-lactadherin. The exosomes were administered to BALB/c mice via intravenous injection. In another study, Gaussia luciferase and metabolic biotinylation

were combined to create a sensitive EV reporter for *in vivo* and *ex vivo*[61]. Recently, Gupta et al.[50] made quantification of extracellular vesicles *in vitro* and *in vivo* using sensitive bioluminescence imaging. In this context, bioluminescence emerges as an effective tool to interrogate mechanisms, verify therapeutic interventions and accelerate the clinical translation of lipid-based carriers[62].
Among several luciferase enzymes, NanoLuc luciferase (NLuc) stands out due to its enhanced stability, small size, 150-fold increase in luminescence and lower background activity[63]. NLuc is a 19.1 kDa luciferase enzyme that relies on the substrate furimazine to produce high intensity, glow-type luminescence. Moreover, it is ATP independent bioluminescent enzyme. Dixon and colleagues engineered a novel binary technology (NanoBiT) that consists of two subunits, high affinity NanoBit (Hi-Bit) and large NanoBit (LgBit). These subunits do not possess enzymatic activity alone, but when combined, they restore their NanoLuc enzymatic activity[64]. This technology was applied to recombinant viruses genetically engineered to express a luciferase produces light from infected cells after substrate (luciferin) administration[65]. Professor Laura Mezzanotte of the Erasmus Medical Center in Rotterdam (Netherlands) developed an innovative system for reporter gene imaging. This technology relays on the LgBit subunit, expressed on the cellular membrane of the infected cells that, upon interaction with the very small HiBiT tag (33 base pairs/11 amino acids), reconstituting the entire Nluc complex, emits light upon the addition of the substrate. Moreover, the infected cells expressed the Green fluorescent proteins. The idea was to take advantage of exosomes' capability of inhering the mother cells' proteins to obtain exosomes with reporter protein that enables their monitoring *in vivo* imaging. In detail, these exosomes isolated from engineered cells display the Lg-Bit units on their external surface and the GFP in their core. Upon interaction with the HiBit units, these EVs restore the Nluc complex, that exhibits a strong bioluminescent signal in the presence of fluorofurimazine substrate. Moreover, the HiBit unit was labelled to radioactive probes, and Indium-DOTA complexes to nuclear medicine.
The idea was to process these engineered cells through an innovative high Throughput Approach Based on a Dynamic High Pressure or microfluidic process for higher scale production of exosomes and for the encapsulation of active agents, such as chemotherapy, for therapeutic applications. Thus, the exosomes would be characterized by the Lg-Bit protein, enabling light emission, and by a therapeutic cargo.
However, to date, we effectively engineered the cells and proved that the exosomes isolated from the cells expose the LgBit unit, which interacts with HiBit tag and successfully emits light. Due to time constraints, we did not process the cells in a microfluidics reactor, nor evaluate the behaviour of produced exosomes *in vivo*. These last steps are currently under investigation.

V.3.2 Result and discussion

Here we reported the development and validation of engineered vesicles by MBA-MB-231 cells for multimodal imaging modalities. The nanosystems are isolated by lentiviral transduction of the human breast cancer cell line MDA-MB-231 with a bioluminescent

reporter, Lg-Bit. Lentivirus technology is an effective tool to transfer heritable genetic material into the genome of any cancer cells. The lentivirus pCDHLgbitTM-EIGFP was produced by the transfection of HEK293T packaging cells with three packaging plasmids pCMV-VSVG, pMDLg-RRE, pRSV-REV and transfer vector plasmid with the Jet-PEI transfection. After 24 -48 h, the medium of the cells containing the lentivirus was collected, centrifuged and filtered (0.45 µm). $70x10^3$ MDA-MB-231 cells were seeded in 24 well plates and transduced with the lentivirus plus polybrene (8 ug/ml). This resulted in the production MDA-MB-231 cells with the expression of the LgBit and green fluorescent proteins as reported in image Figure V-10. The stable clones were selected via the limited dilution method for their GFP expression and Luminescence. The GFP expression was checked by the Echo microscope as shown in figure V-10.

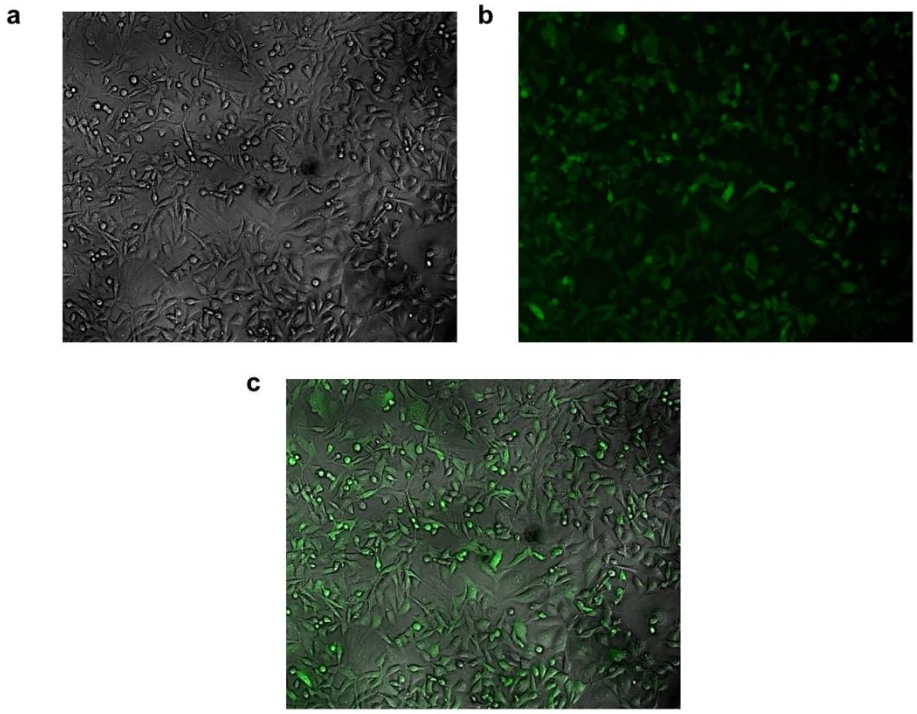

Figure V-10. The expression of GFP of MDA-MB-231 cells for the selected clone after the infection with the lentivirus. Microscope image of MDA-MB-231 cells in **a**) transmission, **b**) fluorescence and **c)** their overlapping.

In order to quantify the expression of Lg-Bit for the infected cells, we seeded the selected clone of MDA-MB-231 cells in a 96-black well plate at a different cellular density ranging from 3.125 to 50.000 cells. The small high-affinity peptide tag was added to the cells at a concentration of 1nM. Then, the bioluminescence signal from wells was measured with IVIS spectrum system (PerkinElmer, Whaltam, MA, USA) at several time points (1, 5, 10, 15, 20, 25 min) post the addition of fluorofurimazine substrate at a concentration of 5 uM. The measurements were run in triplicates. As controls, the luminescence of the untreated cells

and the cells upon the addition of the substrate without the HiBit peptide were evaluated. Data were analysed using Living Image 4.3 software (Perkin Elmer) by drawing the appropriate ROI. As reported in Figure V-11a, the luminescence signal was visible to 25 min. We quantified the luminescence emitted by the cells according to their density in time, as reported in Figure V-11b. A correlation between the signal acquired, and the cellular density is observed above 12500 cells. We observed similar linear kinetics of bioluminescence of MDA-MB-231 cells with a maximum after 25 min of addition of the substrate. This linear increase could be due to the time required by the two subunits to interact and emit light. We effectively produced a viral vector to induce the expression of LgBit and GFP proteins in infected MDA-MB-231 cells. In detail, the LgBit linked to the protein preserved the expression for 25 minutes, confirming the stability of NanoLuc complex. We quantified the fluorofurimazine sensitivity of the engineered cell line at 25 min after the addition of the substrate (Figure V-11c). The signal raised according to the increase of cell number with a high correlation (correlation coefficient 0.99). The nanoLuc/fluorofurimazine pair has already demonstrated the highest bioluminescence intensity, even post-intravenous administration[66]. Therefore, a stable cell line expressing both Lg-Bit unit and GFP was produced.

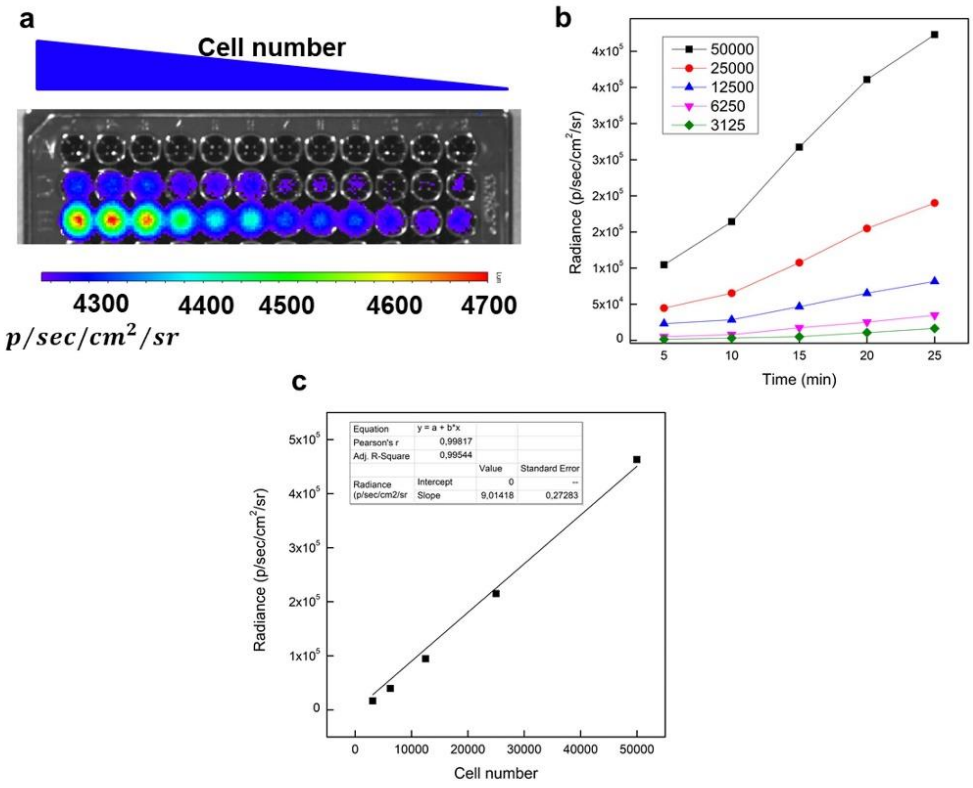

Figure V-11. Correlation between bioluminescence signal and cell number. The MDA-MB-231 cells expressing LgBiT were plated in a 96 black well plates at different cellular densities

from 3125 to 50000. The cells were imaged after the addition of the HiBit peptide (1 nM) and fluorofurimazine (5 uM).**a**) cells imaged after 25 min of addition, first row control cells, second row cells upon the addition of the substrate and third-row cells upon the addition of both the substrate and the peptide, **b**)The cell signal was quantified up to 25 min with an interval of 5 min. **c**) The correlation between the cell number and bioluminescent signal for the timepoint at 25 min.

These MDA-MB-231 cells were cultured in Dulbecco's modified Eagle's medium (DMEM), containing FBS (10% v/v), L-glutamine (1% v/v) and penicillin-streptomycin (1% v/v), at 37 °C in water-saturated air supplemented with 5% CO2. To display the Lg-Bit protein on the EVs surface, we took advantage of the ability of EVs to inherit the proteins, lipids and RNA from the mother cells. This way, a part of proteins linked to LgBit subunit on the cellular membrane of MDA-MB-231 cells were transferred on EV carriers. To isolate exosomes from infected cells, we used the total Exosome Isolation Kit (Invitrogen, life technologies). The cells were seeded in T-75 flask. Two days before collecting the exosomes, the culture medium was replaced with 14 ml of medium without FBS. Then, the collected medium was centrifuged at 2000xg for 30 minutes to remove cell and debris. Next, the total Exosomes isolation reagent was added to the medium in a ratio (1:2) and incubated at 4 °C overnight. After, the sample was centrifuge 10000xg for 1 hour at 4 ° C, the supernatant was removed and the pellet was resuspended in 1 ml of 1X PBS. The sample was diluted in water (1:100) and analysed at NanoSight NS300(NTA) to acquired information on the size and concentration of exosomes produced (Figure VI-7a).

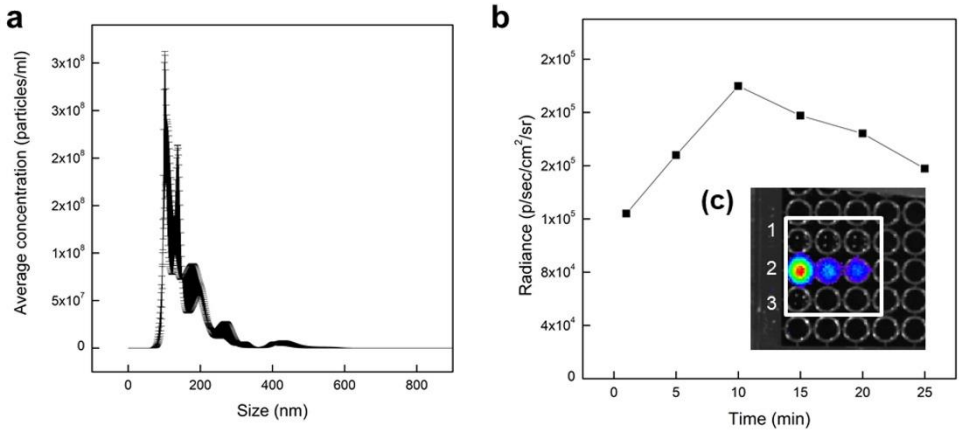

Figure V-12. Exosomes size distribution and their bioluminescent signal. **a**) particle size distribution is expressed as the average and standard error of the mean exosomes (particles/mL) evaluated in water (diluted 1:100) for three measurements; **b**) In vitro bioluminescence imaging following the addition of Hibit peptide (1 nM) and fluorofurimazine (10 uM) substrate to exosomes quantified in time up to 25 min. **c**) The image plate with all conditions tested first row exosomes following the addition of fluorofurimazine, second row exosomes following the addition of peptide and furimazine alone and third row exosomes alone.

The NTA results reported that the mean and the mode of exosomes are 161.4 nm and 110.5 nm, respectively, with 50% of the exosomes being <141.3 nm (Figure V-12a). The exosome concentration was around 1.44xe10 particles/ml. To ensure that the isolated exosomes effectively reported on their membrane, the LgBit, we performed a bioluminescence analysis to quantify the light emitted. 50 ul of exosomes were added to a 96-black well plate with and without adding HiBit peptide (1nM) (Figure V-12b,c). The signals were quantified with the IVIS instrument after adding fluorofurimazine substrate at 10 uM. The graph in the figure reported the luminescence signal emitted by the exosomes upon the interaction with the substrate over time from 0 to 25 min (Figure V-12b).These preliminary results prove that the exosomes extracted by the engineered MDA-MB-231 cells expose on their surface the Lg-Bit that successfully bound the HiBit tag, producing light in presence of fluorofurimazine substrate.

We have demonstrated that this approach can be used to insert exosomes as a target unit for an imaging application. Indeed, these EVs enable valuable data on fate *in vivo* without acquiring information from unlabeled compounds. Bioluminescence represents an ideal imaging modality to follow EVs within the preclinical model. Therefore, this approach that makes the EVs capable of being tracked in the complex biological environment could be used to better understand their *in vivo* fate, making them a detection tool to comprehend the influence exerted by the lipid on nano-bio interactions. To address this point, we plan to inject the produced EVs into a preclinical model in near future. Moreover, the next step will be the production of exosomes by the engineered cells with an innovative approach based on a High Throughput Approach Based on Dynamic High Pressure to improve the physicochemical properties of the EVs and allow their loading with therapeutic compounds[67]. The tissue and tumour targeting ability[68]of exosomes, combined with the possibility to emit light acquired from the engineering cells, make the EVs ideal carriers for theranostic applications.

V.4 CONCLUSIONS

Differently from conventional HFF processes, in coupled HFF, both the middle and side streams are involved in their thermodynamic process and mutually influence the other. This complex interplay between solvent-nonsolvent phases was investigated using a Comsol simulation. Computational fluid dynamics (CFD) provided temporal-spatial distribution of fluid patterns in the microreactor. We studied the effect of the flow rate ratio in modulating the solvent mixing along the device. We related the flow rate ratio to the confinement exerted on the material in the flow focusing, with a parameter *f*. We studied the effect of the *f* parameter, which considers both the FR^2 and the device geometry, on both the nanoprecipitation and the kinetics of vesiculation and, consequently, their effect on the nanocarrier morphology. We identified an operative window where the coupling between the nanoprecipitation and the self-assembly is guaranteed. Once the role of the flow focusing width emerged, we interrogated different HFF processes where single materials (lipid or polymer) were processed to better understand its role in guiding NPs formation. We rationalized the data presented in the literature for the HFF processes to understand the critical parameters in dictating the production of NPs. Interestingly, the correlation between the flow focusing confinement and the resulting NPs size was observed for different HFF processes. Different from the previous model that related the nanoparticle size to the mixing of species, this parameter *f* is associated with the confinement exerted on the molecules and their distribution in the device. Thus, we identified the main players of this linear relationship between the flow focusing confinement to NPs size.

V.5 REFERENCES

[1] M. Antonietti, S. Forster, Vesicles and liposomes: A self-assembly principle beyond lipids, Advanced Materials 15(16) (2003) 1323-1333.
[2] L. Capretto, D. Carugo, S. Mazzitelli, C. Nastruzzi, X.L. Zhang, Microfluidic and lab-on-a-chip preparation routes for organic nanoparticles and vesicular systems for nanomedicine applications, Advanced Drug Delivery Reviews 65(11-12) (2013) 1496-1532.
[3] F. Lince, D.L. Marchisio, A.A. Barresi, Strategies to control the particle size distribution of poly-epsilon-caprolactone nanoparticles for pharmaceutical applications, Journal of Colloid and Interface Science 322(2) (2008) 505-515.
[4] Y.P. Patil, S. Jadhav, Novel methods for liposome preparation, Chemistry and Physics of Lipids 177 (2014) 8-18.
[5] M. Derek, Handbook of Lipid Bilayers, CRC Press2013.
[6] L.H. Salwiczek, N.J. Emery, B. Schlinger, N.S. Clayton, The development of caching and object permanence in western scrub-jays (*Aphelocoma californica*): Which emerges first?, Journal of Comparative Psychology 123(3) (2009) 295-303.
[7] D. Marsh, Thermodynamics of Phospholipid Self-Assembly, Biophysical Journal 102(5) (2012) 1079-1087.
[8] J.N. Israelachvili, Intermolecular and Surface Forces, 3rd Edition, Intermolecular and Surface Forces, 3rd Edition (2011) 1-674.
[9] R. Nagarajan, Molecular packing parameter and surfactant self-assembly: The neglected role of the surfactant tail, Langmuir 18(1) (2002) 31-38.
[10] J. Leng, S.U. Egelhaaf, M.E. Cates, Kinetic pathway of spontaneous vesicle formation, Europhysics Letters 59(2) (2002) 311-317.
[11] D.D. Lasic, THE MECHANISM OF VESICLE FORMATION, Biochemical Journal 256(1) (1988) 1-11.
[12] D.D. Lasic, F.J. Martin, ON THE MECHANISM OF VESICLE FORMATION, Journal of Membrane Science 50(2) (1990) 215-222.
[13] J. Kotoucek, F. Hubatka, J. Masek, P. Kulich, K. Velinska, J. Bezdekova, M. Fojtikova, E. Bartheldyova, A. Tomeckova, J. Straska, D. Hrebik, S. Macaulay, I. Kratochvilova, M. Raska, J. Turanek, Preparation of nanoliposomes by microfluidic mixing in herring-bone channel and the role of membrane fluidity in liposomes formation, Scientific Reports 10(1) (2020).
[14] N.T.K. Thanh, N. Maclean, S. Mahiddine, Mechanisms of Nucleation and Growth of Nanoparticles in Solution, Chemical Reviews 114(15) (2014) 7610-7630.
[15] S.M. D'Addio, R.K. Prud'homme, Controlling drug nanoparticle formation by rapid precipitation, Advanced Drug Delivery Reviews 63(6) (2011) 417-426.
[16] J.S. Tao, S.F. Chow, Y. Zheng, Application of flash nanoprecipitation to fabricate poorly water-soluble drug nanoparticles, Acta Pharmaceutica Sinica B 9(1) (2019) 4-18.
[17] B.K. Johnson, R.K. Prud'homme, Flash NanoPrecipitation of organic actives and block copolymers using a confined impinging jets mixer, Australian Journal of Chemistry 56(10) (2003) 1021-1024.
[18] M.Q. Lu, A. Ozcelik, C.L. Grigsby, Y.H. Zhao, F. Guo, K.W. Leong, T.J. Huang, Microfluidic hydrodynamic focusing for synthesis of nanomaterials, Nano Today 11(6) (2016) 778-792.

[19] B. Amoyav, O. Benny, Controlled and tunable polymer particles' production using a single microfluidic device, Applied Nanoscience 8(4) (2018) 905-914.
[20] A. Jahn, W.N. Vreeland, M. Gaitan, L.E. Locascio, Controlled vesicle self-assembly in microfluidic channels with hydrodynamic focusing, Journal of the American Chemical Society 126(9) (2004) 2674-2675.
[21] A. Jahn, J.E. Reiner, W.N. Vreeland, D.L. DeVoe, L.E. Locascio, M. Gaitan, Preparation of nanoparticles by continuous-flow microfluidics, Journal of Nanoparticle Research 10(6) (2008) 925-934.
[22] A. Jahn, W.N. Vreeland, D.L. DeVoe, L.E. Locascio, M. Gaitan, Microfluidic directed formation of liposomes of controlled size, Langmuir 23(11) (2007) 6289-6293.
[23] A. Jahn, S.M. Stavis, J.S. Hong, W.N. Vreeland, D.L. Devoe, M. Gaitan, Microfluidic Mixing and the Formation of Nanoscale Lipid Vesicles, Acs Nano 4(4) (2010) 2077-2087.
[24] R. Karnik, F. Gu, P. Basto, C. Cannizzaro, L. Dean, W. Kyei-Manu, R. Langer, O.C. Farokhzad, Microfluidic platform for controlled synthesis of polymeric nanoparticles, Nano Letters 8(9) (2008) 2906-2912.
[25] F.S. Majedi, M.M. Hasani-Sadrabadi, S.H. Emami, M.A. Shokrgozar, J.J. VanDersarl, E. Dashtimoghadam, A. Bertsch, P. Renaud, Microfluidic assisted self-assembly of chitosan based nanoparticles as drug delivery agents, Lab on a Chip 13(2) (2013) 204-207.
[26] M. Russo, P. Bevilacqua, P.A. Netti, E. Torino, A Microfluidic Platform to design crosslinked Hyaluronic Acid Nanoparticles (cHANPs) for enhanced MRI, Scientific Reports 6 (2016).
[27] M. Abdelkarim, N.H. Abd Ellah, M. Elsabahy, M. Abdelgawad, S.A. Abouelmagd, Microchannel geometry vs flow parameters for controlling nanoprecipitation of polymeric nanoparticles, Colloids and Surfaces a-Physicochemical and Engineering Aspects 611 (2021).
[28] L. Zhang, Q.H. Chen, Y. Ma, J.S. Sun, Microfluidic Methods for Fabrication and Engineering of Nanoparticle Drug Delivery Systems, Acs Applied Bio Materials 3(1) (2020) 107-120.
[29] J.S. Hong, S.M. Stavis, S.H.D. Lacerda, L.E. Locascio, S.R. Raghavan, M. Gaitan, Microfluidic Directed Self-Assembly of Liposome-Hydrogel Hybrid Nanoparticles, Langmuir 26(13) (2010) 11581-11588.
[30] P.M. Valencia, P.A. Basto, L.F. Zhang, M. Rhee, R. Langer, O.C. Farokhzad, R. Karnik, Single-Step Assembly of Homogenous Lipid - Polymeric and Lipid - Quantum Dot Nanoparticles Enabled by Microfluidic Rapid Mixing, Acs Nano 4(3) (2010) 1671-1679.
[31] B. Gonzalez, N. Calvar, E. Gomez, A. Dominguez, Density, dynamic viscosity, and derived properties of binary mixtures of methanol or ethanol with water, ethyl acetate, and methyl acetate at T=(293.15, 298.15, and 303.15) K, Journal of Chemical Thermodynamics 39(12) (2007) 1578-1588.
[32] B. Gonzalez, A. Dominguez, J. Tojo, Dynamic viscosities, densities, and speed of sound and derived properties of the binary systems acetic acid with water, methanol, ethanol, ethyl acetate and methyl acetate at T = (293.15, 298.15, and 303.15) K at atmospheric pressure, Journal of Chemical and Engineering Data 49(6) (2004) 1590-1596.
[33] S. Amrani, M. Tabrizian, Characterization of Nanoscale Loaded Liposomes Produced by 2D Hydrodynamic Flow Focusing, ACS Biomater Sci Eng 4(2) (2018) 502-513.

[34] A. Jahn, S.M. Stavis, J.S. Hong, W.N. Vreeland, D.L. DeVoe, M. Gaitan, Microfluidic mixing and the formation of nanoscale lipid vesicles, ACS Nano 4(4) (2010) 2077-87.
[35] P. Ninad Dileep Mehendale and Debjani, Hydrodynamic Flow Focusing for Microuidic Cell Sorting Chip, 2014.
[36] C. Kunstmann-Olsen, J.D. Hoyland, H.G. Rubahn, Influence of geometry on hydrodynamic focusing and long-range fluid behavior in PDMS microfluidic chips, Microfluidics and Nanofluidics 12(5) (2012) 795-803.
[37] J. He, L. Wang, Z. Wei, Y. Yang, C. Wang, X. Han, Z. Nie, Vesicular self-assembly of colloidal amphiphiles in microfluidics, ACS Appl Mater Interfaces 5(19) (2013) 9746-51.
[38] H. Lei Wang and Shenghua Ma and Bin Yang and Wenwu Cao and Xiaojun, Morphology-controlled synthesis of Ag nanoparticle decorated poly(o-phenylenediamine) using microfluidics and its application for hydrogen peroxide detection, Chemical Engineering Journal 268 (2015) 102-108.
[39] G.B. Lee, C.C. Chang, S.B. Huang, R.J. Yang, The hydrodynamic focusing effect inside rectangular microchannels, Journal of Micromechanics and Microengineering 16(5) (2006) 1024-1032.
[40] D.E. Hertzog, X. Michalet, M. Jager, X.X. Kong, J.G. Santiago, S. Weiss, O. Bakajin, Femtomole mixer for microsecond kinetic studies of protein folding, Analytical Chemistry 76(24) (2004) 7169-7178.
[41] T.A. Balbino, N.T. Aoki, A.A.M. Gasperini, C.L.P. Oliveira, A.R. Azzoni, L.P. Cavalcanti, L.G. de la Torre, Continuous flow production of cationic liposomes at high lipid concentration in microfluidic devices for gene delivery applications, Chemical Engineering Journal 226 (2013) 423-433.
[42] A. Jahn, F. Lucas, R.A. Wepf, P.S. Dittrich, Freezing Continuous-Flow Self-Assembly in a Microfluidic Device: Toward Imaging of Liposome Formation, Langmuir 29(5) (2013) 1717-1723.
[43] P. Legrand, S. Lesieur, A. Bochot, R. Gref, W. Raatjes, G. Barratt, C. Vauthier, Influence of polymer behaviour in organic solution on the production of polylactide nanoparticles by nanoprecipitation, International Journal of Pharmaceutics 344(1-2) (2007) 33-43.
[44] S. Schenderlein, M. Luck, B.W. Muller, Partial solubility parameters of poly(D,L-lactide-co-glycolide), International Journal of Pharmaceutics 286(1-2) (2004) 19-26.
[45] R.C.S. Bicudo, M.H.A. Santana, Effects of Organic Solvents on Hyaluronic Acid Nanoparticles Obtained by Precipitation and Chemical Crosslinking, Journal of Nanoscience and Nanotechnology 12(3) (2012) 2849-2857.
[46] R.C.S. Bicudo, M.H.A. Santana, Production of hyaluronic acid (HA) nanoparticles by a continuous process inside microchannels: Effects of non-solvents, organic phase flow rate, and HA concentration, Chemical Engineering Science 84 (2012) 134-141.
[47] E. Romano, P.A. Netti, E. Torino, Exosomes in Gliomas: Biogenesis, Isolation, and Preliminary Applications in Nanomedicine, Pharmaceuticals 13(10) (2020).
[48] A.M. Aimaletdinov, M.O. Gomzikova, Tracking of Extracellular Vesicles' Biodistribution: New Methods and Approaches, International Journal of Molecular Sciences 23(19) (2022).

[49] E. Lazaro-Ibanez, F.N. Faruqu, A.F. Saleh, A.M. Silva, J.T.W. Wang, J. Rak, K.T. Al-Jamal, N. Dekker, Selection of Fluorescent, Bioluminescent, and Radioactive Tracers to Accurately Reflect Extracellular Vesicle Biodistribution in Vivo, Acs Nano 15(2) (2021) 3212-3227.
[50] D. Gupta, X.M. Liang, S. Pavlova, O.P.B. Wiklander, G. Corso, Y. Zhao, O. Saher, J. Bost, A.M. Zickler, A. Piffko, C.L. Maire, F.L. Ricklefs, O. Gustafsson, V.C. Llorente, M.O. Gustafsson, R.B. Bostancioglu, D.R. Mamand, D.W. Hagey, A. Gorgens, J.Z. Nordin, S. El Andaloussi, Quantification of extracellular vesicles in vitro and in vivo using sensitive bioluminescence imaging, Journal of Extracellular Vesicles 9(1) (2020).
[51] M.T. Li, Y.C. Wang, M. Liu, X.L. Lan, Multimodality reporter gene imaging: Construction strategies and application, Theranostics 8(11) (2018) 2954-2973.
[52] J.B. Simonsen, Pitfalls associated with lipophilic fluorophore staining of extracellular vesicles for uptake studies, Journal of Extracellular Vesicles 8(1) (2019).
[53] D.C. Watson, D. Bayik, A. Srivatsan, C. Bergamaschi, A. Valentin, G. Niu, J. Bear, M. Monninger, M. Sun, A. Morales-Kastresana, J.C. Jones, B.K. Felber, X.Y. Chen, I. Gursel, G.N. Pavlakis, Efficient production and enhanced tumor delivery of engineered extracellular vesicles, Biomaterials 105 (2016) 195-205.
[54] D.W. Hwang, H. Choi, S.C. Jang, M.Y. Yoo, J.Y. Park, N.E. Choi, H.J. Oh, S. Ha, Y.S. Lee, J.M. Jeong, Y.S. Gho, D.S. Lee, Noninvasive imaging of radiolabeled exosome-mimetic nanovesicle using Tc-99m-HMPAO, Scientific Reports 5 (2015).
[55] Z. Varga, I. Gyurko, K. Paloczi, E.I. Buzas, I. Horvath, N. Hegedus, D. Mathe, K. Szigeti, Radiolabeling of Extracellular Vesicles with Tc-99m for Quantitative In Vivo Imaging Studies, Cancer Biotherapy and Radiopharmaceuticals 31(5) (2016) 168-173.
[56] A. Busato, R. Bonafede, P. Bontempi, I. Scambi, L. Schiaffino, D. Benati, M. Malatesta, A. Sbarbati, P. Marzola, R. Mariotti, Magnetic resonance imaging of ultrasmall superparamagnetic iron oxide-labeled exosomes from stem cells: a new method to obtain labeled exosomes, International Journal of Nanomedicine 11 (2016) 2481-2490.
[57] L.Z. Hu, S.A. Wickline, J.L. Hood, Magnetic resonance imaging of melanoma exosomes in lymph nodes, Magnetic Resonance in Medicine 74(1) (2015) 266-271.
[58] N. Alsawaftah, A. Farooq, S. Dhou, A.F. Majdalawieh, Bioluminescence Imaging Applications in Cancer: A Comprehensive Review, Ieee Reviews in Biomedical Engineering 14 (2021) 307-326.
[59] L. Mezzanotte, M. van 't Root, H. Karatas, E.A. Goun, C. Lowik, In Vivo Molecular Bioluminescence Imaging: New Tools and Applications, Trends in Biotechnology 35(7) (2017) 640-652.
[60] Y. Takahashi, M. Nishikawa, H. Shinotsuka, Y. Matsui, S. Ohara, T. Imai, Y. Takakura, Visualization and in vivo tracking of the exosomes of murine melanoma B16-BL6 cells in mice after intravenous injection, Journal of Biotechnology 165(2) (2013) 77-84.
[61] C.P. Lai, O. Mardini, M. Ericsson, S. Prabhakar, C.A. Maguire, J.W. Chen, B.A. Tannous, X.O. Breakefield, Dynamic Biodistribution of Extracellular Vesicles in Vivo Using a Multimodal Imaging Reporter, Acs Nano 8(1) (2014) 483-494.
[62] G.D. Luker, K.E. Luker, Optical imaging: Current applications and future directions, Journal of Nuclear Medicine 49(1) (2008) 1-4.

[63] C.G. England, E.B. Ehlerding, W.B. Cai, NanoLuc: A Small Luciferase Is Brightening Up the Field of Bioluminescence, Bioconjugate Chemistry 27(5) (2016) 1175-1187.
[64] A.S. Dixon, M.K. Schwinn, M.P. Hall, K. Zimmerman, P. Otto, T.H. Lubben, B.L. Butler, B.F. Binkowski, T. Machleidt, T.A. Kirkland, M.G. Wood, C.T. Eggers, L.P. Encell, K.V. Wood, NanoLuc Complementation Reporter Optimized for Accurate Measurement of Protein Interactions in Cells, Acs Chemical Biology 11(2) (2016) 400-408.
[65] N. Gaspar, G. Zambito, I.J.C. Dautzenberg, S.J. Cramer, R.C. Hoeben, C. Lowik, J.R. Walker, T.A. Kirkland, T.P. Smith, W.M. van Weerden, J. de Vrij, L. Mezzanotte, NanoBiT System and Hydrofurimazine for Optimized Detection of Viral Infection in Mice-A Novel in Vivo Imaging Platform, International Journal of Molecular Sciences 21(16) (2020).
[66] N. Gaspar, J.R. Walker, G. Zambito, K. Marella-Panth, C. Lowik, T.A. Kirkland, L. Mezzanotte, Evaluation of NanoLuc substrates for bioluminescence imaging of transferred cells in mice, Journal of Photochemistry and Photobiology B-Biology 216 (2021).
[67] E. Romano, P.A. Netti, E. Torino, A High Throughput Approach Based on Dynamic High Pressure for the Encapsulation of Active Compounds in Exosomes for Precision Medicine, International Journal of Molecular Sciences 22(18) (2021).
[68] S.M. Patil, S.S. Sawant, N.K. Kunda, Exosomes as drug delivery systems: A brief overview and progress update, European Journal of Pharmaceutics and Biopharmaceutics 154 (2020) 259-269.

DISCUSSION AND CONCLUSIONS

Stability is defined as the extent to which a product preserves the properties and characteristics acquired at the time of manufacturing[1]. Stability is a transversal concept that runs through manufacturing, storage, *in vitro*/*in vivo* applications, and finally, shipping. Generally, it is classified in chemical, physical, microbiological, therapeutic, and toxicological terms[1]. It is of paramount importance in the pharmaceutical industry because it directly impacts the safety and efficacy of drug products[2]. This challenging issue has gathered the regulatory authorities of Europe, Japan and the USA, and experts from the pharmaceutical industry to discuss scientific and technical aspects of drug-product registration at the International Conference on Harmonisation of Technical Requirements for Registration of Pharmaceuticals for Human Use (ICH). The defined guidelines and recommendations outlined in the ICH guidelines Q1A(R2), Q1C, and Q5C have become the standards for stability in the pharmaceutical industry[2-4].

The concept of stability also affects basic research because it alters the NPs physiochemical properties (size, shape and charge), directly influencing the *in vitro* behaviour (morphological evaluation, imaging, cell uptake, cytotoxicity, dose calculation) and *in vivo* outcome (pharmacokinetics, biodistribution, toxicity) of NPs[5]. All mentioned makes it difficult to assess and rationalize the nanoparticles' biological and therapeutic contributions, *in vitro* and *in vivo*, among nanoformulations.

To date, many efforts have been made to overcome instability. However, the efficacy of several nanoformulations still needs to be improved due to their poor physiochemical and biological stability. In this framework, liposomes have been widely investigated as a drug carrier for cancer treatment showing promising results [4], even though stability issue arises from their constitutive component, the lipids, that can undergo chemical degradation reactions such as hydrolysis of the ester bonds linking the fatty acids to the glycerol backbone and peroxidation of unsaturated acyl chains[4, 6, 7].

Then, the fusion, aggregation and coalescence alter the liposome formulation's physical stability, resulting in the formation of large vesicles or altered morphologies, compromising the cargo loading[8]. These instabilities pathways not only alter the liposomes in self-storage or shipping but also in biological contexts characterized by harsh temperatures and environmental conditions[8]. All these instabilities directly alter their biological activity with safety concerns. Indeed, the larger particles (>5 µm) could lead to capillary blockade and embolism after intravenous administration[9]. Moreover, the uncontrolled release or leakage of the encapsulated core may lead to off-target accumulation of undesired and toxic material[8].

Furthermore, the absence of control of size, shape and charge due to physiochemical instabilities leads to a loss of predictability of liposome formulation upon systemic administration. The physicochemical properties of liposomes dictate the adsorption of biomolecules on their surface, which becomes the new interface seen during the nano-cellular interactions across the multiple barriers during their in vivo journey[10-12]. Therefore, the stability issue arises in a dynamic interplay between synthetic identity, biological identity, and their *in vivo* fate, making this biological framework even more complex for liposomes.

Despite these instability issues, lipid-based formulations present several advantages, such as high biocompatibility, low immunogenicity and improved deformability[13, 14]. Due to their soft colloidal nature, lipid composition and tunable fluidity, the liposomes stand out in the cell/ tissue interactions[15-17]. They easily penetrate the tumour by particle diffusion through the intercellular space[18-20]. The lipid-based carriers are internalized in the cells through many endocytic routes, adding the fusion with the plasma membrane [14].

The rapid elimination from the blood, the low stability of liposomes and consequently, the low tumour accumulations have led to the development of several strategies for improving their efficacy. Among them, surface modification of liposomes with PEG-ylation[21], ligand molecules, such as aptamer[22] and peptides/proteins[23] can be mentioned. Moreover, other radical strategies employment of stimulus-responsive features[24] on the surface of the liposome or to the constituent building blocks have been employed[25]. However, any modifications, especially on the liposomes' surface, can alter and limit the biomimetic nature of lipid components, so losing their peculiar affinity with cells, as already reported for PEGylated liposomes[25, 26].

Compared to these complex modifications, we *firstly* demonstrated that it is possible to preserve the advantageous features of the lipids assembly, such as the "deformability" and cellular uptake behaviour, but in concert, improve their loading ability, stability to the hemodynamics and tissue penetration, integrating a polymer component to the nanoformulation[27, 28]. We produced hybrid lipid-polymer nanoparticles (LiPoNs) made up of a chitosan core covered by a lipid bilayer that not only took advantage of the inherent properties of each bulk material but their combination provided new functionality to the carrier. We have rationally programmed the material configuration/assembly in lipid-polymer NPs, where each building block addressed stability upon nano-bio interactions. Indeed, the lipid bilayer, composed of a mixture of phosphatidylcholine (PC) and cholesterol aimed to confer fluidity, cohesiveness and biomimetic nature to the carriers, reducing the destabilization upon protein interactions [29-31]. On the other hand, the chitosan matrix provided mechanical strength and acted as a reservoir for multiple compounds loading. At the cellular level, the lipophilic surface enhanced the intracellular delivery of complex as demonstrated by the high cell internalization in the first 4 hours of LiPoNs. We assumed that the un-crosslinked core in LiPoNs could confer a moderate

elasticity to nanoparticles, mediating both fusion and endocytosis internalization pathways, and enhancing the delivery of compounds to the cells[32]. In this sense, the LiPoNs mediated-delivery speeded up the chemotherapy uptake and increased the cytotoxicity at a reduced concentration on U-87 MG cells.

The results prove that there is no need to create or synthesize new materials with unknown biological properties to improve the efficacy of nanoparticles but exploiting the available ones in a different manner creates new nano-bio interfaces. The stability aspect has to be considered from the development phase through the lifecycle of the drug product in order to ensure a safe and effective formulation [4]. In this context, the proper design of the materials was combined with a manufacturing procedure that guaranteed a homogeneous reaction environment to obtain the hybrid LiPoNs, in a predictable and reproducible manner, like microfluidics.

Microfluidics is a key player in programming each building block's assembly, which guides the lipid and polymer coupling spatially and temporally. A considerable effort has been made to study the synthesis in microfluidics of lipid-based and polymer-based NPs, separately[33]. Generally, in the hydrodynamic flow focusing process, the nanoparticles are produced by injecting the lipid or polymer material in the main stream dissolved in a solvent phase that is focused by a nonsolvent phase flowing through side streams[34-36]. For the production of hybrid NPs, the hydrodynamic flow focusing has been linked or modified with other flow patterns to face the complexity of guiding both mechanisms of formation[37-39], lipid self-assembly and polymer nanoprecipitation in one device. Here is presented an innovative hydrodynamic flow focusing approach for producing hybrid lipid-polymer NPs (LiPoNs). The coupled hydrodynamic flow focusing (cHFF) is implemented by injecting the chitosan dissolved in an acid solution in the middle stream while the lipids dissolved in an ethanol/water solution are injected from the side streams[40]. In this way, each material is involved in its own thermodynamic process and mutually influences the other one. The cHFF features govern the competition of two solvent extractions and consequently coordinate the relative kinetics of nuclei and the growth of two phenomena, self-assembly and nanoprecipitation. In the focusing region, there is the rapid extraction of acetic acid that leads to the formation of chitosan nuclei. Simultaneously, the increase in the microenvironmental polarity due to ethanol extraction induces the formation of lipid bilayer fragments. Then, these bilayer fragments cover the polymer precipitate stabilizing the whole LiPoNs complex.

The assembly of the building blocks, polymer and lipids into higher-order nanostructures is highly susceptible to the microenvironmental conditions, the degree of solvent exchange and the ratio of component concentrations. In this context, the cHFF does not represent a simple shrinking of a batch process, but the mass transfer phenomena and hydrodynamics have a fundamental role in the coupling phenomenon. The cHFF, working in laminar flow conditions, offers well-defined and predictable interfacial regions to manipulate solvent

transversal diffusion and mediate colloid assembly into an ordered structure via forced interaction of intermediate precipitate. By governing the mixing rate across the exchange areas and the fluid dynamics, it is possible to control the relative kinetics of both mechanisms of formations to obtain NPs with different material extent and, consequently, morphologies. These results open new possibilities to guide and couple separately thermodynamics mechanisms in one step process to produce a library of NPs with different materials, physiochemical and mechanical properties[41].

These results support the concept that the microfluidics governing the material conformation, the component concentrations, solvent displacement, and the amount of water entrapped between the polymer and lipid shell could provide hybrid NPs with well-defined properties to fill the gap of knowledge on the role exerted by the rigidity of NPs on biological barriers. It is worth mentioning that by changing the extent of crosslinking of the polymer core and the extent of water between the lipid shell and polymer core[42] is possible to tune the mechanical properties of lipid-polymer NPs. Any changes in these sophisticated nanoparticles guide different nano-bio interactions, as demonstrated by Sun et al.[39], who observed that the rigidity, induced by the different lipid coverage, changed the cell–particle interaction.

Subsequently, to further elucidate the role of materials and their complexation in presenting a stable cargo to the cells, we selected very challenging biologics characterized by low intrinsic stability, like microRNAs.
We identified two highly dysregulated microRNAs in breast cancer, miR-21 (upregulated)[43, 44] and miR-622 (downregulated)[45]. Therefore, we entrapped in LiPoNs and delivered to the cells an antisense oligonucleotide, AntimiR-21, to block the miR-21 processing and miR-622 to restore its tumour suppressor function separately.

The microRNAs have been defined as master regulators in cancer due to their involvement in several oncogenic pathways, spanning from cell cycle regulation, metabolism, cell death and metastasis[46]. The high selectivity and specificity of nucleic acids at the molecular level have made them a promising tool for cancer treatments. However, no miRNAs-based drugs have entered Phase III clinical trials, and only ten have reached the clinical trials, with half halted [47]. Several concerns are related to their clinical use, such as low stability and integrity in blood circulation, low cellular uptake and intracellular release[48]. Moreover, they showed undesired toxicity and activation of the immune system upon intravenous administration[46]. Thus, many strategies to face their big challenge, stability, have been investigated, from chemical modifications to viral-based and non-viral-based approaches. The former modified the structure chemically to reduce the nuclease degradation[49, 50], however, this approach does not promote their tissue penetration and intracellular delivery. Differently, the viral based strategies showed the highest and longest transfection efficacy with respect to the other methods[51, 52], but their use is limited due to safety concerns[53]. In this scenario, materials science, through the rational design of a

component, represents the most promising approach for microRNAs, as already proved by the success of lipid nanoparticles for mRNA vaccines[14, 54]. Among the lipid-based carriers, the cationic lipids have shown promising results due to their high interaction with the cell membrane[55]. However, they induce vacuolization, reduce cell activity, cause liver toxicity and induce immune response through type I and type II interferon[25, 46, 56]. Nevertheless, these findings on cationic lipid-based NPs have demonstrated the effective contribution of both the lipid matrix and the positive charge in improving cellular interactions, leading to the development of programmable lipid-based carriers such as liposomes with ionizable lipids[14].

In this scenario, the idea was to take advantage of the LiPoNs to stabilize the nucleic acids at nano-bio interactions without chemically modifying or physically altering the microRNAs' structure to preserve their functioning. Among natural polymers, chitosan stands out for its low immunogenicity, excellent biocompatibility, and high positive charge. At acid pH, the amine groups of the chitosan are protonated and become cationic, making the complexation with negatively charged nucleic acid easy, establishing a strong electrostatic interaction and producing a stable complex against nuclease degradation[48, 57]. This positive nanocomplex has a favourable electrostatic interaction with the negatively charged cell membrane, increasing the possibility of its cellular uptake. Upon internalization, the acid pH of the endosomes protonates the amine groups of the chitosan leading to an influx of water and chloride ions to neutralize these charges, which may lead to a rapture of endosomes and the final release of the microRNAs[58-60]. Simultaneously, the lipid coverage can present the chitosan-microRNA complex directly to the cell cytoplasm through the fusion with the cell membrane[59, 60]. Thus, the role of chitosan is to protect the nucleic acids from both extracellular and intracellular degradation, as proved by the enhanced capability of AntimiR-21 loaded LiPoNs to bind the miR-21 effectively and induce its silencing respect to naked miR-21 and Lipofectamine mediated delivery. A reduction of miR-21 expression from 1 to 0.08 is reported for the cells treated with AntimiR-21- LiPoNs compared to 0.26 of Lipofectamine-mediated delivery. The enhanced blockage of miR-21, promoted by the AntimiR-21- LiPoNs, prevented its binding to target mRNA and consequently induced the upregulation of its targeted genes, PTEN and PDCD4. Moreover, the release AntmiR-21 properly functioned by upregulating the PTEN expression up to 4.77, while PDCD4 to 7.3 times concerning the control LiPoNs treated cells. No increase of both target genes is reported for free AntimiR-21, underlying the inefficient internalization of naked antisense miRNA. As a result, the MDA-MB-231 cells transfected with the AntimiR-21- LiPoNs reduce their motility and invasion ability.

Going beyond cellular delivery, further challenges to delivery of microRNAs are the targeting and the penetration in the tumour site. We preliminary study the biodistribution of LiPoNs in the orthotopic syngeneic murine model of breast cancer. From *ex vivo* analysis, LiPoNs seem effectively exploit the EPR effect to accumulate in the tumour tissue, with a

moderate location in the liver. Then, the antitumoral effect of miR-622-Gd-DTPA loaded LiPoNs was evaluated, reporting an inhibition of tumour growth.
The delivery of stable and functional microRNAs is evidence that the chitosan-miRNA complex enveloped in a lipid shell provides higher protection for microRNA molecules to RNA nuclease in a medium containing 10 % of serum and in a complex biological environment. The lipid cover represents a beneficial strategy to limit the blood proteins that can compete with nucleic acids and promote their premature release[61, 62]. Moreover, this lipid bilayer enhances the cellular penetration of the chitosan complexes due to their biomimetic nature. Thus, the chitosan can gain entry without compromising its integrity and avoiding the unfavourable cytotoxic effects reported by the interaction of positive NPs with the cellular membrane.

The ability of LiPoNs to present the microRNA in the cytoplasm without losing material in and out of the cells could allow for keeping the dose as low as possible, facing the lack of knowledge on the off-target and on-target toxicity of microRNAs. One of the major obstacles in microRNA use *in vivo* is identifying the proper dosage that is beyond the physiological range but does not induce any unpredictable off-target effects[46-48, 63]. Indeed, one single microRNA can regulate several genes inducing several off-target toxicities[48]. Moreover, an excessive amount of exogenous microRNAs can lead to competition for the RISC complex that can oust other endogenous miRNAs from it[63], altering the physiology of the cells. Therefore, the LiPoNs targeting the cancer cells could reduce the off-target effect on healthy cells and the use of excessive exogenous microRNAs.

From a technological perspective, we designed an innovative microfluidics process that sheeting a chitosan solution containing the microRNAs with two lipids streams forces the entrapment of the microRNAs in the hybrid Lipid-Polymer NPs, stabilizing the whole complex. The microfluidics potential has already been exploited to entrap large biomolecules such as siRNA, mRNA and DNA [64-67]. However, to the best of our knowledge, fewer efforts have been made to use it to produce microRNAs loaded nanoparticles. Microfluidics, with respect to the available approaches, provides fine control over process parameters reducing the potential risk for miRNA degradation and obtaining particles with tunable features, controlled size distribution, high-loading ability and programmable release rate [68, 69]. Indeed, the employment of lipid-polymer NPs in miRNA delivery is still limited by the extreme processing conditions, such as harsh temperatures, pH, potentially toxic solvents, and post-production steps, that pose a challenge for the entrapping of miRNAs [48, 69]. Moreover, the miniaturisation [70] and eventually the parallelisation [65]of batch systems down to a few centimetre squares through a microfluidic device lead to a homogeneous reaction environment obtaining a fine-tuning of the process parameters even at large-scale production, paving the way for a clinical translation[71]. Indeed, one of the obstacles faced by the pharmaceutical

companies for the production of the mRNA vaccines was the industrial scale-up of conventional batch methods for massive production of LNPs[69].

After, the role of nanomaterials in mediating cell-nano-bio interactions was investigated with a high throughput cell scanning instrument. During the contact with LiPoNs, the dynamic of live cells was analysed for 48 hours in terms of morphology, proliferation and motility.

Massive efforts have been made to find a relationship between NPs' synthetic properties, including size, shape, charge and surface coating, and cell internalization pathways[72-74]. Despite NP's capability to impact and alter cellular physiology at function levels, there still needs to be a greater understanding of these interactions. Indeed, several studies have focused on evaluating these internalization mechanisms on cell biological response, mainly cytotoxicity [72-74]. Among these changes, abnormal mitochondrial activity, ROS production, cytoskeletal alteration, intracellular calcium accumulation and membrane currents alteration were reported by Panariti et.[17].
The increased generation of reactive oxygen species (ROS) following the exposure of NPs, a symptom of an inflammatory reaction, is interconnected with cytoskeleton reorganization. Indeed, the reduction in mitochondrial activity induces a decrease in ATP production, which is necessary for cell functioning, such as motility and intracellular trafficking[75]. Furthermore, any alterations to cell mechanics directly affect movement, division, healing and endocytosis of the cells[72, 76]. The latter aspect is of particular interest for NPs since, upon their internalization are accumulated and moved in the perinuclear region against diffusion gradient, probably due to local energy generated by the cytoskeleton[77-80]. From an energetical point of view, this active transport of NPs leads to energy consumption for the cells that have to be accounted for and summed up to regular cell requests, maybe saturating the pre-existing routes[79]. Furthermore, as previously reported, an increased concentration of Ca^{2+} upon contact with cation NPs/zinc oxide/cerium directly impacts intracellular signalling pathways due to the activation of protein kinase C[81-84]. Finally, the impact of tangential forces on the CM is directly transfected to the cytoskeleton or activated channels that increase the cell curvature and alter the ion-channel activity[85, 86].
From these considerations, the NPs stand out not only as passive carriers but as active players in cell molecular processes[17]. In the same direction, we reported an alteration of cell morphology, motility and proliferation upon interaction with LiPoNs. We observed a change in cell morphology upon the LiPoNs contact that progressively disappeared in time. Following this transitory phase, the cells seemed to reduce their proliferation and growth rate, as confirmed by the rise in doubling time, reduction in cell count and slow increase in the total dry mass. We hypothesized a slowdown of the cell function but not their arrest since the cells do not lose the capability of undergoing mitotic events. Interestingly, the cells increased their instantaneous velocity over a longer time, maybe due to the reduction of cell duplications that led them to preserve their shape and path.

These results demonstrate the impact of LiPoNs on cell machinery. This physical manipulation of cells, as inhibition of cell attachment and reduced cell spreading, was observed under exposure to acoustic fields and fluid flows[87]. Devendran et al.[87] reported that this altered state could be due to an increase in cellular metabolic activity without any impact on viability rates. Therefore, we hypothesized that the cells, following mechanical resistance exerted by LiPoNs, modified their shape, and slow down their biological functions without altering their viability rate, as confirmed by the MTT assay. Therefore, there could be a change in the cell metabolic activity. However, this behaviour required further investigation. The data collected on cell alterations upon the treatments with microRNA loaded NPs show a distinguished behaviour of cells with respect to control cells and cells transfected with common available transfecting agents. However, no differences with the treatment of LiPoNs alone were reported. It might need a longer time of observation to complete the cell cycle.

These results demonstrated a scientific knowledge gap on the nano-cell interface that should be filled to develop a safer and more effective therapy. Indeed, when the NPs are exploited for therapy, it becomes crucial to understand the detrimental and beneficial effects of NPs[17]. It becomes even more relevant for biologics delivery, especially microRNAs, where the cargo acts on molecular pathways. In this case, understanding which pathways of the cells are activated or inhibited by the NPs makes the difference on the outcome of the therapy.

Moreover, this lack of knowledge could have unexplored beneficial effects both in drug delivery field and science applications not yet investigated. A transient condition of cells could be exploited to design and open new possibilities in drug delivery. He et al.[88] highlighted the possibility of exploiting actin organisation to drive the internalisation of drug delivery vectors carrying macromolecular therapeutics. They observed that disruption of actin in some cell types promoted cell uptake of specific molecules.

In the last part of the thesis, the validation of the proposed fluid dynamic process for ensuring stable nanoparticles is presented. Starting from the operative conditions and system parameters such as device geometry, solvents processed, and flow rate tested, we built a fluid dynamic simulation in Comsol to analyse the mixing dynamics and solvent interdiffusion along the microfluidic device. The goal was to learn how mutual solvent interdiffusion guides the coupled nanoprecipitation and self-assembly and their effect on LiPoNs morphologies. The effect exerted by the flow rate ratio and the device geometry on the thinning of the diffusion mixing path was studied and integrated into a parameter f, already presented by Kunstmann-Olsen[89]. Analysing other HFF processes for the production of NPs, we found a correlation between the flow focusing confinement and the final NPs size. We preliminary analysed the main contributions of this relationship.

Despite the wide use of microfluidics reactors for nanoparticle production, there is still a lack of fundamental understanding of the mechanisms of nanoparticle formation[33]. Up

to now, the evaluation of mixing time, as the flow focusing width square over the diffusion coefficient of solvent, has been used to control the nanoparticle characteristic[36]. However, this simplified model only considers part of the microfluidic process and all the parameters involved in nanoparticle synthesis. In particular, in microreactors, such as the HFF, the influence of process conditions such as flow rate ratio, geometry and species residence time has been proven to influence the formation mechanism immensely[33]. Capretto et al. [90] reported that device geometry, fluid physical properties and the flow rate act in concert to govern the dimensional properties of polymeric micelles[33].
Different from previous models that relate the nanoparticle size to the mixing of species, where the complete exchange of solvent stabilizes the NPs for further addition, here the nanoparticle formation is correlated to the location and the confinement of molecules within the flow focusing region. Indeed, nanoparticle growth is described as the addition of molecules to a stable complex in a confinement zone dependent on both flow rate and device geometry. This addition is guided by number density (concentration), the fluid motion, the material properties, and their affinity with the solvent. We proved the crucial impact of the flow focusing confinement in mediating the nanoparticles' growth. This model deeps the knowledge, still poor, on the solvent-nonsolvent-material interrelation in confined reactors to advance in the mechanism of formation for organic nanoparticles[91, 92]. Therefore, this analysis of the key determinants for nanoparticle synthesis refines the role of microfluidics regarding the batch process. This prediction model, supported by further investigations, could save time and effort for scientists or companies interested in developing or optimising devices for nanoparticle synthesis.

In conclusion, this works highlights that stability can be addressed only through a more rational approach, where all its governing phenomena should be considered. Indeed, stability emerged as a complex and transversal concept that crosses engineering, biologics, physics and also material science. We faced the stability from different perspectives and application fields, providing a framework for studying and realizing new material combinations, processing strategies and delivery approaches for the development of safe, stable and effective nanovector for diagnosis, therapy and science applications.

REFERENCES

[1] Handbook of Pharmaceutical Analysis by HPLC, Handbook of Pharmaceutical Analysis by Hplc 6 (2005) 1-658.
[2] M.S. Muthu, S.S. Feng, Pharmaceutical stability aspects of nanomedicines, Nanomedicine 4(8) (2009) 857-860.
[3] K. Pathak, S. Pattnaik, Stability Testing Parameters and Issues for Nanotechnology-Based Drug Products, Methods for Stability Testing of Pharmaceuticals (2018) 293-305.
[4] A.V. Yadav, M.S. Murthy, A.S. Shete, S. Sakhare, Stability Aspects of Liposomes, Indian Journal of Pharmaceutical Education and Research 45(4) (2011) 402-413.
[5] T.L. Moore, L. Rodriguez-Lorenzo, V. Hirsch, S. Balog, D. Urban, C. Jud, B. Rothen-Rutishauser, M. Lattuada, A. Petri-Fink, Nanoparticle colloidal stability in cell culture media and impact on cellular interactions, Chemical Society Reviews 44(17) (2015) 6287-6305.
[6] W.W. Gao, C.M.J. Hu, R.H. Fang, L.F. Zhang, Liposome-like nanostructures for drug delivery, Journal of Materials Chemistry B 1(48) (2013) 6569-6585.
[7] P. Nakhaei, R. Margiana, D.O. Bokov, W.K. Abdelbasset, M.A.J. Kouhbanani, R.S. Varma, F. Marofi, M. Jarahian, N. Beheshtkhoo, Liposomes: Structure, Biomedical Applications, and Stability Parameters With Emphasis on Cholesterol, Frontiers in Bioengineering and Biotechnology 9 (2021).
[8] M. Anderson, A. Omri, The effect of different lipid components on the in vitro stability and release kinetics of liposome formulations, Drug Delivery 11(1) (2004) 33-39.
[9] V.B. Patravale, A.A. Date, R.M. Kulkarni, Nanosuspensions: a promising drug delivery strategy, Journal of Pharmacy and Pharmacology 56(7) (2004) 827-840.
[10] W. Poon, B.R. Kingston, B. Ouyang, W. Ngo, W.C.W. Chan, A framework for designing delivery systems, Nature Nanotechnology 15(10) (2020) 819-829.
[11] E. Blanco, H. Shen, M. Ferrari, Principles of nanoparticle design for overcoming biological barriers to drug delivery, Nature Biotechnology 33(9) (2015) 941-951.
[12] L.A. Lane, Physics in nanomedicine: Phenomena governing the in vivo performance of nanoparticles, Applied Physics Reviews 7(1) (2020).
[13] T.T.H. Thi, E.J.A. Suys, J.S. Lee, D.H. Nguyen, K.D. Park, N.P. Truong, Lipid-Based Nanoparticles in the Clinic and Clinical Trials: From Cancer Nanomedicine to COVID-19 Vaccines, Vaccines 9(4) (2021).
[14] X.C. Hou, T. Zaks, R. Langer, Y.Z. Dong, Lipid nanoparticles for mRNA delivery, Nature Reviews Materials 6(12) (2021) 1078-1094.
[15] J. Bompard, A. Rosso, L. Brizuela, S. Mebarek, L.J. Blum, A.M. Trunfio-Sfarghiu, G. Lollo, T. Granjon, A. Girard-Egrot, O. Maniti, Membrane Fluidity as a New Means to Selectively Target Cancer Cells with Fusogenic Lipid Carriers, Langmuir 36(19) (2020) 5134-5144.
[16] I. Rivolta, A. Panariti, B. Lettiero, S. Sesana, P. Gasco, M.R. Gasco, M. Masserini, G. Miserocchi, CELLULAR UPTAKE OF COUMARIN-6 AS A MODEL DRUG LOADED IN SOLID LIPID NANOPARTICLES, Journal of Physiology and Pharmacology 62(1) (2011) 45-53.
[17] A. Panariti, G. Miserocchi, I. Rivolta, The effect of nanoparticle uptake on cellular behavior: disrupting or enabling functions?, Nanotechnology Science and Applications 5 (2012) 87-100.

[18] A.T. Florence, "Targeting" nanoparticles: The constraints of physical laws and physical barriers, Journal of Controlled Release 164(2) (2012) 115-124.
[19] Y. Gao, M.G. Li, B. Chen, Z.C. Shen, P. Guo, M. GuillaumeWientjes, J.L.S. Au, Predictive Models of Diffusive Nanoparticle Transport in 3-Dimensional Tumor Cell Spheroids, Aaps Journal 15(3) (2013) 816-831.
[20] M.G. Wientjes, B.Z. Yeung, Z. Lu, J.L.S. Au, Predicting diffusive transport of cationic liposomes in 3-dimensional tumor spheroids, Journal of Controlled Release 192 (2014) 10-18.
[21] F. Mastrotto, C. Brazzale, F. Bellato, S. De Martin, G. Grange, M. Mahmoudzadeh, A. Magarkar, A. Bunker, S. Salmaso, P. Caliceti, In Vitro and in Vivo Behavior of Liposomes Decorated with PEGs with Different Chemical Features, Molecular Pharmaceutics 17(2) (2020) 472-487.
[22] S.A. Moosavian, A. Sahebkar, Aptamer-functionalized liposomes for targeted cancer therapy, Cancer Letters 448 (2019) 144-154.
[23] J.J. Tang, Q.T. Wang, Q.W. Yu, Y. Qiu, L. Mei, D.D. Wan, X.H. Wang, M. Li, Q. He, A stabilized retro-inverso peptide ligand of transferrin receptor for enhanced liposome-based hepatocellular carcinoma-targeted drug delivery, Acta Biomaterialia 83 (2019) 379-389.
[24] M.A. Aghdam, R. Bagheri, J. Mosafer, B. Baradaran, M. Hashemzaei, A. Baghbanzadeh, M. de la Guardi, A. Mokhtarzadeh, Recent advances on thermosensitive and pH-sensitive liposomes employed in controlled release, Journal of Controlled Release 315 (2019) 1-22.
[25] J. Cao, D. Huang, N.A. Peppas, Advanced engineered nanoparticulate platforms to address key biological barriers for delivering chemotherapeutic agents to target sites, Advanced Drug Delivery Reviews 167 (2020) 170-188.
[26] Y. Fang, J.X. Xue, S. Gao, A.Q. Lu, D.J. Yang, H. Jiang, Y. He, K. Shi, Cleavable PEGylation: a strategy for overcoming the "PEG dilemma" in efficient drug delivery, Drug Delivery 24(2) (2017) 22-32.
[27] A. Mukherjee, A.K. Waters, P. Kalyan, A.S. Achrol, S. Kesari, V.M. Yenugonda, Lipid-polymer hybrid nanoparticles as a next-generation drug delivery platform: state of the art, emerging technologies, and perspectives, International Journal of Nanomedicine 14 (2019) 1937-1952.
[28] K. Hadinoto, A. Sundaresan, W.S. Cheow, Lipid-polymer hybrid nanoparticles as a new generation therapeutic delivery platform: A review, European Journal of Pharmaceutics and Biopharmaceutics 85(3) (2013) 427-443.
[29] C.Y. Meng, Z. Chen, G. Li, T. Welte, H.F. Shen, Nanoplatforms for mRNA Therapeutics, Advanced Therapeutics 4(1) (2021).
[30] K.A. Hajj, K.A. Whitehead, Tools for translation: non-viral materials for therapeutic mRNA delivery, Nature Reviews Materials 2(10) (2017).
[31] J. Kim, Y. Eygeris, M. Gupta, G. Sahay, Self-assembled mRNA vaccines, Advanced Drug Delivery Reviews 170 (2021) 83-112.
[32] P. Guo, D.X. Liu, K. Subramanyam, B.R. Wang, J. Yang, J. Huang, D.T. Auguste, M.A. Moses, Nanoparticle elasticity directs tumor uptake, Nature Communications 9 (2018).

[33] L. Capretto, D. Carugo, S. Mazzitelli, C. Nastruzzi, X.L. Zhang, Microfluidic and lab-on-a-chip preparation routes for organic nanoparticles and vesicular systems for nanomedicine applications, Advanced Drug Delivery Reviews 65(11-12) (2013) 1496-1532.
[34] M. Russo, P. Bevilacqua, P.A. Netti, E. Torino, A Microfluidic Platform to design crosslinked Hyaluronic Acid Nanoparticles (cHANPs) for enhanced MRI, Scientific Reports 6 (2016).
[35] A. Jahn, W.N. Vreeland, D.L. DeVoe, L.E. Locascio, M. Gaitan, Microfluidic directed formation of liposomes of controlled size, Langmuir 23(11) (2007) 6289-6293.
[36] R. Karnik, F. Gu, P. Basto, C. Cannizzaro, L. Dean, W. Kyei-Manu, R. Langer, O.C. Farokhzad, Microfluidic platform for controlled synthesis of polymeric nanoparticles, Nano Letters 8(9) (2008) 2906-2912.
[37] P.M. Valencia, P.A. Basto, L.F. Zhang, M. Rhee, R. Langer, O.C. Farokhzad, R. Karnik, Single-Step Assembly of Homogenous Lipid - Polymeric and Lipid - Quantum Dot Nanoparticles Enabled by Microfluidic Rapid Mixing, Acs Nano 4(3) (2010) 1671-1679.
[38] Y.T. Kim, B.L. Chung, M.M. Ma, W.J.M. Mulder, Z.A. Fayad, O.C. Farokhzad, R. Langer, Mass Production and Size Control of Lipid-Polymer Hybrid Nanoparticles through Controlled Microvortices, Nano Letters 12(7) (2012) 3587-3591.
[39] J.S. Sun, L. Zhang, J.L. Wang, Q. Feng, D.B. Liu, Q.F. Yin, D.Y. Xu, Y.J. Wei, B.Q. Ding, X.H. Shi, X.Y. Jiang, Tunable Rigidity of (Polymeric Core)-(Lipid Shell) Nanoparticles for Regulated Cellular Uptake, Advanced Materials 27(8) (2015) 1402-+.
[40] F. Roffo, A.M. Ponsiglione, P.A. Netti, E. Torino, coupled Hydrodynamic Flow Focusing (cHFF) to Engineer Lipid-Polymer Nanoparticles (LiPoNs) for Multimodal Imaging and Theranostic Applications, Biomedicines 10(2) (2022).
[41] L. Wang, S. Sanchez, Self-assembly via microfluidics, Lab on a Chip 15(23) (2015) 4383-4386.
[42] Y. Hui, X. Yi, F. Hou, D. Wibowo, F. Zhang, D.Y. Zhao, H.J. Gao, C.X. Zhao, Role of Nanoparticle Mechanical Properties in Cancer Drug Delivery, Acs Nano 13(7) (2019) 7410-7424.
[43] E.D. Arisan, O. Rencuzogullari, C. Cieza-Borrella, F.M. Arenas, M. Dwek, S. Lange, P. Uysal-Onganer, MiR-21 Is Required for the Epithelial-Mesenchymal Transition in MDA-MB-231 Breast Cancer Cells, International Journal of Molecular Sciences 22(4) (2021).
[44] M.J. Goldman, B. Craft, M. Hastie, K. Repecka, F. McDade, A. Kamath, A. Banerjee, Y.H. Luo, D. Rogers, A.N. Brooks, J.C. Zhu, D. Haussler, Visualizing and interpreting cancer genomics data via the Xena platform, Nature Biotechnology 38(6) (2020) 675-678.
[45] F.M. Orlandella, R.M. Mariniello, P. Mirabelli, A.E. De Stefano, P.L.C. Iervolino, V.A. Lasorsa, M. Capasso, R. Giannatiempo, M. Rongo, M. Incoronato, F. Messina, M. Salvatore, A. Soricelli, G. Salvatore, miR-622 is a novel potential biomarker of breast carcinoma and impairs motility of breast cancer cells through targeting NUAK1 kinase, British Journal of Cancer 123(3) (2020) 426-437.
[46] Y.C. Chen, D.Y. Gao, L. Huang, In vivo delivery of miRNAs for cancer therapy: Challenges and strategies, Advanced Drug Delivery Reviews 81 (2015) 128-141.
[47] S.R. El Sayed, J. Cristante, L. Guyon, J. Denis, O. Chabre, N. Cherradi, MicroRNA Therapeutics in Cancer: Current Advances and Challenges, Cancers 13(11) (2021).

[48] S.W.L. Lee, C. Paoletti, M. Campisi, T. Osaki, G. Adriani, R.D. Kamm, C. Mattu, V. Chiono, MicroRNA delivery through nanoparticles, Journal of Controlled Release 313 (2019) 80-95.
[49] S. Davis, B. Lollo, S. Freier, C. Esau, Improved targeting of miRNA with antisense oligonucleotides, Nucleic Acids Research 34(8) (2006) 2294-2304.
[50] J. Elmen, M. Lindow, A. Silahtaroglu, M. Bak, M. Christensen, A. Lind-Thomsen, M. Hedtjarn, J.B. Hansen, H.F. Hansen, E.M. Straarup, K. McCullagh, P. Kearney, S. Kauppinen, Antagonism of microRNA-122 in mice by systemically administered LNA-antimiR leads to up-regulation of a large set of predicted target mRNAs in the liver, Nucleic Acids Research 36(4) (2008) 1153-1162.
[51] S. Kasar, E. Salerno, Y. Yuan, C. Underbayev, D. Vollenweider, M.F. Laurindo, H. Fernandes, D. Bonci, A. Addario, F. Mazzella, E. Raveche, Systemic in vivo lentiviral delivery of miR-15a/16 reduces malignancy in the NZB de novo mouse model of chronic lymphocytic leukemia, Genes and Immunity 13(2) (2012) 109-119.
[52] Y. Liu, L.H. Lai, Q.Y. Chen, Y.J. Song, S. Xu, F. Ma, X.J. Wang, J.L. Wang, H. Yu, X.T. Cao, Q.Q. Wang, MicroRNA-494 Is Required for the Accumulation and Functions of Tumor-Expanded Myeloid-Derived Suppressor Cells via Targeting of PTEN, Journal of Immunology 188(11) (2012) 5500-5510.
[53] D.S. Anson, The use of retroviral vectors for gene therapy-what are the risks? A review of retroviral pathogenesis and its relevance to retroviral vector-mediated gene delivery, Genet Vaccines Ther 2(1) (2004) 9.
[54] X.C. Hou, T. Zaks, R. Langer, Y.Z. Dong, Lipid nanoparticles for mRNA delivery, Nature Reviews Materials.
[55] Y. Wu, M. Crawford, B. Yu, Y.C. Mao, S.P. Nana-Sinkam, L.J. Lee, MicroRNA Delivery by Cationic Lipoplexes for Lung Cancer Therapy, Molecular Pharmaceutics 8(4) (2011) 1381-1389.
[56] C.V. Pecot, G.A. Calin, R.L. Coleman, G. Lopez-Berestein, A.K. Sood, RNA interference in the clinic: challenges and future directions, Nature Reviews Cancer 11(1) (2011) 59-67.
[57] Y. Cao, Y.F. Tan, Y.S. Wong, M.W.J. Liew, S. Venkatraman, Recent Advances in Chitosan-Based Carriers for Gene Delivery, Marine Drugs 17(6) (2019).
[58] A. Parodi, C. Corbo, A. Cevenini, R. Molinaro, R. Palomba, L. Pandolfi, M. Agostini, F. Salvatore, E. Tasciotti, Enabling cytoplasmic delivery and organelle targeting by surface modification of nanocarriers, Nanomedicine 10(12) (2015) 1923-1940.
[59] Y. Gao, Z.W. Zhang, L.L. Chen, W.W. Gu, Y.P. Li, Chitosan N-betainates/DNA self-assembly nanoparticles for gene delivery: In vitro uptake and transfection efficiency, International Journal of Pharmaceutics 371(1-2) (2009) 156-162.
[60] M. Malhotra, C. Tomaro-Duchesneau, S. Prakash, Synthesis of TAT peptide-tagged PEGylated chitosan nanoparticles for siRNA delivery targeting neurodegenerative diseases, Biomaterials 34(4) (2013) 1270-1280.
[61] M. Ruponen, P. Honkakoski, M. Tammi, A. Urtti, Cell-surface glycosaminoglycans inhibit cation-mediated gene transfer, Journal of Gene Medicine 6(4) (2004) 405-414.
[62] K. Buyens, S.C. De Smedt, K. Braeckmans, J. Demeester, L. Peeters, L.A. van Grunsven, X.D. du Jeu, R. Sawant, V. Torchilin, K. Farkasova, M. Ogris, N.N. Sanders, Liposome based systems for systemic siRNA delivery: Stability in blood sets the requirements for optimal carrier design, Journal of Controlled Release 158(3) (2012) 362-370.

[63] C. Diener, A. Keller, E. Meese, Emerging concepts of miRNA therapeutics: from cells to clinic, Trends in Genetics 38(6) (2022) 613-626.
[64] S.J. Shepherd, C.C. Warzecha, S. Yadavali, R. El-Mayta, M.G. Alameh, L.L. Wang, D. Weissman, J.M. Wilson, D. Issadore, M.J. Mitchell, Scalable mRNA and siRNA Lipid Nanoparticle Production Using a Parallelized Microfluidic Device, Nano Letters 21(13) (2021) 5671-5680.
[65] P.M. Valencia, O.C. Farokhzad, R. Karnik, R. Langer, Microfluidic technologies for accelerating the clinical translation of nanoparticles, Nature Nanotechnology 7(10) (2012) 623-629.
[66] D.L. Chen, K.T. Love, Y. Chen, A.A. Eltoukhy, C. Kastrup, G. Sahay, A. Jeon, Y.Z. Dong, K.A. Whitehead, D.G. Anderson, Rapid Discovery of Potent siRNA-Containing Lipid Nanoparticles Enabled by Controlled Microfluidic Formulation, Journal of the American Chemical Society 134(16) (2012) 6948-6951.
[67] A.K.K. Leung, Y.Y.C. Tam, S. Chen, I.M. Hafez, P.R. Cullis, Microfluidic Mixing: A General Method for Encapsulating Macromolecules in Lipid Nanoparticle Systems, Journal of Physical Chemistry B 119(28) (2015) 8698-8706.
[68] S.J. Shepherd, D. Issadore, M.J. Mitchell, Microfluidic formulation of nanoparticles for biomedical applications, Biomaterials 274 (2021).
[69] M.S. Ali, N. Hooshmand, M. El-Sayed, H.I. Labouta, Microfluidics for Development of Lipid Nanoparticles: Paving the Way for Nucleic Acids to the Clinic, ACS Applied Bio Materials (2021).
[70] P. Tabeling, Introduction to microfluidics, OUP Oxford2005.
[71] L. Capretto, W. Cheng, D. Carugo, O.L. Katsamenis, M. Hill, X.L. Zhang, Mechanism of co-nanoprecipitation of organic actives and block copolymers in a microfluidic environment, Nanotechnology 23(37) (2012).
[72] A.S. Kashani, M. Packirisamy, Cancer-Nano-Interaction: From Cellular Uptake to Mechanobiological Responses, International Journal of Molecular Sciences 22(17) (2021).
[73] P. Foroozandeh, A.A. Aziz, Insight into Cellular Uptake and Intracellular Trafficking of Nanoparticles, Nanoscale Research Letters 13 (2018).
[74] S. Behzadi, V. Serpooshan, W. Tao, M.A. Hamaly, M.Y. Alkawareek, E.C. Dreaden, D. Brown, A.M. Alkilany, O.C. Farokhzad, M. Mahmoudi, Cellular uptake of nanoparticles: journey inside the cell, Chemical Society Reviews 46(14) (2017) 4218-4244.
[75] C.W. Gourlay, K.R. Ayscough, The actin cytoskeleton: a key regulator of apoptosis and ageing?, Nature Reviews Molecular Cell Biology 6(7) (2005) 583-U5.
[76] D.A. Fletcher, D. Mullins, Cell mechanics and the cytoskeleton, Nature 463(7280) (2010) 485-492.
[77] C.P. Brangwynne, G.H. Koenderink, F.C. MacKintosh, D.A. Weitz, Intracellular transport by active diffusion, Trends in Cell Biology 19(9) (2009) 423-427.
[78] S.K. Chakraborty, J.A.J. Fitzpatrick, J.A. Phillippi, S. Andreko, A.S. Waggoner, M.P. Bruchez, B. Ballou, Cholera toxin B conjugated quantum dots for live cell Labeling, Nano Letters 7(9) (2007) 2618-2626.
[79] I. Rivolta, A. Panariti, M. Collini, B. Lettiero, L. D'Alfonso, L. Sironi, G. Miserocchi, G. Chirico, A biophysical model of intracellular distribution and perinuclear accumulation of particulate matter, Biophysical Chemistry 158(2-3) (2011) 134-140.

[80] S.K. Lai, K. Hida, C. Chen, J. Hanes, Characterization of the intracellular dynamics of a non-degradative pathway accessed by polymer nanoparticles, Journal of Controlled Release 125(2) (2008) 107-111.
[81] A.M. Scherbart, J. Langer, A. Bushmelev, D. van Berlo, P. Haberzettl, F.J. van Schooten, A.M. Schmidt, C.R. Rose, R.P.F. Schins, C. Albrecht, Contrasting macrophage activation by fine and ultrafine titanium dioxide particles is associated with different uptake mechanisms, Particle and Fibre Toxicology 8 (2011).
[82] H.J. Wang, A.C. Growcock, T.H. Tang, J. O'Hara, Y.W. Huang, R.S. Aronstam, Zinc oxide nanoparticle disruption of store-operated calcium entry in a muscarinic receptor signaling pathway, Toxicology in Vitro 24(7) (2010) 1953-1961.
[83] R.R. Arvizo, O.R. Miranda, M.A. Thompson, C.M. Pabelick, R. Bhattacharya, J.D. Robertson, V.M. Rotello, Y.S. Prakash, P. Mukherjee, Effect of Nanoparticle Surface Charge at the Plasma Membrane and Beyond, Nano Letters 10(7) (2010) 2543-2548.
[84] J.P. Decuypere, G. Bultynck, J.B. Parys, A dual role for Ca2+ in autophagy regulation, Cell Calcium 50(3) (2011) 242-250.
[85] S. Hughes, A.J. El Haj, J. Dobson, Magnetic micro- and nanoparticle mediated activation of mechanosensitive ion channels, Medical Engineering & Physics 27(9) (2005) 754-762.
[86] J. McCarthy, X. Gong, D. Nahirney, M. Duszyk, M.W. Radomski, Polystyrene nanoparticles activate ion transport in human airway epithelial cells, International Journal of Nanomedicine 6 (2011) 1343-1356.
[87] C. Devendran, J. Carthew, J.E. Frith, A. Neild, Cell Adhesion, Morphology, and Metabolism Variation via Acoustic Exposure within Microfluidic Cell Handling Systems, Advanced Science 6(24) (2019).
[88] L. He, E.J. Sayers, P. Watson, A.T. Jones, Contrasting roles for actin in the cellular uptake of cell penetrating peptide conjugates, Scientific Reports 8 (2018).
[89] C. Kunstmann-Olsen, J.D. Hoyland, H.G. Rubahn, Influence of geometry on hydrodynamic focusing and long-range fluid behavior in PDMS microfluidic chips, Microfluidics and Nanofluidics 12(5) (2012) 795-803.
[90] L. Capretto, D. Carugo, W. Cheng, M. Hill, X.L. Zhang, Continuous-flow production of polymeric micelles in microreactors: Experimental and computational analysis, Journal of Colloid and Interface Science 357(1) (2011) 243-251.
[91] R.C.S. Bicudo, M.H.A. Santana, Production of hyaluronic acid (HA) nanoparticles by a continuous process inside microchannels: Effects of non-solvents, organic phase flow rate, and HA concentration, Chemical Engineering Science 84 (2012) 134-141.
[92] R.C.S. Bicudo, M.H.A. Santana, Effects of Organic Solvents on Hyaluronic Acid Nanoparticles Obtained by Precipitation and Chemical Crosslinking, Journal of Nanoscience and Nanotechnology 12(3) (2012) 2849-2857.

VI APPENDIX

VI.1 Study of the concentration of the reagents and of solvent–nonsolvent ratio for the production of LiPoNs

A preliminary study was performed (TableI-1) evaluating the concentration of the reagents (lipid concentration: 0.016 and 0.0072% *w/v* and chitosan concentration: 0.01% *w/v* and 0.0375% *w/v*) and the effect of solvent–nonsolvent ratio (EtOH/Water: 80/20% *v/v* and 65/35% *v/v* and AcOH/Water: 10/90% *v/v* and 1/99 % *v/v*) on the morphology of LiPoNs and their physiochemical properties at fixed FR^2 of 0.51 (obtained at 21 µL/min in the middle phase and 41 µL/min in the side phase) and water collection volume of 2mL.

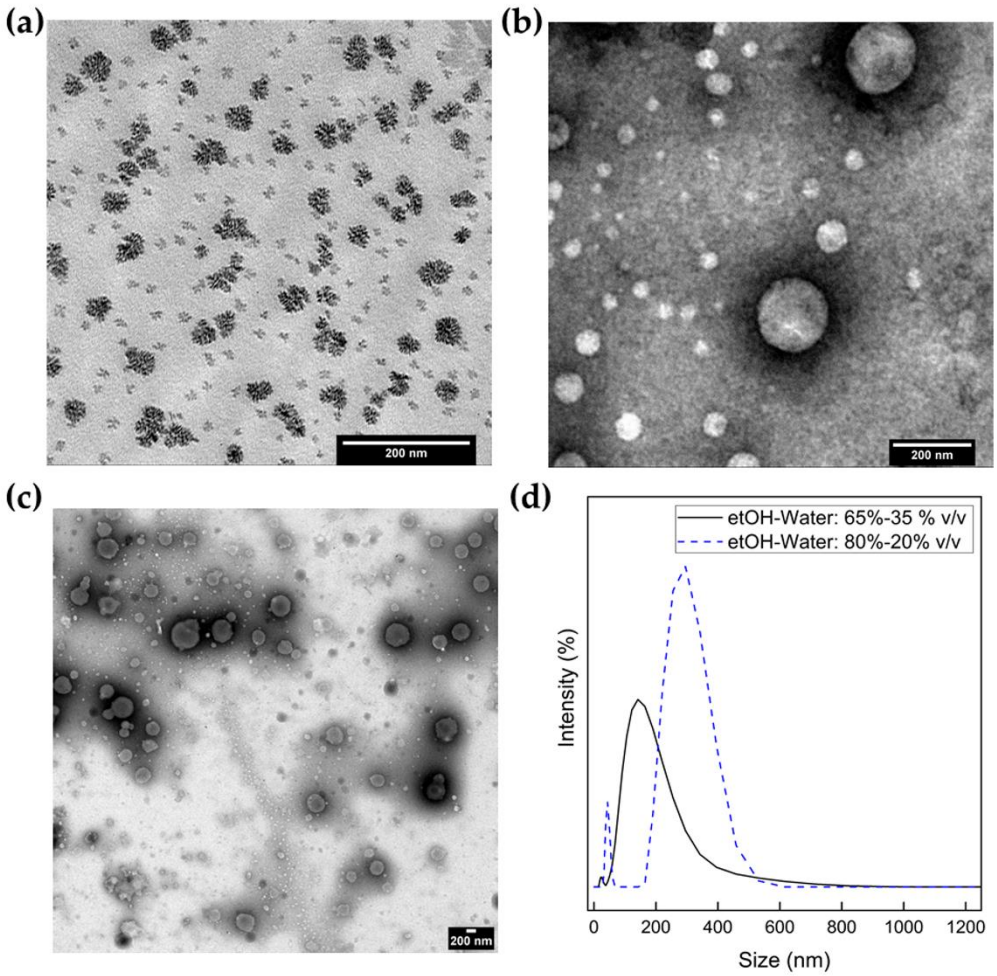

Figure VI-1. Effect of lipids concentration and EtOH/Water ratio on liposomes morphology evaluated by TEM. Hydrodynamic Flow Focusing at FR^2 equal to 0.51 performed by injecting in the side channels different Lipids concentration for a fixed mass ratio (8:1- SPC:Chol). (**a**) 0.016*% w/v* of Lipids dissolved in etOH/Water (64/36*% v/v*); (**b**) 0.0072% *w/v* of Lipids dissolved in etOH/Water (65/35% *v/v*) and **(c)** 0.0072% *w/v* of Lipids dissolved in etOH/Water (80/20 % *v/v*) ; (**d)** Size distribution of NPs obtained for 0.0072 % *w/v* of lipids dissolved in etOH/Water (80/20 *% v/v*) and etOH/Water (65/35 % *v/v*).

Firstly, the lipids, at fixed composition (mass ratio 8:1- SPC:Chol), were dissolved in etOH/Water (65-64/35-36% *v/v*) at two different concentrations (0.016 and 0.0072% *w/v*) and were injected from the side channels sheeting the middle water stream (at FR^2 equal to 0.51). As shown in Figure VI-1a for lipids concentration of 0.016% *w/v* an uncontrolled precipitation was observed, while the formation of liposomes structure was obtained for a Lipids concentration of 0.0072% *w/v* (Figure VI-1b). To evaluate the effect of etOH/Water percentage on the production of liposomes, the Lipids at 0.0072% *w/v* were dissolved in a different etOH/Water ratio (80/20% *v/v*) and injected into the microfluidic device (Figure VI -1c). Smaller liposomes, as observed in Figure VI-1b and reported in DLS distribution (Figure VI-1d), were obtained for the lower ethanol fraction (etOH/Water -65/35% *v/v*) due to enhanced ethanol extraction at microfluidics focusing. Therefore, the etOH/Water mixture at 65/35% *v/v* was selected for subsequent studies.

Then, still at constant FR^2 of 0.51, the effect of the acetic acid (1% *v/v* and 10% *v/v*) and the chitosan addition at different concentration (0.01% *w/v* and 0.0375% *w/v*) on the liposome structure was evaluated in Figure VI-2-3. The absence of massive precipitation, combined with the evaluation of the morphologies obtained by TEM images (Figure VI-2a,b- VI-3a-c) and DLS data (Figure VI-2c- VI-3d), were used to identify the reagent concentrations (0.0072% *w/v* of Lipids - 0.01% *w/v* of chitosan) and the solvent-non solvent ratios (etOH/Water 65 /35% *v/v,* AcOH/Water 1/99% *v/v*) for successive studies.

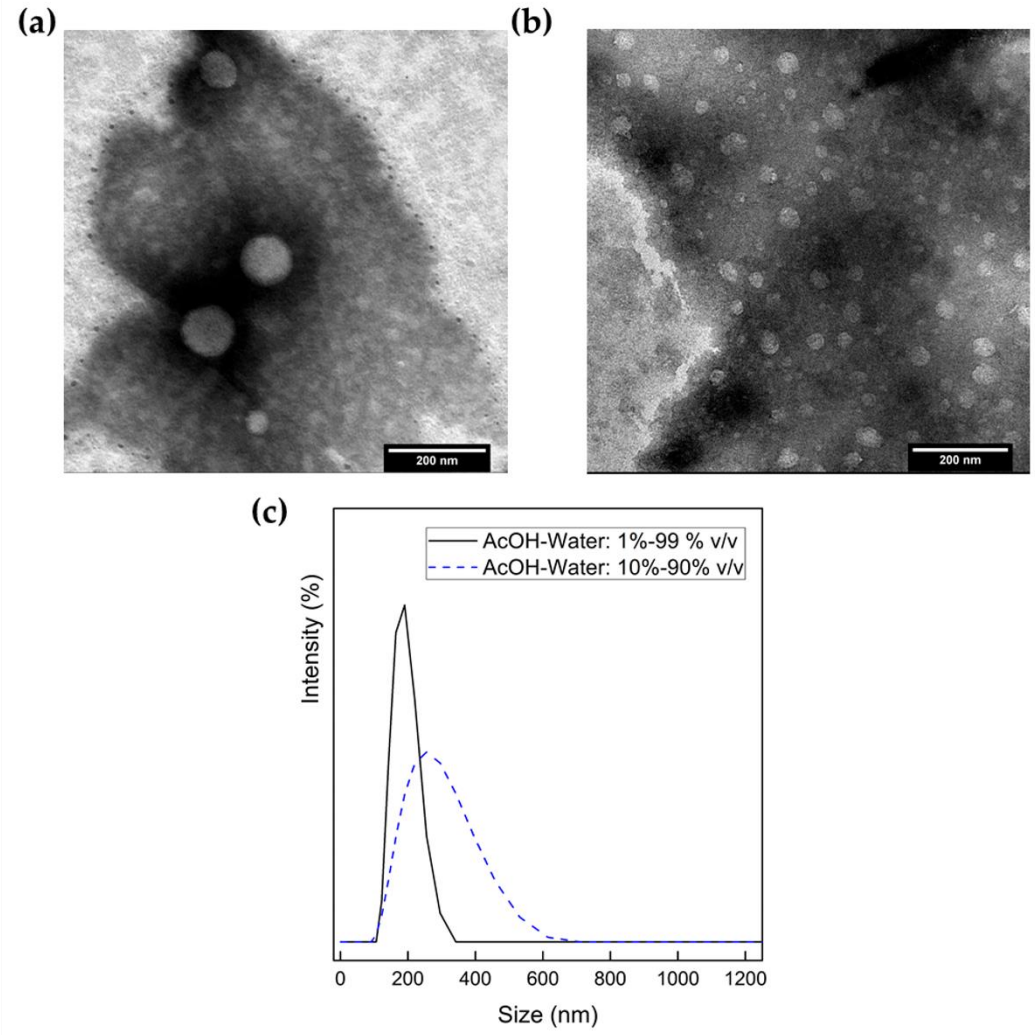

Figure VI-2. Effect of AcOH volume percentage on liposomes morphology evaluated by TEM. Hydrodynamic Flow Focusing performed by injecting in the side channels Lipids (0.0072*% w/v)* dissolved in etOH/Water (65/35% *v/v*) with different percentage of Acetic Acid (AcOH) in the middle channel: (a) 1 % *v/v* and (b) 10 % *v/v.* (c) The effect of AcOH (1% *v/v*- 10% *v/v*) on NPs' size distribution.

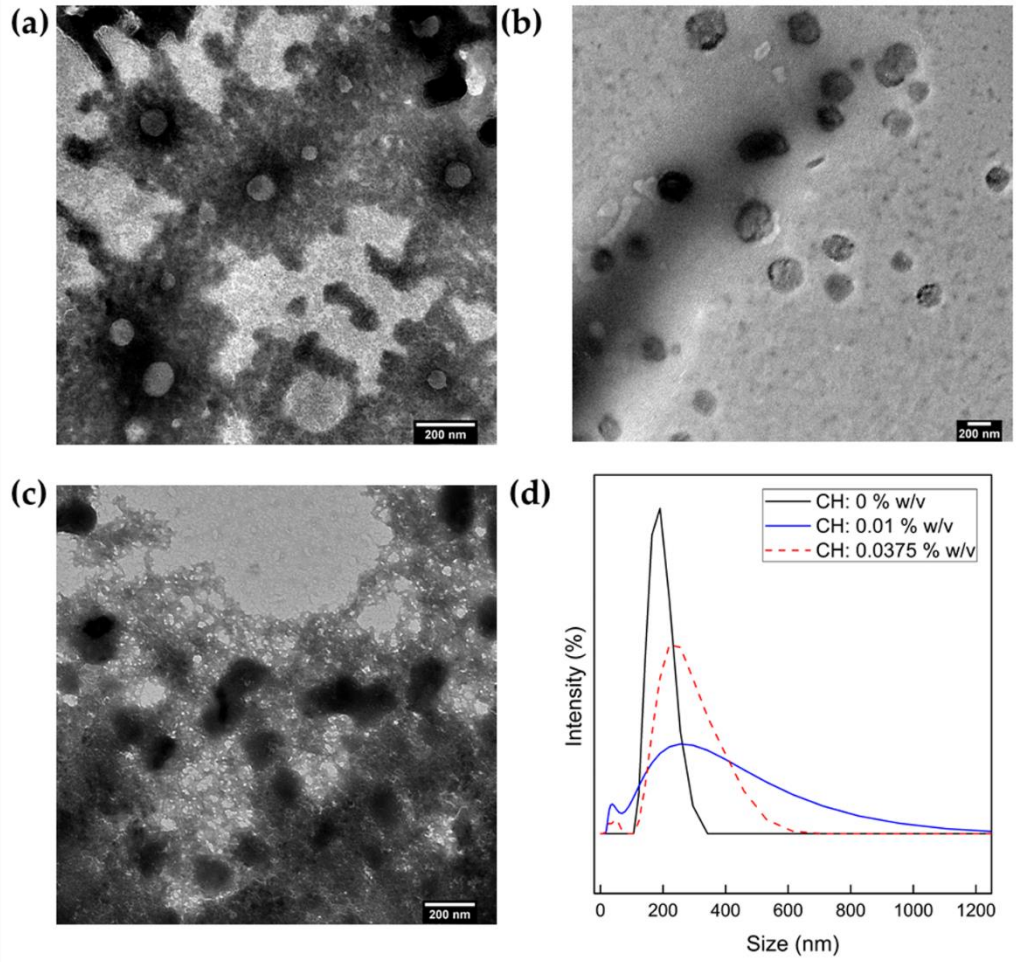

Figure VI-3. Effect of chitosan concentration on Lipid-Polymer NPs' morphology. coupled Hydrodynamic Flow Focusing performed injecting 0.0072% w/v of Lipids in the side channels dissolved in etOH/Water (65 /35% *v/v*),while in the middle channel different concentrations of chitosan are dissolved in a mixture of AcOH/Water at 1% *v/v*) : (**a**) 0% *w/v*, (**b**) 0.01% *w/v* and (**c**) 0.0375% *w/v*. (**d)** The effect of chitosan concentration (0.01% *w/v* and 0.0375% *w/v*) dissolved in a mixture of AcoH/Water (1/99 % *v/v*) on NPs' size distribution.

VI.2 The effect of FR2 on the morphology of LiPoNs

The effect of FR^2 is studied by keeping constant the reagent concentration (0.0072% *w/v* of Lipids and 0.01% *w/v* of chitosan) and the solvent-non solvent ratios (etOH/Water: 65/35% *v/v* and AcOH/Water: 1/99 % *v/v),* optimised in previous paragraphs. The role FR^2 on the morphology of LiPoNs nanostructure were observed by varying the FR^2, obtained at constant side flow rate of 41 µL/min and changing the middle flowrate alternatively (1-3-7-14-21-28 µL/min), always keeping constant the collection volume equal to 2 mL of water.

The DLS distributions in Figure VI-4 show a monodisperse population of nanoparticle for lower FR^2 of 0.024 and 0.073, while a bimodal distribution is reported for higher FR^2 from 0.17 to 0.68.

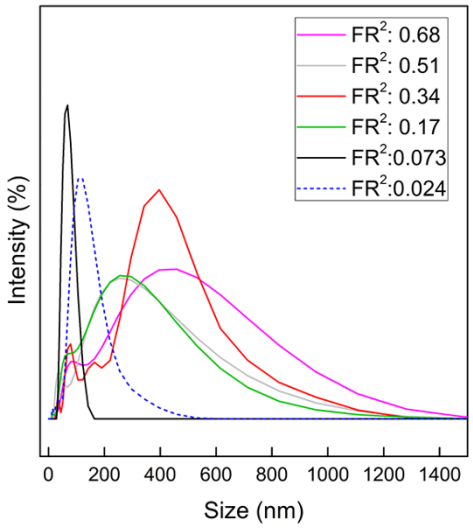

Figure VI-4. Effect of FR^2 on Lipid-Polymer NPs morphology. Lipids (0.0072 *% w/v*) are injected into the side channels dissolved in etOH/Water (65 /35*% v/v*), while the chitosan (0.01% w/v) in acid solution (1*% v/v*) is injected into the middle one. (**a**) Size distribution of LiPoNs for different volumetric flow rate ratios (FR^2).

The previous experimental campaign allows the definition of a reduced operative window for the FR^2 ranging from 0.024 to 0.17. A further study was conducted in this window to analyse the role of solvent displacement and residence time distribution on the morphology of nanoparticles (Chapter V).

VI.3 The effect of the collection volume on the morphology of LiPoNs

In the following steps, we investigated the influence of the collection volume on liposome morphology at fixed FR^2 of 0.073 and *optimal conditions*. DLS measurement and TEM images show an enlargement of LiPoNs' size as the collection volume increases up to 8 mL (2, 3.5 and 8 mL) (Figure VI-5a). In this step, the collection volume was firstly set at 3.5 mL instead of 2 mL to reduce the residual ethanol in the final formulation and prevent re-solubilisation of formed lipid–polymer structures since no effect on the final LiPoN size was observed due to this variation (Figure VI-5a). However, an increase in the collection volume to 8mL produces an increase in size. Indeed, the rapid change in pH around the liposome, as they are produced, could lead to a diffusion of water inside the liposome to balance the pH difference created between the newly formed chitosan core and neutral pH of the collection volume [1-3]. Moreover, at the lower collection volume of 3.5 mL, the high residual ethanol amount could decrease the water permeability by replacing the water in

the hydration shells of the head groups and accumulating itself in transient defects in the hydrophobic part of the bilayer [4]. The assumption perfectly matches the irregular and swelled shape of the LiPoNs observed in the TEM images (Figure VI-5b–c) obtained at 3.5 and 8 mL.

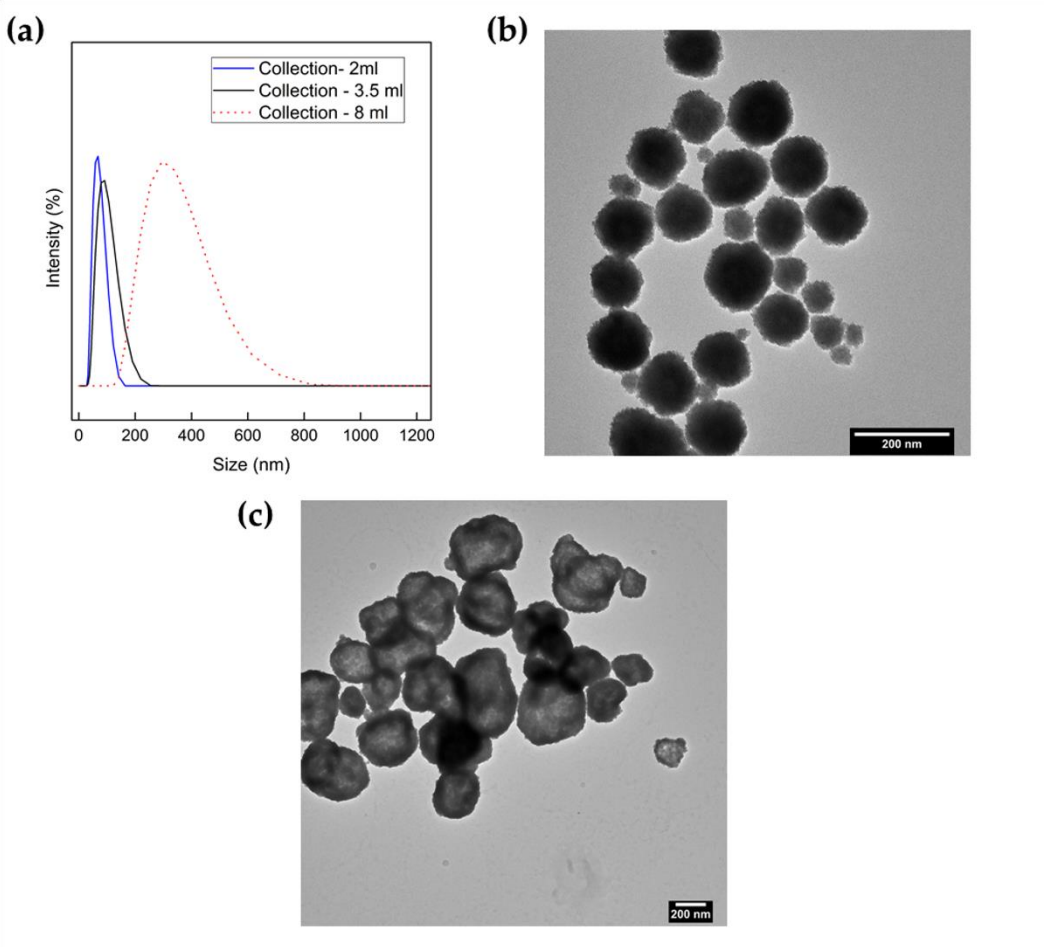

Figure VI-5. Effect of collection volume on LiPoNs morphology. **(a)** Nanoparticle size distribution of LiPoNs produced by injecting Lipids in the side channels dissolved in etOH/Water (65%35 *% v/v*), while the chitosan (0.01 *% w/v*) in acid solution (1*% v/v*) is injected into the middle one Lipids (0.0072 *% w/v*) at FR^2 of 0.073 for different volumes of water collection: 2ml, 3.5 mL and 8 mL. Morphological characterisation by TEM of LiPoNs stained with osmium smoke at different water collection volumes: (**b**) 3.5 mL and (**c**) 8 mL of water.

These results highlight the importance, as reported in recent studies [5-7], of considering the effect of the whole microfluidic channel path on NPs' morphologies and not only at the microfluidic junction. Indeed, the length of the microfluidic chip should be suitable for

completing the mixing among solvents to avoid incomplete or disassemble processes in nanoparticle formation.

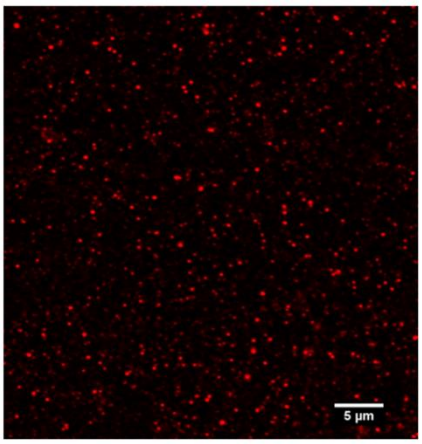

Figure VI-6. Confocal image of LiPoNs stained with CellMask™ Orange Plasma membrane stain (dilution 1:10^4) performed at optimal conditions FR^2 of 0.073.

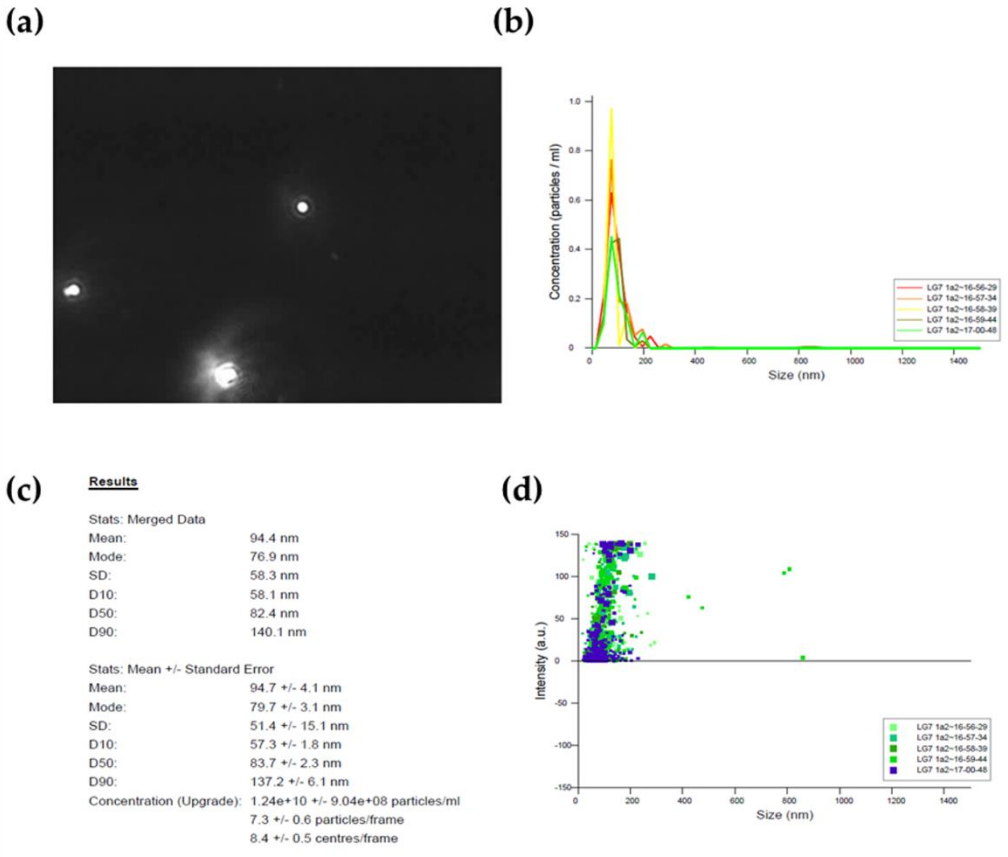

Figure VI-7. Structure investigation of LiPoNs: **(a)** Frame of NTA video of LiPoNs performed at *optimal conditions* diluted 1:200 in PBS; **(b)** Different colours represent measures of LiPoNs' size distribution in function of the mean nanoparticle concentration from five independent experiments; **(c)** Quantitative evaluation of LiPoNs' size distribution; (**d**) Different colours and sizes of markers represent measures of particle size and scattered light intensity of single particle from the five independent experiments.

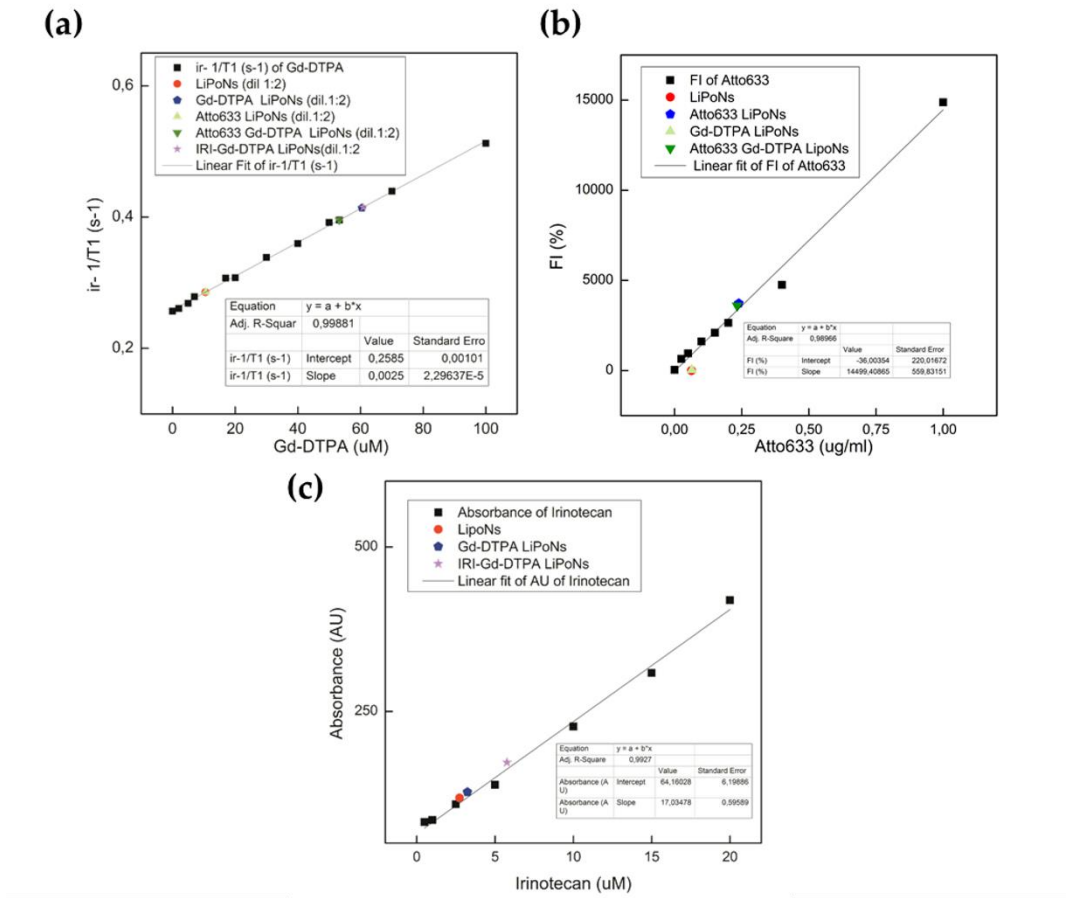

Figure VI-8. Calibration curves of Gd-DTPA, Atto 633, Irinotecan: **(a)** Gd-DTPA calibration curve (dispersed in water) for ir sequence (1/T1) and LiPoNs, Gd-DTPA-loaded LiPoNs, Atto633-loaded LiPoNs, Atto633-Gd-DTPA co-loaded LiPoNs, IRI-Gd-DTPA co-loaded LiPoNs localisation within the curve. **(b)** Atto 633 calibration curve and LiPoNs, Gd-DTPA LiPoNs, Atto 633 LiPoNs, Atto633-Gd-DTPA LiPoNs and their localisation within the curve. The Atto633 calibration curve reported in the figure VI 8b is a part of the complete calibration curve 25 ng/ml-4 µg/ml to graphically localize the NPs within the curve. **(c)** Irinotecan calibration curve and LiPoNs, Gd-DTPA LiPoNs and IRI-Gd-DTPA LiPoNs localisation within the curve. The Irinotecan calibration curve is reported in the figure VI -8c is a part of the complete calibration curve 0.5-100 µM to graphically localize the NPs within the curve.

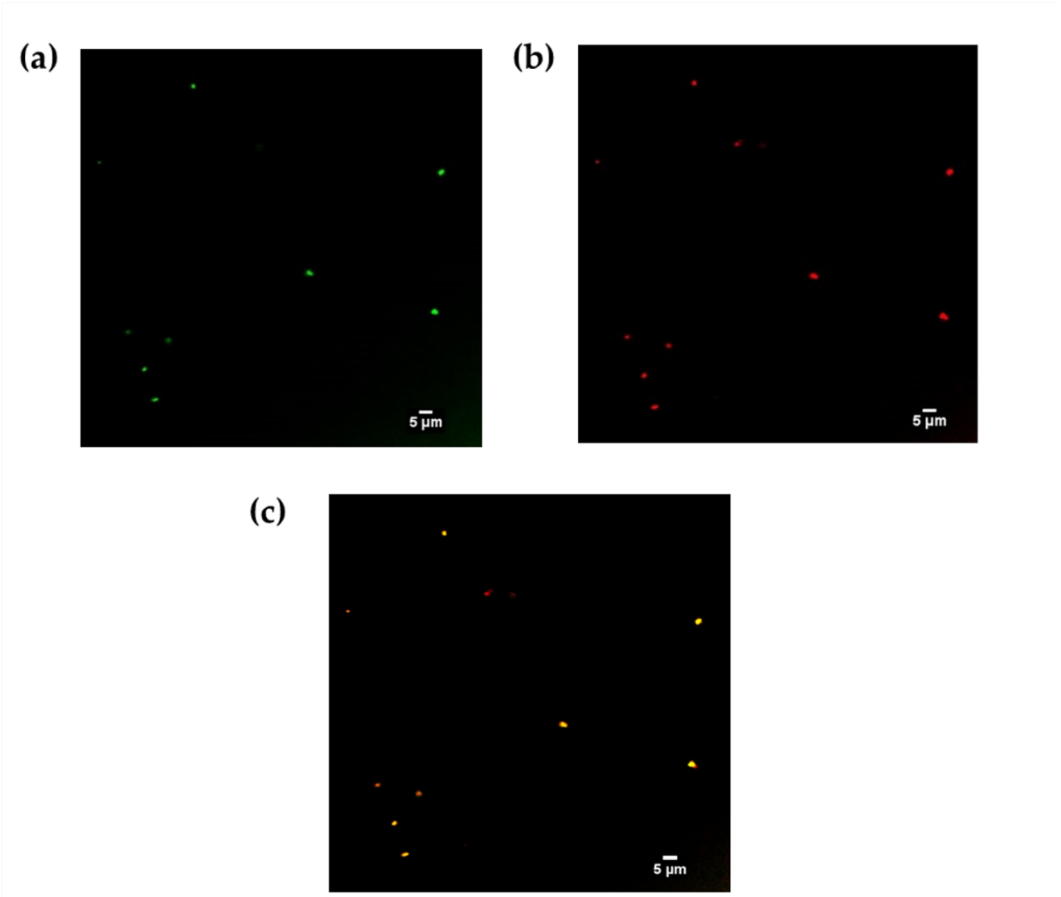

Figure VI-9. (**a**) Optical imaging of Atto633-Gd-DTPA co-loaded LiPoNs by confocal microscopy; (**b**) Optical imaging of Atto633-Gd-DTPA LiPoNs stained with CellMask™ Orange Plasma membrane stain (dilution 1:10^4) by confocal microscopy; (**c**) Merge fluorescent image of Atto633 (green) and CellMask (red) of Atto633- Gd-DTPA-loaded LiPoNs stained with CellMask™ Orange Plasma membrane stain (dilution 1:10^4).

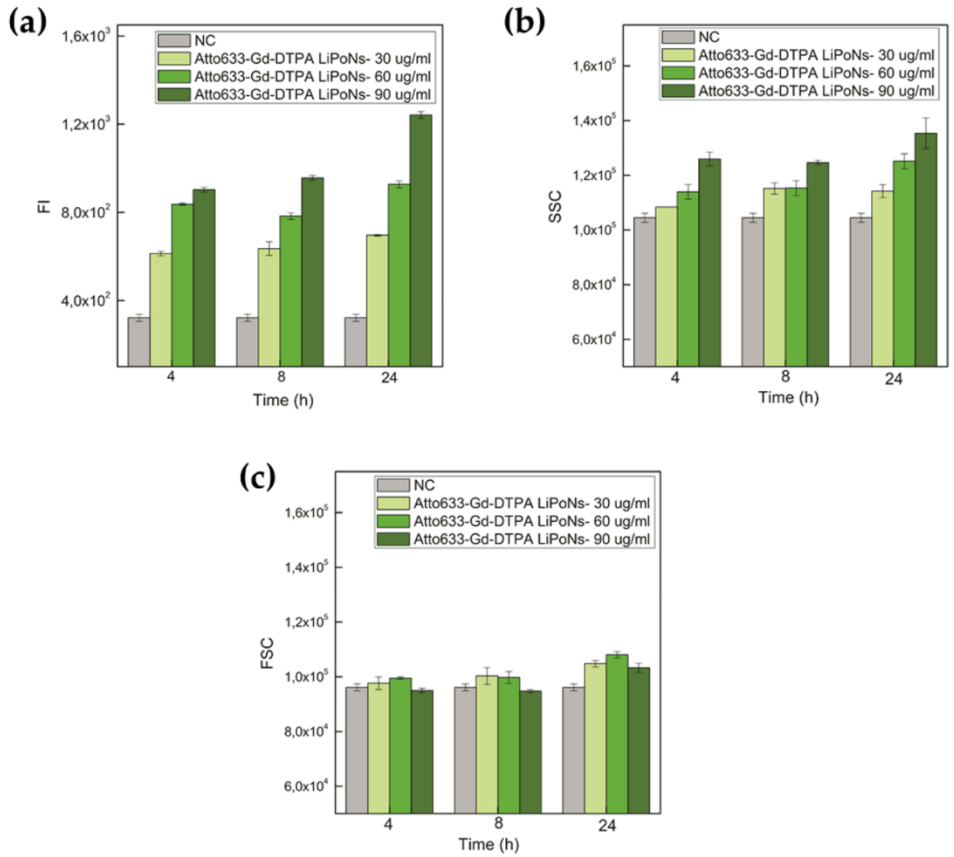

Figure VI-10. Quantitative uptake of multimodal imaging LiPoNs by U-87 MG cells. **(a)** Fluorescent Intensity (FI), **(b)** Forward Scattering Area (FSC) and **(c)** Side scattering Area (SSC) of U-87 MG cells exposed to an increasing concentration of Atto633- Gd-DTPA co-loaded LiPoNs Lipids(Lipid conc: 30, 60 and 90 µg/ml, Atto 633 conc.: 0.2, 0.4 and 0.6 µg/ml, Gd-DTPA conc.: 75-150-225 µM) for different time points: : 4h,8h, 24 h.

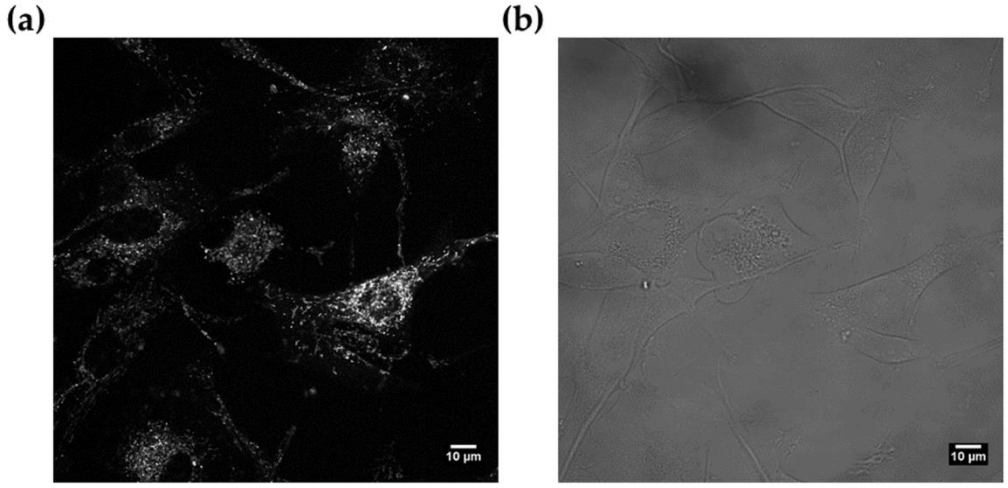

Figure VI-11. Confocal image of U-87 MG cells exposed to Atto633-Gd-DTPA co-loaded LiPoNs Lipids(lipid conc.: 90 µg/ml, Atto 633 conc.: 0.6 µg/ml, Gd-DTPA conc.: 225 µM) for 24 hours in (**a**) transmission and (**b**) fluorescence (Atto 633).

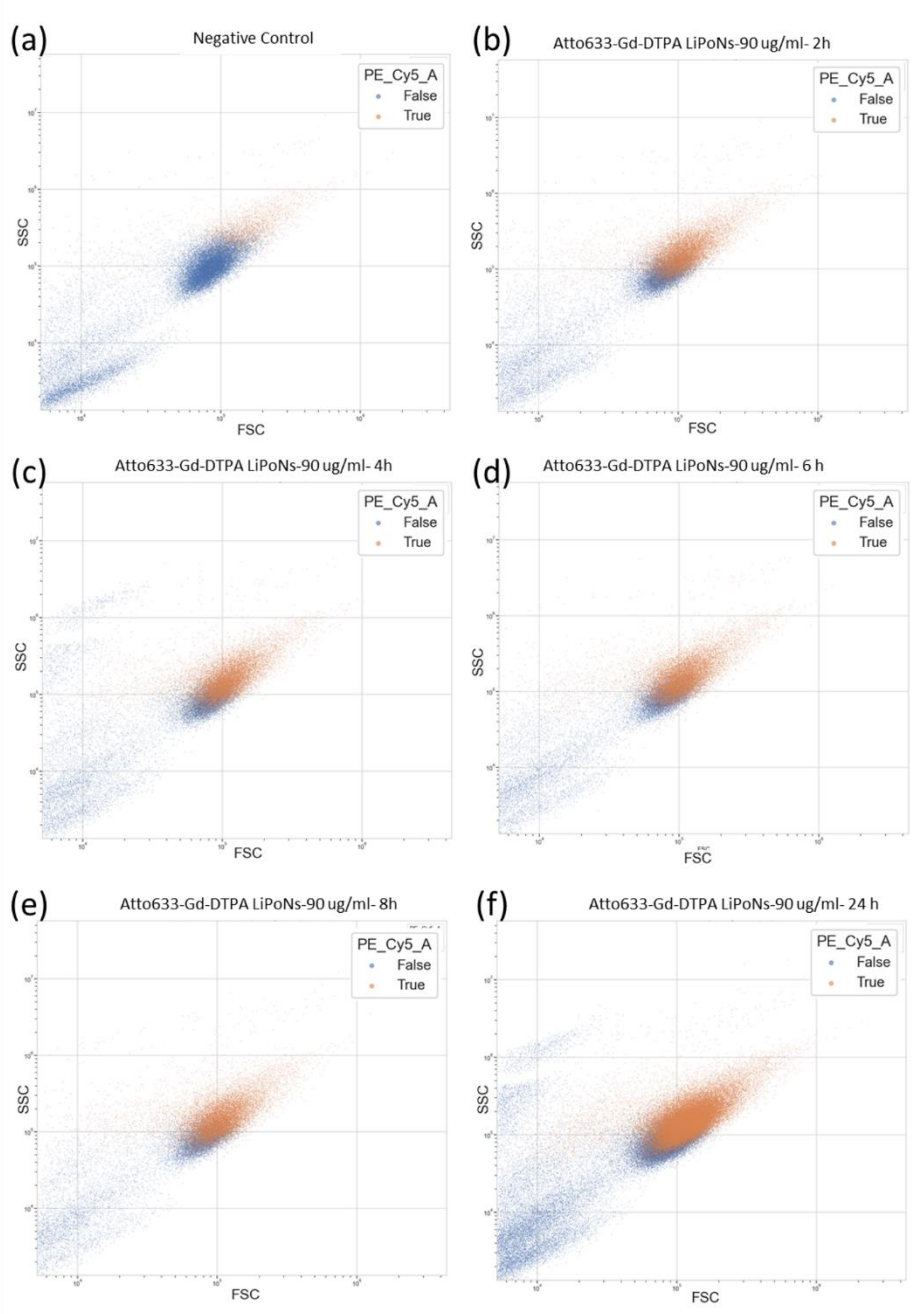

Figure V-12. Raw flow cytometry data. Identification of PE_CY5_A fluorescence of the U-87 MG cell population: (**a**) unexposed and (**b–f**) exposed to Atto633-Gd-DTPA LiPoNs (Lipids conc.: 90 µg/ml) for different time points: (**b**) 2h, (**c**) 4h, (**d**) 6h, (**e**) 8h and (**f**) 24 h.

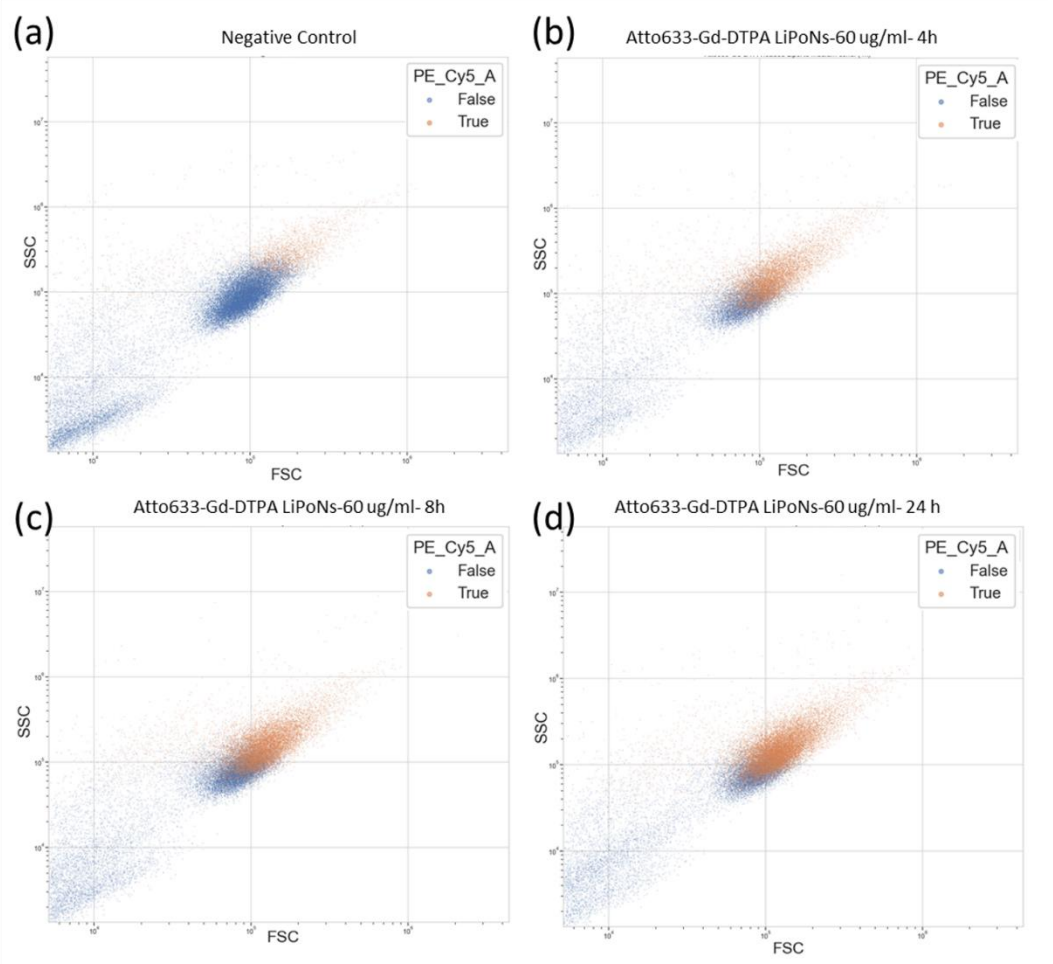

Figure V-13. Raw flow cytometry data. Identification of PE_CY5_A fluorescence of the U-87 MG cell population: (**a**) unexposed and (**b–d**) exposed to Atto633-Gd-DTPA LiPoNs (Lipids conc.: 60 µg/ml) for different time points: (**b**) 4h, (**c**) 8h and (**d**) 24h.

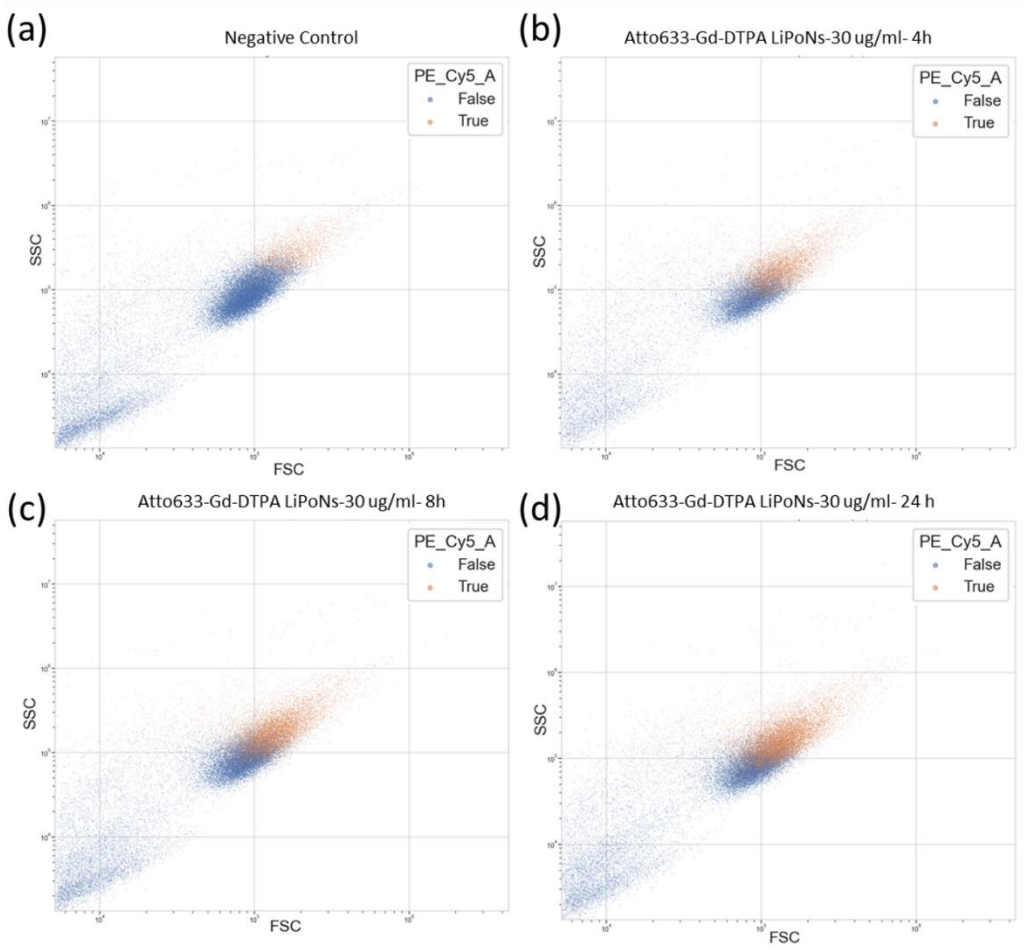

Figure VI-14. Raw flow cytometry data. Identification of PE_CY5_A fluorescence of the U-87 MG cell population: (**a**) unexposed and (**b–d**) exposed to Atto633-Gd-DTPA LiPoNs (Lipids conc.: 30 µg/ml) for different time points: (**b**) 4h, (**c**) 8h and (**d**) 24h.

Table VI-1. Geometrical details of the device architecture.

Parameter	Value
AC segment [mm]	6.5
BC segment [mm]	7.19
CD segment [mm]	16
AD segment [mm]	22.5
α angle (°)	45

Table VI-1. Material properties of the mixtures used for numerical simulations, obtained by combining two components in proper amounts: x_1 (water molar fraction) and x_2 (cosolvent molar fraction) that was chosen to be acetic acid (acOH) or ethanol (etOH) according to the solution to be prepared.

Solvent ratio % v/v	X_1 (Water molar fraction)	X_2 (cosolvent molar fraction)	10^{-3} ρ [kg·m^{-3}]	10^3 μ [Pa·s]	Reference
Water/etOH=35/65	0.598	etOH = 0.401	0.879	1.66	[8]
Water/acOH =99/1	0.997	acOH = 0.003	0.997	0.890	[9]

Table VI-3. Computational Parameters used for Mesh Modelling and their Values from Amrani et. al.[10]

Parameters	Value
Maximum element size	0.0025 m
Minimum Element Size	2.32X10^{-4}m
Maximum Element Growth rate	1.08
Curvature Factor	0.25
Resolution of Narrow regions	1

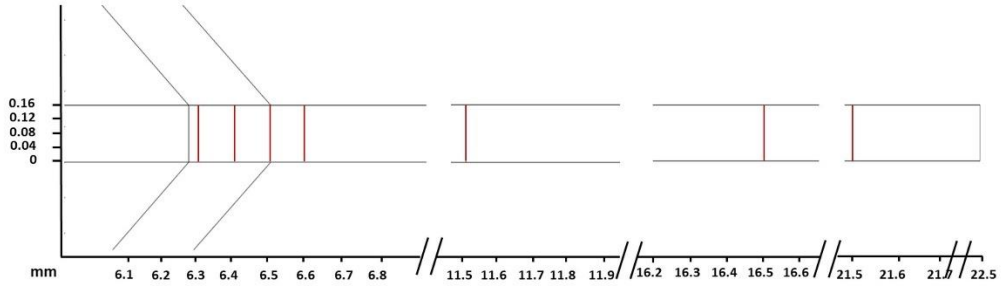

Figure VI-15. Representation of selected 2D Cutlines positions along the device selected for the quantitative studies on solvent interdiffusion. The main channel was investigated by spanning from xr =-200 µm, defined through a vertical cut line with coordinates (x1=6.3 mm, y1=0 mm) and (x2=6.3 mm, y2=0.16 mm), to xr =15000 µm (x1=21.5 mm, y1=0 mm - x2=21.5 mm, y2=0.16 mm).

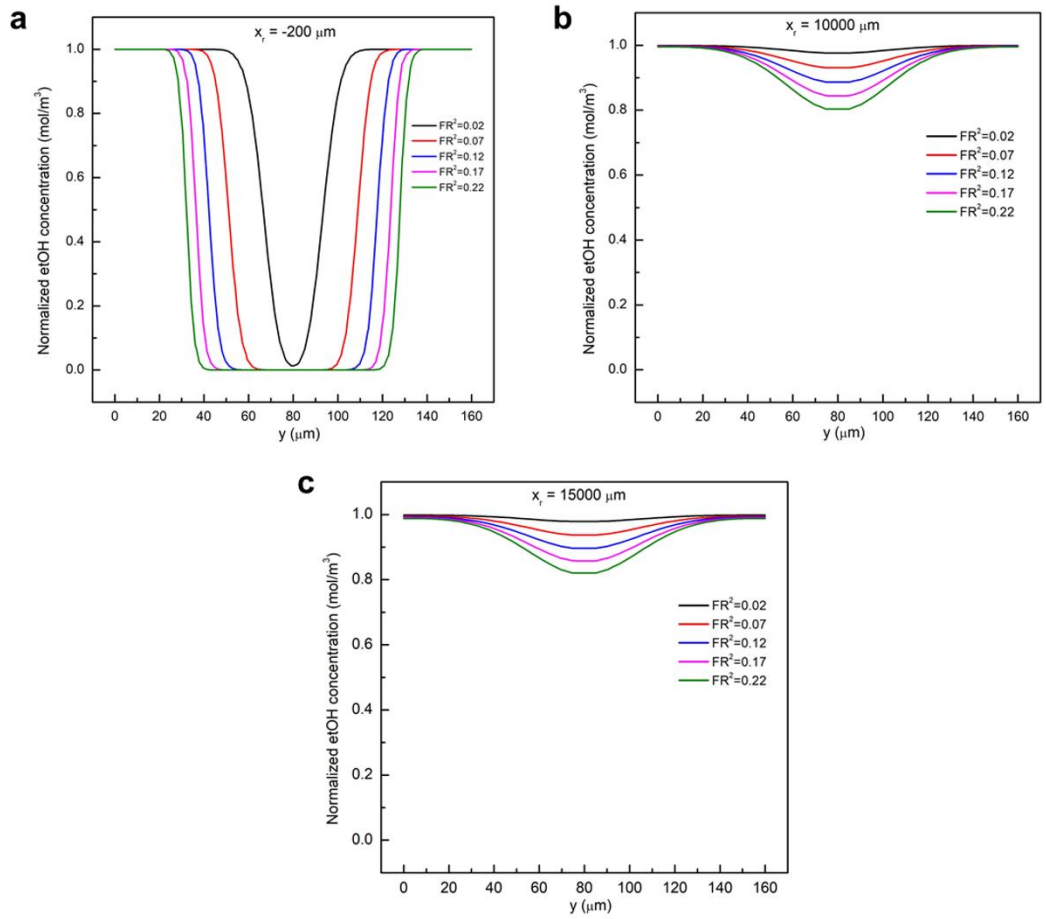

Figure VI-16. The impact of FR^2(0.02-0.22) on the ethanol interdiffusion in terms of normalized ethanol (etOH) concentration in the main channel width (1-160 um) at different locations (x_r) along the channel length (1-16 mm) evaluated with 2D comsol simulation : (**a**) x_r:-200 um, (**b**) x_r: 10000 um, (**c**) x_r: 15000 um.

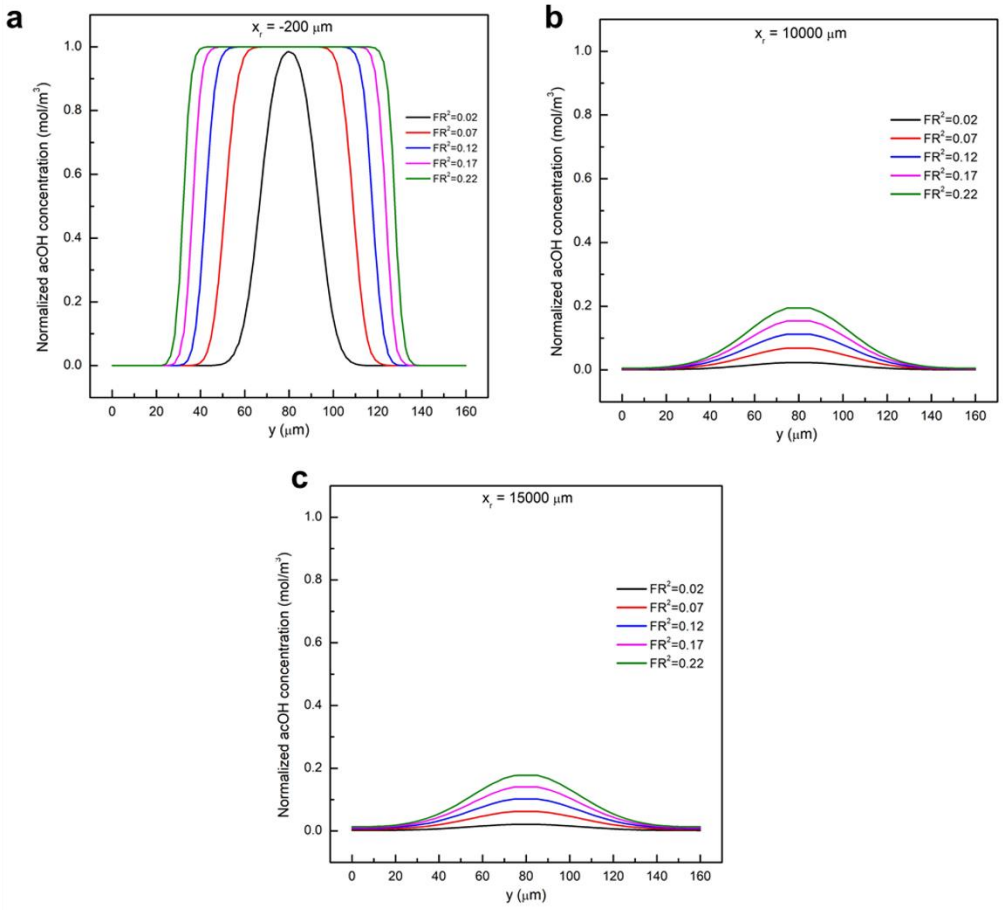

Figure VI-17. Impact of FR^2(0.02-0.22) on the acetic acid interdiffusion in terms of normalized acetic Acid (acOH) concentration in the main channel width (1-160 um) at different locations (x_r) along the channel length (16 mm) evaluated with 2D comsol simulation : **a**) x_r:-200 um, (**b**) x_r: 10000 um, (**c**) x_r: 15000 um.

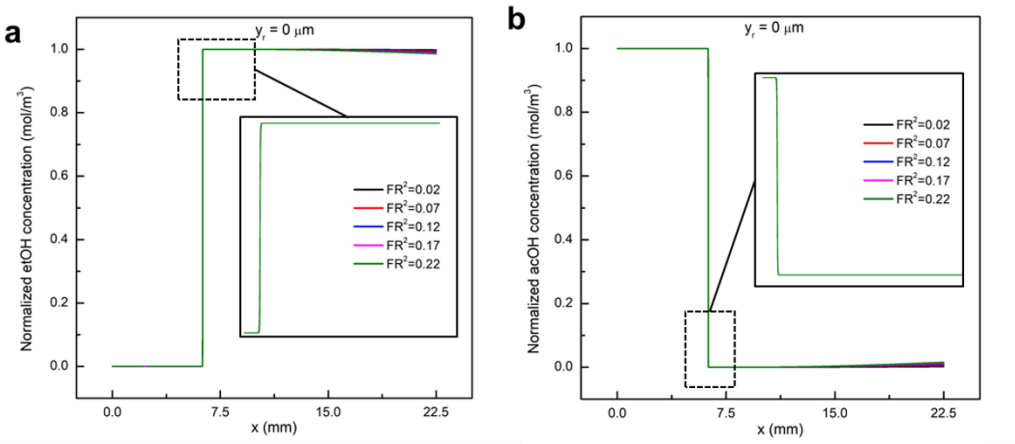

Figure VI-18. Impact of FR^2(0.02-0.22) on the development of normalized concentration profiles across the whole channel at the reference position y_r= 0 µm along the channel width, evaluated with 2D comsol simulation for: (a) ethanol etOH, (b) acetic acid acOH.

Table VI-4. Value used for the linear fitting in chapter V.

Geometry	Material	Qm/(2Qs)	r	f	NPs diameter (nm)	Reference
X-Junction Width (10 µm) Depth (36 µm)	Total Lipids Conc.:5mmol/L	0.03	18	0.02	54	[11]
		0.04	12	0.04	62	
		0.08	6	0.07	80	
		0.11	4.5	0.1	90	
		0.16	3	0.15	156	
Y-Junction Width (65 µm) Depth (120 µm)	Total Lipids Conc.:5mmol/L	0.02	24	0.02	60	[11]
		0.03	18	0.03	64	
		0.04	13	0.04	76	
		0.06	8.5	0.06	90	
		0.08	6	0.08	142	
X-Junction Width (20 µm) Depth (60 µm)	Poly(lactic-co-glycolic acid) 15kDa-PEG 3.4 KDa Conc.: 20 mg/mL	0.03	16.67	0.03	19	[12]
		0.04	12.5	0.04	22	
		0.05	10	0.04	22.2	
		0.06	8.33	0.05	24	
		0.07	7.14	0.06	24.5	
		0.08	6.25	0.07	24.8	
		0.09	5.55	0.08	25	
		0.1	5	0.09	26	
X-Junction Width (390 µm) Depth (190 µm)	Sodium Hyaluronate- 42 kDa Conc.:0.5 mg/mL	0.1	5	0.09	40	[13]
		0.13	4	0.11	53	
		0.17	3	0.15	58	
		0.20	2.5	0.18	128.9	
		0.33	1.5	0.29	197.7	

Notes:

Qm represents the volumetric flow rate of the middle stream. while Qs presents the volumetric flow rate of the side stream. r is the ratio between the one volumetric side flowrate and the middle one.

The lipids composition is Dimyristoylphosphatidylcholine (DMPC). cholesterol and dihexadecyl phosphate (DCP) in a molar ratio of 5:4:1.

VI. REFERENCES

[1] E.V. Tazina, K.V. Kostin, N.A. Oborotova, SPECIFIC FEATURES OF DRUG ENCAPSULATION IN LIPOSOMES (A REVIEW), Pharmaceutical Chemistry Journal 45(8) (2011) 481-490.
[2] M. Gabba, J. Frallicciardi, J. van't Klooster, R. Henderson, L. Syga, R. Mans, A.J.A. van Maris, B. Poolman, Weak Acid Permeation in Synthetic Lipid Vesicles and Across the Yeast Plasma Membrane, Biophysical Journal 118(2) (2020) 422-434.
[3] N. Monteiro, A. Martins, R.L. Reis, N.M. Neves, Liposomes in tissue engineering and regenerative medicine, Journal of the Royal Society Interface 11(101) (2014).
[4] M. Jansen, A. Blume, A COMPARATIVE-STUDY OF DIFFUSIVE AND OSMOTIC WATER PERMEATION ACROSS BILAYERS COMPOSED OF PHOSPHOLIPIDS WITH DIFFERENT HEAD GROUPS AND FATTY ACYL CHAINS, Biophysical Journal 68(3) (1995) 997-1008.
[5] M. Abdelkarim, N.H. Abd Ellah, M. Elsabahy, M. Abdelgawad, S.A. Abouelmagd, Microchannel geometry vs flow parameters for controlling nanoprecipitation of polymeric nanoparticles, Colloids and Surfaces a-Physicochemical and Engineering Aspects 611 (2021).
[6] E. Lallana, R. Donno, D. Magri, K. Barker, Z. Nazir, K. Treacher, M.J. Lawrence, M. Ashford, N. Tirelli, Microfluidic-assisted nanoprecipitation of (PEGylated) poly (D,L-lactic acid-co-caprolactone): Effect of macromolecular and microfluidic parameters on particle size and paclitaxel encapsulation, International Journal of Pharmaceutics 548(1) (2018) 530-539.
[7] R. Donno, A. Gennari, E. Lallana, J.M.R. De La Rosa, R. d'Arcy, K. Treacher, K. Hill, M. Ashford, N. Tirelli, Nanomanufacturing through microfluidic-assisted nanoprecipitation: Advanced analytics and structure-activity relationships, International Journal of Pharmaceutics 534(1-2) (2017) 97-107.
[8] D. Begoña González and Noelia Calvar and Elena Gómez and Ángeles, Density, dynamic viscosity, and derived properties of binary mixtures of methanol or ethanol with water, ethyl acetate, and methyl acetate at T=(293.15, 298.15, and 303.15)K, The Journal of Chemical Thermodynamics 39(12) (2007) 1578-1588.
[9] A.D. Begona Gonzalez, and Jose Tojo, Dynamic Viscosities, Densities, and Speed of Sound and Derived Properties of the Binary Systems Acetic Acid with Water, Methanol, Ethanol, Ethyl Acetate and Methyl Acetate at T) (293.15, 298.15,and 303.15) K at Atmospheric Pressure. 2004).
[10] S. Amrani, M. Tabrizian, Characterization of Nanoscale Loaded Liposomes Produced by 2D Hydrodynamic Flow Focusing, Acs Biomaterials Science & Engineering 4(2) (2018) 502-513.
[11] A. Jahn, S.M. Stavis, J.S. Hong, W.N. Vreeland, D.L. Devoe, M. Gaitan, Microfluidic Mixing and the Formation of Nanoscale Lipid Vesicles, Acs Nano 4(4) (2010) 2077-2087.
[12] R. Karnik, F. Gu, P. Basto, C. Cannizzaro, L. Dean, W. Kyei-Manu, R. Langer, O.C. Farokhzad, Microfluidic platform for controlled synthesis of polymeric nanoparticles, Nano Letters 8(9) (2008) 2906-2912.

[13] M. Russo, P. Bevilacqua, P.A. Netti, E. Torino, A Microfluidic Platform to design crosslinked Hyaluronic Acid Nanoparticles (cHANPs) for enhanced MRI, Scientific Reports 6 (2016).

Attended conferences, oral presentations, posters

- "Optimal design of nucleic acids-materials complexation to improve their bio-nano interactions". Poster session at 62th annual Meeting of the Italian Cancer Society, The exciting path from preclinical research to clinical application. Venice, Italy, 16-18 November 2022.

- "Microfluidics for optimal design of RNAs-materials complexation to improve their bio-nano interactions". Poster session at CRS 2022 Annual Meeting. Montreal, Canada, 11-15 July 2022.

- "Biodegradable lipid-polymer nanoparticles with predictable in vivo miRNA delivery activity". Poster session at Applied Nanotechnology and Nanoscience International Conference – ANNIC 2021, Virtual Edition, 24-26 March 2021.

Publications

- Roffo F., Ponsiglione A.M., Netti P. & Torino E. “coupled Hydrodynamic Flow Focusing (cHFF) to Engineer Lipid–Polymer Nanoparticles (LiPoNs) for Multimodal Imaging and Theranostic Applications” Biomedicines %@ 2227-9059 10(2) (2022) 438. doi:10.3390/biomedicines10020438

- Roffo F., Orlandella F.M., Luciano N., Salvatore G., Netti P. & Torino E. “Lipid-Polymer Nanoparticles (LiPoNs) mediated Codelivery of AntimiR-21 and Gadolinium Chelate in Triple Negative Breast Cancer Theranostics- under revision

- Roffo F., Silvestri S. & Torino E. “Insight into the mutual solvent extraction in coupled Hydrodynamic Flow Focusing to produce Lipid-Polymer NPs”-under preparation

- Lipid-Polymer Nanoparticles (LiPoNs) Mediated Codelivery of miR-622 for Achieving Triple Negative Breast Cancer Theranostics - under preparation

- Cellular detechnment upon nanomaterials interactions: lipid vs polymer dynamics – under preparation

- Nanoparticle production in Hydrodynamic Flow Focusing : a general interpretation and universal model proposal – under preparation

Staying at international research institutions

- I have been hosted at Erasmus University Medical Center (The Netherlands) Department Radiology & Nuclear Medicine- in the Genetic Engineering for Multimodality Imaging laboratory- led by Prof. Laura Mezzanotte from June 26th to October 24th 2022. The project involved the development of labelled lipid-based nanoparticle for Optical and Nuclear Imaging applications.

Relevant achievements

- Expert on the field of Bioengineering in the disciplinary area of ING/ND-34 – Master degree Course DIAGNOSTIC DEVICES AND DRUG DELIVERY

Academic activities within host Institution

- Tutoring activity of type B to the teaching of Mathematical analysis I, University of Naples Federico II, from 26-11-2020 to 29-07-2021

- Tutoring of the master student, Simona Silvestri, “Engineering of lipid polymer nanoparticles for theranostic application in triple negative breast cancer (TNBC)”, Supervisor:Prof. Enza Torino, from February 2020 -May 2021.

- Tutoring of master student, Claudia Latte Bovio, “Droplet Generation by a pilot microfluidics system for application in ocular drug delivery”, Supervisor:Prof. Enza Torino, Co-supervisor: Ing. Alessio Smeraldo, Dr. Maurizio Mangiulli, from September 2020- May 2021.

Participation in national or international projects funded by government institutions or private companies

- EIT Slim Project: 4-month course. 29/07/2020- 13/11/2020

Topic: this project seeks to support healthcare start-ups in their professional development using on-site Bootcamp training in two InnoStars regions combined with remote training and coaching. It gives further support to the start-ups by linking them with appropriate living labs and tracking their progress with a special monitoring tool. It is organized by EIT Health and Department of Economics, Management, Institutions (DEMI) of University of Naples "Federico II " with the partnership of Delft University of Technology (Netherland), University of Evora (Portugal), The Success Detectives (dutch training company) and in collaboration with Universidad Politécnica de Madrid (Spain).

- Freeze Drying - LYO Master Academy BUCHI, 23/04/2020-21/10/2020

Topic: BUCHI e-Learning training path to deepen and develop your knowledge and skills of the Lyophilization process and all its phases. The training cycle consists of 5 webinars.

Collaborations

- CEINGE - Biotecnologie Avanzate S.c.a.r.l., Gaetano Salvatore 486, 80131 Naples, Italy

In vitro analysis of the microRNAs and their target detection were performed in the istitute, CEINGE, that is a specialized group in molecular cell biology.

- Institute of Biostructures and Bioimaging, Via Tommaso De Amicis, 95, 80145 Naplesm, Italy

In vivo MRI analysis were performed in the Istitute of Biostructures and Bioimaging, that is a group of specialist clinics in the diagnostic laboratory and imaging.

- The model to predict the NPs size in HFF has been developeed in collaboration with Prof. Patrick Tabeling. The Prof. Tabeling is a French physicist researcher at the École supérieure de physique et de chimie industrielles de la ville de Paris (ESPCI ParisTech). He is a microfluidics pioneer and he has been the director of the Pierre Gilles de Gennes Institute for Microfluidics (IPGG).